

Spin Dynamics and Manipulation of THz Generation

Dissertation
zur Erlangung des Doktorgrades
an der Fakultät für Mathematik,
Informatik und Naturwissenschaften
Fachbereich Physik
der Universität Hamburg

vorgelegt von
Elias Kueny

Hamburg
2024


Gutachter der Dissertation:	Prof. Dr. Franz X. Kärtner Prof. Dr. Ralf Röhlsberger
Zusammensetzung der Prüfungskommission:	Prof. Dr. Franz X. Kärtner Prof. Dr. Ralf Röhlsberger Prof. Dr. Daniela Pfannkuche Dr. Ilie-Elian Radu Dr. Anne-Laure Calendron
Vorsitzende(r) der Prüfungskommission:	Prof. Dr. Daniela Pfannkuche
Datum der Disputation:	27. September 2024
Vorsitzender Fach-Promotionsausschusses Physik:	Prof. Dr. Markus Drescher
Leiter des Fachbereichs Physik:	Prof. Dr. Wolfgang Parak
Dekan der Fakultät MIN:	Prof. Dr.-Ing. Norbert Ritter

Eidesstattliche Versicherung

Hiermit versichere ich an Eides statt, die vorliegende Dissertationsschrift selbst verfasst und keine anderen als die angegebenen Hilfsmittel und Quellen benutzt zu haben. Sofern im Zuge der Erstellung der vorliegenden Dissertationsschrift generative Künstliche Intelligenz (gKI) basierte elektronische Hilfsmittel verwendet wurden, versichere ich, dass meine eigene Leistung im Vordergrund stand und dass eine vollständige Dokumentation aller verwendeten Hilfsmittel gemäß der Guten wissenschaftlichen Praxis vorliegt. Ich trage die Verantwortung für eventuell durch die gKI generierte fehlerhafte oder verzerrte Inhalte, fehlerhafte Referenzen, Verstöße gegen das Datenschutz- und Urheberrecht oder Plagiate.

Hiermit versichere ich an Eides statt, die vorliegende Dissertationsschrift selbst verfasst und keine anderen als die angegebenen Hilfsmittel und Quellen benutzt zu haben. Sofern im Zuge der Erstellung der vorliegenden Dissertationsschrift generative Künstliche Intelligenz (gKI) basierte elektronische Hilfsmittel verwendet wurden, versichere ich, dass meine eigene Leistung im Vordergrund stand und dass eine vollständige Dokumentation aller verwendeten Hilfsmittel gemäß der Guten wissenschaftlichen Praxis vorliegt. Ich trage die Verantwortung für eventuell durch die gKI generierte fehlerhafte oder verzerrte Inhalte, fehlerhafte Referenzen, Verstöße gegen das Datenschutz- und Urheberrecht oder Plagiate.

Hamburg, den 14. Juni 2024.



Elias Kueny

Summary

Terahertz (THz) spintronics is an emerging field of research that combines ultrafast optics with spintronics, the manipulation of the spin degree of freedom of electrons. The field of spintronics has led to many advances in the development of electronic devices in recent decades. By integrating it with ultrafast magnetism, it becomes possible to leverage the femtosecond speed of lasers to stimulate the launch of spin currents. The use of THz radiation presents an energy-efficient alternative to optical pulses as it directly targets the excitation of magnons. Conversely, magnetic processes on a picosecond timescale result in the emission of THz radiation.

This work explores both aspects of the topic of THz spintronics. First, we develop a high-energy THz source based on optical rectification in LiNbO_3 , with the goal of resonantly exciting the spin dynamics of antiferromagnets. We observe the ferromagnetic and antiferromagnetic uniform magnon modes in the model canted antiferromagnet FeBO_3 . In a second part, we explore spintronic THz emitter designs to find novel approaches for manipulating spin currents. These devices, which consist of pairs of ferromagnetic and non-magnetic layers, convert the picosecond dynamics of spin currents into transient charge currents, resulting in the emission of THz pulses. They enable the probing of the dynamics of the ultrafast demagnetization ferromagnets, while also offering an efficient and practical tool for THz generation. Using spin valve-like samples, this work demonstrates their ability to dynamically enhance or suppress the THz emission with the application of a magnetic field, as well as switch the orientation of the THz polarization.

Zusammenfassung

Die Terahertz-Spintronik ist ein aufstrebendes Forschungsgebiet, das die ultraschnelle Optik mit der Spintronik, der Manipulation des Spin-Freiheitsgrads von Elektronen, verbindet. Das Gebiet der Spintronik hat in den letzten Jahrzehnten zu zahlreichen Fortschritten bei der Entwicklung elektronischer Geräte geführt. Durch die Integration von Spintronik und ultraschnellem Magnetismus wird es möglich, die Femtosekundengeschwindigkeit von Lasern zu nutzen, um den Start von Spinströmen zu stimulieren. Die Verwendung von THz-Strahlung stellt eine energieeffiziente Alternative zu optischen Pulsen dar, da sie direkt auf die Anregung von Magnonen abzielt. Umgekehrt führen magnetische Prozesse auf einer Pikosekunden-Zeitskala zur Emission von THz-Strahlung.

Diese Arbeit erforscht beide Aspekte des Themas THz-Spintronik. Zuest Mal entwickeln wir eine hochenergetische THz-Quelle, die auf optischer Gleichrichtung in LiNbO_3 basiert, mit dem Ziel, die Spindynamik von Antiferromagneten resonant anzuregen. Wir beobachten die ferromagnetischen und antiferromagnetischen gleichförmigen Magnonenmoden in dem verkanteten Modell-Antiferromagneten FeBO_3 . In einem zweiten Teil untersuchen wir spintronische THz-Emitterdesigns, um neue Ansätze zur Manipulation von Spinströmen zu finden. Diese Bauelemente, die aus Paaren von ferromagnetischen und nichtmagnetischen Schichten bestehen, wandeln die Pikosekunden-Dynamik von Spinströmen in transiente Ladungsströme um und emittieren THz-Pulse. Sie ermöglichen die Untersuchung der ultraschnellen Entmagnetisierungsdynamik von Ferromagneten und bieten gleichzeitig eine effiziente und praktische Methode zur Erzeugung von Terahertzimpulsen. Mit Hilfe von Spin-Ventil-ähnlichen Proben wird in dieser Dissertation die Fähigkeit demonstriert, die THz-Emission durch Anlegen eines Magnetfeldes dynamisch zu verstärken oder zu unterdrücken sowie die Orientierung der THz-Polarisation zu verändern.

Résumé

La spintronique térahertz (THz) est un champ de recherche émergent qui combine la photonique ultrarapide et la spintronique, c'est-à-dire la manipulation du degré de liberté du spin. L'étude de la spintronique a permis de nombreuses avancées dans le développement de dispositifs électroniques au cours des dernières décennies. En combinant ce domaine avec celui du magnétisme ultrarapide, il devient possible d'exploiter la rapidité des lasers femtosecondes pour émettre des courants de spin. L'utilisation de rayonnement dans la bande de fréquence THz est une alternative énergétiquement efficace aux impulsions optiques, car elle permet d'influencer directement l'émission de magnons. De même, certains phénomènes magnétiques à l'échelle de la picoseconde entraînent l'émission de rayonnement THz.

Ce travail explore ces deux aspects du thème de la spintronique THz. Tout d'abord, une source THz à haute énergie basée sur le principe de rectification optique dans un cristal de LiNbO_3 est présentée, qui a été développée dans le but d'exciter de manière résonnante la dynamique de spin de matériaux antiferromagnétiques. Nous observons les deux modes de précession uniforme dans le matériau FeBO_3 , qui est ordonné antiferromagnétiquement avec une faible composante ferromagnétique. Dans une deuxième partie, nous explorons différentes structures d'émetteurs THz spintroniques afin de trouver de nouvelles approches pour manipuler les courants de spin. Ces émetteurs, qui consistent en un ensemble de couches minces comportant une ou plusieurs paires de métaux ferromagnétiques et non magnétiques, transforment la dynamique des spins en un courant de charge transitoire, ce qui entraîne l'émission d'une impulsion THz. Ils permettent de suivre la réduction ultrarapide de l'aimantation dans les métaux de transition ferromagnétiques, mais offrent également une source d'émission THz efficace et flexible. En utilisant des émetteurs imitant la structure des valves de spin, ce travail démontre leur potentiel pour accroître ou supprimer dynamiquement l'émission de rayonnement THz par l'application d'un champ magnétique, ainsi que de changer l'orientation de la polarisation du champ THz.

Acknowledgments

Firstly, I'm extremely grateful to my PhD supervisors Prof. Dr. Franz X. Kärtner as well as Prof. Dr. Ralf Röhlsberger, for giving me the opportunity to work on this project and the time to finish it. Words cannot express my gratitude to Dr. Anne-Laure Calendron, for your support, your magic fingers in the lab, and particularly for your uninterrupted participation and supervision within the last years, that extended far beyond your commitments.

Special thanks to all who proofread variously advanced drafts of this thesis: Anne-Laure, Selen, Halil, and Joachim. As well as Prof. Dr. Daniela Pfannkuche and Dr. Ilie-Elian Radu for graciously accepting to be part of the defense committee.

I would also like to extend my thanks to Lars Bocklage and Sven Velten for the enjoyable collaboration, initiating many of the ideas and providing all the samples; Claas Albert from TU Wien for the micromagnetic simulations of FeBO_3 ; as well as Romain Peretti and Mélanie Lavancier from the TeraHertz Photonics Group in Lille for the many meetings helping us use Fit@TDS. This works would not have been possible without the engineering skills of Thomas Tilp, Matthias Schust and Andrej Berg, who built the experimental chamber, the sample holders and the THz horn. I'm indebted as well to Hubertus Bromberger for regularly intervening at short notice to repair the laser. I am also particularly grateful for the administrative support of Uta Freydank, Christine Berber and Neda Lotfiomran.

Thank you to the whole of the UFOX group and the IMPRS-UFAST for contributing to the lively, diverse and inspiring environment I've had the pleasure of working in. And last but not least, I'd like to recognize that maybe the real treasure was the friends we made along the way: the inimitable Lu with her awe-inspiring determination; Anchita, who left too soon but not before helping me rise to fame as a magazine cover illustrator; Igor, who kept patiently re-explaining to me how to make FFTs behave; and my enchanting officemate Erwin, full of stories and dance moves.

Contents

List of Figures	xiii
List of Tables	xvi
List of Abbreviations	xvii
1 Introduction	1
1.1 Spintronics	1
1.2 THz generation	2
1.3 This thesis	3
2 THz generation by optical rectification	5
2.1 Optical rectification	5
2.1.1 Theory	5
2.1.2 Optimization of TPF setups	12
2.2 Experimental setups	17
2.2.1 The 1030 nm setup	17
2.2.2 The 800 nm setup	29
2.3 Applications of the THz radiation	34
2.3.1 THz horn	35
2.3.2 Measurement of a prototypical canted antiferromagnet	43
2.4 Conclusion	51
3 Theory of magnetism	53
3.1 Magnetostatic fields	53
3.1.1 Magnetic fields in vacuum	53
3.1.2 The magnetization of matter	54
3.1.3 The dipolar field	55
3.1.4 Susceptibility and classification of materials	57
3.2 The quantum origin of magnetism	61
3.2.1 Magnetic moment of a bound electron	61
3.2.2 Magnetic moment of an isolated atom	68

3.2.3	Influence of the crystal field	79
3.2.4	Collective behaviors of magnetic atoms	87
3.3	Manipulation of the magnetization	106
3.3.1	Shape anisotropy	106
3.3.2	Stoner-Wohlfarth model of the hysteresis	107
3.3.3	Dynamics of the magnetization	109
3.4	Conclusion	119
4	Spintronic THz emitters	121
4.1	Theory and model	121
4.1.1	Spin current	122
4.1.2	Inverse spin Hall effect and THz emission	124
4.1.3	THz propagation and EOS	126
4.2	Experimental setup	128
4.2.1	Sample design and fabrication	128
4.2.2	Laser setup	132
4.3	Experimental results	138
4.3.1	Influence of the pump energy	139
4.3.2	Identification of the origin of the signal	140
4.3.3	Influence of OID	143
4.3.4	AFM samples	145
4.3.5	Orthogonal magnetizations	155
4.4	Conclusion	161
5	Conclusion	163
A	Material characterization	165
A.1	Principle of time-domain spectroscopy	165
A.2	Fit of the permittivity	168
A.3	Results	171
B	Electro-optic sampling	183
B.1	Theory	183
B.2	Interfaces and reflections: T_{inter}	184
B.3	Nonlinear process: T_{crystal} and T_{env}	186
B.4	Polarization angles: T_{pol}	188
B.5	Propagation to the EOS crystal: T_{prop}	188
B.6	Probe size: T_{overlap}	189
B.7	Balanced photodetectors	189
C	Spintronic THz emitters sources	193
C.1	Single punctual source	194

CONTENTS

C.2 Single punctual source at the output interface	195
C.3 Several punctual sources	197
C.4 Extended sources	198
List of Publications	199
Bibliography	200

List of Figures

2	THz generation by optical rectification	5
2.1	Tilted pulse front caused by refraction and diffraction.	11
2.2	TPF scheme with a $4f$ imaging configuration.	15
2.3	Scheme of the 1030 nm TPF THz setup.	18
2.4	Camera capture of the imaged slits.	19
2.5	Gaussian parameters of the beam.	20
2.6	Beam profile near the LiNbO ₃ crystal.	21
2.7	Beam profiles of the IR pump and the THz collected by the OAPs.	22
2.8	Optimization of the position of the LiNbO ₃ crystal.	23
2.9	Influence of the TPF grating on the THz emission.	24
2.10	THz output measured for different pump energies.	26
2.11	Influence of the compressor misalignment on the THz setup.	28
2.12	Scheme of the rebuild 800 nm TPF THz setup.	30
2.13	Spectrum of the IR pump with and without band-pass filter.	31
2.14	Influence of the TPF grating on the THz emission.	32
2.15	Characterization of the THz radiation.	34
2.16	Scheme of a focusing THz horn.	35
2.17	Simulation of $E_y(\omega)$ in the horn.	38
2.18	Simulated THz pulse along the z axis of the horn.	39
2.19	EOS traces of the THz beam focused in free space and after the horn.	41
2.20	Spatial dependency of the EOS amplitude.	42
2.21	Structure of FeBO ₃ .	44
2.22	Measured MO signal versus H_{DC} .	49
2.23	Measured MO signal versus sample and mount angles.	50
3	Theory of magnetism	53
3.1	Models of a magnetic moment.	55
3.2	Uniformly magnetized cylinders.	55
3.3	Dipolar field lines inside and outside a magnetized material.	56
3.4	Hysteresis curves of different types of magnetic materials.	59

3.5	Lowest energy eigenstates of an hydrogen-like atom.	63
3.6	Vector model of the angular momentum.	64
3.7	Vector model for the L - S and j - j coupling schemes.	76
3.8	Lowest energy levels of an isolated Fe^{2+} ion.	77
3.9	Effective potential of orbitals.	80
3.10	Density of states of free electrons in a magnetic field.	92
3.11	Landau levels in momentum space	94
3.12	Larmor precession of the orbital angular momentum of an electron.	95
3.13	Spontaneous magnetization created by the molecular field.	99
3.14	Energy density of a ferromagnet and corresponding hysteresis curves.	108
3.15	Normalized energy densities in FeBO_3	111
3.16	Comparison of theoretical qFMR and qAFMR frequencies.	118
4	Spintronic THz emitters	121
4.1	Spin Hall effect and inverse spin Hall effect.	125
4.2	Schematic representation of the field addition.	126
4.3	Comparison between the emitted and measured THz field.	127
4.4	Self-shadowing during OID.	129
4.5	Simulated magnetization an OID layer.	130
4.6	Scheme of trilayer and five-layer samples.	131
4.7	Schematized setup for the measurement of the spintronics emitters.	132
4.8	Calibration of the magnetic field from the electromagnet.	134
4.9	Spectrum and beam profile of the probe beam.	136
4.10	Amplitude transfer function of the EOS crystals.	138
4.11	Influence of the pump fluence and spintronics emitters temperature.	139
4.12	Asymmetry in the emitted THz.	141
4.13	Schemes of Fe W and $\text{Fe}^* \text{W}$	143
4.14	Measurements of $\text{Fe}^* \text{W}$ and Fe W	144
4.15	Scheme of $[\text{Pt} \text{Fe}^* \text{W}]_2$	146
4.16	Measurements of $[\text{Pt} \text{Fe}^* \text{W}]_2$ and $[\text{Pt} \text{Fe}^*]_2$	147
4.17	Factors contributing to the THz output.	148
4.18	Experimental and simulated THz waveforms from the bilayer samples.	152
4.19	Comparison of measured and simulated samples.	153
4.20	Scheme of $[\text{Fe}^{90^\circ} \text{W}]_2$	156
4.21	Simulated properties of $[\text{Fe}^{90^\circ} \text{W}]_2$	157
4.22	Measurements of $[\text{Fe}^{90^\circ} \text{W}]_2$	160
A	Material characterization	165
A.1	Example TDS measurement.	167
A.2	Other sources of errors in the TDS data.	168
A.3	Fit of fused silica.	171

A.4	Fit of KTP.	172
A.5	Fit of Kapton.	172
A.6	Fit of FeBO_3	173
A.7	Fit of Al_2O_3	175
A.8	Temperature-dependence of Al_2O_3	175
A.9	Fit of MgO.	177
A.10	Fit of Pt.	177
A.11	Thickness-dependence of the conductivity.	178
A.12	Fit of Fe.	179
A.13	Fit of Py.	179
A.14	Fit of W.	181
A.15	Fit of ZnTe.	181
B	Electro-optic sampling	183
B.1	Demonstration of the EOS deconvolution.	185
B.2	Simulation of a signal cleaned by the lock-in amplifier.	190
C	Spintronic THz emitters sources	193
C.1	Transfer-matrix method for one punctual source.	195
C.2	Transfer-matrix method for a source at the output interface.	196
	List of Publications	199

List of Tables

3	Theory of magnetism	53
3.1	Parallels between the electric and magnetic fields.	54
3.2	Effective magnetic fields characterizing FeBO ₃ .	112
4	Spintronic THz emitters	121
4.1	Input parameters for the spin current model.	124
4.2	List of spintronic THz emitters.	133
4.3	Absorbed fraction of the pump power.	151
4.4	Direction of the spin and charge currents in each FM layer.	158
A	Material characterization	165
A.1	THz refractive index fit parameters.	182

List of Abbreviations

AFM	Antiferromagnetic
CEP	Carrier-envelope phase
DC	Direct current
DCM	Dichroic chirped mirror
DFG	Difference frequency generation
DM	Dzyaloshinskii–Moriya
DOS	Density of states
EOS	Electro-optic sampling
FM	Ferromagnetic
FROG	Frequency-resolved optical gating
FWHM	Full width half maximum
GDD	Group delay dispersion
GVD	Group velocity dispersion
IR	Infrared
ISHE	Inverse spin Hall effect
LLG	Landau-Lifshitz-Gilbert
MCB	Magnetic circular birefringence
MCD	Magnetic circular dichroism
MLB	Magnetic linear birefringence
MLD	Magnetic linear dichroism
MO	Magneto-optic
MOKE	Magneto-optic Kerr effect
NM	Non-magnetic
OAP	Off-axis parabola
OID	Oblique incidence deposition
OR	Optical rectification
qAFMR	Quasi-antiferromagnetic resonance
qFMR	Quasi-ferromagnetic resonance
RKKY	Ruderman-Kittel-Kasuya-Yosida
SFG	Sum frequency generation

SHG	Second harmonic generation
SPM	Self-phase modulation
TDS	Time-domain spectroscopy
TFP	Thin film polarizer
TPF	Tilted pulse front

Mathematical notations

These conventions are used to distinguish related quantities that are denoted by the same letter:

A : real

\vec{A} : vector

\mathcal{A} : complex

\mathbf{A} : matrix or tensor

\hat{A} : quantum operator

Introduction

1.1 Spintronics

From the first magnetic recorders of the late 19th century to current hard drives, magnetic storage has played a crucial role in the development of information technology. The advent of quantum physics and the discovery of the intrinsic magnetic moment carried by electrons, their spin, unlocked a new understanding of the origin of magnetism. During most of the 20th century, charge and spin have however been treated as conceptually separate systems.

This changed with the discovery of the tunneling magnetoresistance [1] and giant magnetoresistance [2, 3], which prompted interest in the spin-dependent transport of electrons in magnetic materials. A few years later, the discovery of the ultrafast demagnetization of nickel when the electrons are heated by a femtosecond laser [4] asserted the link between the dynamics of electrons and spins.

These experiments initiated two related fields: spintronics, or spin-based electronics, concerns the transport of spin currents, while ultrafast magnetism involves the manipulation of the magnetic order on sub-picosecond timescales using laser ultrafast pulses. The development of spintronic devices has led to faster, more efficient and more compact electronic devices, and today spintronic components such as spin valves, magnetic tunnel junctions, and spin transistors are used in the reading head of hard drives, magnetic sensors and magnetic random-access memory.

As our understanding of the spin interactions in the solid state progresses, so do the opportunities for technological applications. Developing the next generation of memory storage requires faster, more energy-efficient methods of switching the magnetization of memory cells, increasing their density and stability. The sensitivity of spintronic sensors must grow accordingly, in order to accommodate denser storage. The current directions of research encompass a large variety of phenomena related to the generation, detection and manipulation of the electron spin, in order to increase the efficiency and controllability of the transfer of angular momentum [5, 6]. Many approaches are studied to find efficient ways of injecting a spin current into different materials. This involves optimizing both the generation of an electrical current, using electric fields,

electromagnetic waves or thermal gradients, and the spin polarization of this current, exploiting among others the spin-dependence of the conductivity, interface transmission, and mean free path of electrons. Multilayer stacks of magnetic and non-magnetic materials are investigated for their potential to sustain a spin current for long distances and efficiently transmit the current through interfaces. At the same time, new materials that combine the properties of semiconductors used in electronics with the spintronic properties of ferromagnets are explored, in order to bring the spin manipulation closer to the electronic devices.

Such studies require measurement techniques that can resolve the fast dynamics of the spin system, which occur in the gigahertz to terahertz range. This connects the spintronics research with the field of ultrafast magnetism, in which femtosecond lasers are used to manipulate the magnetization and monitor its evolution. Recently, the reproducible all-optical switching of the magnetization without the use of a magnetic field was shown possible [7]. Fundamental questions relevant to both fields have been highly discussed in the last years, such as the nature of the channels allowing the dissipation of angular momentum during the ultrafast demagnetization of ferromagnetic films [8, 9], and the role played in it by spin transport [10, 11].

Spintronics and ultrafast magnetism have spawned several subfields, due to the variety of materials and phenomena they encompass. The emergent field of magnon spintronics has become of interest for its capacity to transport information at long distances, using spin waves instead of itinerant electrons as the carrier of a spin current [12]. As they involve localized spins, spin waves propagate in insulators and suffer fewer losses than conventional conductors, and find applications for example as computing elements [13]. At the same time, the field of spin-orbitronics develops the electrical writing and reading of antiferromagnetic memory elements. Antiferromagnetic materials, which have several sublattices whose magnetization cancel, have the benefits of not emitting a stray field, while also having faster dynamics than ferromagnets [14, 15]. Terahertz (THz) spintronics is the use of electromagnetic pulses in the THz range rather than optical. It overlaps with the frequency range of spin waves, allowing their resonant and thus more efficient excitation. Indeed, THz pulses have been shown to coherently turn on and off spin waves in antiferromagnets [16].

Not all mechanisms of magnetization switching, ultrafast demagnetization and spin transport are well-understood even today. Deciphering the out-of-equilibrium processes and complex interactions in solids is still challenging, and the difficulty increases with the large variety of complex materials and structures used in spintronic applications [17].

1.2 THz generation

The link between THz radiation and magnetism goes both ways, as spintronic devices have advanced the technology of THz generation. This frequency band between mi-

crowaves and infrared hosts many low-energy excitation in matter, such as spin waves, lattice and molecular vibrations. It is of interest for spectroscopy, medical imaging and wireless communication.

There is a large variety of mechanisms that generate THz radiation. Finding the right source depends on the balance between the peak electric field, bandwidth and degree of coherence required from the THz pulses, as well as the emission efficiency, damage threshold, size and required infrastructure of the emitting device. Classical tabletop sources comprise photoconductive antennas, optical rectification, optical parametric oscillation and plasma-based sources, all but the first exploiting the nonlinear response of optically pumped materials. Quantum cascade lasers can emit THz radiation directly but typically need to be operated at cryogenic temperatures, while sources based on particle acceleration such as synchrotrons, klystrons or free-electron lasers [18] can reach high output power, but do not have the accessibility of tabletop sources.

While the emission of THz radiation following the dissipation of a spin current in a non-magnetic layer was first seen as a useful probe of the magnetization dynamics [19, 20], spintronic THz emitters are now an established source in their own right. Their main advantages are their ease of operation and their large bandwidth, reaching up to 30 THz [21]. They can be upscaled to emit electric fields up to 300 kV cm^{-1} [22], comparable to the highest-intensity photoconductive antennas [23] and the typical emission by optical rectification in LiNbO_3 . The latter has been shown to emit up to 1.2 MV cm^{-1} [24], and remain one of the preferred methods for generating high-energy single-cycle pulses.

1.3 This thesis

This thesis explores both sides of the topic of THz spintronics. The first goal of this project was the development of a high-energy THz source to resonantly trigger spin dynamics in antiferromagnets. The second was the exploration of spintronic THz emitters designs and new ways to manipulate the spin current.

Chapter 2 – THz generation by optical rectification concerns the development of a single-cycle THz source using the pulse front tilt technique in LiNbO_3 . It starts by laying some theoretical background about nonlinear optics, then expands on the experimental techniques to implement a pulse front tilt scheme. It continues with a description of the THz sources that were build for this project, as well as a THz horn designed to enhance their peak electric field. Finally, it describes the use of the THz radiation to trigger the two spin precession modes in the model antiferromagnet FeBO_3 .

Chapter 3 – Theory of magnetism is mainly aimed at an audience unfamiliar with magnetism. It provides an overview of the origin of the magnetic phenomena mentioned in this thesis and the theoretical foundations necessary to understand the challenges of spintronics. Starting with the basic quantum properties of electrons, it paints a broad

picture of the emergence of magnetic properties as the system increases in complexity. It concludes by bringing these concepts together into a model of spin precession as used for FeBO_3 , and paves the way for a description of spin currents in conductors.

[Chapter 4 – Spintronic THz emitters](#) concerns the design and measurement of spintronic THz emitters. After an overview of the spintronic phenomena on which such emitters rely, it describes our concept for samples that can operate without the need for an external magnetic field to stabilize the magnetization. It follows with the measurement of the THz emission by different classes of samples, with varying number of layers and magnetic configurations. The accompanying simulations of the spin current and THz emission are used to analyze the behavior of the different samples and further our understanding of the spin current.

Finally, the appendices offer additional details. [Appendix A – Material characterization](#) lists the optical properties in the THz range of the materials used throughout this work. [Appendix B – Electro-optic sampling](#) and [Appendix C – Spintronic THz emitters sources](#) describe the numerical model used to recover the spectrum of emitted THz radiation, notably inside the spintronic THz emitters.

THz generation by optical rectification

In this first chapter, our objective is the generation of high-energy THz pulses to excite the magnetization dynamics of antiferromagnets. Such materials have magnon frequencies typically in the few hundreds of GHz, whose resonant excitation enables the coherent control and the switching of the magnetization [25]. While THz radiation is able to efficiently target the high magnon frequencies of antiferromagnets, achieving a high-energy pulse would open the way to the study of the nonlinear regime [26–28]. To test the capabilities of the setup, we measure FeBO_3 , a well-studied canted antiferromagnet known for its large Faraday rotation and transparency in the visible range [29].

Radiation in the 0.1 THz to 10 THz range is typically generated through the down-conversion of optical or infrared (IR) lasers, resulting in relatively weak pulses due to the lower photon energy. Record energy conversions efficiencies for the generation of single-cycle pulses range from 2.36 % [30] to 3.7 % [31]. Pulse front tilting in cryogenically cooled LiNbO_3 is a prominent technique to achieve such pulses, as it allows the constructive buildup of the THz radiation by matching its phase velocity to the group velocity of the pump, therefore permitting the repeated down-conversion of the pump photons.

Section 2.1 introduces the fundamentals of nonlinear optics enabling the IR-to-THz conversion, as well as the functioning and optimization principles of tilted pulse front (TPF) setups. Our setups are then described in Section 2.2. Finally, Section 2.3 will demonstrate the application of the THz radiation to the excitation of the uniform magnon modes of FeBO_3 .

2.1 Optical rectification

2.1.1 Theory

We begin this chapter with an overview of the mathematical formalism surrounding THz generation via optical rectification (OR), in order to understand the reason behind the use of TPF schemes.

2.1.1.1 Nonlinear optics principles

Electrons are polarized by the presence of electric fields. In a medium, they generally do not respond instantaneously, so that the polarization of the material with the response function $\mathbf{R}(\tau)$ when an electric field is applied is $\vec{\mathbf{P}}(t) = \epsilon_0 \int_{-\infty}^0 \mathbf{R}(\tau) \vec{\mathbf{E}}(t - \tau) d\tau$. In the frequency domain, the polarization is described by the electronic susceptibility tensor χ :

$$\vec{\mathbf{P}}(\omega) = \epsilon_0 \chi \vec{\mathbf{E}}(\omega). \quad (2.1)$$

From the Taylor expansion of the position of an electron in an anharmonic potential, the susceptibility can be expanded as the power series $\chi = \chi^{(1)} + \chi^{(2)} \cdot \vec{\mathbf{E}} + (\chi^{(3)} \cdot \vec{\mathbf{E}}) \cdot \vec{\mathbf{E}} + (\dots)$. Each component $\chi^{(n)}$ of the susceptibility is a tensor of rank $n + 1$, whose coefficients are frequency-dependent. Using the multiple dots operator to represent the successive inner products, the first three orders are written:

$$\vec{\mathbf{P}} = \epsilon_0 (\chi^{(1)} \cdot \vec{\mathbf{E}} + \chi^{(2)} : \vec{\mathbf{E}}^2 + \chi^{(3)} : \vec{\mathbf{E}}^3), \quad (2.2)$$

where $\vec{\mathbf{E}}^2$ is a shortcut for the outer product $\vec{\mathbf{E}} \otimes \vec{\mathbf{E}}$. This can equivalently be written, with implicit summation on repeated indices:

$$P_i = \epsilon_0 (\chi_{ij}^{(1)} E_j + \chi_{ijk}^{(2)} E_j E_k + \chi_{ijkl}^{(3)} E_j E_k E_l). \quad (2.3)$$

In the low field regime, the higher-order perturbations are small and only the first order is not negligible. In this case, the dielectric constant is expressed as $\epsilon_r = \mathbf{n}_2 = 1 + \chi^{(1)}$, and the electric displacement $\vec{\mathbf{D}} = \epsilon_0 \vec{\mathbf{E}} + \vec{\mathbf{P}} = \epsilon_0 (1 + \chi^{(1)}) \vec{\mathbf{E}}$ is linear with the applied electric field.

The first experimental demonstration of the existence of the nonlinear regime was the observation that a strong direct current (DC) electric field can induce birefringence in solids, and was named the DC Kerr effect [32]. It is a third-order nonlinear effect of the form $\vec{\mathbf{P}} = \epsilon_0 (\chi^{(1)} + \chi^{(3)} : \vec{\mathbf{E}}_{\text{DC}}^2) \cdot \vec{\mathbf{E}}$.

The properties of the susceptibility tensor are determined by those of the material. In a lossless and dispersionless medium, all coefficients of χ are real and frequency-independent, in which case Eq. (2.1) is also valid in the time domain [33, chapter 1]. In media with inversion symmetry, all even components of χ vanish. Indeed, when a material is transformed using a transformation matrix \mathbf{A} , the coefficients of a given component of the susceptibility tensor are transformed according to the model [34, chapter 3]:

$$\chi'_{ijk\dots}{}^{(n)} = A_{i\alpha} A_{j\beta} A_{k\gamma} \dots \chi_{\alpha\beta\gamma\dots}{}^{(n)}. \quad (2.4)$$

In the case of inversion symmetry, the transformation matrix is:

$$\mathbf{A} = \begin{bmatrix} -1 & 0 & 0 \\ 0 & -1 & 0 \\ 0 & 0 & -1 \end{bmatrix}. \quad (2.5)$$

Because all other components vanish, $\chi_{ijk\dots}^{(n)} = A_{ii}A_{jj}A_{kk} \dots \chi_{ijk\dots}^{(n)} = (-1)^n \chi_{ijk\dots}^{(n)}$. Since the physical properties of a material must have the same symmetries as the material itself (Neumann's principle), $\chi_{ijk\dots}^{(n)} = \chi_{ijk\dots}^{(n)}$. Consequently, if n is pair, all coefficients of $\chi^{(n)}$ must be zero.

In lossy or dispersive media, the nonlinear susceptibility is a complex quantity relating the complex amplitudes of the electric field and the polarization. We use the complex electric field $\vec{\mathcal{E}}(t)$ defined as:

$$\begin{aligned}\vec{\mathcal{E}}(\vec{r}, t) &= \vec{\mathcal{E}}(\vec{r})e^{i\omega t} = \vec{E} e^{i(\omega t - \vec{k} \cdot \vec{r})} \\ \vec{E}(\vec{r}, t) &= \frac{1}{2} (\vec{\mathcal{E}}(\vec{r}, t) + \vec{\mathcal{E}}^*(\vec{r}, t))\end{aligned}\tag{2.6}$$

where $\vec{\mathcal{E}}(\vec{r})$ is the complex field amplitude and \vec{E} the spatially slowly varying amplitude. A field composed of several monochromatic components is thus:

$$\vec{E}(t) = \sum_{\omega>0} \vec{E}_{\omega}(t) = \frac{1}{2} \sum_{\omega} \vec{\mathcal{E}}_{\omega} e^{i(\omega t)}.\tag{2.7}$$

Because of the factor $1/2$, the real Fourier component $E(\omega)$ (in $\text{V m}^{-1} \text{ Hz}^{-1}$) should not be confused with the complex field amplitude \mathcal{E}_{ω} (in V m^{-1}).

Using Eq. (2.7), we can expand the second-order sum of two fields at the frequencies ω_1 and ω_2 to find the different components generated by their interaction. The corresponding effects are second harmonic generation (SHG) with a susceptibility of the form $\chi^{(2)}(2\omega; \omega, \omega)$, sum frequency generation (SFG) with $\chi^{(2)}(\omega_1 + \omega_2; \omega_1, \omega_2)$, difference frequency generation (DFG) with $\chi^{(2)}(\omega_1 - \omega_2; \omega_1, \omega_2)$, and OR with $\chi^{(2)}(0; \omega_1, \omega_2)$. If one of the two fields is a DC field, we find the Pockels effect, with $\chi^{(2)}(\omega; \omega, 0)$.

$$\begin{aligned}E^2 &= (E_1 + E_2)^2 = (\mathcal{E}_1 e^{i\omega_1 t} + \mathcal{E}_2 e^{i\omega_2 t} + \text{c.c.})^2 \\ &= \mathcal{E}_1^2 e^{i2\omega_1 t} + \mathcal{E}_2^2 e^{i2\omega_2 t} + \text{c.c.} && \text{(SHG)} \\ &\quad + 2\mathcal{E}_1 \mathcal{E}_2 e^{i(\omega_1 + \omega_2)t} + \text{c.c.} && \text{(SFG)} \\ &\quad + 2\mathcal{E}_1 \mathcal{E}_2^* e^{i(\omega_1 - \omega_2)t} + \text{c.c.} && \text{(DFG)} \\ &\quad + 2\mathcal{E}_1 \mathcal{E}_1^* + 2\mathcal{E}_2 \mathcal{E}_2^*. && \text{(OR)}\end{aligned}\tag{2.8}$$

In practical cases, one is usually only interested in the component of the polarization at a specific frequency. For example, the amplitude along the direction i of the second-order polarization at the frequency $\omega_3 = \omega_1 + \omega_2$ created by SFG from two fields of amplitude $\vec{\mathcal{E}}(\omega_1)$ and $\vec{\mathcal{E}}(\omega_2)$ can be explicitly written as:

$$\mathcal{P}_i^{\text{SFG}}(\omega_3) = 2 P_i^{\text{SFG}}(\omega_3) = 2\epsilon_0 \sum_p \sum_{jk} \chi_{ijk}^{(2)}(\omega_3; \omega_1, \omega_2) \frac{1}{2} \mathcal{E}_j(\omega_1) \frac{1}{2} \mathcal{E}_k(\omega_2),\tag{2.9}$$

where the indices i, j, k independently take the value of each spatial direction, and the summation over p indicates the possible permutations of the frequencies ω_1 and ω_2 .

Spelling out the latter gives [35]:

$$\begin{aligned} \mathcal{P}_i^{\text{SFG}}(\omega_3) &= \frac{\epsilon_0}{2} \sum_{jk} \chi_{ijk}^{(2)}(\omega_3; \omega_1, \omega_2) \mathcal{E}_j(\omega_1) \mathcal{E}_k(\omega_2) + \frac{\epsilon_0}{2} \sum_{jk} \chi_{ijk}^{(2)}(\omega_3; \omega_2, \omega_1) \mathcal{E}_j(\omega_2) \mathcal{E}_k(\omega_1) \\ &= \frac{\epsilon_0}{2} \sum_{jk} \left(\chi_{ijk}^{(2)}(\omega_3; \omega_1, \omega_2) + \chi_{ikj}^{(2)}(\omega_3; \omega_2, \omega_1) \right) \mathcal{E}_j(\omega_1) \mathcal{E}_k(\omega_2). \end{aligned} \quad (2.10)$$

Using the intrinsic permutation symmetry convention that the indices corresponding to the input pulses can be freely permuted, $\chi_{ijk}^{(2)} = \chi_{ikj}^{(2)}$ and we obtain:

$$\mathcal{P}_i^{\text{SFG}}(\omega_3) = \epsilon_0 \sum_{jk} \chi_{ijk}^{(2)}(\omega_3; \omega_1, \omega_2) \mathcal{E}_j(\omega_1) \mathcal{E}_k(\omega_2). \quad (2.11)$$

The general expression of the polarization amplitude for a process of any order is [36, chapter 2]:

$$\mathcal{P}_i^{(n)}(\omega) = p_n 2^{l+m-n} \epsilon_0 \sum_{jk\dots z} \chi_{ijk\dots z}^{(n)}(\omega; \omega_1, \omega_2, \dots, \omega_n) \mathcal{E}_j(\omega_1) \mathcal{E}_k(\omega_2) \dots \mathcal{E}_{z,n}, \quad (2.12)$$

where p_n is the number of distinct permutations of the input frequencies, $l = 0$ if $\omega = 0$ or 1 if $\omega \neq 0$, m is the number of zero frequencies to the right of the semicolon, and n is the order of the process.

2.1.1.2 Phase matching in the case of optical rectification

THz generation by optical rectification occurs when two frequencies inside the pump spectrum, which are separated by the THz frequency, interact. Although it is strictly speaking a case of DFG, the THz field is almost constant from the point of view of a femtosecond pump, hence its description as optical rectification. For both cases, the nonlinear polarization amplitude is respectively:

$$\vec{\mathcal{P}}_{\text{OR}}(0) = \frac{1}{2} \epsilon_0 \chi^{(2)}(0; \omega, -\omega) : \vec{\mathcal{E}}(\omega) \otimes \vec{\mathcal{E}}(\omega); \quad (2.13)$$

$$\vec{\mathcal{P}}_{\text{DFG}}(\Omega) = \epsilon_0 \chi^{(2)}(\Omega; \omega_1, \omega_2) : \vec{\mathcal{E}}(\omega_1) \otimes \vec{\mathcal{E}}(\omega_2). \quad (2.14)$$

Using the DFG notation, we define the coordinate system so that the pump beam is propagating along z and linearly polarized along x . From the $\vec{\mathcal{E}}(\omega_1) \otimes \vec{\mathcal{E}}(\omega_2)$ tensor, only one element does not cancel, and the polarization vector at the THz frequency simplifies to:

$$\begin{aligned} \vec{\mathcal{P}}(\Omega) &= \begin{bmatrix} \mathcal{P}_x \\ \mathcal{P}_y \\ \mathcal{P}_z \end{bmatrix} = \epsilon_0 \begin{bmatrix} \chi_{xxx}^{(2)} \\ \chi_{yxx}^{(2)} \\ \chi_{zxx}^{(2)} \end{bmatrix} \mathcal{E}_x(\omega_1) \mathcal{E}_x^*(\omega_2) \\ &= \epsilon_0 \begin{bmatrix} \chi_{xxx}^{(2)} \\ \chi_{yxx}^{(2)} \\ \chi_{zxx}^{(2)} \end{bmatrix} \hat{E}_x(\omega_1) \hat{E}_x^*(\omega_2) e^{-i(\kappa_z(\omega_1) - \kappa_z(\omega_2))z}. \end{aligned} \quad (2.15)$$

The pump thus generates a polarization of the material at the THz frequency propagating with a complex wavevector $\vec{\mathcal{K}}(\omega_1) - \vec{\mathcal{K}}(\omega_2)$ of magnitude $(n(\omega_1)\omega_1 - n(\omega_2)\omega_2)/c$. However, the freely propagating THz field generated by the polarization has a wavevector $\vec{\mathcal{K}}(\Omega)$ of magnitude $n(\Omega)\Omega/c$. This defines the phase mismatch parameter Δk between the already existing and the newly generated THz field:

$$\Delta\vec{\mathcal{K}} = (\vec{\mathcal{K}}(\omega_1) - \vec{\mathcal{K}}(\omega_2)) - \vec{\mathcal{K}}(\Omega). \quad (2.16)$$

In the undepleted pump approximation, the amplitude of the THz field evolves in space as $\hat{E}_{\text{THz}} \propto z \text{sinc}(\Delta\mathcal{k}z/2)$ [35, chapter 2]. If $\Delta\mathcal{k} = 0$, the THz field can consistently build up and its amplitude increases linearly. Otherwise, the THz amplitude oscillates with a spatial period of $2L_{\text{coh}}$, where the coherence length $L_{\text{coh}} = \pi/|\Delta\mathcal{k}|$ is the distance after which the phase of the newly emitted THz field has fully reversed. As the refractive index of the material varies with the frequency, $\Delta\mathcal{k} \approx 0$ for a limited range thereof. Although all nonlinear effects of a certain order occur if the laser intensity is sufficient and the symmetries of the medium do not suppress them, this fact allows the targeting of a specific effect by controlling the phase matching.

Intra-pulse DFG can generate any frequency up to the bandwidth of the pulse. For example, the spectrum of a transform-limited 35 fs Gaussian pulse is 12.5 THz wide, which gives the condition $0 < \Omega < 12.5$ THz. Which frequency is generated depends then on which one, if any, can be phase-matched. In addition, the pump spectrum contains many pairs of frequencies (ω_1, ω_2) separated by a given Ω . Which pump frequencies are used can be seen experimentally in the pump depletion.

Expressing the phase mismatch as a function the two pump frequencies, $\Delta k(\omega_1, \omega_2) = k(\omega_1 - \omega_2) + k(\omega_2) - k(\omega_1)$, we can fix ω_2 and do a Taylor expansion of the phase mismatch around ω_1 :

$$\begin{aligned} \Delta k(\omega, \omega_2) &= \Delta k(\omega_1, \omega_2) + (\omega - \omega_1) \left. \frac{\partial \Delta k(\omega, \omega_2)}{\partial \omega} \right|_{\omega_1} \\ &= \Delta k(\omega_1, \omega_2) + (\omega - \omega_1) \left(\left. \frac{\partial k(\omega - \omega_2)}{\partial \omega} \right|_{\omega_1} - \left. \frac{\partial k(\omega)}{\partial \omega} \right|_{\omega_1} \right) \\ &= \Delta k(\omega_1, \omega_2) + (\omega - \omega_1) \left(\frac{1}{v_g(\omega_1 - \omega_2)} - \frac{1}{v_g(\omega_1)} \right). \end{aligned} \quad (2.17)$$

Assuming that the pump frequencies are chosen so that they are phase-matched and $\Delta k(\omega_1, \omega_2) = 0$, the frequencies $\omega = \omega_1 \pm \delta\omega$ are partially phase-matched as well and generate THz radiation with a frequency $\Omega \pm \delta\omega$. In the first order, what limits the phase-match bandwidth is the difference between the group velocity of the pump $v_g(\omega_1)$ and the one of the THz field $v_g(\omega_1 - \omega_2)$. This causes a narrowing of the generated spectrum in addition to a spatial walk-off. Thus to optimize the efficiency and generate shorter THz pulses, one has to match the group velocities in addition to the wavevectors.

As derived by Vallejo and Hayden [37], we can simplify the phase-matching condition as a function of the central frequency of the pump pulse by setting $\omega_1 = \omega_0 + \Omega/2$ and

$\omega_2 = \omega_0 - \Omega / 2$. The phase mismatch is then:

$$\Delta k = k(\Omega) + k\left(\omega_0 - \frac{\Omega}{2}\right) - k\left(\omega_0 + \frac{\Omega}{2}\right) \quad (2.18)$$

$$c\Delta k = n(\Omega)\Omega + n\left(\omega_0 - \frac{\Omega}{2}\right)\left(\omega_0 - \frac{\Omega}{2}\right) - n\left(\omega_0 + \frac{\Omega}{2}\right)\left(\omega_0 + \frac{\Omega}{2}\right). \quad (2.19)$$

Performing a first-order Taylor expansion of $n(\omega_0 \pm \Omega / 2)$ around Ω , the expression simplifies to:

$$\begin{aligned} c\Delta k &= \left(n(\Omega) - n(\omega_0) - \omega_0 \left. \frac{dn}{d\omega} \right|_{\omega_0} \right) \Omega \\ &= (n(\Omega) - n_g(\omega_0)) \Omega. \end{aligned} \quad (2.20)$$

The phase-matching condition is then equivalent to $n(\Omega) = n_g(\omega_0)$. This means that to avoid interfering destructively, the generated THz field needs to be in phase across the whole crystal, as the group velocity of the pump needs to match the phase velocity of the THz field.

Phase matching in general can be accomplished if the two beams propagate colinearly with compatible refractive indices. For example, one can exploit the birefringence of a positive uniaxial crystal by propagating the beam of highest angular frequency ω_0 as an ordinary wave, minimizing its refractive index to $n_o(\omega_0)$, and the beam of lowest angular frequency Ω as an extraordinary wave, maximizing its refractive index to $n_o(\Omega) \leq n(\Omega) \leq n_e(\Omega)$. Then, under the condition that $n_o(\Omega) \leq n_o(\omega_0) \leq n_e(\Omega)$, there is an angle between the propagation axis and the optical axis of the crystal for which both beams propagate at the same velocity. Another possibility to obtain colinear phase matching is to choose the frequencies so that they make use of the anomalous dispersion of the refractive index near an absorption feature. Due to the frequent presence of phonons in the THz range, the THz bandwidth that can be phase-matched to the pump in this way is limited.

Another method, proposed by Hebling et al. [38], is the TPF scheme, which works by tilting the intensity front of the pump pulse with respect to its phase front by an angle γ . While the pump propagates perpendicularly to its phase front, the generated THz field propagates perpendicularly to the pulse front according to Huygens' principle: $\angle(\vec{k}(\omega_0), \vec{k}(\Omega)) = \gamma$. As we will see in the following section, γ is connected to the angular dispersion of the pump. In this noncolinear geometry, Eq. (2.20) is modified as [39]:

$$c\Delta k = \left(n(\Omega) - \frac{n_g(\omega_0)}{\cos \gamma} \right) \Omega. \quad (2.21)$$

The phase-matching condition is then:

$$\cos \gamma = \frac{n_g(\omega_0)}{n(\Omega)}. \quad (2.22)$$

This method has the advantage that it allows phase matching even in materials whose optical and THz refractive indices differ too much for the colinear geometry to be possible.

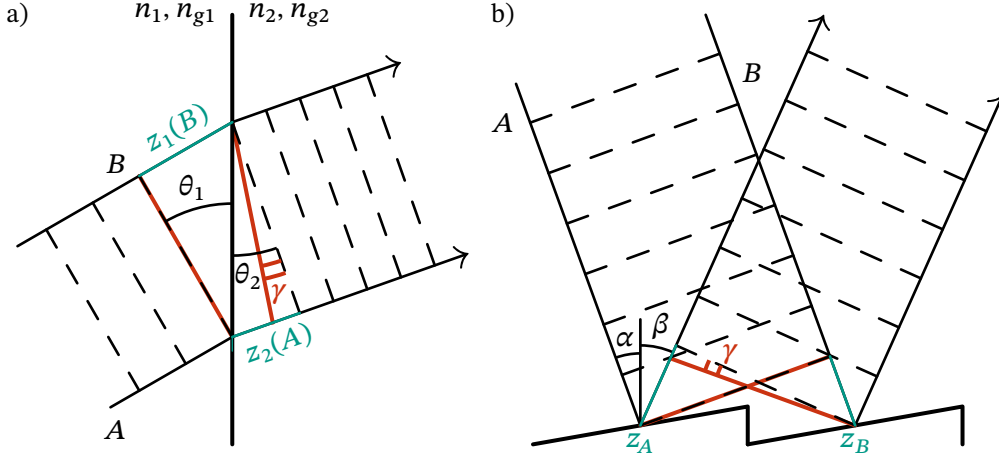


Figure 2.1: Tilted pulse front caused by a) refraction and b) diffraction. The dashed lines represent the phase front, while the red lines are the pulse front, tilted by an angle γ .

2.1.1.3 Pulse front tilt formation

Before going into details, it is necessary to clarify the difference between the phase front and the pulse front. The phase front is the surface of constant phase of each frequency component, which is by definition normal to the direction of its propagation. The pulse front is the surface where the intensity of the pulse is at its peak, or in other words where all frequency components are in phase [40]. A pulse front tilt is thus a transverse group dispersion across the beam.

This group dispersion can be caused by refraction, as illustrated by Fig. 2.1a. When a beam travels through a series of media with refractive index n_i and group index n_{gi} , the phase delay between two phase fronts is identical for all rays in the beam. The group delay however depends on the path of each ray.

Let us consider a beam of diameter d_1 crossing an interface with an angle θ_1 with respect to the normal to the surface. It is refracted with an angle θ_2 following Snell's law, $n_1 \sin \theta_1 = n_2 \sin \theta_2$. Let us assume that the pulse front and the phase front are initially parallel. When the first edge of the pulse (ray A) crosses the interface, the other edge (ray B) still has a distance $z_1(B) = d_1 \tan \theta_1$ to travel until the interface, which it reaches at the time $t_g(B) = n_{g1} z_1 / c$. When ray B crosses the interface, the phase front of ray A has advanced a distance $z_2(A) = d_2 \tan \theta_2$, which satisfies $ct_\phi = n_1 z_1(B) = n_2 z_2(A)$. The pulse front on ray A covers the same distance in $t_g(A) = n_{g2} z_2 / c$. This delay of one edge of the pulse compared to the other creates a pulse front tilt:

$$\tan \gamma = \frac{\Delta z}{d_2} = \frac{c(t_g(A) - t_g(B))}{n_{g2} d_2} = \left(1 - \frac{n_2 n_{g1}}{n_1 n_{g2}}\right) \tan \theta_2. \quad (2.23)$$

If the beam goes through the interface at normal incidence or if both media are non-dispersive, then $\gamma = 0$. Similarly, in the case of a beam going through a prism with rays

A and B respectively propagating a distance z_A and z_B inside the prism, the edge of the pulse along ray A is retarded by:

$$\Delta z = (n_g - n)(z_A - z_B) = -(z_A - z_B) \lambda \frac{dn}{d\lambda}, \quad (2.24)$$

where we see the link between the dispersion of the material and the pulse front tilt. It can thus be expressed in term of the angular dispersion [41]:

$$\tan \gamma = -\lambda \frac{d\epsilon}{d\lambda}, \quad (2.25)$$

where ϵ is the angle of the output ray with respect to the input beam.

Although not by the same physical mechanism, gratings create the same effect, as illustrated by Fig. 2.1b. Because the beam is diffracted, the phase delay t_ϕ between an incident phase front and a diffracted phase front is not identical for all rays, except for the order $m = 0$. With $\theta_i > 0$ and $\theta_d < 0$ the incident and diffracted angle respectively, the path difference between rays on adjacent grooves separated by d is:

$$\Delta z = z_A - z_B = -d(\sin \theta_i + \sin \theta_d) = -m\lambda, \quad (2.26)$$

according to the grating equation. As the group velocity is constant, this creates again a transverse group delay. The angular dispersion of the grating is [42]:

$$\frac{d\epsilon}{d\lambda} = \frac{m}{d \cos \theta_d}. \quad (2.27)$$

The pulse front tilt is thus again $\tan \gamma = \Delta z / d_2 = -\lambda d\epsilon/d\lambda$.

More generally, inside a medium with refractive index n and group velocity n_g , a beam with an angular dispersion $d\epsilon/d\lambda$ has a pulse front tilt [40]:

$$\tan \gamma = -\lambda_0 \frac{n}{n_g} \frac{d\epsilon}{d\lambda}, \quad (2.28)$$

where λ_0 is the central wavelength in vacuum. Given the value of γ required for phase-matching the pump beam and the generated THz radiation in Eq. (2.22), Eq. (2.28) expresses the necessary angular dispersion to apply to the pump beam.

2.1.2 Optimization of TPF setups

Having discussed the mathematical formalism that describes phase matching and the pulse front tilt, we now consider the practical requirements in order to implement an efficient THz generation setup based on the TPF scheme.

2.1.2.1 Choice of the nonlinear material

Following Eq. (2.1), the amplitude of the generated radiation scales with the nonlinear polarization. A good material to perform DFG thus necessitates a large $\chi^{(2)}$ coefficient.

This is the case of dielectric materials with a large bandgap. Using a simple nearly free electron model, the optical susceptibility is expressed as [43]:

$$\chi \approx \left(\frac{\hbar\omega_p}{E_g} \right)^2, \quad (2.29)$$

where ω_p is the plasma frequency and E_p the effective bandgap energy, which is a function of the bonds between adjacent atoms. In crystals with several types of bonds, the bulk susceptibility can be obtained from the superposition of the susceptibilities of individual bonds, whose anharmonic motions are the source of nonlinear susceptibility. LiNbO₃ at room temperature is a ferroelectric material with a large nonlinear susceptibility coming from its different Ni-O bonds. It is heavily used in optical communication systems for its strong Pockels effect [44]. It is birefringent, with a constant ordinary and extraordinary refractive index in the 0.25 THz to 1.4 THz range of 5.5 and 7.3 respectively [45]. At 800 nm, they are respectively of 2.18 and 2.25 [46]. Because of this mismatch, it is impossible to use LiNbO₃ with a colinear geometry and we use instead the TPF geometry.

LiNbO₃ has the advantage that large crystals are available, which allows to scale the THz generation by increasing the pump energy while keeping its fluence under the damage threshold. The critical fluence is 0.3 J cm⁻² for a 30 fs pulses with a repetition rate of 1 kHz [47, 48].

Another important characteristic in the choice of a material is the transparency at the pump and THz frequencies. LiNbO₃ has a wide transparency window with a low absorption under 3.25 eV (above 380 nm), which corresponds to its band gap [49]. The far IR frequencies are however home to optical phonons, the most prominent at low frequencies being centered at 7.6 THz [50–52]. In addition to limiting the THz bandwidth by preventing phase matching, this phonon causes a high absorption coefficient with an order of magnitude of 10 cm⁻¹ at 1 THz, which means that 95 % of the THz radiation is absorbed after only 3 mm of propagation. The transparency can be improved by cooling down the material, which decreases the ordinary and extraordinary absorption coefficients by approximately a factor 2 when cooling down to 80 K [51, 53], and little additional improvement at lower temperatures [52]. This increases the THz output by a factor 3 [54]. As cooling also changes the refractive index [55], it has an influence on the optimal phase-matching angle.

2.1.2.2 Alignment of the crystal

As mentioned in Section 2.1.1.2, the TPF method requires an angle γ between the direction of propagation of the IR pump and the THz radiation. To optimize the transmission of both beams through the interfaces, the crystal is cut so that the IR and THz beams have a normal incidence on the input and output surface, respectively. We use a prism-shaped crystal with the angle of the apex matching the optimal value of γ given by Eq. (2.22), tailored to the pump frequency and the temperature of the crystal.

To further reduce the high Fresnel losses of the THz beam, we coat the output surface of the prism with Kapton polyimide tape, which is an anti-reflection coating suitable for frequencies under 4 THz [56] and adapted to use in vacuum at cryogenic temperatures [57]. While uncoated LiNbO₃ has an interface transmittance at 1 THz of at best 52% (for the ordinary index $n = 5.5$), it increases up to 93% using a Kapton coating with silicon adhesive amounting to a total thickness of $d = 125 \mu\text{m}$ [58]:

$$T = \frac{1}{n} \left| \frac{4nn_c \exp(-i\Omega n_c d / c)}{(n_c + 1)(n + n_c) + (n_c - 1)(n - n_c) \exp(-2i\Omega n_c d / c)} \right|^2, \quad (2.30)$$

where $n_c \approx 1.8$ for both the silicon adhesive [59] and the Kapton tape. Our measurement of the refractive index of Kapton can be found in Fig. A.5.

With the TPF scheme, the optimal propagation length of the pump in LiNbO₃ is limited by cascading rather than by the phase mismatch [60]. In the absence of cascading, each pump photon can be converted into one THz photon and one idler photon at frequency $\omega - \Omega$. The efficiency of the energy conversion is thus limited by the Manley-Rowe quantum efficiency limit: $\eta \leq \hbar\Omega / \hbar\omega$. If the idler photon also satisfies the phase-matching conditions, the conversion can cascade: it is converted into a second THz photon and another idler photon at frequency $\omega - 2\Omega$, and so on [61].

The direction of the successive conversions is governed by the Manley-Rowe relations: in a nonlinear system containing the frequencies $\omega_{mn} = m\omega_1 + n\omega_0$, where m and n are integers, the conservation of energy requires that $\sum_{mn} W_{mn} = 0$, where W_{mn} is the loss at the frequency ω_{mn} . The Manley-Rowe relations thus state that [62, 63]:

$$\sum_{mn} m \frac{W_{mn}}{\omega_{mn}} = 0 \quad \text{and} \quad \sum_{mn} n \frac{W_{mn}}{\omega_{mn}} = 0. \quad (2.31)$$

The DFG process is initially favored over the back-conversion from THz photons into pulse photons via SFG because of the higher number of pump photons. The energy flow however changes sign when the pump is depleted, or earlier if $\Delta k \neq 0$ [64].

Although cascading improves the intrinsic efficiency of the THz emission, the creation of the idler photons also shifts and broadens the pump spectrum, which increases the phase-mismatch and causes a spatio-temporal breakup of the pulse. For a TPF scheme in LiNbO₃, the useful propagation length of the pump is limited to a few millimeters, after which the THz radiation is only absorbed [60]. For this reason, we align the pump close to the apex of the prism. The crystal is mounted on a stage that can be laterally translated to find the optimal position, which depends on the diameter and energy of the pump beam [65].

2.1.2.3 Optimization of the imaging

When it comes to the alignment of the pump beam, three conditions must be met to optimize the THz generation: obtaining the correct pulse front tilt γ inside the crystal, keeping the pulse front flat, and minimizing the pump duration across the pulse front [39].

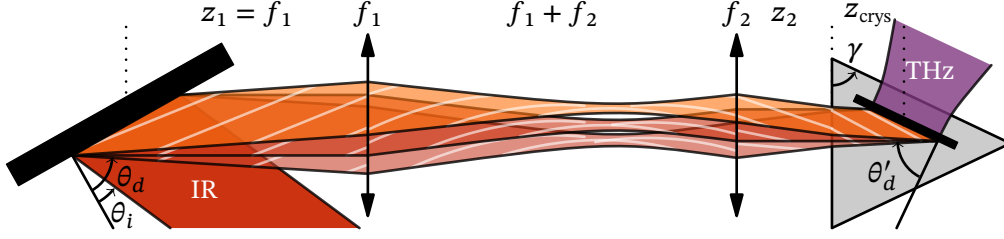


Figure 2.2: TPF scheme with a $4f$ imaging configuration. Represented are three wavelengths within the beam, with slightly differing pulse fronts (white lines). θ_i and M are chosen to satisfy $\theta'_d = -\gamma$ for the central wavelength.

The divergence of the pulse front is mitigated by imaging the grating that introduced the angular dispersion inside the crystal. To minimize the pulse duration across the pulse front, we overlap the image with the pulse front. The diffracted beam has an angle θ_d with respect to the normal to the grating. Due to the demagnification of the beam and the refractive index of the crystal, the image has a different angle θ'_d with respect to the propagation direction (see Fig. 2.2). The imaging is typically done either by a single lens of focal length f at a distance z_1 of the grating, or by a two-lens telescope in a $4f$ configuration with $z_1 = f_1$. The latter has the advantage that the pump can be collimated on the grating and in the crystal, ensuring a flat pulse front. The angle of the image is then [39, 66]:

$$\begin{aligned} \tan \theta'_d &= -\frac{nf}{z_1 - f} \tan \theta_d && \text{(single lens)} \\ &= -\frac{nf_2}{f_1} \tan \theta_d. && \text{(4f telescope)} \end{aligned} \quad (2.32)$$

At the same time, the demagnification and the entry into the crystal affect the pulse front tilt. The initial angular dispersion of the grating is given by Eq. (2.27). It is modified as:

$$\begin{aligned} \frac{d\epsilon}{d\lambda} &= -\frac{z_1 - f}{nf} \frac{d\epsilon_{\text{gr}}}{d\lambda} && \text{(single lens)} \\ &= -\frac{f_1}{nf_2} \frac{d\epsilon_{\text{gr}}}{d\lambda}. && \text{(4f telescope)} \end{aligned} \quad (2.33)$$

According to Eq. (2.28), the pulse front tilt inside the crystal is thus:

$$\tan \gamma = \frac{f_1}{n_g f_2} \frac{m\lambda}{d \cos \theta_d}. \quad (2.34)$$

The value of γ is fixed by Eq. (2.22) to ensure the phase-matching condition. To minimize the pump duration, we set $\theta'_d = -\gamma$. The optimal incidence angle is then [39, 66]:

$$\sin \theta_i = \frac{m\lambda}{d} \left(1 - \frac{M^2}{nn_g} \right), \quad (2.35)$$

where the magnification M is:

$$M^2 = \frac{n^2 n_g d}{2m\lambda} \sqrt{\frac{\lambda^2 m^2}{n_g^2 d^2 \tan^4 \gamma} + \frac{4}{n^2}} - \frac{n^2}{2 \tan^2 \gamma}; \quad (2.36)$$

$$M = \frac{z_1 - f}{f} \quad (\text{single lens}), \text{ or } M = \frac{f_1}{f_2} \quad (4f \text{ telescope}). \quad (2.37)$$

The distance between the grating and the first or single lens is respectively $z_1 = f_1$ or $f(M + 1)$. With z_2 the distance between the second or single lens and the input face of the crystal, the image of the grating is at a depth $z_{\text{crys}} = n(z_1 / M - z_2)$ [39, 66]. We thus mount the crystal on a stage that can be translated longitudinally to find the optimal value of z_2 for a given imaging system.

The last free parameters are the groove spacing d and the diffraction order m of the grating. We use a blazed grating, whose diffraction efficiency is maximal when the diffraction angle matches the reflection angle on the grooves. This is typically achieved for a specific wavelength in the first-order Littrow configuration, with $\theta_d = \theta_i$ and $m = 1$. According to the grating equation:

$$\sin \theta_{\text{Littrow}} = \frac{m\lambda}{2d}. \quad (2.38)$$

Combining Eqs. (2.35), (2.36) and (2.38), we get the optimal groove spacing of the grating if $\theta_i = \theta_{\text{Littrow}}$ [66]:

$$d = \frac{\lambda}{2} \sqrt{1 + \frac{2n}{n_g \tan^2 \gamma}} \quad (2.39)$$

$$M^2 = \frac{nn_g}{2}. \quad (2.40)$$

In practice however, we need to separate the incident and diffracted beams, which offsets the optimal value of d [39].

An additional concern in the setup design is the control of the pump fluence on the LiNbO₃ crystal. On one hand, increasing the fluence improves the conversion efficiency and the THz energy output. On the other hand, it can reduce the spatial quality of the THz beam [65] and must be kept under the damage fluence of LiNbO₃. In the 4f configuration, the pump beam is collimated on the crystal. This allows easily controlling its fluence by scaling the beam with an additional telescope before the grating. In addition, to obtain a round THz beam, the pump needs to have a round projection on the output surface of the prism. Since it is parallel to the image of the grating, this means that the projection of the pump beam on the grating should itself be round. We can thus use a cylindrical telescope with a magnification of $\cos \theta_i$ to reduce the horizontal diameter of the incident beam while keeping the vertical diameter unchanged.

2.2 Experimental setups

We now describe two cryogenic TPF setups that are based on these principles, each adapted to a different laser pump. The first setup was designed and built for a 1030 nm Yb:YAG laser driver. The second was rebuilt and experimentally optimized from a 150 fs, 7.5 mJ 800 nm Ti:sapphire driver, to a 35 fs, 4.9 mJ one.

2.2.1 The 1030 nm setup

The 1030 nm driver for THz generation is a complex laser system based on successive chirped pulse amplification stages. One of its long-term goals is to provide a 200 mJ pump to generate a 1 mJ single-cycle THz pulse for electron acceleration [67]. Ultimately, it aims to provide up to 1 J pulses in order to simultaneously drive several such accelerators.

The laser system is seeded by an Yb:KYW oscillator delivering 4 pJ, 210 fs pulses centered at 1029.5 nm with a repetition rate of 42.5 MHz. The oscillator is followed by a commercial amplifier module composed of several Yb-doped fiber amplifiers. After the first amplifier, a 60 pJ beam is split up and sent to a stretcher module, which is composed of four chirped fiber Bragg gratings with a 6 nm bandwidth, interspaced with two fiber amplifiers to compensate the losses. The stretcher is designed to introduce a stretching ratio of 0.8 ns nm^{-1} , in order to maintain the pulse intensity in the following amplification stages under the thresholds for damage and nonlinear behavior. It increases the pulse duration from 750 fs to 2.35 ns. Within the stretcher module, two additional fiber amplifiers increase the energy of the stretched pulses to 1 nJ. This beam is then used to seed an Yb:KYW regenerative amplifier, which delivers 6.5 mJ pulses at 1 kHz. A part of the output is used for further amplification. Several booster stages were developed: a cryogenically cooled thin-disk Yb:YAG amplifier, a cryogenically cooled Yb:YAG rod amplifier [68] and a room-temperature Yb:YAG rod amplifier [69]. Another part of the output of the regenerative amplifier is immediately recompressed with double-pass Treacy compressor using two dielectric gratings, compressing the 2.35 ns pulses down to 615 fs.

2.2.1.1 Choice of parameters

Our THz setup is build and optimized using the compressed beam from the regenerative amplifier, with the future possibility of upgrading to the 10 Hz, 50 mJ room-temperature Yb:YAG amplifier. The available LiNbO_3 crystals are congruent Z-cut $\text{MgO}:\text{LiNbO}_3$ prisms with an apex of 56.2° and two angles of 61.9° , which is close to the optimal value of γ for a 1030 nm pump as well as a 800 nm pump, both at room and cryogenic temperature. We expect to phase-match slightly different THz frequencies in different conditions.

For our calculations, we use the values $n = 2.3019$ and $n_g = 2.2343$ at 1030 nm, and $n_{\text{THz}} = 4.8890$ [53]. According to Eq. (2.39), the most efficient grating for $\gamma = 62^\circ$ would

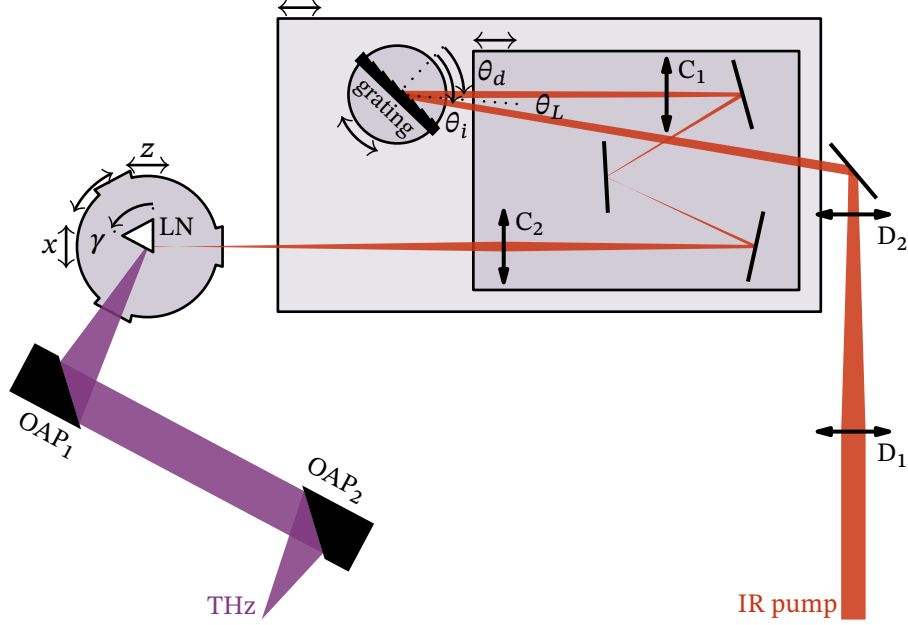


Figure 2.3: Scheme of the 1030 nm TPF THz setup. C: cylindrical telescope; D: demagnetizing telescope; LN: LiNbO₃.

have 1543.53 grooves/mm. We use a 1500 grooves/mm blazed grating optimized for first-order refraction, which has a Littrow angle of 50.58° . From Eqs. (2.35) and (2.36), the superposition of the grating image onto the pulse front is then optimized for $M = 1.63$ and $\theta_i = 48.16^\circ$. We can obtain a close magnification using lenses of 400 mm and 250 mm focal lengths, giving $M = 1.6$. The optimal angle of the grating to obtain the correct pulse-front tilt is then given by Eq. (2.34): $\theta_i = 47.42^\circ$.

We implemented the telescope with cylindrical lenses (C_1 and C_2 in Fig. 2.3). This has the advantage that only one axis of the beam is focused inside the telescope, which prevents the intensity at the waist from reaching the threshold for nonlinear behavior. While the vertical diameter d_y of the IR beam is unchanged, the horizontal diameter d_x is affected by the grating and the telescope. At the output of the prism, the projection of the pump has an ellipticity $d_x / d_y = \cos \theta_d / (M \cos \theta_i \cos \gamma) = 1.16$ if we use the grating at the optimal angle. This is close enough to a round beam that, for the simplicity of the setup, we do not implement another cylindrical telescope to adjust d_y .

To stay under the damage threshold of LiNbO₃ (about 100 mJ cm^{-2}), we aim at a fluence on the crystal of 55 mJ cm^{-2} , with an available energy of 2.5 mJ. This is obtained for an input diameter $d_y = 4.62 \text{ mm}$. We measured the beam from the compressor to have a diameter of 15 mm. To reduce it, we implemented at the input of the setup a demagnetizing telescope using lenses with 150 mm and -50 mm focal lengths (D_1 and D_2 in Fig. 2.3), which gives $d_y = 5 \text{ mm}$.

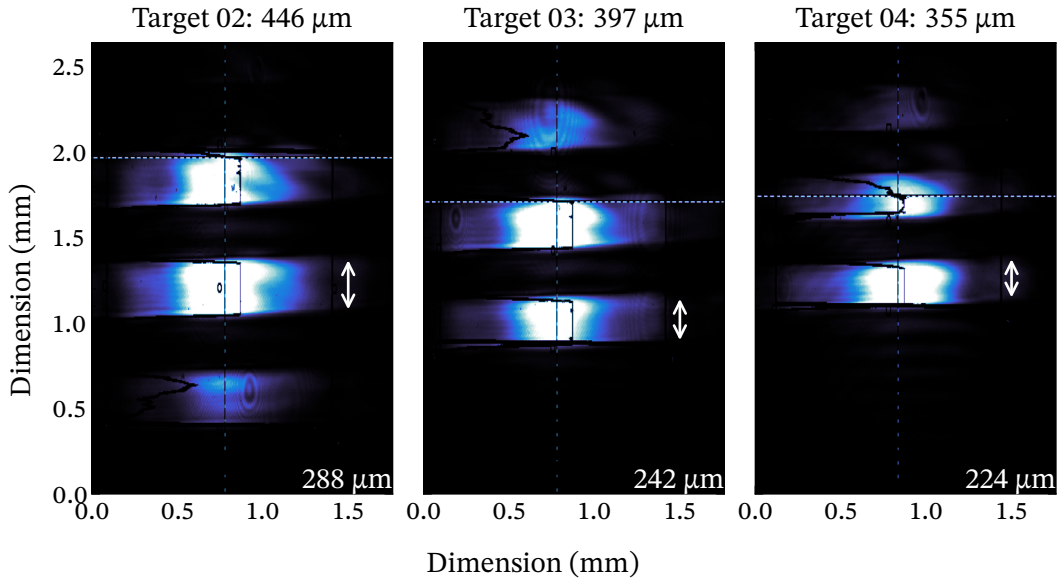


Figure 2.4: Camera capture of the imaged slits from three adjacent targets with different spatial frequencies. The lines visible in the beam are due to the data being extracted from a screenshot.

2.2.1.2 Optimization

Fig. 2.3 shows the scheme of the setup. To facilitate its optimization, we placed the grating on a breadboard with a translation stage, and the cylindrical telescope on a second translatable breadboard on top. This allows us to tweak the distance between the grating or the crystal and the telescope, without changing the alignment of the latter. Instead of moving the crystal, which would influence the THz collection, moving the large breadboard only involves realigning the input beam onto the grating. We however placed the crystal on short longitudinal (z) and a lateral (x) translation stages, to optimize the position of the crystal around the image of the grating.

At the time we built this setup, the work of Tokodi, Hebling, and Pálfalvi [66], which clarifies the difference between the optimization of $4f$ and single-lens TPF configurations, was not yet published. For this reason, we optimized the magnification of the cylindrical telescope and the imaging of the grating, without addressing the influence of the distance between the grating and the first lens on the pulse front tilt. We also accepted that the focus of the cylindrical telescope was placed a few centimeters before the optimized crystal, as this had been measured to improve the THz generation efficiency by other group members having experience with single-lens TPF setups.

We first aligned the cylindrical telescope using a shear plate interferometer to ensure the collimation of the beam at the input and output of the telescope. The spectral bandwidth of the KYW regenerative amplifier was too large to produce visible fringes on the shear plate, so we used instead a 1030 nm alignment laser. To verify its magnification,

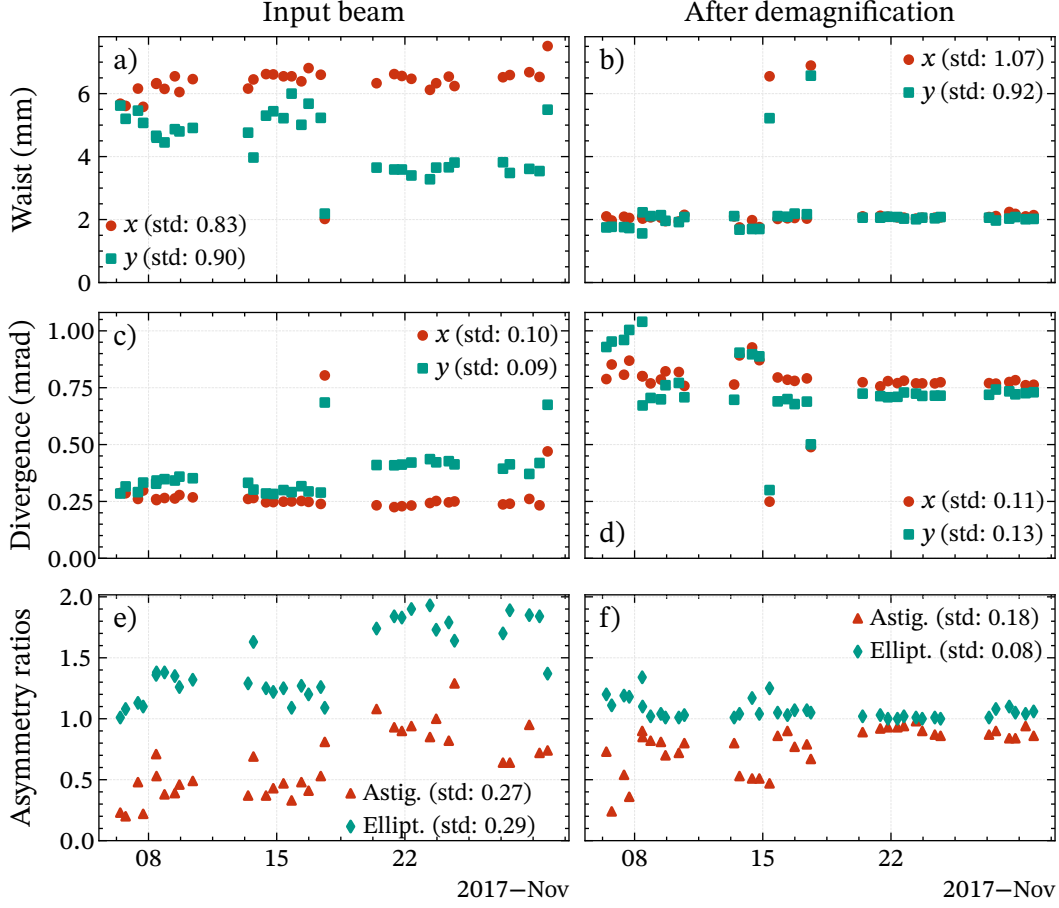


Figure 2.5: Gaussian beam parameters extracted from twice-daily measurements with a beam propagation analyzer, before (left column) and after the demagnifying telescope (right column): a–b) calculated waist diameter, c–d) full divergence angle, e–f) astigmatism and ellipticity. The astigmatism is calculated as $2|Z_0^x - Z_0^y| / (Z_R^x + Z_R^y)$, where Z_0 is the waist distance and Z_R the Rayleigh length.

we replaced the grating by a mirror and inserted a resolution target in the input beam. The resolution target was a thin opaque plate with several groups of slits with a known spatial frequency. With a camera at the position where the image of the slits is sharp, measuring their spatial frequency gives the magnification of the telescope. As shown in Fig. 2.4, we measured a magnification of 0.65, 0.61 and 0.63 for three groups of slits, close to the nominal magnification of 0.6.

We then replaced the alignment laser by the compressed beam from the KYW system. With the demagnetizing telescope to increase the fluence on the crystal, the amplified astigmatism of the input beam creates a horizontal focus close to the crystal. As shown

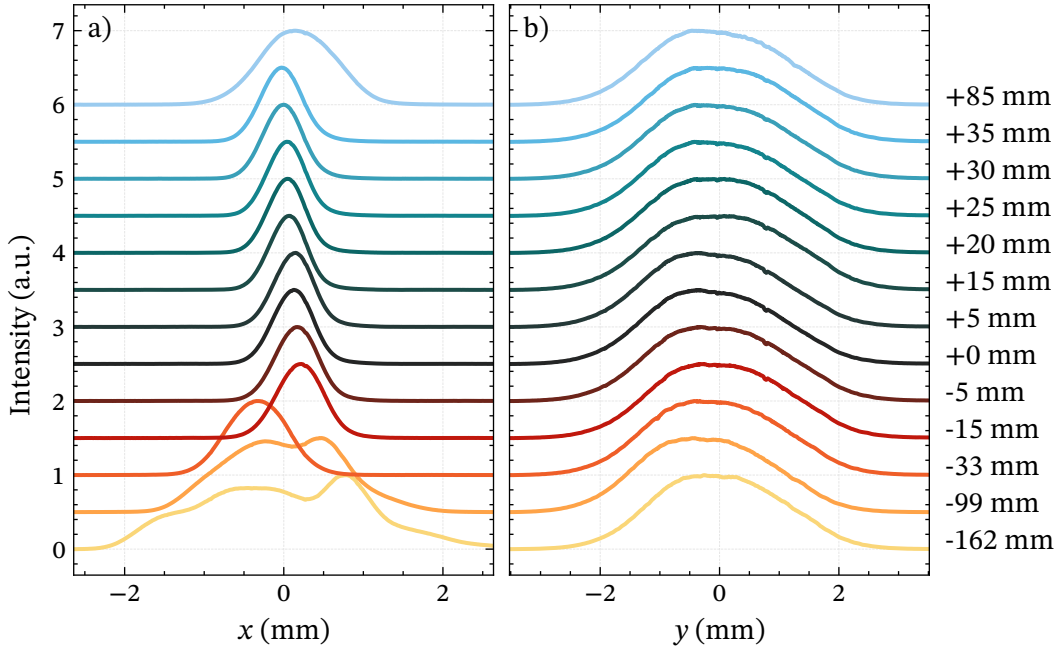


Figure 2.6: a) Horizontal and b) vertical beam profile after the cylindrical telescope, at varying distances from the LiNbO_3 crystal. The cylindrical lens C_2 is approximately at the position -300 mm.

by Fig. 2.5, the ellipticity and astigmatism of the compressed beam change over time, in spite of the laser system having a pointing stabilizer, which prevents us from durably keeping the input beam collimated. We compensate for it by realigning the input beam daily and reoptimizing the position of the crystal to make up for the moving focus.

Fig. 2.6 shows the pump profile at different distances from the input face of the crystal. While the IR beam is as planned vertically collimated with a $1/e^2$ diameter of 4.2 mm), it shows a horizontal focus. Its waist is 0.9 mm $1/e^2$, and the diameter stays under 1.2 mm between -15 mm and $+35$ mm. Before the focus, vertical diffraction lines are visible in the beam profile, whose origin we have not identified. Fig. 2.7a shows the full beam at the position of the crystal.

We calculated the fluence of the pump incident on the LiNbO_3 crystal using the measured beam profile at the same distance from the cylindrical telescope as the crystal. Due to other experiments running in parallel, we typically have 1.22 mJ available at the input of the setup. The proportion of energy diffracted by the grating instead of being reflected in the 0th order is controlled by the polarization of the beam. Maximizing the first order gives an energy incident on the crystal of 1.16 mJ. This corresponds to a fluence in the focus of $8E / (\pi d_x d_y) = 78 \text{ mJ cm}^{-2}$, which is slightly higher than our aim.

During the work described in this chapter, we use several different pyroelectric THz detectors, depending on their availability. Their response is frequency-dependent and

generally uncalibrated. As they are also sensitive to IR radiation, they are shielded with a layer of silicon or polyethylene, which also influence their sensitivity to THz radiation. We conducted most measurements with a Gentec SDX-1152 detector. From cross-calibration against other calibrated detectors, we estimate its sensitivity at 0.4 THz to be $94 \pm 10 \text{ mV } \mu\text{J}^{-1}$.

Fig. 2.8 shows the influence of the crystal position on the THz energy measured at the output face of the crystal. Minimizing the distance to the detector is necessary to capture the full THz beam despite its divergence, which we expect to change with the position of the crystal with respect to the IR focus. Fig. 2.8a shows the full 12 mm extent of the longitudinal translation stage. We took this measurement with a different cylindrical telescope, with lenses of 300 mm and 200 mm focal length. The pump caustic near the focus is thus not directly comparable to Fig. 2.6. We can however expect that the beam profile does not significantly change within 12 mm of the focus, thus we mainly attribute the variation of the THz generation to the phase matching. Fig. 2.8b shows that the highest output was obtained with the IR beam as close to the edge of the crystal as possible without losing energy by clipping. This is expected with an uncollimated pump, as the pulse front tilt depends on its diameter and thus varies in space. The phase-matched volume is reduced and it is most advantageous to shorten the THz absorption.

Once the optimal crystal position was determined, we added a pair of gold-coated OAPs to collect and refocus the THz radiation. We aligned them on a separate breadboard using a helium-neon alignment laser, propagating horizontally and along a well-defined axis. To simulate the divergent THz beam, we created a spherical wave with a pinhole in the focal plane of a short lens. We placed the first OAP so that the pinhole lies in its focal point and the beam is reflected at 90° from its original propagation axis. We used a shear plate interferometer to ensure the collimation of the alignment beam along both axes, as tilted fringes indicate an error in the position and curved fringes indicate that the OAP

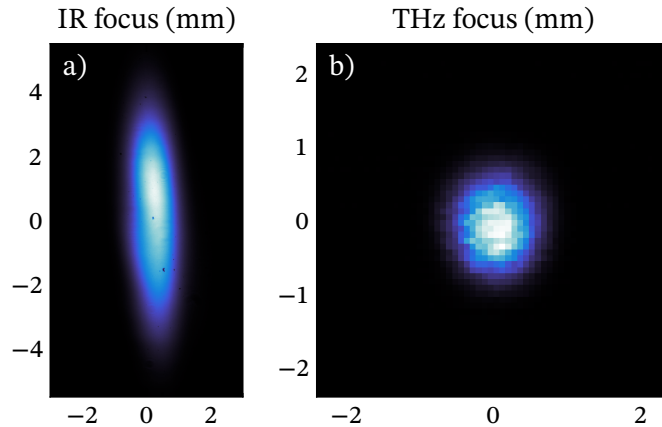


Figure 2.7: Beam profiles of a) the IR pump at the position of the crystal and b) the THz collected by the off-axis parabolas (OAPs).

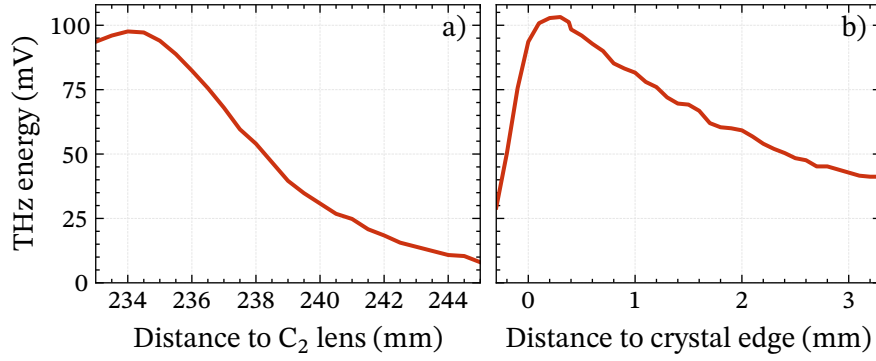


Figure 2.8: Optimization of the position of the LiNbO₃ crystal, using a) the z and b) the x translation stage indicated in Fig. 2.3. The THz detector was placed directly at the output face of the crystal. The C₂ lens has here a focal length of 200 mm.

is tilted or decentered. We then placed the second OAP, adjusting its angle so that the beam is reflected parallel to its original direction, and the distance between the OAPs so that the pinhole is imaged in the focal plane of the second OAP.

Although the goal is to refocus the THz beam as tightly as possible, we are limited by the available OAPs, which need a large diameter to collect the highly diverging THz radiation. In addition, the second OAP needs a suitable hole to superpose an IR probe to the THz beam, in preparation of electro-optic sampling (EOS). The best combination is a pair with reflected focal lengths of 6" and 4" and diameters of 3" and 2", respectively. With a 0.9 mm × 4.2 mm pump incident on the crystal, thus 1.9 mm × 4.2 mm projected on the output surface, we assume a 1.34 mm × 2.97 mm waist in the input focal plane of the first OAP. According to a reZonator simulation, we can thus expect to obtain a 0.90 mm × 1.98 mm focus after the second OAP, with a collimated beam of 0.85" × 0.4" diameter between the OAPs. In addition to measuring the energy of the THz pulse, we use EOS to probe its waveform. The principles of EOS measurements are detailed in Appendix B.

In practice, although the THz beam seemed indeed collimated, it was clipping on the 2" second OAP. In addition, the THz detector measured in the focus only 40 % of the energy at the output of the crystal. As the reflectivity of gold-coated OAPs is close to 1 [70], this points to a poor THz beam quality. Fig. 2.7b shows a measurement of the beam profile in the OAP focus, with a $1/e^2$ diameter of 1.4 mm × 1.9 mm. The fact that the y axis behaves as expected hints that the problem is due to the uncorrected divergence on x of the pump beam.

After aligning the OAPs, we installed the cryogenic chamber. It has an anti-reflection-coated fused silica input window, and a 5 mm-thick TPX output window, with an 88 % THz transmissivity. A second window allows for the output of the pump and its green second harmonic, which experience near-total internal reflection on the THz output face. The crystal was fixed between layers of indium foil, to ensure the thermal contact with

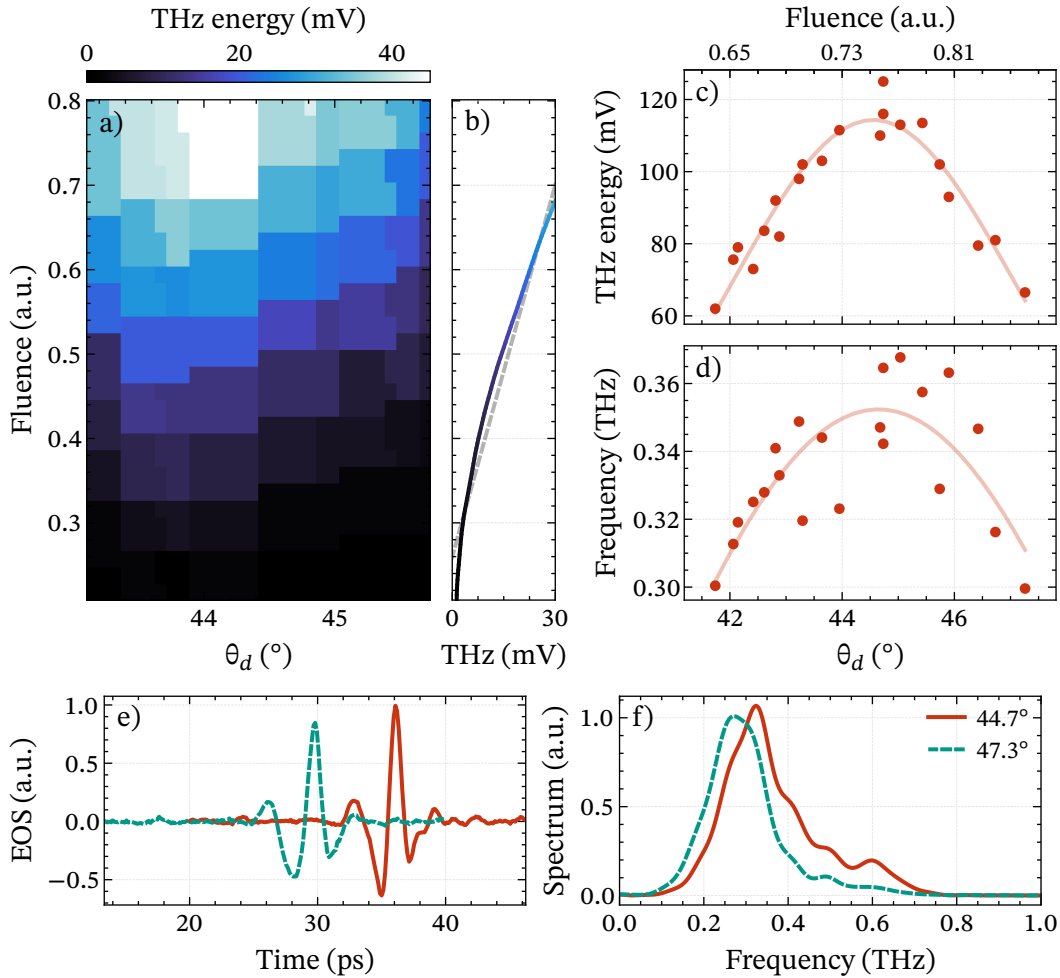


Figure 2.9: Influence of the TPF grating on the THz emission. a) Emitted THz energy at the output of the chamber, while scanning the pump energy and the diffracted angle θ_d . b) Average normalized influence of the fluence on the THz energy, with linear fit (dashed line). THz c) energy and d) mean frequency, while scanning the diffracted angle at constant energy. e) EOS traces and f) their Fourier spectra at two angles giving the maximum and minimum THz energy, respectively.

the liquid nitrogen-cooled internal chamber. We first attempted to optimize the chamber at room temperature, in which case the phase-matching conditions do not change. And indeed, we observed that the physical angle of the grating maximizing the THz energy is the same with and without the chamber.

Fig. 2.9 shows the outcomes of rotating the grating. The measurements were taken with the chamber at room temperature, and the THz detector positioned at the output window. The grating was mounted on a graduated rotating stage, centered on the axis

of the cylindrical telescope so that its rotation does not influence its imaging. Since it is required to maintain the alignment of the diffracted beam through the telescope, we moved the incident beam each time we incremented the angle ψ characterizing the orientation of the grating. The diffracted angle θ_d was thus linearly following the rotation of the grating:

$$\begin{aligned}\theta'_d &= \theta_d + \Delta\psi; \\ \sin \theta'_i &= \frac{m\lambda}{d} \sin(\theta_d + \Delta\psi).\end{aligned}\tag{2.41}$$

To calibrate the correspondence between the angle of the rotation stage and the incident and diffracted angles, we used our knowledge of the Littrow angle (see Eq. (2.38)). Keeping the incident beam aligned, we rotated the grating until the diffracted beam was superposed to it, at the angle ψ_{Lit} . In this case, the value of the incident angle follows the rotation of the grating:

$$\begin{aligned}\theta_i &= \theta_{\text{Lit}} + \psi - \psi_{\text{Lit}}; \\ \sin \theta_d &= \frac{m\lambda}{d} \sin(\theta_{\text{Lit}} + \psi - \psi_{\text{Lit}}).\end{aligned}\tag{2.42}$$

With a perfect alignment, calculating θ_d from either Eq. (2.41) or Eq. (2.42) should give the same values. However, we found that in average, for a rotation $\Delta\psi$, the value of θ_d calculated from the measurement of the Littrow angle was only changing by about $\Delta\psi/2$. Due to the bandwidth of the pump, the diffracted beam spans an angle of 0.5° to 0.6° at the relevant incident angles. On one hand, since Eq. (2.42) is unchanged in the case of optical misalignments and only depends on superposing the diffracted beam on top of the incident beam, this is the upper limit of the error on ψ_{Lit} , which leads to a maximum error on θ_d of $\pm 0.25^\circ$. On the other hand, Eq. (2.41) assumes that the diffracted beam does not move, which is difficult to ensure in practice. We used as reference two irises placed before the telescope, with a limited distance between them to avoid clipping the incident beam. In addition to the same error due to the bandwidth, we can estimate, for two irises separated by 150 mm and an alignment precision within 1 mm on each of them, a maximum error of $\pm 0.76^\circ$ on θ_d . We estimated the value in Fig. 2.9 using the weighted mean of both methods.

In Figs. 2.9a and 2.9b, we scanned the pump energy from 0.3 mJ to 1 mJ for each alignment of the grating. We did not measure the beam profile, hence the fluence is given as $F \propto E \cos \theta_i / \theta_d$. Its average influence on the THz energy is shown in Fig. 2.9b. As a second-order nonlinear process, the THz output energy depends on the square of the pump fluence, as is shown by Fig. 2.10, in which we measured the THz output for fluences up to 130 mJ cm^{-2} . However, we attribute this to the response of the detector, which is not guaranteed to be linear, rather than to the THz generation. Assuming a calibration of $94 \text{ mV } \mu\text{J}^{-1}$, we reached a THz emission of $19 \text{ } \mu\text{J}$ for a 21.7 mJ pump, or conversion efficiency of 8.8×10^{-4} .

The measurement in Figs. 2.9a and 2.9b was made using the 2" LiNbO₃ crystal originally in the chamber. The other subplots are extracted from a different measurement

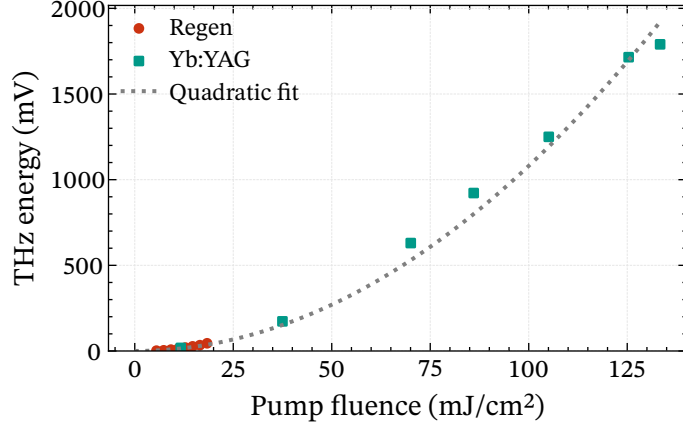


Figure 2.10: THz output measured for different pump energies, with the usual beam of the regenerative amplifier (data from Fig. 2.9a, for $\theta_d = 44^\circ$), and with the beam of the Yb:YAG amplifier, compressed as well. The diameter of the latter was measured to $5.6 \text{ mm} \times 7.4 \text{ mm}$, and the diameter of the beam from the regenerative amplifier is estimated to $1.9 \text{ mm} \times 7.3 \text{ mm}$.

made using the same LiNbO_3 crystal we previously used without the chamber, during which we took for every angle of the grating an EOS measurement of the THz beam in the OAP focus. Fig. 2.9c shows the evolution of the THz energy with θ_d , with a Gaussian fit linearly biased by the variable fluence. The optimal angle is 44.7° , with the small difference compared to Fig. 2.9a likely coming from a change in the divergence of the pump beam between the two measurements.

With a bandwidth of 4.5 nm, the pump could generate THz radiation with a frequency up to 2.5 THz. The measured central frequency is controlled by the phase matching: from Eq. (2.22), $n(\Omega) = n_g(\omega_0) / \cos \gamma$. As we rotate the grating, the pulse front tilt of each frequency component in the IR pump beam is monotonously increasing with θ_d (see Eq. (2.34)), within the range of the measurement. Assuming that we always phase-match the central wavelength and that $n(\Omega)$ is monotonously increasing with Ω , the increased γ would lead to a higher THz frequency Ω . Reciprocally, the value of γ that maximizes the out-coupling of the THz beam is fixed, notably by the cut of the crystal and the position of the output window of the chamber. As the same pulse front tilt is achieved by lower wavelengths, which have a larger group index, preserving γ while increasing θ_d would also lead to a monotonously increasing THz frequency.

However, Fig. 2.9d shows that we observe instead a Gaussian behavior, with the highest central frequency found at the same angle as the highest THz output. This unexpected coupling implies that the loss of THz energy is associated with the narrowing of the useful pump bandwidth. Since the optimal grating angle is a balance between the pulse-front tilt and the imaging of the grating, and the pump is angularly dispersed, we can assume that the reduction of the THz frequency is due to the rotation of the grating

image, which overlaps the pulse-front tilt for fewer frequencies at the same time. The central frequency of 0.30 THz to 0.35 THz indicate that only a 1.1 nm to 1.3 nm-wide bandwidth of the pump is used. This might be caused by the divergence of the pump, as the pulse front and the image have different curvatures if the pump is not collimated on the grating. It also explains the large variance of the measured central frequency, as the position of the grating image depends on the precise alignment of the incident beam on the grating.

Lastly, we study the influence of the compression of the pump on the THz emission. We scanned the distance L between the two gratings of the Treacy compressor, which linearly changes group delay dispersion (GDD) of the pump beam:

$$\frac{d^2\phi}{d\omega^2} = \text{GVD} \times L = -\frac{Nm^2\lambda^3L}{2\pi c^2 d^2} \left(1 - \left(-\frac{m\lambda}{d} - \sin\theta_i\right)^2\right)^{-\frac{3}{2}}, \quad (2.43)$$

with $N = 2$ the number of passes, m the diffraction order and d and grating period. The pulse duration then evolves as:

$$\tau = \tau_0 \sqrt{1 + \left(\frac{2(\phi_0'' + \phi'')}{\tau_0^2}\right)^2}, \quad (2.44)$$

where $2\tau_0$ is the $1/e$ duration of the compressed pulse, and ϕ_0'' is the preexisting GDD introduced by the stretcher. Fig. 2.11a shows the pulse duration measured by autocorrelator at the output of the compressor, from which we calculate the total GDD $\phi_0'' + \phi''$ using Eqs. (2.43) and (2.44). We measured the THz output while changing the GDD before and after the installation of the THz chamber. As mentioned in Section 2.1.2.3, one of the conditions to optimize the setup is to minimize the pulse duration across the pulse front. Without chamber, there is a clear influence of the compression of the pump on the THz emission. It peaks for a slight negative GDD of $-2.9 \times 10^{-3} \text{ ps}^2$, which precompensates some of the dispersion that the pumps undergoes in the THz setup. With the chamber, the THz energy is lower, due to the additional losses at the windows. The output peaks for a larger negative GDD of $-2.6 \times 10^{-2} \text{ ps}^2$, which cannot be caused only by dispersion of the input window, as its GDD is $9.5 \times 10^{-5} \text{ ps}^2$.

With the LiNbO₃ crystal in the chamber, we also recorded the position of the translation stages holding the latter at which the THz output is maximized. The lateral position (x on Fig. 2.3), which controls the distance of the pump to the edge of the crystal, is stable. The longitudinal position (z) by constant increases linearly with the GDD. As we saw in Fig. 2.8a, an 8 mm displacement is enough to move the crystal out of the focus of the beam, which would be visible in the THz energy. It is here more likely that the focus itself moves as we misalign the compressor.

Fig. 2.11d shows the central frequency of the THz, extracted from EOS traces such as in Figs. 2.11e and 2.11f. Its shift is significant and it reaches its maximum when the THz output is the largest. Contrarily to the dependence of the THz frequency on the grating,

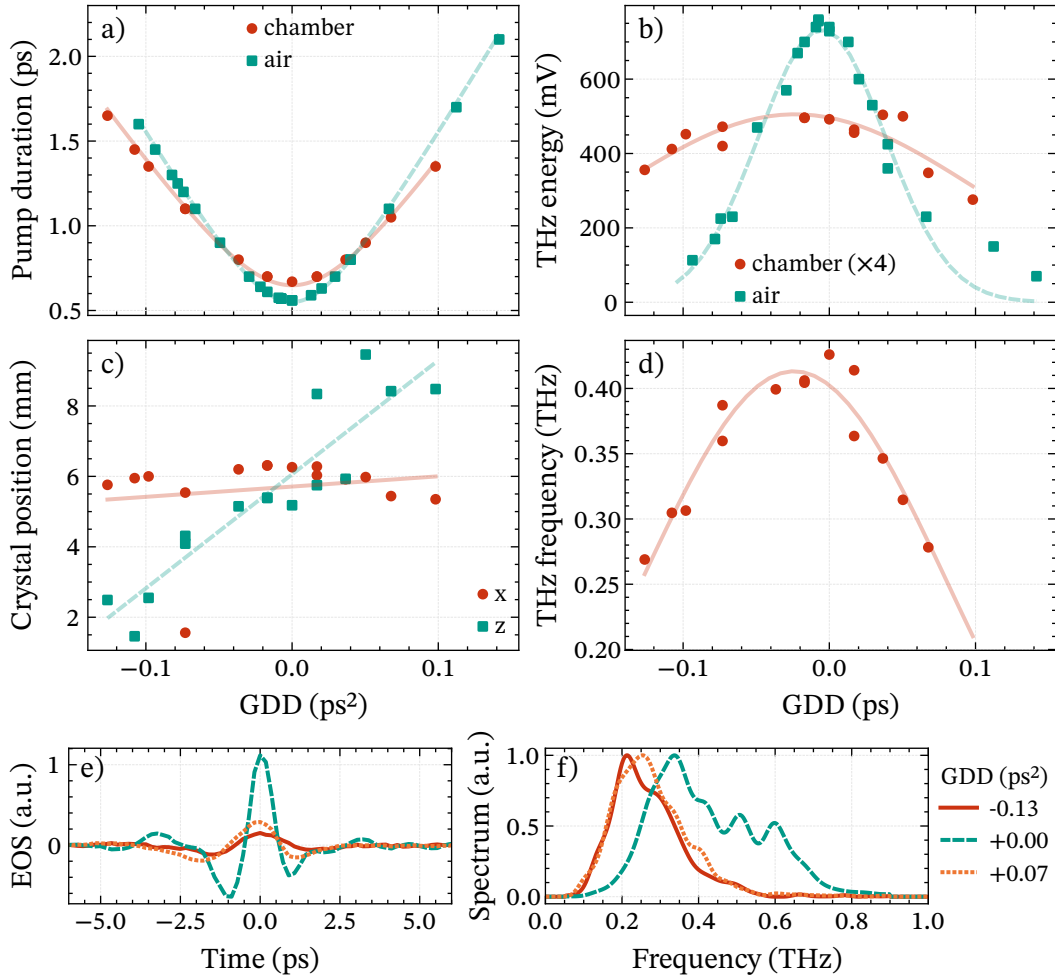


Figure 2.11: Influence of the compressor misalignment on the THz setup. a) Pulse duration of the IR beam at the output of the compressor, measured by autocorrelation and fitted by Eq. (2.44). b) THz energy measured at the output of the crystal or THz chamber (after optimization of its position), with a Gaussian fit. c) Position of the THz chamber optimized for THz energy (x and z as indicated in Fig. 2.3), with a linear fit. d) Mean THz frequency extracted from EOS traces, with a Gaussian fit. e–f) EOS traces taken in the OAP focus and their spectra. Plots c–f) correspond to the measurement with the LiNbO₃ crystal in the THz chamber.

here the drop in central frequency is directly linked to the dispersion of the pump, as it limits its instantaneous bandwidth.

2.2.2 The 800 nm setup

This concludes our description of the first TPF THz setup, designed for an 1030 nm pump. We switched to a different laser system when the Yb:KYW driver became unavailable for the foreseeable future, and took over a preexisting setup, adapted to a 180 fs, 7.5 mJ Ti:sapphire driver [68, 71]. We rebuilt and adapted it for a different Ti:sapphire laser system, providing 35 fs, 3 kHz, 4.9 mJ pulses.

2.2.2.1 Initial setup parameters

Contrarily to the 1030 nm setup that was designed in the frame of this work, this new setup had to be adjusted with minimal changes to the existing optics. Its LiNbO₃ prism is doped with 5 % MgO and has a 13 mm × 0.5" input face, as before with two angles of 61.9° and an apex of 56.2°. Its output face is covered with a 125 μm-thick layer of Kapton polyimide tape, increasing the THz transmission by 40 % as given by Eq. (2.30). It is mounted in a cryogenic chamber and cooled down to 88 K. The chamber has two windows: a 2"-diameter anti-reflection-coated fused silica input window, and a 5 mm-thick TPX window with 88 % transmissivity to couple out the THz beam.

The grating is a gold-coated blazed grating with 2000 grooves/mm and 85 % diffraction efficiency in the $m = 1$ order. The initial incident and diffracted angles are respectively 61° and 46.5°. A single spherical lens with a focal length of $f = 150$ mm images the grating into the crystal, with an demagnification of $f / (z_1 - f) = 0.5$. The pump beam is collimated before the grating to a diameter of 13 mm, reaching on the crystal a fluence of 31.84 mJ cm⁻².

The THz beam is collected by a pair of OAPs with parent focal lengths of 2" and 1". With the original 7.5 mJ pump, the measured THz energy in the focus is 2.2 V, or ~23 μJ.

2.2.2.2 Rebuilding the setup

While rebuilding the setup, several repairs to the laser system lead to a lower pulse energy than initially planned. The system is composed of a regenerative amplifier followed by a two-crystals booster and a compressor. Pumped at maximum intensity, the regenerative amplifier produces chirped pulses of 1.35 mJ. After the two-crystal booster stage, the pulses reach 5.1 mJ. The compressor then has a transmission of 83 %, after which the beam is separated with a waveplate and thin film polarizer (TFP) into two arms with an adjustable energy ratio. One is dedicated to the currently discussed TPF THz setup, and can at most reach a pump energy of 3.9 mJ at the entrance of the setup. The other arm of the laser is used for the spintronic THz emitters setup that will be the topic of Chapter 4.

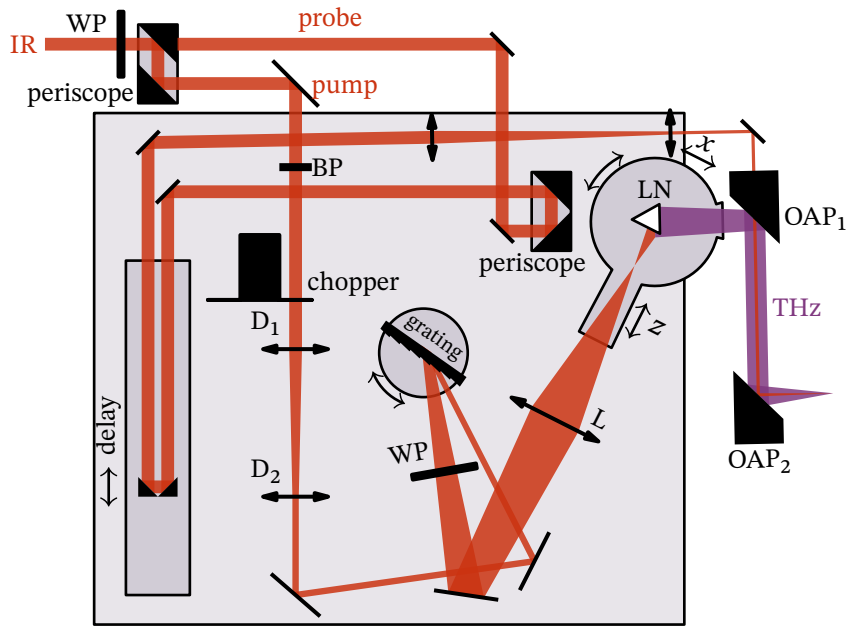


Figure 2.12: Scheme of the rebuilt 800 nm TPF THz setup. D: demagnetizing telescope; L: 150 mm lens; WP: $\lambda / 2$ waveplate; BP: band-pass filter; LN: LiNbO_3 .

The rebuilt setup is constrained to a $60 \text{ cm} \times 60 \text{ cm}$ breadboard to allow its transport, as the whole laser system is scheduled to be moved in the near future. We plan to use the generated THz beam in a custom experimental chamber, which will contain the collecting OAP. The THz chamber must thus be on the edge of the breadboard. The THz beam must also exit the LiNbO_3 crystal by the right face, which constrains the direction of its pulse front tilt and thus of the grating.

To match the height of the beam in the experimental chamber, two periscopes bring the beam up from the level of the laser output. The bottom mirror of the first periscope is a 45° TFP, which is used to separate the beam into the reflected pump and the transmitted probe for the EOS. The ratio is controlled by a half waveplate. We align the periscope so that the energy in the probe beam can be fully extinguished. After the grating, the polarization of the pump beam is rotated again from horizontal to vertical to match the optical axis of the LiNbO_3 crystal.

The beam size at the output of the laser system is $11 \text{ mm} \times 13 \text{ mm}$. Planning for 4.9 mJ, the ideal diameter to maintain the same fluence is 8.5 mm, assuming no changes in the rest of the setup. We thus started with a telescope with lenses of +150 mm and -100 mm (D_1 and D_2 in Fig. 2.12). However, with the decreases in laser energy and the differences in alignment, we tried different telescopes, with a magnification spanning 0.67 to 0.17.

This 35 fs Ti:Sapphire system has a larger bandwidth than the original 180 fs system, as shown in Fig. 2.13. This triples the spread of the diffracted pump beam from 3.0° to 9.3° , which impedes the reproducibility of the alignment onto the crystal. For this reason, we use a band-pass filter (BP in Fig. 2.12) while aligning the setup. The filter

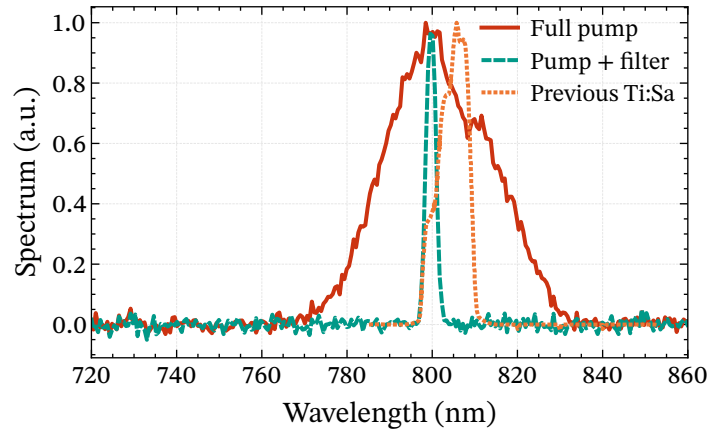


Figure 2.13: Spectrum of the IR pump with and without band-pass filter, as well as the spectrum of the previous laser system (data from Wu et al. [72]).

has a bandwidth of 3 nm and is nominally centered at 808 nm, the wavelength shifting when it is used at non-normal angles of incidence. Tilting the filter, we optimize the setup for the central wavelength of 800 nm. The distances between the grating and the lens, and the lens and the crystal, for which the grating is imaged onto the crystal, are respectively 450 mm and 225 mm. The diameter of the lens (L in Fig. 2.12) is increased to 3" to collect the full spectrum. The bandwidth of the pump on the crystal is however ultimately limited by the aperture of the window of the chamber. With the pump beam collimated on the grating, we observe the vertical focus in the focal plane of the lens, but the horizontal focus is pushed back to 210 mm after the lens due to the additional divergence, 15 mm before the crystal.

In addition to the THz radiation, parts of the reflected pump and its blue second harmonic also exit the chamber through the THz window, as they have no dedicated output window. The pump and its initially co-propagating second harmonic are refracted with different angles as they leave the crystal, such that both beams are separated when they exit the chamber. During the alignment of the chamber, care is taken to protect the THz sensor from the reflected IR beam, which may overlap with the THz beam and damage the silicon piece protecting the sensor, reducing its transmissivity. We first realigned the setup at room temperature. To find the optimal angle of the grating, we conducted similar scans than presented in Section 2.2.1. With the band-pass filter narrowing the diffracted beam so it can be realigned identically for each iteration, we rotated the grating and used the mirrors preceding it to move the incident beam. We then adjusted the translation stages holding the lens and the crystal to optimize the THz output. Finally, we rotated the grating until the angle of the incident beam corresponds to the Littrow angle.

Figs. 2.14a and 2.14b shows the results without the THz chamber. For each angle of the grating, we also rotated the waveplate that controls the total energy available to

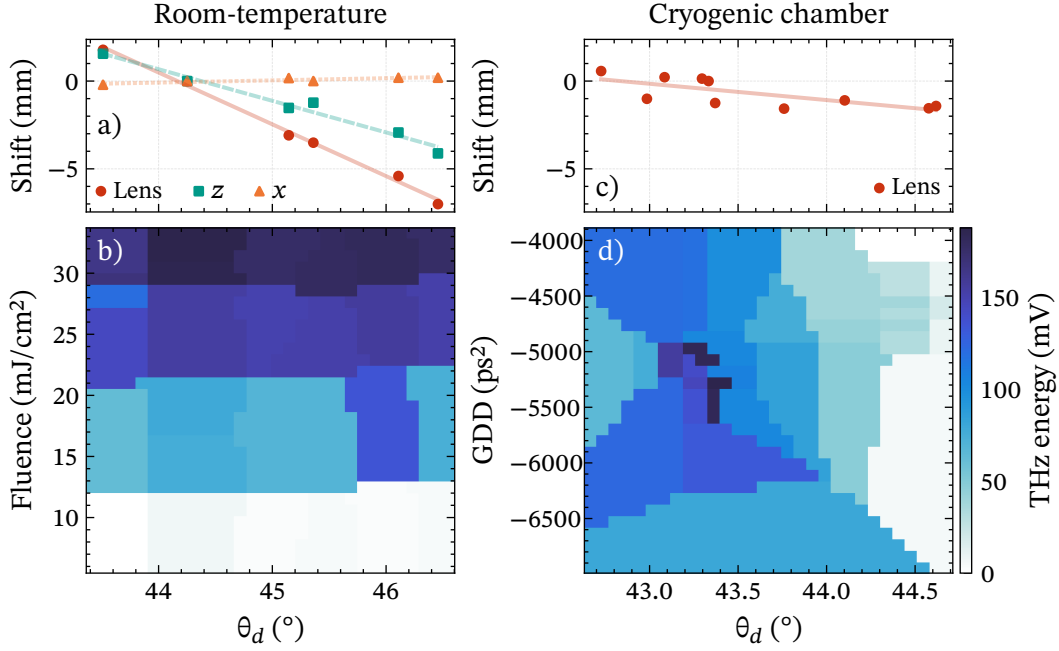


Figure 2.14: Influence of the TPF grating on the THz emission, at a–b) room and c–d) cryogenic temperature. a, c) Position of the lens and crystal (z longitudinal, x lateral) maximizing the THz emission, compared to their nominal positions. Lens and longitudinal crystal positions: a higher value means a larger distance from the grating. Lateral crystal position: a larger value means a longer propagation in the crystal. Emitted THz energy at the output of the chamber, while scanning the diffracted angle θ_d and b) the pump energy or d) the compressor alignment.

the setup, changing the energy on the crystal from 0.5 mJ to 2.2 mJ. We estimated the corresponding fluence using the angle of the grating and the measured position of the lens and the crystal stages, assuming an initial diameter of 6.5 mm incident on the grating and that the maximum THz output was obtained when the lens and crystal were at their nominally optimal positions (0 mm on the plot).

The optimal distance between the grating and the lens increases by 9 mm as θ_d increases, while the optimal distance between the lens and the crystal decreases by 3 mm, with the movements of the lens taken into account. This matches the displacement of the grating image as the lens is moved. As the lens is shifted forward, the horizontal focus of the pump beam moves closer to the image of the grating, increasing the fluence.

We found the optimal diffraction angle to be 44.2° , which is as expected a bit off from the nominal value at cryogenic temperatures of 46.5° . Cooling down the LiNbO_3 crystal from 234 K to 89 K, the THz output drops by 66 % as the phase matching is impaired by the change of refractive index. We thus need to adjust the pulse front tilt. In Figs. 2.14c

and 2.14d, the optimal angle is 43.3° , which is also slightly off from the nominal value.

We performed this scan at cryogenic temperatures while scanning the distance between the two gratings of the compressor. Its stage has no reference, thus we extracted the GDD of the laser output by fitting the results of FROG measurements performed on the probe beam of the parallel experiment (see Section 4.2.2.3). This arm of the laser is reflected on all TFPs to minimize its dispersion, and thus shows a probe duration similar to the one at the output of the compressor. The THz signal is maximized for a negative GDD, which precompensates the dispersion of the pump of the optics on the TPF setup. We scan the compressor length by 4 mm, which corresponds to a pulse duration of 1.5 ps to 2.7 ps at the output of the compressor. Compared to the measurement in Fig. 2.11, a smaller GDD lead to a larger pulse duration because of the large bandwidth of the laser.

To collect the THz radiation, we use a pair of OAPs with focal lengths of 4" and 3". Fig. 2.15a shows the caustic of the THz beam, measured with a THz camera. Before the focus, only the vertical diameter can be measured 10 mm due to lack to space. The size of the waist is $0.8 \text{ mm} \times 0.9 \text{ mm}$, which corresponds to the wavelength of the central frequency. We fitted the diameter near the waist as $d^2(z) = d_0^2 + M^2 z^2 (\lambda / \pi d_0)^2$ [73], with gives $M^2 \approx 1$, but finds a frequency of 0.6 THz and 1 THz, which indicates that the camera likely only captured the central part of the beam.

As can be seen from the inserts, the beam is strongly elliptical. Its polarization is plotted in Fig. 2.15d, which we measured by inserting a wire-grid polarizer before the THz detector. At the output of the chamber, the polarization is tilted 1.6° off from the vertical, which might be due to a misalignment of the vacuum chamber. After the OAPs, the polarization is tilted by 10.2° . In both cases, the measurement can be fitted by a linearly polarized beam. We expect mainly the second OAP to be responsible for the ellipticity and the polarization rotation, as its holder is not fully adjustable.

Finally, Figs. 2.15b and 2.15c show the waveform and spectrum of the THz beam in the focus. We took the current measurement with a $500 \mu\text{m}$ -thick ZnTe crystal, while the EOS measurement on the original laser system was taken with a $200 \mu\text{m}$ -thick ZnTe crystal and an additional plastic piece to filter the EOS. To compare both traces, we deconvoluted the measurements by their transfer functions. This process is detailed in Appendix B. The additional bandwidth of the pump with the current laser does not translate into a broader THz bandwidth.

After optimization, we reached a maximum THz output of 188 mV measured in the focus, which we estimate to correspond to $2.6 \mu\text{J}$, or 11 % of the estimated $23 \mu\text{J}$ obtained on the initial laser. The corresponding IR-to-THz conversion efficiencies are respectively 1.2×10^{-3} and 3.2×10^{-3} . While the reduced pump energy is responsible for part of the drop in THz output, we only reached 36 % of the efficiency of the setup on its original laser system. This is mainly due to the four times larger $1/e^2$ bandwidth of the pump, which is accompanied by a four times larger change in group index in LiNbO_3 and thus an increased phase-mismatch with the THz radiation.

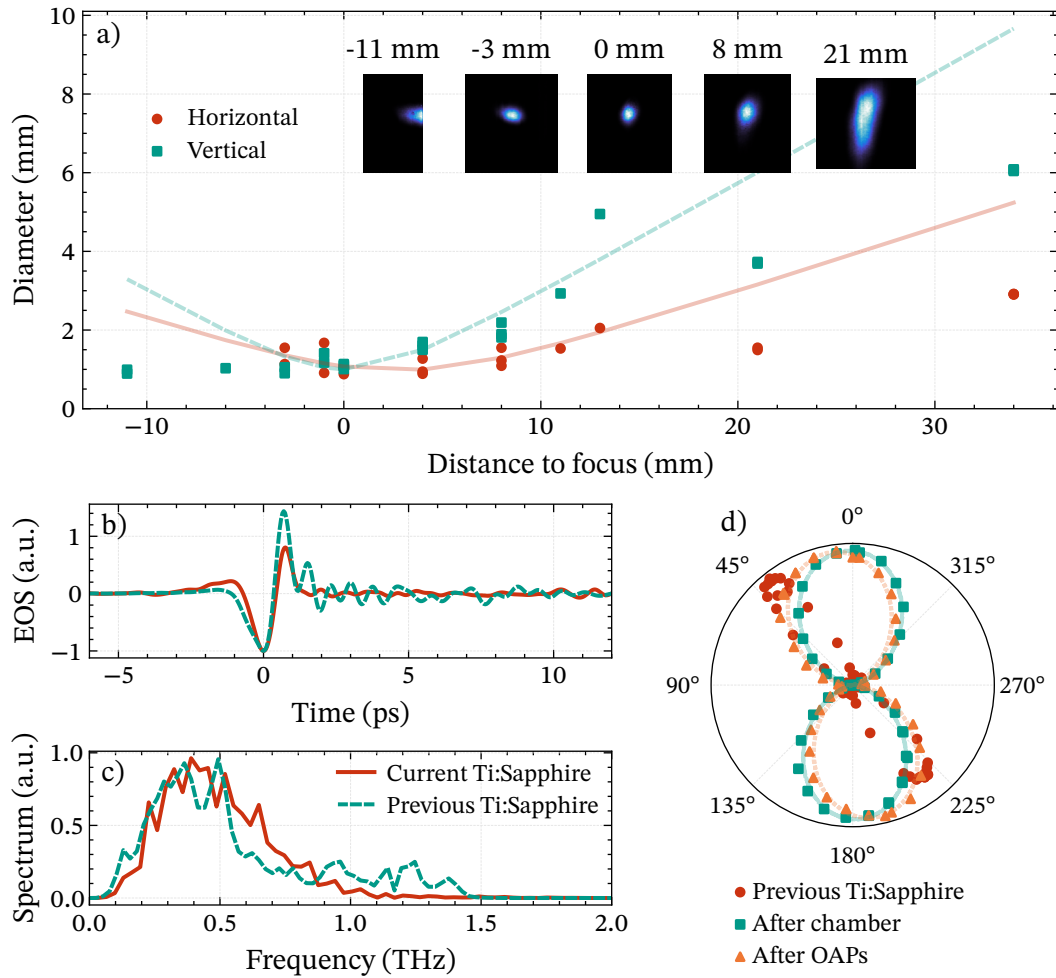


Figure 2.15: Characterization of the THz radiation. a) Horizontal and vertical D4 σ diameter, calculated from camera images (in inserts) taken around the focus. b) EOS trace and c) its spectrum, compared to before moving the setup. d) Transmission of the rotating polarizer, with fits (full lines) of the THz polarization as linear.

2.3 Applications of the THz radiation

We have described the TPF setups built with the aim of exciting magnetization dynamics. Before addressing this subject in the following section, we first introduce an additional element of the THz toolkit that was designed to enhance the maximum magnetic field strength.

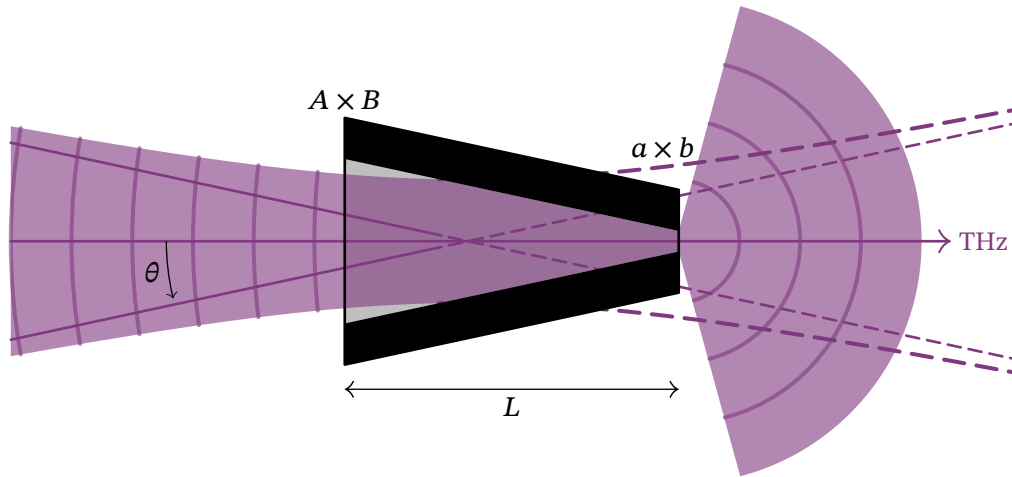


Figure 2.16: Scheme of a focusing THz horn.

2.3.1 THz horn

One of the applications of THz radiation is the resonant excitation of magnons, which we will demonstrate in [Section 2.3.2](#) using measurements obtained with $23 \mu\text{J}$ of THz energy. However, we have seen that after being rebuilt with for different pump, the TPF setup presented in [Section 2.2.2](#) generates only $2.6 \mu\text{J}$, due to a lower conversion efficiency and a lower pump energy. To continue the experiments in similar conditions, we are looking for a way to increase the THz energy by a factor 9, and thus the electric and magnetic fields by a factor 3.

2.3.1.1 Design

To obtain a higher THz field when the generation efficiency is limited, one solution is to focus the field tighter. In the case of the central 0.4 THz component shown in [Fig. 2.15c](#), focused by a $D = 3''$ OAP with a $f = 3''$ reflected focal length, the diffraction-limited waist diameter is $d_0 = 4f\lambda/\pi D = 0.95 \text{ mm}$. The 0.9 mm diameter measured in [Fig. 2.15a](#) is thus already tightly focused and highly nonparaxial, as $d_0 \approx \lambda$. To enhance the electric field by a factor 3 would require a similarly large optic with a $1''$ focal length, which is not possible with an OAP.

It is however possible to focus the beam under its diffraction limit over a short distance. This can be accomplished for example with a focusing horn, which is a linearly tapered rectangular waveguide. The already-focused field is guided through the horn and an evanescent high-intensity field forms at the small aperture. This is illustrated by [Fig. 2.16](#).

Let us consider that the horn is aligned on the z axis and its small and large openings have the area $a \times b$ and $A \times B$, respectively. The boundary conditions inside an empty rectangular waveguide with perfectly conducting walls impose that the tangential component of the electric field and the normal component of the magnetic field vanish

at the walls, allowing the electromagnetic field to propagate only in discrete TE and TM modes. The wavenumber has the transverse components $k_x = m\pi / a$ and $k_y = n\pi / b$. If the frequency-dependent longitudinal component $k_z = \sqrt{(\omega / c)^2 - k_x^2 - k_y^2}$ is real, the mode can propagate through the waveguide; otherwise it is evanescent. The transition occurs for $k_z = 0$. The lowest propagating frequency for the TE_{mn} mode is thus:

$$f_c = \frac{c}{2} \sqrt{\left(\frac{m}{a}\right)^2 + \left(\frac{n}{b}\right)^2}. \quad (2.45)$$

The dominant mode, whose cutoff frequency is the smallest, is the TE_{10} mode, for which the cutoff depends only on the length of the longest side: $f_c = c / 2a$. The value of a should be chosen long enough to transmit the lowest frequencies of the THz spectrum through the small end of the horn. The dimensions of the input are fixed by the criterion that the horn must keep the same proportions over its length: $a / A = b / B$, with the smallest side $b \geq 0.5$ mm due to manufacturing limitations. In addition, the beam should be focused a few millimeters inside the horn to maximize its coupling, so both opening dimensions must be bigger than the focus diameter: $A > d_0$ and $B > d_0$. Finally, to minimize the internal reflections and maximize the coupling efficiency, the tapering angle of the horn must match the divergence angle θ of the incoming THz beam, which determines its length L .

The lowest frequency in the THz spectrum according to Fig. 2.15 is 0.1 THz. With our OAPs, its diffraction-limited waist has a diameter of 3.8 mm. The beam is horizontally elongated before the focus, which is helpful to make use of the full rectangular aperture. We choose $B = 4$ mm, which is sufficient to contain most of the energy of the low frequencies, and $b = 0.5$ mm. To discourage the TE_{01} mode and keep a clean polarization, the ratio a / b should be as large as possible. However, a should be sufficiently small to also focus the beam in the horizontal direction. We choose $a = 2$ mm, which leads to $A = 16$ mm. Assuming that the beam fills a $4 \text{ mm} \times 4 \text{ mm}$ surface at the input and the whole output, its cross-section is reduced by a factor 16, increasing the intensity at the output plane by the same factor, and thus enhancing the field by a factor 4.

The divergence of the beam is difficult to reliably estimate from the beam profiles captured with the THz camera. As the beam is mainly diverging horizontally before the focus and only E_x varies in the TE_{10} mode, we use the value of the horizontal divergence, which is 8.6° . We thus choose $\theta = 10.5^\circ$ for the horn, which gives a length of $L = B / \tan(\theta) = 21.59$ mm.

We can analytically calculate some properties of the resulting horn. The phase and group velocities are frequency-dependent:

$$v_\phi = \frac{\omega}{k_z}; \quad v_g = \frac{k_z c^2}{\omega} \quad (2.46)$$

This makes the horn dispersive, with a spatially dependent group velocity dispersion

(GVD) for the TE₁₀ mode of:

$$GVD(z) = \frac{d^2 k_z}{d\omega^2} = -\frac{\pi^2 a(z) c}{(a^2(z) \omega^2 - \pi^2 c^2)^{3/2}} \quad (2.47)$$

with $a(z) = A + (a - A)z / L$. Integrated over $L = 21.59$ mm, the GDD introduced by the horn is -0.128 ps². Assuming a Fourier-limited Gaussian THz pulse, it would be stretched from 0.49 ps to 0.72 ps duration.

Unfortunately, the large bandwidth of the THz beam means that many modes have the possibility to propagate. The 2 mm × 0.5 mm output aperture supports modes with $m \leq 13$ and $n \leq 3$, until TE_{13,0} and TE₅₃ whose cutoff are both at 974 GHz. The main part of the spectrum, under 600 GHz, can supports modes with $m \leq 7$ and $n \leq 1$. The cutoff of the TE₁₀ mode at this aperture is 75 GHz. It is reduced to 9 GHz at the 16 mm × 4 mm input aperture, which means that we can expect some of the evanescent low frequencies to still reach the output of the horn.

We choose copper as material, as it has a high DC conductivity $\sigma_0 = 5.98 \times 10^7$ S m⁻¹. In the THz range, the Drude model gives its frequency-dependent conductivity: $\sigma(\omega) = \sigma_0 / (1 + i\omega\tau)$, with the damping frequency $1 / \tau = 6.71$ THz [74]. The field penetrates in the walls over the skin depth $\delta = \sqrt{2 / (\mu_0 \sigma \omega)} = 0.11$ μm at 0.4 THz, generating a longitudinal current within the walls and thus losses as the pulse propagates. The absorption coefficient for the TE₁₀ mode is [75, chapter 8]:

$$\alpha(\omega, z) = \frac{2 \left(\frac{\pi}{a}\right)^2 \left(b + \frac{a}{2} \left(\frac{\omega a}{\pi c}\right)^2\right)}{\omega \mu_0 a b k_z \sigma \delta}. \quad (2.48)$$

At the output aperture, where it is the largest, it has a minimum $\alpha(L) = 6.78 \times 10^{-1}$ m⁻¹ at 160 GHz, then increases with the frequency until 1.00 m⁻¹ at 1 THz. Near the cutoff frequency, it diverges to infinity as the wave becomes evanescent. Integrating the losses over the length of the horn, only 0.52 % of the 0.4 THz component is absorbed.

However, the approximation of perfectly conducting walls breaks down in the THz range. The longitudinal field component E_z created by the wall current can no longer be neglected, and the modes are hybrid between TE and TM, which prevents there from being an analytical expression of k_x and k_y . In this situation, the above losses are underestimated. Extrapolation from the calculations of Ho et al. [76] for a 13 mm × 6.4 mm copper rectangular waveguide, we can expect α for the TE₁₀ mode to be respectively 4.5 % and 21 % higher at 0.4 THz and 1 THz, which is ins this case negligible.

The tapering of the horn brings additional losses that we have so far neglected, as parts of the THz beam are reflected on the wall. Using the equations of Waldron [77], we estimate a reflection coefficient of $R = 1.1 \times 10^{-2}$, excluding the losses when coupling the THz beam into the horn.

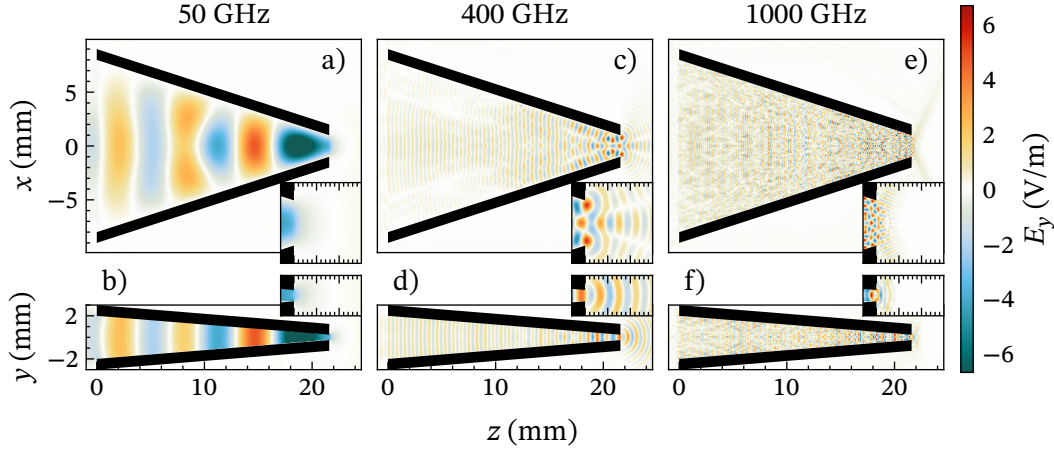


Figure 2.17: Simulation of $E_y(\omega)$ on the xz (upper row) and yz (lower row) planes. Inserts: zoom on the 3 mm after the horn output. The phase is 90° . Each frequency has an initial amplitude $E_y(z = 0) = 1 \text{ V m}^{-1}$.

2.3.1.2 Simulations

We simulated the propagation of the THz through the horn in CST Studio [78]. The horn is a linearly tapered rectangular tube. We used 1 mm-thick copper walls, defined as a lossy metal with permeability $\mu = 1$, impedance $Z = 0.16 \Omega$ at 0.4 THz, and conductivity $\sigma_0 = 5.96 \times 10^7 \text{ S m}^{-1}$.

The input field is a Gaussian pulse with a spectrum covering 50 GHz to 1 THz ($\lambda_{\min} = 300 \mu\text{m}$ and $\lambda_{\max} = 6 \times 10^3 \mu\text{m}$). It is focused inside the horn at $z = 3 \text{ mm}$, with a waist of 7.6 mm for λ_{\max} . It is propagating along the z axis and linearly polarized along the y axis. At $t = 0$ and $x = y = z = 0$, it has an amplitude of $|\vec{E}| = E_y = 1 \text{ V m}^{-1}$ and $|\vec{H}| = H_x = 2.6 \text{ mA m}^{-1}$. The source region is cropped to a height of B , so that it exactly covers the input aperture. Along the x axis, its width cannot be changed.

We use the time-domain solver to calculate the propagation of the field. To ensure the accuracy of the field at the output of the horn, we set up the bounding box to end with at a distance of $\lambda_{\max} / 2$ from the horn. We use a hexahedral mesh with five cells per λ_{\min} near the horn, which is sufficient to sample all frequencies. Along the z axis, the resolution is uniform with 60 μm -long cells. The bounding box has non-reflective open-space boundaries. To minimize the calculation domain, we set up symmetry planes: xz as an electrical boundary ($E_x = E_z = 0$), and yz as a magnetic boundary ($H_y = H_z = 0$).

Fig. 2.17 shows the amplitude of the E_y field for individual frequency components. The 50 GHz component is under the 75 GHz cutoff of the output aperture, and thus starts decaying as it reaches the end of the horn. Its amplitude is however still superior to 1 V m^{-1} up to 460 μm after the output. The 0.4 THz and 1 THz components show interference patterns due to the superposition of several modes. The 1 THz component

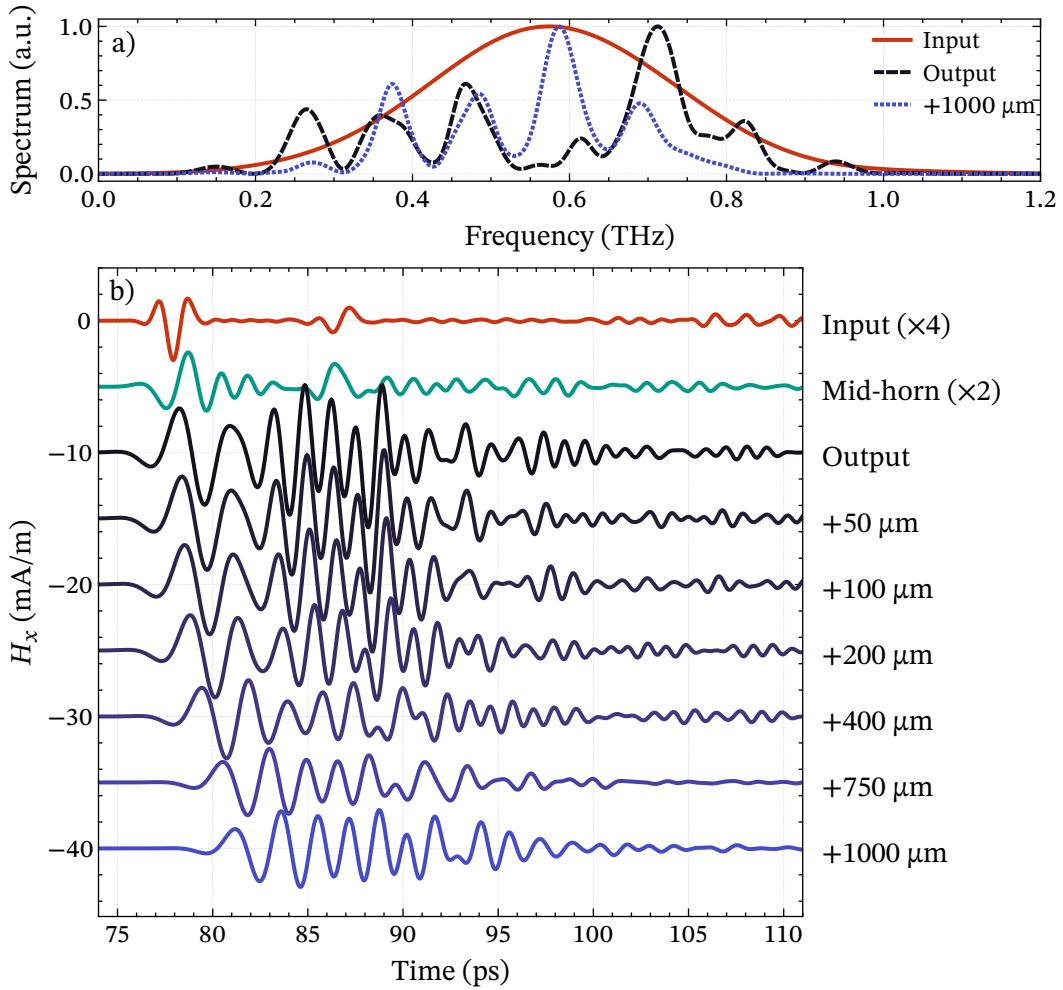


Figure 2.18: Simulated THz pulse along the z axis. a) Spectra of the input and output pulses. b) Magnetic field measured at the input plane ($z = 0$), inside the horn ($z = L/2$), at the output plane ($z = L$), and after propagation up to $z = L + 1000 \mu\text{m}$. The input and mid-horn waveforms are shifted by 74 ps and 36 ps, respectively.

forms a destructive interference pattern and vanishes within 1 mm after the output. The 0.4 THz component can reach at most the TE_{31} mode at the horn output, and therefore has fewer interference. It reaches a maximum amplitude of 5.51 V m^{-1} in the side lobes $90 \mu\text{m}$ after the output. On the z axis, its maximum is 2.99 V m^{-1} , $785 \mu\text{m}$ after the output. It vanishes slowly, which gives us a chance to place a sample close enough to the horn to use most of the energy of the pulse.

Fig. 2.18 shows the effect of the horn on the THz pulse. The input field at $z = 0$ is a single-cycle pulse. Immediately after, some ripples are visible and originate from the

reflected radiation that failed to couple in the horn. After 16 ps, a second pulse crosses the $z = 0$ plane. Its timing indicates that it was reflected at the beginning of the THz waist, when the divergence of the beam becomes mismatched with the tapering angle of the horn. Halfway inside the horn, the main pulse has doubled its amplitude and shows negative GDD, with a stronger broadening than we calculated for the TE₁₀ mode. As this is after the waist, a large part of the beam has started reflecting on the walls, and the amplitude of the reflections approaches that of the main pulse. At the output of the horn, there is no more visible difference between the main pulse and the reflections. The waveform is dominated by the high-frequency components. As the pulse propagates further on the z axis, they destructively interfere as shown in Figs. 2.17e and 2.17f, leaving a narrower spectrum. The peak magnetic field amplitude is enhanced by a factor 7.3 at the output, and a factor 4 within the first millimeter of propagation. This corresponds to our expectations, and would be sufficient to reach the desired field.

As we calculated in the previous section, the losses in the horn are low: the losses in the walls are of 5.8×10^{-10} W at 0.4 THz and increase up to 5.4×10^{-9} W at 1 THz. The energy inside the bounding box reaches its maximum at $t = 14.8$ ps, when the source has finished emitting the pulse. It decreases slowly with a few inflection point, as parts of the beam are reflected backwards after some propagation inside the horn. At $t = 87.5$ ps, the bounding box still contains 93.9 % of the maximum energy. It then drops sharply as the main pulse exits the system at $z = L + 3$ mm. By $t = 115$ ps, the main part of the pulse is out of the bounding box, carrying 50.8 % of the initial energy. Another sharp decrease takes place at $t = 180$ ps, when radiation that reflected on the output aperture of the horn exits the bounding box by the input side.

2.3.1.3 Measurements

The horn was manufactured by the DESY workshop and installed in the focus of the THz beam. We optimize its alignment by fixing the THz detector at its output and maximizing the transmitted THz energy, blocking the remaining surface of the detector. We obtained up to 47 % of the signal measured in the focus without the horn, which is the order of magnitude that we expected the pulse to carry according to the simulation. Because of the distance between the entrance of the THz detector and the surface of the sensor, the diverging beam is only partially collected and the value is approximate.

Fig. 2.19 shows EOS traces of the THz pulse with and without the horn. The ZnTe crystal is placed in the THz focus or as close as possible to the horn output, respectively. We usually use EOS in transmission, with the THz and probe beams coming from the same side of the crystal. A perfect superposition requires the first OAP to be adjusted so that the THz beam is centered on the hole by which the probe is inserted, and so that they both travel colinearly. As the propagation of the THz beam is sensitive to the alignment on the pump beam and thus varies slightly every day, the superposition is not sufficient for the probe to travel through the horn without hitting its walls. This degrades

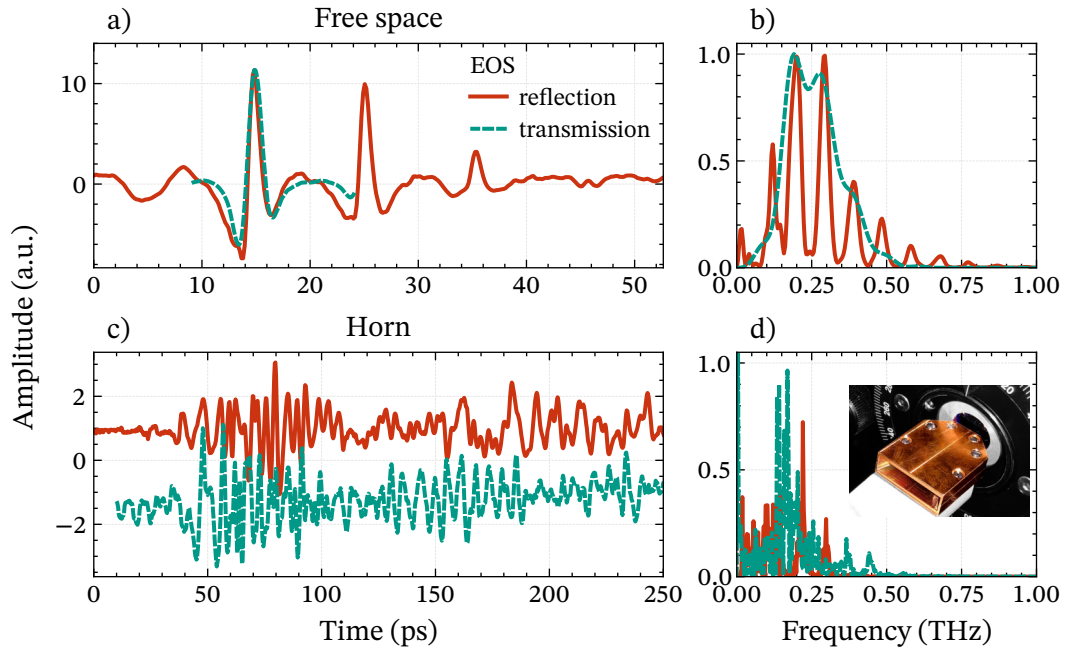


Figure 2.19: EOS traces of the THz beam a) focused in free space and b) after the horn. Insert: horn next to the ZnTe crystal.

the probe quality and makes its alignment difficult. For this reason, we also try EOS in reflection, in which the probe beam is incident on the face of the crystal opposite to the horn. The refractive index of the THz beam in ZnTe is almost identical to the group index of the probe, and it takes both of them 5.4 ps to traverse the 500 μm -thick crystal. The counter-propagating probe thus travels across the entire THz pulse and its polarization is in average not rotating. Its internal reflection is however phase-matched with the THz pulse. We thus expect the measured waveform to not be significantly distorted compared to EOS in transmission, but noisier, as most of the probe energy is transmitted instead of reflected.

We see in Fig. 2.19a the THz pulse measured without horn. The spectrum is narrower than the one in Fig. 2.15c, as repairs to the laser system have changed the characteristics of the pump, and is centered at 250 GHz. Several reflections of the THz pulse are visible. Their relative amplitude does not decrease linearly, indicating that they likely had a spatial offset and the probe was better superposed to the second reflection.

Fig. 2.19c shows the waveform of the THz beam after the horn. The signal-to-noise ratio is better in reflection, as the probe loses less energy traveling through the crystal than through the horn. We install the EOS crystal as close as possible to the horn without risking contact, at a distance which we estimate to be 1 mm to 2 mm. From Fig. 2.17, we can thus expect the absence of high-frequency components, whose different modes interfere destructively. We indeed observe no signal above 0.6 THz, and a spectrum

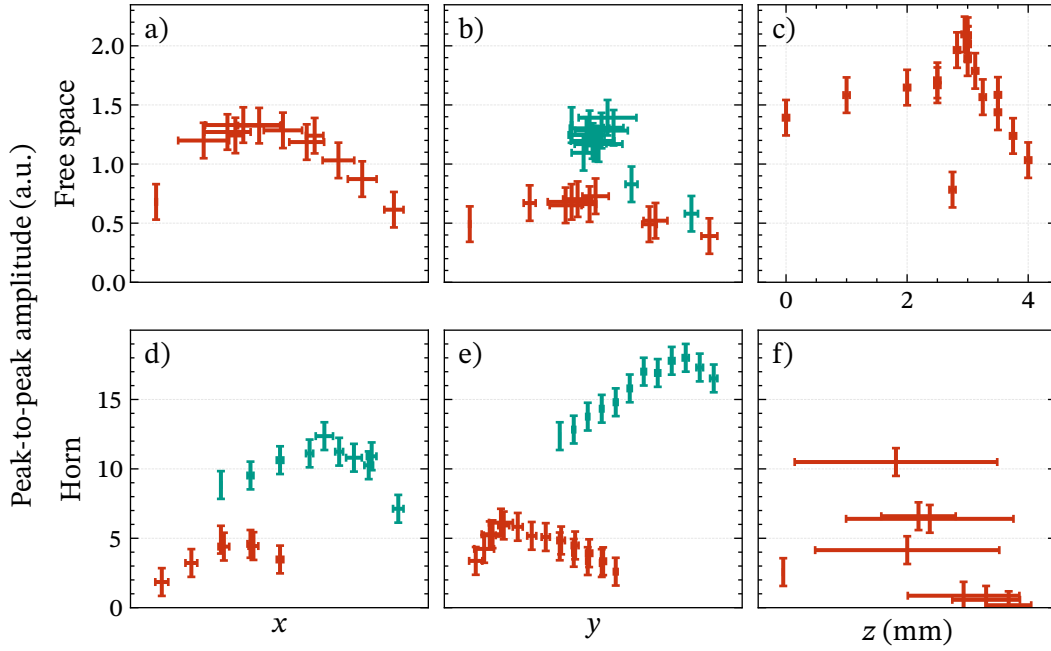


Figure 2.20: Spatial dependency of the EOS amplitude, a–c) focused in free space and d–f) after the horn. The positions are measured in arbitrary steps whose scale is not comparable between subplots. The horizontal errorbar are estimations of the likelihood that the order of the points is incorrect, taking into account the hysteresis of the mirror screws. Only c): z scale in mm. A lower number corresponds to the crystal moving towards the OAPs.

centered lower around 0.15 THz. The waveform shows many interferences, as the beam can be reflected not only in the crystal, but also on surface of the horn. We can however still recognize the expected chirp in the pulse.

To find the optimal position for a sample and compare the peak magnetic field of the THz with and without the horn, we attempted a three-dimensional EOS scan of the beam. The z axis corresponds to the distance between the ZnTe crystal and the horn, and the xy plane corresponds to the position of the probe beam on the crystal, which we are able to control when using the reflection scheme. We send the reflected probe with a combination of flip mirrors either to the EOS setup, to a camera after 199 mm of propagation, or to the same camera after 388 mm of propagation. By tracking the location of the beam on the camera at both distances, we minimize the uncertainty on the relative movements of the beam in the xy plane due to the hysteresis of the alignment mirror.

Fig. 2.20 shows the EOS amplitude that we measured while scanning the uncalibrated position of the probe, optimizing one axis at a time. The focus in free space fills a large part of the 5 mm-wide crystal, while the THz beam is significantly smaller at the output of the horn. We scanned the x and y axes twice, for different positions of the crystal

along z . The discontinuities in the x profile with the horn expected from Fig. 2.17 are not visible. The z axis has a large influence in the absence of the horn, and the optimal position is restricted to a 200 μm -wide range. With the horn, a quantitative measure of the distance within which the THz is detectable was not possible.

We performed the optimization of the position of the probe with and without horn back-to-back, with the same energy in the probe beam. We can thus compare the amplitudes of the EOS traces. At its maximum, we found a peak-to-peak amplitude of 2.1 in the free-space focus, after optimizing the crystal along the z axis. Further movement of the probe along the x and y axes only lowered the signal. Using the horn, the last scan on the y axis gave a maximum peak-to-peak amplitude of 18, or 8.6 times more. The single-peak amplitude has a less coherent behavior and varies too much shot-to-shot to be able to compare the two beams. It seems however likely that the horn is producing at least the field enhancement that we designed it for.

2.3.2 Measurement of a prototypical canted antiferromagnet

The intended application for the THz radiation generated in this chapter is the excitation of magnons, or spin waves, in antiferromagnetic (AFM) materials. The origin of the magnetic phenomena will be treated in details in Chapter 3; we focus here on the point of view of the magneto-optic (MO) measurements.

The sample is inserted in the focus of the THz beam, which excites spin waves upon incidence. They perturb the optical properties of the material, inducing a nonlinear susceptibility depending on the magnetization of the medium. Due to this induced change in refractive index, the polarization of the probe beam is rotated by the birefringence of the sample as it travels through it. The spin waves can thus be measured by the same detection setup as for EOS, only replacing the EOS crystal by the AFM sample.

2.3.2.1 Uniform magnetization precession in FeBO_3

As a proof of concept, we performed the experiment on the iron borate FeBO_3 , using the original 800 nm setup. This material was predicted and first synthesized by Bernal, Struck, and White [79], and extensively studied in the following decades for its uncommon properties: spontaneous magnetization at room temperature coexisting with transparency to visible light, which made this material advantageous for applications such as optical modulators, isolators, or electronically tunable cavities [29].

It has a rhombohedral lattice structure of space group $R\bar{3}c$, with a three-fold symmetry around the $[001]$ or c axis, represented in Fig. 2.21. It is classified as an AFM material, which means that it has two sublattices with equal but opposite magnetizations \vec{M}_1 and \vec{M}_2 of the same magnitude M_i . However, due to a break in the symmetry of the covalent bonds of the Fe ions with oxygen, the magnetizations are both tilted by 1.6×10^{-2} rad [80] with respect to the AFM alignment and do not perfectly cancel each

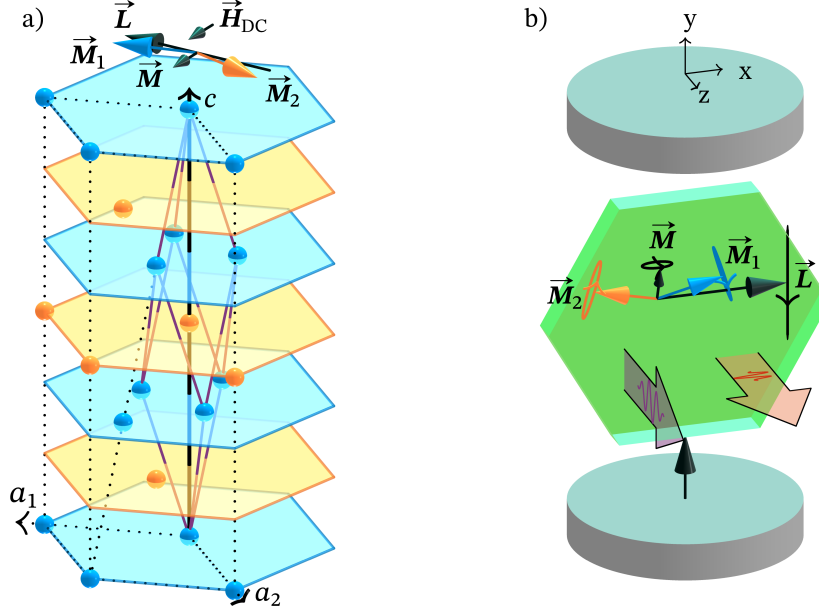


Figure 2.21: a) Structure of FeBO₃. Full lines: rhombohedral unit cell. Dotted lines: hexagonal unit cell. Thick line: hard c axis. Blue (red) spheres: Fe atoms with magnetization \vec{M}_1 (\vec{M}_2). Blue (red) hexagons: antiferromagnetic sublattices in the basal plane. The canting is exaggerated for readability. The net magnetization $\vec{M} = \vec{M}_1 + \vec{M}_2$ is aligned on the external field \vec{H}_{DC} . b) Geometry of the measurement: the magnetization precession is induced by a THz pulse and probed by an IR pulse. The indicated precession corresponds to the qFMR mode (see Eq. (2.49a)).

other, resulting in a small net magnetization $\vec{M} = \vec{M}_1 + \vec{M}_2$. The mechanism causing this canting is explored in Section 3.2.4.6 [81]. FeBO₃ has an easy-plane type of magnetocrystalline anisotropy, which means that the sublattice magnetization and thus \vec{M} is preferably aligned in the basal plane. An external magnetic field of 2 mT [82] is sufficient to remove the magnetic domain structure of the crystal, so that the magnetization can be considered homogeneous.

As detailed in Section 3.3.3.3, a short varying magnetic field perturbs the magnetization of the material. Both sublattice magnetizations start precessing right-handedly around their equilibrium position following the Landau-Lifshitz equation of motion $\partial \vec{M}_i / \partial t = -\gamma \mu_0 \vec{M}_i \wedge \vec{H}_i$. If the magnetization precesses uniformly throughout the sample, this is an acoustic spin wave with wavevector $k = 0$. The motion eventually decays and the magnetization returns to its equilibrium position along the effective field \vec{H}_i .

The behavior of the two-sublattice system can be equivalently described by the ferromagnetic (FM) vector \vec{M} and the AFM vector $\vec{L} = \vec{M}_1 - \vec{M}_2$, each precessing around the external magnetic field \vec{H}_{DC} . We define the coordinate system so that $z \parallel c$ is the out-of-plane axis, $\vec{M} \parallel \vec{H}_{DC} \parallel y$ and $\vec{L} \parallel x$ at equilibrium (see Fig. 2.21b).

Since FeBO_3 has two sublattices, the system has two degrees of freedom and there exist two modes of uniform precession, distinguished by the relative phase between the precession of $\vec{\mathbf{M}}_1$ and $\vec{\mathbf{M}}_2$. In the quasi-ferromagnetic resonance (qFMR) mode, the sublattices precess in phase, so that the magnetization displacements are related by $\delta M_{x1} = \delta M_{x2}$, $\delta M_{y1} = -\delta M_{y2}$ and $\delta M_{z1} = \delta M_{z2}$. This results in the precession of the net FM moment $\vec{\mathbf{M}}$ in the xz plane, giving its name to the mode, and the oscillation of L_y . Due to the strong anisotropy, the precession is elliptical and mostly confined in the basal plane: $\delta L_y / \delta M_z \approx 10^3$ [83]. In the quasi-antiferromagnetic resonance (qAFMR) mode, the sublattices precess with opposite phase, so that $\delta M_{x1} = -\delta M_{x2}$, $\delta M_{y1} = \delta M_{y2}$ and $\delta M_{z1} = -\delta M_{z2}$. This results in the precession of $\vec{\mathbf{L}}$ in the xz plane and the oscillation of M_y . In this mode, the canting angle between the two sublattices is perturbed. Since the force responsible for the canting in FeBO_3 is stronger than the anisotropy of the sample, the precession is here mainly out-of-plane: $\delta L_z / \delta M_y \approx 300$. In purely AFM materials, only this mode is measurable, as it leads to the appearance of a non-zero magnetization.

The precession frequencies are sample-, temperature- and geometry-dependent. For FeBO_3 , they are modeled as [83]:

$$\left(\frac{\omega_{\text{qFMR}}}{\mu_0\gamma}\right)^2 = H_{\text{DC}}(H_{\text{DC}} + H_D) + 2H_E H'_A \quad (2.49a)$$

$$\left(\frac{\omega_{\text{qAFMR}}}{\mu_0\gamma}\right)^2 = H_D(H_{\text{DC}} + H_D) + 2H_E H_A, \quad (2.49b)$$

where H_D , H_E , H_A and H'_A are effective magnetic fields corresponding to internal forces affecting the orientation of the sublattice magnetizations, whose values are given in Table 3.2. The origin of these forces and the calculation of the precession frequencies are discussed in Section 3.3.3.3. For $H_{\text{DC}} = 100$ mT, we predict $\omega_{\text{qFMR}} = 22$ GHz and $\omega_{\text{qAFMR}} = 315$ GHz.

The frequency of the qAFMR mode coincides with the central frequency of the THz pulses, whose spectrum is shown in Fig. 2.15c. A resonant magnetic dipole excitation of this mode using the THz magnetic field is thus possible. The field exerts a polarization-dependent torque $\vec{\mathbf{M}}_i \wedge \vec{\mathbf{H}}_{\text{THz}} = (\pm L_x H_y / 2 - M_y H_x / 2) \vec{\mathbf{z}}$ on the sublattice magnetizations. The H_y component thus results in $\delta M_{z1} = -\delta M_{z2}$, which corresponds to the qAFMR mode. Fig. 2.15d shows that the polarization of the THz pulses of the original 800 nm setup is near 45° , that is to say $H_y \approx H_x$. We thus expect to be able to pump the qAFMR mode.

It has recently been shown that the excitation of the qFMR mode in FeBO_3 by THz pulses is caused by a different mechanism than the qAFMR mode [84, 85]. The pulse is short compared to the qFMR precession, so that the direction of the torque reverses before the magnetization has significantly moved. It is thus modeled, as in the case of excitation using IR pulses, by inverse Brillouin scattering or equivalently by inverse MO effects [86, 87].

2.3.2.2 Magneto-optic measurements

The interaction of the probe beam with a material depends on the polarizability of its ions, which is influenced by their spin. Although FeBO₃ is a magnetic material, we describe the propagation of light assuming a relative permeability $\mu_r = 1$ without loss of generality, by including the magnetic susceptibility into an effective electronic susceptibility $\chi_{\text{eff}} = \chi^e + \chi^m (1 + \chi^e)$ [88]. Similarly to the expression of the nonlinear polarization (see Eq. (2.2)), the electronic susceptibility can be expanded into powers of the magnetization. Thus the effective relative permittivity is:

$$\begin{aligned}\epsilon_{\text{eff}} &= 1 + \chi^{(0)} + \chi^{(1)} \cdot \vec{M} + \chi^{(2)} : \vec{M}^2 \\ &= \epsilon_{\text{eff}}^{(0)} + \epsilon_{\text{eff}}^{(1)} + \epsilon_{\text{eff}}^{(2)}.\end{aligned}\quad (2.50)$$

ϵ_{eff} can be separated into a symmetric part, depending on even powers of the magnetization, and an antisymmetric part, depending on odd powers of the magnetization. Expressed as a function of the FM and AFM vectors up to the second order, we obtain the dielectric tensors [89]:

$$\begin{aligned}\epsilon_{ij}^a &= \alpha_{ijk} M_k + \beta_{ijk} L_k \\ \epsilon_{ij}^s &= \epsilon_{ij}^{(0)} + a_{ijkl} M_k M_l + b_{ijkl} L_k L_l + c_{ijkl} M_k L_l.\end{aligned}\quad (2.51)$$

In the absence of absorption, ϵ_{ij}^a is purely imaginary and ϵ_{ij}^s purely real, both resulting in a phase difference between the two eigenmodes of the polarization. They are respectively associated to magnetic circular birefringence (MCB) and magnetic linear birefringence (MLB). In the presence of absorption, the real part of ϵ_{ij}^a and the imaginary part of ϵ_{ij}^s lead to magnetic circular dichroism (MCD) and magnetic linear dichroism (MLD), respectively. The first-order effects are in general visible only when light travels along the direction of the magnetization, as the left- and right-handed circular polarizations are aligned or opposed to the angular momentum of the material, while the second-order effects are visible when the magnetization is transverse.

To the first order in the displacements δM and δL , the permittivity tensor of FeBO₃ has the form [86]:

$$\begin{aligned}\epsilon_{\text{eff}} &= \begin{bmatrix} \epsilon_{\perp} & 0 & 0 \\ 0 & \epsilon_{\perp} & 0 \\ 0 & 0 & \epsilon_{\parallel} \end{bmatrix} && \text{(no magnetism)} \\ &+ \begin{bmatrix} \epsilon_{xx}^{Ss} & 0 & 0 \\ 0 & \epsilon_{yy}^{Ss} & \epsilon_{yz}^{Ss} \\ 0 & \epsilon_{yz}^{Ss} & \epsilon_{zz}^{Ss} \end{bmatrix} + \begin{bmatrix} 0 & 0 & 0 \\ 0 & 0 & i\epsilon_{yz}^{Sa} \\ 0 & -i\epsilon_{yz}^{Sa} & 0 \end{bmatrix} && \text{(static magnetization)}\end{aligned}$$

$$\begin{aligned}
 & + \begin{bmatrix} 0 & \epsilon_{xy}^{Fs} & \epsilon_{xz}^{Fs} \\ \epsilon_{xy}^{Fs} & 0 & 0 \\ \epsilon_{xz}^{Fs} & 0 & 0 \end{bmatrix} + \begin{bmatrix} 0 & i\epsilon_{xy}^{Fa} & i\epsilon_{xz}^{Fa} \\ -i\epsilon_{xy}^{Fa} & 0 & 0 \\ -i\epsilon_{xz}^{Fa} & 0 & 0 \end{bmatrix} & \text{(qFMR mode)} \quad (2.52) \\
 & + \begin{bmatrix} \epsilon_{xx}^{As} & 0 & 0 \\ 0 & \epsilon_{yy}^{As} & \epsilon_{yz}^{As} \\ 0 & \epsilon_{yz}^{As} & \epsilon_{zz}^{As} \end{bmatrix} + \begin{bmatrix} 0 & 0 & 0 \\ 0 & 0 & i\epsilon_{yz}^{Aa} \\ 0 & -i\epsilon_{yz}^{Aa} & 0 \end{bmatrix}, & \text{(qAFMR mode)}
 \end{aligned}$$

where the superscripts s and a refer to the symmetric and antisymmetric parts of the tensor, and the capital superscripts S, F and A to the static, qFMR and qAFMR components of the magnetization, respectively. As FeBO₃ is transparent at 800 nm, the symmetric and antisymmetric parts are purely real and imaginary, respectively. It is here assumed that the probe propagates along the z axis and the external magnetic field is aligned along the y axis.

In the case of a static magnetization, the elements of the permittivity tensor given above [86] are the same than those given by Akhmadullin et al. [90] for α -FeO₃, whose crystallographic and magnetic structure is similar to FeBO₃. The authors show that since $\epsilon_{xy} = 0$, a linearly polarized probe pulse is rotated by an angle ϕ , defined by:

$$\tan(2\theta_p - 2\phi) = \cos(2\eta) \tan(2\theta_p) \quad (2.53)$$

$$2\eta \approx (G_1 L_x^2 + G_2 M_y L_x) \pi z / \lambda \sqrt{\epsilon_{\perp}} \quad (2.54)$$

where θ_p is the angle between the polarization of the incident probe and \vec{H}_{DC} , and 2η is the phase difference between the two eigenmodes of the polarization. The quadratic MO constants $G_1 = b_{xxxx} - b_{yyxx}$ and $G_2 = c_{xxyx} + c_{yyyx}$ are defined according to Eq. (2.51). The resulting static rotation can be experimentally compensated by the balance of the EOS setup in order to measure only the dynamic part of the permittivity.

A similar result is obtained for the polarization rotation induced by the qAFMR mode, as its contribution to the permittivity has the same diagonal form as the static magnetization. Assuming that the static rotation is removed, the phase difference becomes:

$$2\eta = (G_1 L_x \delta L_y + G_3 L_x \delta L_z + G_4 M_y \delta L_z) \pi z / \lambda \sqrt{\epsilon_{\perp}}, \quad (2.55)$$

where $G_3 = 2b_{xxxz}$ and $G_4 = 2c_{xxyx}$. According to Eq. (2.53), the probe is the most sensitive to the induced phase difference 2η for θ_p near but different from $\pm 45^\circ$.

The tensor elements corresponding to the qFMR mode are [86]:

$$\begin{aligned}
 \epsilon_{xy}^{Fs} &\approx G_1 L_x \delta L_y, & \epsilon_{xy}^{Fa} &= K_1 \delta M_z, \\
 \epsilon_{xz}^{Fs} &\approx G_5 L_x \delta L_y, & \epsilon_{xz}^{Fa} &\approx K_2 \delta L_y,
 \end{aligned} \quad (2.56)$$

where the K and G are linear and quadratic MO constants, respectively, and $G_5 = 2b_{yzyx}$, $K_1 = \alpha_{yxz}$, $K_2 = \beta_{yzy}$. As the probe propagates along the z axis, only ϵ_{xy} contributes. The effective dielectric tensor:

$$\epsilon_{\text{eff}}^{\text{F}} = \begin{bmatrix} \epsilon_{\perp} & \epsilon_{xy}^{\text{Fs}} + i\epsilon_{xy}^{\text{Fa}} & 0 \\ \epsilon_{xy}^{\text{Fs}} - i\epsilon_{xy}^{\text{Fa}} & \epsilon_{\perp} & 0 \\ 0 & 0 & \epsilon_{\parallel} \end{bmatrix} \quad (2.57)$$

has for eigenvalues $n^2 = \epsilon_{\perp} \pm \sqrt{(\epsilon_{xy}^{\text{Fs}})^2 + (\epsilon_{xy}^{\text{Fa}})^2}$ and eigenvectors:

$$\vec{E}_1 = \begin{bmatrix} +\alpha \\ 1 \\ 0 \end{bmatrix}; \quad \vec{E}_2 = \begin{bmatrix} -\alpha \\ 1 \\ 0 \end{bmatrix}, \quad (2.58)$$

where:

$$\alpha = \frac{i\sqrt{(\epsilon_{xy}^{\text{Fa}})^2 + (\epsilon_{xy}^{\text{Fs}})^2}}{\epsilon_{xy}^{\text{Fa}} + i\epsilon_{xy}^{\text{Fs}}} = \exp\left(\frac{\pi}{2} - \tan^{-1}\left(\frac{G_1 L_x \delta L_y}{K_1 \delta M_z}\right)\right). \quad (2.59)$$

The normal modes of the electric field in the crystal thus correspond to a left- and a right-handed elliptical polarization. For the probe orientation $\theta_p = 90^\circ$, the rotation of the polarization is now [89, 90]:

$$\tan \phi = -\frac{2\alpha(\alpha^2 + 1) \sin 2\eta}{4\alpha^2 \cos 2\eta + (\alpha^2 - 1)^2}. \quad (2.60)$$

FeBO_3 is known for high large Faraday rotation in the visible range [91]. At 800 nm, the MO coefficients K and G have similar values [86]. However, the ellipticity of the qFMR mode ($\delta L_y \gg \delta M_z$) ensures that Eq. (2.59) is dominated by the quadratic MO effects. We thus measure mainly the rotation of the probe due to MLB, called the Voigt or Cotton-Mouton effect.

2.3.2.3 Results in FeBO_3

The spin waves in FeBO_3 have been measured using the initial 800 nm THz setup discussed in Section 2.2.2. As shown in Fig. 2.15, its spectrum is centered around 400 GHz and its polarization is rotated by 40° from the vertical in the focus. The probe is horizontally polarized. The FeBO_3 sample is glued at the center of a rotating mount. Two permanent magnets whose distance can be adjusted provide the DC magnetic field on the sample and are fixed to the same rotating mount. We measured the corresponding magnetic field using a Hall sensor at the position of the crystal. For the initial orientation of the mount, $\vec{H}_{\text{DC}} \parallel y$, $\theta_p = 90^\circ$ and $\theta_{\text{THz}} = 40^\circ$.

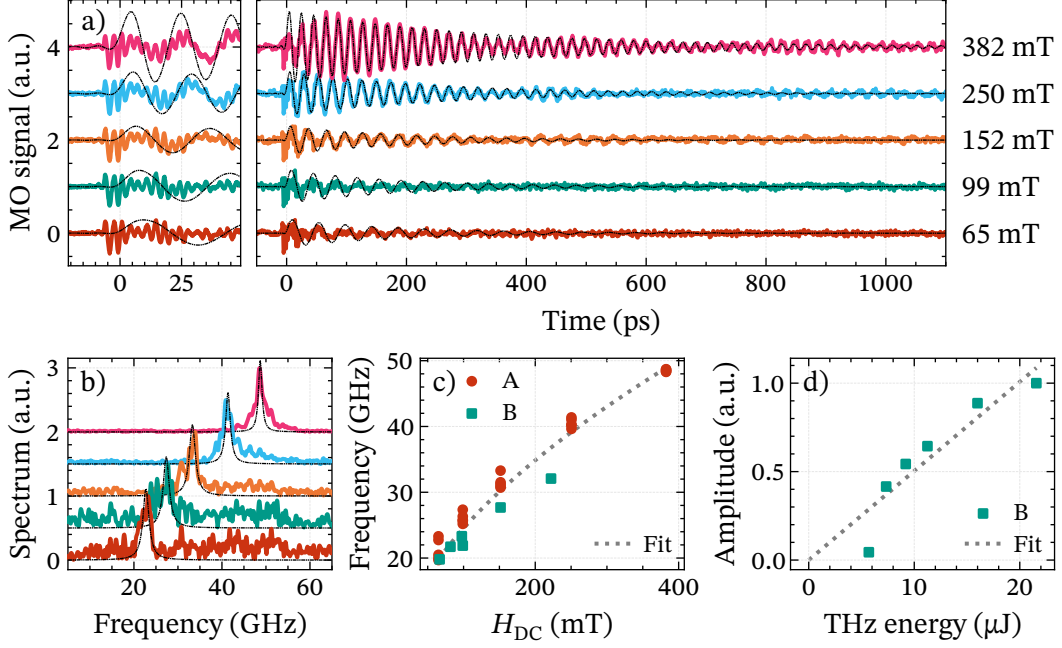


Figure 2.22: a) Measured MO signal and b) its spectrum for different strengths of \vec{H}_{DC} , measured immediately following the THz pulse (left) and long-term (right). Dashed black lines: Lorentzian fit of the qFMR peak. c) Measured qFMR frequency from two sets of experiments, with fit according to Eq. (2.49a). d) Amplitude of qFMR peak while varying the pump energy.

We varied the distance of the magnets, the angle of the mount and the IR energy incident on the THz setup. In each configuration, we took two measurements: one with low resolution to measure the nanosecond-scale behavior of the magnetization precession, and one with higher resolution recording the first picoseconds after excitation. All measurements shown were taken with a monocrystalline FeBO_3 sample (label A), except for Figs. 2.22c and 2.22d (label B) which were taken using a polycrystalline sample.

Figs. 2.22a and 2.22b shows the measured MO signal with the magnets horizontally aligned with the sample ($\vec{H}_{DC} \parallel x$). At the incidence of the THz pulse, the magnetization oscillates at the frequency of the THz field for two to three cycles, following its magnetic field. After 10 ps to 30 ps, the signal settles into oscillations corresponding to the free precession of the magnetization. As shown by Fig. 2.22c (label A), the frequency of the oscillations matches the frequency predicted by Eq. (2.49a) if \vec{H}_{DC} is scaled by a factor 1.2, which can be caused by an imprecision in our calibration of the field. Their amplitude is expected to be linearly proportional to the THz energy [84], which agrees with our measurements except in the case of the lowest incident IR energy (Fig. 2.22d).

The precession oscillations are well-fitted by a Lorentz peak at the qFMR frequency. As reported by Kalashnikova et al. [92], their initial phase is independent of \vec{H}_{DC} . They

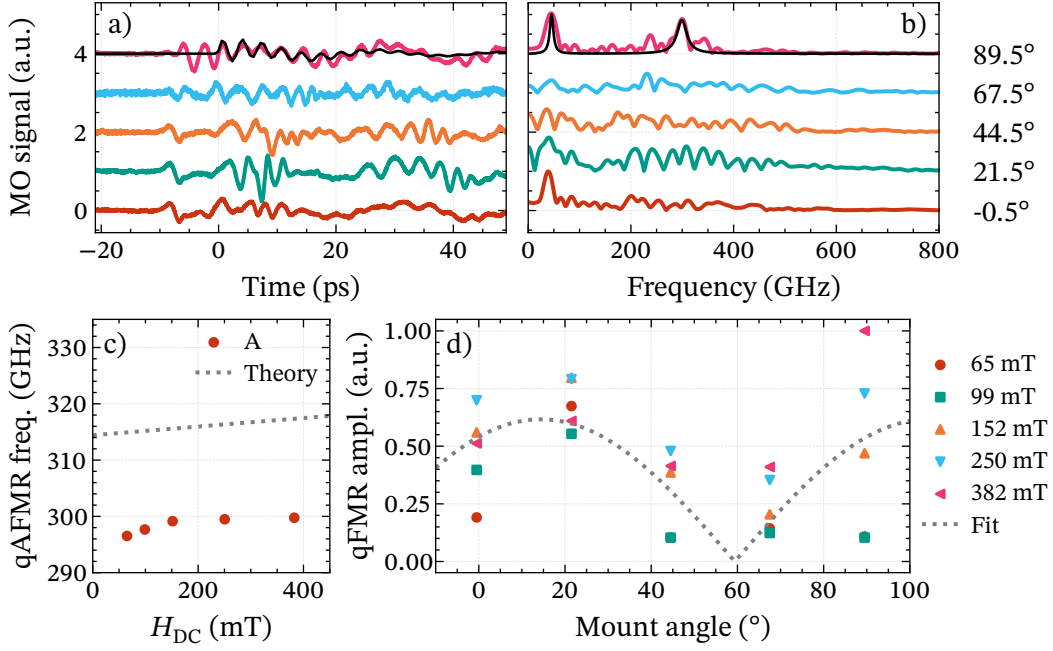


Figure 2.23: a) Measured MO signal and b) its spectrum for different angles of the sample and magnets mount. Dashed black lines: Lorentzian fit of the qFMR and qAFMR peaks. c) Measured qAFMR frequency and its theoretical value according to Eq. (2.49b). d) Variation of the qFMR amplitude with the rotation of the sample and H_{DC} , and fit of the average amplitude.

decay within 400 ps to 1400 ps, in some cases with a slow modulation of the envelope, showing amplitude minima after 390 ps and 780 ps. These modulation corresponds to additional peaks widening the qFMR spectrum and could be caused by additional non-uniform magnon modes [93, 94].

Figs. 2.23a and 2.23b shows the influence of the rotation of the sample mount on the initial oscillations after excitation, with 90° corresponding to the measurements A of Fig. 2.22. While the initial oscillations are independent of H_{DC} in shape and amplitude, they vary with the angle of the mount, which involves the rotation of the sample and of the magnets. We expect that these oscillations are driven by the internal reflections of the THz pulse inside the FeBO_3 sample and vary due to the inhomogeneity of its thickness.

Depending on the angles of the mount, up to two clear peaks are visible in the spectrum. One is centered at 46 GHz and corresponds to the qFMR mode. The other is centered at 300 GHz and is corresponds to the qAFMR mode. Both frequencies are influenced by H_{DC} , indicating a magnetic origin. As shown by Fig. 2.23c, there is an offset between the observed frequency and the theoretical qAFMR frequency according to Eq. (2.49b), which cannot be explained by an error in the calibration of H_{DC} and necessitate to reduce either H_D by 20 %, which also decreases the qFMR frequency, or H_E or H_A

by 15 %.

The rotation of the magnets determines both angles θ_p and θ_{THz} , corresponding respectively to the orientation of the probe and THz polarizations with respect to H_{DC} . Both angles then influence the amplitude of the measured signal. For a given precession amplitude, the MO signal is a nonlinear function of α , η and θ_p [90], and the change in measured amplitude when rotating the magnets cannot be analytically calculated. The qFMR and qAFMR modes are expected to have a precession amplitude varying as $\sin 2\theta_{\text{THz}}$ and $-\sin \theta_{\text{THz}}$ respectively [84, 85], where due to the tilted THz polarization, $\theta_{\text{THz}} = 90^\circ$ for a mount angle of 50° . As shown in Fig. 2.23d, the measured qFMR amplitude exhibits a compatible tendency. The qAFMR precession amplitude varying with half the frequency, we observe a single well-defined peak for a mount angle of 90° , while the qFMR amplitude at 0° and 90° is approximately the same.

We have thus observed the THz excitation of the qFMR mode in FeBO_3 , and found that its behavior agrees with what has been reported in the literature. A second mode, which we expect to be the qAFMR mode, can be seen in some measurements but does not match the theory as well as our observations of the qFMR mode. To understand the discrepancy, we had planned to repeat and continue the measurements after the reconstruction of the THz setup.

2.4 Conclusion

In this chapter, we have focused on nonlinear optics and in particular optical rectification, which is the phenomenon we exploit for THz generation in tilted pulse front setups. We have detailed the experimental parameters that can be chosen to optimize the THz output by improving the phase-matching between the pump pulse and the THz radiation: the density and angle of the grating creating the pulse front tilt, the material and cut of the nonlinear crystal, as well as the telescope imaging the pulse into the crystal. Then, we have presented the two setups built in order to provide a THz pump for the rest of the experiments. To the best of our estimations, the 1030 nm setup, which we designed for a high-energy pump, has delivered 2.3 ps pulses with an energy up to $19 \mu\text{J}$ from a 21.7 mJ pump. This corresponds to an energy conversion efficiency of 8.8×10^{-4} , and a quantum efficiency of 0.85. The 800 nm setup, which we rebuilt, has delivered 1.6 ps pulses of up to $2.6 \mu\text{J}$ with a 2.2 mJ pump, or a energy conversion efficiency of 1.2×10^{-3} and quantum efficiency of 1.46. To increase the THz electric field, we have designed, simulated and tested a focusing horn that increased the maximum field amplitude by a factor of 8.6, at the price of dispersing the pulse in time. We then examined a magneto-optic application of the THz radiation, in which a THz pulse triggers both modes of uniform resonance of the magnetization of the canted antiferromagnet FeBO_3 .

In the following chapters, we will continue on the subject of magnetism. First, Chapter 3 will introduce the fundamentals of the theory of magnetism, allowing us to

understand the origin of the magnetization precession we have observed in FeBO_3 . Then [Chapter 4](#) will come back to the subject of THz generation, this time exploiting ultrafast spin dynamics instead of optical rectification.

Theory of magnetism

We have with the measurements of FeBO₃ been introduced to magnetic materials, and the concepts of magnetization precession and spin waves. To calculate the allowed precession modes and their frequencies, we used effective magnetic fields representing material-specific internal forces that we did not define.

To understand the nature of these forces and pave the way to spintronic THz emitters, this chapter provides an overview of the theoretical concepts of magnetism. We will first consider classical magnetic fields, then look at the origin of magnetism in matter. Finally, we will discuss how the orientation of the magnetization can be manipulated, first with the static hysteresis curve and then the dynamic precession of the magnetization.

3.1 Magnetostatic fields

3.1.1 Magnetic fields in vacuum

The Maxwell equations define two fields of interest in magnetism: the magnetic field \vec{H} and the magnetic induction \vec{B} . Depending on the author, the latter is also called the magnetic field or magnetic flux density, while \vec{H} is also called the magnetic field strength, magnetizing force, or auxiliary field. In this manuscript, we chose the nomenclature that emphasizes the parallel with the electric field.

The magnetic induction is the quantity that exerts a force on a moving particle of charge q and velocity \vec{v} according to Lorentz's law:

$$\vec{F} = q(\vec{E} + \vec{v} \wedge \vec{B}), \quad (3.1)$$

and induces a torque $\vec{\tau}$ on a magnetic dipole with moment $\vec{\mu}$:

$$\vec{\tau} = \vec{\mu} \wedge \vec{B}. \quad (3.2)$$

In vacuum, the magnetic induction is related to the magnetic field by the vacuum permeability:

$$\vec{B} = \mu_0 \vec{H}. \quad (3.3)$$

Table 3.1: Equivalent formulas between the electric and magnetic fields. Respectively, \vec{E} and \vec{H} are the fields, \vec{D} and \vec{B} the inductions, \vec{P} and \vec{J} the polarizations, χ_e and χ_m the susceptibility tensors, and ϵ and μ the permittivity and permeability tensors.

Electricity	Magnetism
$\vec{D} = \epsilon_0 \vec{E} + \vec{P}$	$\vec{B} = \mu_0 \vec{H} + \vec{J}$
$\vec{P} = \epsilon_0 \chi_e \cdot \vec{E}$	$\vec{J} = \mu_0 \chi_m \cdot \vec{H}$
$\epsilon = \epsilon_0 (1 + \chi_e)$	$\mu = \mu_0 (1 + \chi_m)$

The value of μ_0 was redefined in 2019 from exactly $\mu_0 = 4\pi \times 10^{-7} \text{ H m}^{-1}$ to depend on the fine structure constant α , which is the fundamental constant quantifying the electromagnetic interaction: at present $\mu_0 = 2\hbar\alpha / ce^2 \approx (4 + 8.4 \cdot 10^{-10}) \pi \times 10^{-7} \text{ H m}^{-1}$ [95], where \hbar is the reduced Planck constant, c the velocity of light in vacuum and e the elementary charge.

3.1.2 The magnetization of matter

Similarly to how matter is polarized by an electric field, it can be magnetized by a magnetic field. This is described macroscopically by the magnetization \vec{M} as the average density of magnetic moments $\vec{\mu}$ in a body of volume V :

$$\vec{M} = \frac{1}{V} \sum_i \vec{\mu}_i. \quad (3.4)$$

Magnetic moments are the source of the magnetic induction field in matter, represented in Fig. 3.1a. The three magnetic vectors fields are related by:

$$\vec{B} = \mu_0 (\vec{H} + \vec{M}), \quad (3.5)$$

with \vec{B} in T and \vec{H} and \vec{M} in A m^{-1} . The magnetization can also be expressed as the magnetic polarization (also called the intrinsic induction) $\vec{J} = \mu_0 \vec{M}$, which highlights the parallel with the electric field vectors, as shown in Table 3.1.

Magnetic moments can be equivalently represented by two models: either as magnetic dipoles, which we can picture as microscopic pairs of positive and negative monopoles of strength $\pm p$ separated by a length l , or by microscopic current loops of surface A and current I . Both models produce the same magnetic field lines and moment at the limit $l \rightarrow 0$ and $A \rightarrow 0$: $|\vec{\mu}| = pl = IA$.

If a body is uniformly magnetized, it can be seen as a single macroscopic moment. Neighboring dipoles or current loops cancel each other inside its volume. On the surface,

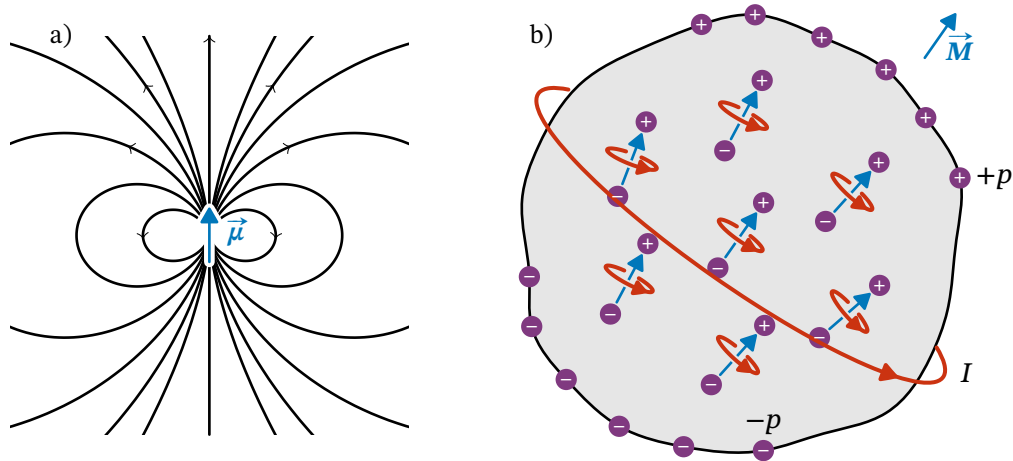


Figure 3.1: Models of a magnetic moment: a) lines of force of the \vec{B} field created by a magnetic dipole moment and b) macroscopic magnetization represented by surface poles and a surface current.

the breaking of symmetry leads to the accumulation of magnetic poles with opposite strength on opposing surfaces, or equivalently to a net surface current. The whole body is then equivalent to a dipole or to a current loop with the moment $\vec{\mu}_{\text{macro}} = V\vec{M}$, as schematized in Fig. 3.1b.

3.1.3 The dipolar field

Since magnetic dipoles generate a magnetic field, we could expect that two bodies equivalent to the same macroscopic dipole $\vec{\mu}_{\text{macro}}$ generate the same \vec{B} field. Let us consider the case of two cylinders with the same uniform magnetization normal to their base and the same volume, but different aspect ratios (see Fig. 3.2).

According to the current loop model, both cylinders are equivalent to non-magnetized

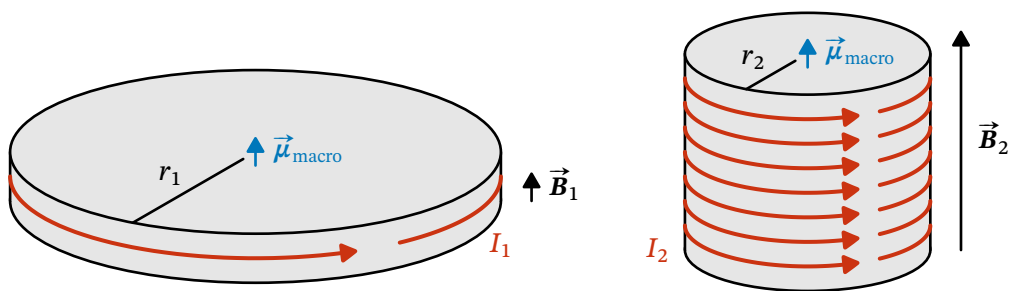


Figure 3.2: Uniformly magnetized cylinders with the same volume and magnetization. They are equivalent to the same macroscopic magnetic moment $\vec{\mu}_{\text{macro}}$ but generate a different \vec{B} field (arrow length proportional to the field at the center of the cylinders).

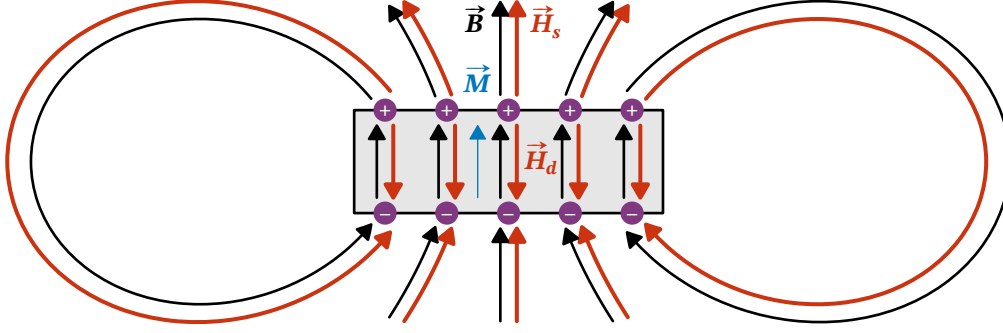


Figure 3.3: Dipolar field lines inside and outside a magnetized material.

bodies with a current loop around their curved surface, whose intensity is inversely proportional to the area of their base:

$$\mu_{\text{macro}} = I_1 \pi r_1^2 = I_2 \pi r_2^2, \quad (3.6)$$

so that $I_1 / I_2 = (r_2 / r_1)^2$. However, the magnetic induction at the center of a current loop is:

$$B = \frac{\mu_0 I}{2r}. \quad (3.7)$$

Combining Eq. (3.6) and Eq. (3.7), we can see that:

$$\frac{B_1}{B_2} = \frac{I_1 r_2}{I_2 r_1} = \left(\frac{r_2}{r_1} \right)^3. \quad (3.8)$$

In other words, the \vec{B} field created by a magnetized body depends on its shape. We introduce the dipolar field $\vec{H} = \vec{B} / \mu_0 - \vec{M}$ to account for the difference.

The lines of force of \vec{B} , as expressed by the Maxwell-Gauss equation $\vec{\nabla} \cdot \vec{B} = 0$, are closed loops curling around the surface currents (see Fig. 3.1a). The dipolar field instead has the same sources and sinks as the magnetization [96]:

$$\vec{\nabla} \cdot \vec{H} = -\vec{\nabla} \cdot \vec{M}. \quad (3.9)$$

In analogy to the electric charges, we represent in the dipole model \vec{H} as arising from the positive poles and sinking in negative poles, as schematized in Fig. 3.3. Outside the material, the dipolar field is called the stray field \vec{H}_s . In the absence of additional fields, its lines of force coincide with those of \vec{B} . Inside, it is called the demagnetizing field \vec{H}_d , according to Eq. (3.9) it is opposed to the direction of the magnetization. Eq. (3.5) becomes:

$$\vec{B}(\vec{r}) = \mu_0 (\vec{H}_d(\vec{r}) + \vec{M}) \quad \text{for } \vec{r} \in V, \quad (3.10a)$$

$$\vec{B}(\vec{r}) = \mu_0 \vec{H}_s(\vec{r}) \quad \text{for } \vec{r} \notin V. \quad (3.10b)$$

The dipolar fields \vec{H}_s and \vec{H}_d depend on the magnetization and the shape of the material, and are expressed as a function of a depolarization tensor \mathbf{N} :

$$\vec{H}_d(\vec{r}) = -\mathbf{N}_d(\vec{r}) \cdot \vec{M} \quad \text{for } \vec{r} \in V, \quad (3.11a)$$

$$\vec{H}_s(\vec{r}) = \mathbf{N}_s(\vec{r}) \cdot \vec{M} \quad \text{for } \vec{r} \notin V. \quad (3.11b)$$

\mathbf{N}_s is always position-dependent, as outside the material the field strength falls with the distance, while \mathbf{N}_d is constant in the case of uniformly magnetized ellipsoids. Both tensors can only be exactly calculated for a few geometries. In the case of a sphere of radius R [97]:

$$\mathbf{N}_d = \begin{bmatrix} \frac{1}{3} & 0 & 0 \\ 0 & \frac{1}{3} & 0 \\ 0 & 0 & \frac{1}{3} \end{bmatrix}, \quad (3.12a)$$

$$\mathbf{N}_s(\vec{r}) = \frac{R^3}{3|\vec{r}|^5} \begin{bmatrix} 3r_x^2 - |\vec{r}|^2 & 3r_x r_y & 3r_x r_z \\ 3r_y r_x & 3r_y^2 - |\vec{r}|^2 & 3r_y r_z \\ 3r_z r_x & 3r_z r_y & 3r_z^2 - |\vec{r}|^2 \end{bmatrix}. \quad (3.12b)$$

Replaced in Eq. (3.10), this set of demagnetization tensors satisfies the continuous boundary condition for the normal component of \vec{B} : $B_\perp(R) = 2\mu_0|\vec{M}|/3$. For a cuboid with sides of length a , b and c uniformly magnetized along c , the diagonal components of \mathbf{N}_d are approximately $-4ab/(4ab + 3c(a + b))$ [98]. In the case of a thin sample such as FeBO₃ in Section 2.3.2, we approximate the material as an infinite plane normal to the z axis, that is to say a flattened ellipsoid, for which we use:

$$\mathbf{N}_d = \begin{bmatrix} 0 & 0 & 0 \\ 0 & 0 & 0 \\ 0 & 0 & 1 \end{bmatrix}. \quad (3.13)$$

In this case, there is no demagnetization for the in-plane magnetization components, and inside the sample $B_x = \mu_0 M_x$, $B_y = \mu_0 M_y$. The out-of-plane magnetization component is however completely canceled: $B_z = 0$.

3.1.4 Susceptibility and classification of materials

Materials are classified according to their response to magnetic fields. Paramagnetic and diamagnetic materials have no intrinsic magnetization and are magnetized by an applied

field. The induced magnetization is characterized by the magnetic susceptibility tensor χ_m with:

$$\vec{M} = \chi_m \cdot \vec{H}_{\text{in}}, \quad (3.14)$$

where $\vec{H}_{\text{in}} = \vec{H}_{\text{app}} + \vec{H}_d$ is the total magnetic field inside the material. Similarly to the definition of the relative permeability, we define the relative permeability as $\mu_r = 1 + \chi_m$.

Replacing Eq. (3.11a) in Eq. (3.14), we obtain:

$$\vec{M} = \underbrace{\left(\mathbf{1} + \chi_m \cdot N_d \right)^{-1}}_{\chi_{\text{eff}}} \cdot \chi_m \cdot \vec{H}_{\text{app}}, \quad (3.15)$$

which defines the effective susceptibility tensor of the magnet χ_{eff} , taking into account both the material through χ_m and the specific shape of the body through N_d . As in the general case N_d is unknown, it is the effective susceptibility which is measured in practice as a function of the applied field.

The total induction field inside the material is then:

$$\begin{aligned} \vec{B} &= \mu_0 \left(\vec{H}_{\text{app}} + (\mathbf{1} - N_d) \cdot \vec{M} \right) \\ &= \mu_0 \left(\mathbf{1} + (\mathbf{1} - N_d) \cdot \chi_{\text{eff}} \right) \cdot \vec{H}_{\text{app}} \\ &= \mu_0 \left(\mathbf{1} + \chi_m^{-1} \right) \cdot \left(\mathbf{1} + \chi_m \cdot N_d \right) \cdot \chi_m \cdot \vec{H}_{\text{app}}, \end{aligned} \quad (3.16)$$

and the measured relative permeability of the magnet is:

$$\mu_{\text{eff}} = \mathbf{1} + (\mathbf{1} - N_d) \cdot \chi_{\text{eff}}. \quad (3.17)$$

Diamagnetism

When bound electrons are subject to a magnetic field, the latter exerts a torque on their orbital angular momentum, making their orbits precess around \vec{B} . This precession produces a magnetic moment in the opposite direction. All materials have this diamagnetic response to an applied field, but the weakness of this effect makes it apparent only in materials whose atoms have otherwise no magnetic moments, where it induces a small magnetization opposed to the applied field. These materials are called diamagnetic and are characterized by a small negative susceptibility, typically $|\chi_m| < 10^{-5}$.

An example is water, with $\chi_m = -9.04 \times 10^{-6}$ at 20 °C [99, chapter 1]. A perfect diamagnet would have $\chi_m = -1$, from which follows that $B = 0$ inside the material regardless of the applied field. The permeability μ is then zero, which highlights that the material is impermeable to any magnetic field.

Paramagnetism

Materials whose atoms have a small magnetic moment but no spontaneous ordering are called paramagnetic. Without an applied field, the individual atomic moments can point

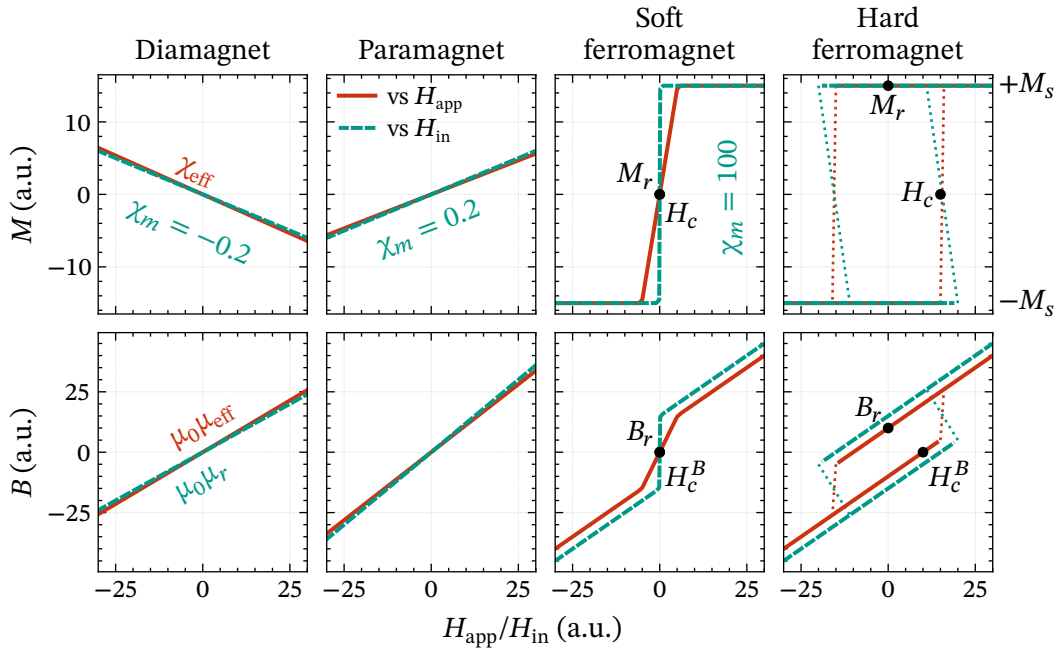


Figure 3.4: Hysteresis curves of the magnetization M or induction B for different types of magnetic materials, with respect to the applied field (full lines) and the total internal field (dashed lines). For visibility, χ_m is chosen closer to 1 than in typical materials, $M_s = 15$ a.u., and $N_d = 1/3$.

in any direction and result in no net magnetization. When a field is applied, the moments progressively align on it, resulting in a small positive susceptibility, typically in the range of 10^{-5} to 10^{-3} . An example is O_2 with $\chi_m = 1.94 \times 10^{-6}$ at 20°C [99, chapter 1].

As the thermal agitation reduces the ability of the moments to align on an applied field, the susceptibility of the material obeys the classical Curie law $\chi_m = C/T$, described in Section 3.2.4.3.

Ferromagnetism

Other materials have a strong interaction between neighboring atoms, leading to the spontaneous alignment of their magnetic moments and the formation of regions of uniform magnetization called domains. The formation of domains helps to minimize the energy of the dipolar field by reducing the net magnetization of the sample, but their number is limited by the additional energy associated with domains boundaries.

A material whose atomic moments have a spontaneous parallel alignment is called ferromagnetic (FM). Because of the domains, the response of such material to an applied field is nonlinear and often irreversible. The domain boundaries move and their magnetization align on the field until the sample is uniformly magnetized. If the applied field is then reduced, the interaction between neighboring moments keep the material from

immediately breaking off into domains again. This is the source of the characteristic hysteresis of magnetic materials.

Due to their nonlinear behavior, ferromagnetic materials do not have a fixed susceptibility and Eq. (3.14) is not valid. Instead, their hysteresis curve can be locally described by the differential susceptibilities $\chi_m = d\vec{M}/d\vec{H}_{\text{in}}$ and $\chi_{\text{eff}} = d\vec{M}/d\vec{H}_{\text{app}}$. The susceptibility drops to zero once the magnetization reaches its saturation value $|\vec{M}| = M_s$. As shown on Fig. 3.4, specific values characterize the behavior of a ferromagnet. When the applied field is removed after the magnetization has been saturated, the remaining magnetization is called the remanence $\vec{M}_r = \vec{M}(\vec{H}_{\text{app}} = 0)$. The remanent induction $\vec{B}_r = (\mathbf{1} - N_d) \cdot \vec{M}_r$ determines the magnetic field generated by permanent magnets. The necessary applied field to finally reverse the direction of the magnetization is called the intrinsic coercivity $\vec{H}_c = \vec{H}_{\text{app}}(\vec{M} = 0)$. The reversal of the magnetic field emitted by the material occurs for a different value of the applied field called coercivity as well, $\vec{H}_c^B = \vec{H}_{\text{app}}(\vec{B} = 0)$. For all ferromagnetic materials, $\vec{H}_c \geq \vec{H}_c^B$.

For the same reason than the paramagnetic susceptibility decreases with increasing temperature, the value of the saturation magnetization M_s is lowered. Ferromagnetic materials have a critical temperature known as the Curie temperature T_C , at which the thermal energy is stronger than the exchange energy that aligns of the moments. Above this temperature, the materials become paramagnetic and follow the Curie-Weiss law $\chi_m = C / (T - T_C)$. The material with the highest Curie temperature is cobalt with $T_C = 1388$ K.

Ferromagnetic materials exist on a spectrum from soft to hard, depending on their intrinsic coercivity. A material with $H_c < 1$ kA m⁻¹ is referred to as soft, and a material with $H_c > 100$ kA m⁻¹ as hard [99, chapter 1]. On one hand, an ideal soft ferromagnet as shown in Fig. 3.4 has an intrinsic coercivity of zero. For $|\vec{M}| \leq M_s$, its susceptibility tends towards at the limit $\chi_m = +\infty$, from which follows that $\chi_{\text{eff}} = 1 / N_d$ [96]. The magnetization saturates easily at a small field $\vec{H}_{\text{app}} = N_d \cdot \vec{M}_s$. Above that, the magnetization cannot increase and the susceptibilities are both zero. Similarly to paramagnetic materials, soft ferromagnets have no hysteresis. On the other hand, an ideal hard ferromagnet behaves like a single magnetic moment and its magnetization is always saturated. $\chi_{\text{eff}} = \chi_m = 0$ everywhere except for a discontinuity at $\vec{H}_{\text{app}} = \pm \vec{H}_c$, where the magnetization inverts its sign. Real ferromagnetic materials have an intermediate behavior, with hysteresis and a smoother switching of the magnetization.

Antiferromagnetism and ferrimagnetism

Finally, the interaction between neighboring atoms does not always lead to the atoms having the same magnetic moment. In antiferromagnetic (AFM) materials, it leads to an antiparallel alignment instead of a parallel one. Within each domain, these materials are said to possess two sublattices with equal but opposite magnetization, $\vec{M}_A = -\vec{M}_B$. The net magnetization of the material is then zero. The antiferromagnetic equivalent of the

Curie temperature is the Néel temperature T_N , above which the spontaneous alignment vanishes. In ferrimagnetic materials, the alignment of neighboring moments is parallel but their value is different: $\vec{M}_A < \vec{M}_B$. There is thus a net magnetization.

The hysteresis curves of Fig. 3.4 do not apply to such materials. Instead, the equilibrium alignment of the sublattice magnetizations depend on the relative strength of the force exerted by the external field, compared to the force of the exchange interaction between the different sublattices. An example of calculation of the equilibrium magnetization for the antiferromagnet FeBO_3 is given in Section 3.3.3.2.

Considering the macroscopic properties of magnetic materials, we have introduced the notion of magnetic moments and the coupling between them, without explaining their nature. We will now take a step back to discuss their origin in the spin of electrons, and show how the different properties of magnetic materials arise.

3.2 The quantum origin of magnetism

In this section, we will look at the emergence of the magnetic properties from quantum physics. We will first calculate the magnetic moment of a single electron, then of an atom. Afterwards, we will consider the susceptibility of materials. Finally, we will look into the exchange forces at the origin of the ferromagnetic and antiferromagnetic order.

3.2.1 Magnetic moment of a bound electron

Magnetism in solids has its origin in the quantum properties of electrons. In a first time, we consider a single electron orbiting a nucleus. Its Hamiltonian is composed of its kinetic energy and the electrostatic potential of the nucleus:

$$\hat{H} = \frac{\hat{\mathbf{p}}^2}{m_e} - \frac{Ze^2}{4\pi\epsilon_0|\vec{\mathbf{r}}|}, \quad (3.18)$$

where the operator $\hat{\mathbf{p}} = -i\hbar\hat{\nabla}$ describes the canonical momentum of the electron and $\hat{\mathbf{r}}$ is its position with respect to the nucleus. We are interested in stationary states, which satisfy the time-independent Schrödinger equation:

$$\hat{H}|\psi_i\rangle = E_i|\psi_i\rangle, \quad (3.19)$$

and are thus characterized by their well-defined energy. Because of the spherical symmetry of the potential, we can separate the radial and angular dependencies of the Hamiltonian. Its eigenfunctions are the orbitals $\varphi(r, \theta, \phi) = R_{n,l}(r) Y_l^{m_l}(r, \theta, \phi)$, where $Y_l^{m_l}$ is a complex spherical harmonic that describes the angular momentum of the electron, and $R_{n,l}$ is a radial function that describes the energy of the electron in the potential modified by the centrifugal force.

3.2.1.1 Description of the quantum states

Each electron on an atom is uniquely characterized by a set of quantum numbers:

- The principal quantum number $n \geq 1$ is an integer that defines the shell on which the electron orbitates. It determines the radius of the orbital and thus is the largest contributor to the energy of the electron. Shells are labeled in spectroscopic notation by K, L, M, etc.
- The azimuthal quantum number $0 \leq l < n$ defines the orbital angular momentum of the electron and thus the shape of the orbital, with $l = 0$ being the closest to a classical circular orbit. States with the same n and l form the subshell nl , where the integer l is replaced by the label s, p, d, f, etc.
- The orbital magnetic quantum number m_l quantifies the projection of the orbital angular momentum along an arbitrary quantization axis, describing the orientation of the spherical harmonic. It can take $2l + 1$ discrete values with $|m_l| \leq l$. The quantization axis, usually z , defines the spatial coordinates system chosen to decompose the wavefunction. Together, n , l and m_l define a specific orbital.
- Besides their orbital motion, electrons also have an intrinsic spin angular momentum, defined by the quantum number $s = 1/2$. The corresponding spin magnetic quantum number m_s quantifies its projection along the quantization axis. Similarly to m_l , it has $2s + 1 = 2$ allowed values satisfying $|m_s| \leq s$, that is to say $m_s = \pm 1/2$.
- Although the quantum numbers above are sufficient to uniquely characterize each base eigenstate, we also introduce the quantum number j to describe the total angular momentum, with $|l - s| \leq j \leq l + s$. States with the same j within a subshell form a multiplet and are labeled $n^{2s+1}l_j$. Each multiplet allows $2j + 1$ different values of the projection quantum number $|m_j| \leq j$. For a single electron, we have $m_j = m_l + m_s$.

Fig. 3.5 shows the first ten energy eigenstates of our hydrogen-like atom, that form the basis on which we decompose the wavefunction of an electron: $|\psi\rangle = \sum_i c_i |\varphi_i\rangle$. The eigenstates of Eq. (3.18) are the energies $E_n \propto -1/n^2$, forming the gross structure of the spectroscopy lines in hydrogen. The value of l is taken into account through relativistic corrections to the kinetic energy, in the order of 10^{-5} . Together with j , which will enter the Hamiltonian in Section 3.2.2.3, it creates the fine structure of the spectroscopy lines. The spatial orientation of the angular momenta only influences the energy when the spherical symmetry of the potential is broken, for example in the presence of magnetic fields. For the electron to be in a stationary state, its wavefunction must be an eigenstate of the Hamiltonian and can thus only be formed by a superposition of degenerate eigenstates.

The operators for the orbit, spin and total angular momentum are \hat{L} , \hat{S} and \hat{J} , respectively. Because their individual components do not commute, we do not use these

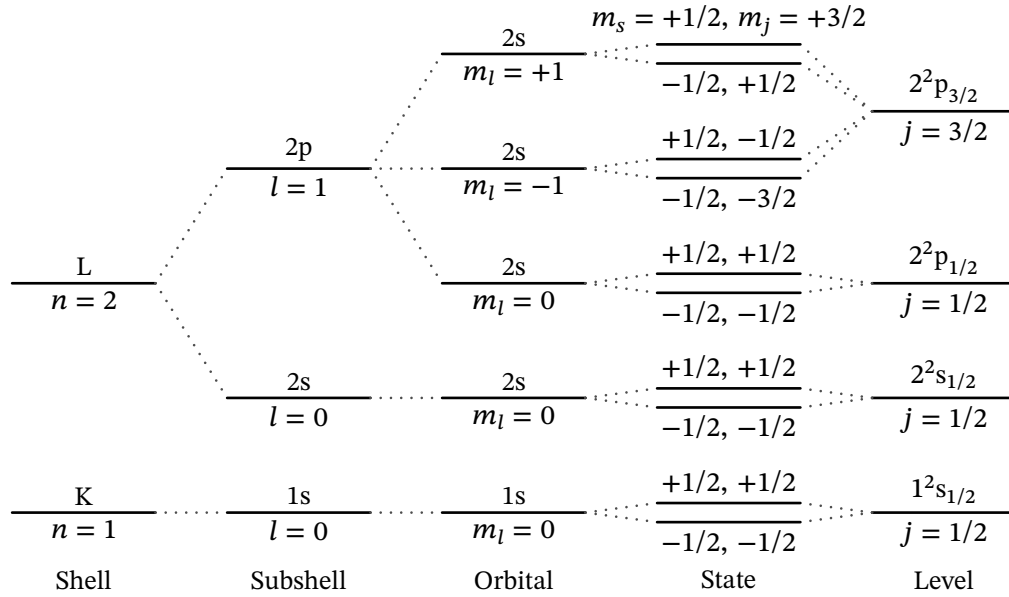


Figure 3.5: Lowest energy eigenstates of an hydrogen-like atom, with their labels and the corresponding quantum numbers. The levels are not ordered by energy.

operators directly, but rather their squared magnitude and a single of their components. Except for n , each of the quantum numbers we introduced is the eigenvalue of one of the derived operators:

$$\hat{L}^2|l\rangle = l(l+1)\hbar^2|l\rangle, \quad \hat{L}_z|m_l\rangle = m_l\hbar|m_l\rangle, \quad (3.20a)$$

$$\hat{S}^2|s\rangle = s(s+1)\hbar^2|s\rangle, \quad \hat{S}_z|m_s\rangle = m_s\hbar|m_s\rangle, \quad (3.20b)$$

$$\hat{J}^2|j\rangle = j(j+1)\hbar^2|j\rangle, \quad \hat{J}_z|m_j\rangle = m_j\hbar|m_j\rangle. \quad (3.20c)$$

Let us start with the orbital angular momentum, $\hat{L} = \hat{\mathbf{r}} \wedge \hat{\mathbf{p}}$. The two observables \hat{L}^2 and \hat{L}_z have for eigenfunctions the complex spherical harmonics. All possible orbital angular momenta can be decomposed in the basis of the vectors $\{|l, m_l\rangle\}$. Since \hat{L}^2 , \hat{L}_z and the Hamiltonian \hat{H} commute in a spherical potential, we can form a common basis $\{|n, l, m_l\rangle\}$ of simultaneous eigenvectors of all three operators, that each identifies an orbital. Their space representation is given by $\varphi(\vec{\mathbf{r}}) = R_{n,l}(\vec{\mathbf{r}}) Y_l^{m_l}(\vec{\mathbf{r}}) = \langle \vec{\mathbf{r}} | n, l, m_l \rangle$. However, they are not eigenvectors of the operators \hat{L}_x or \hat{L}_y : the x and y components of the orbital angular momentum do not have well-defined values in this basis.

To understand this uncertainty, we can use the vector model, shown in Fig. 3.6. The angular momentum of a given orbital is represented by the classical vector $\vec{\mathbf{l}}$, whose magnitude is $\sqrt{l(l+1)}\hbar$ and z component $m_l\hbar$. The uncertainty on the transverse components can be classically described by picturing that $\vec{\mathbf{l}}$ precesses around the quantization axis. This does not however correspond to a physical precession of the angular momentum, as $|n, l, m_l\rangle$ is an eigenstate of the Hamiltonian and the electron does not evolve in time.

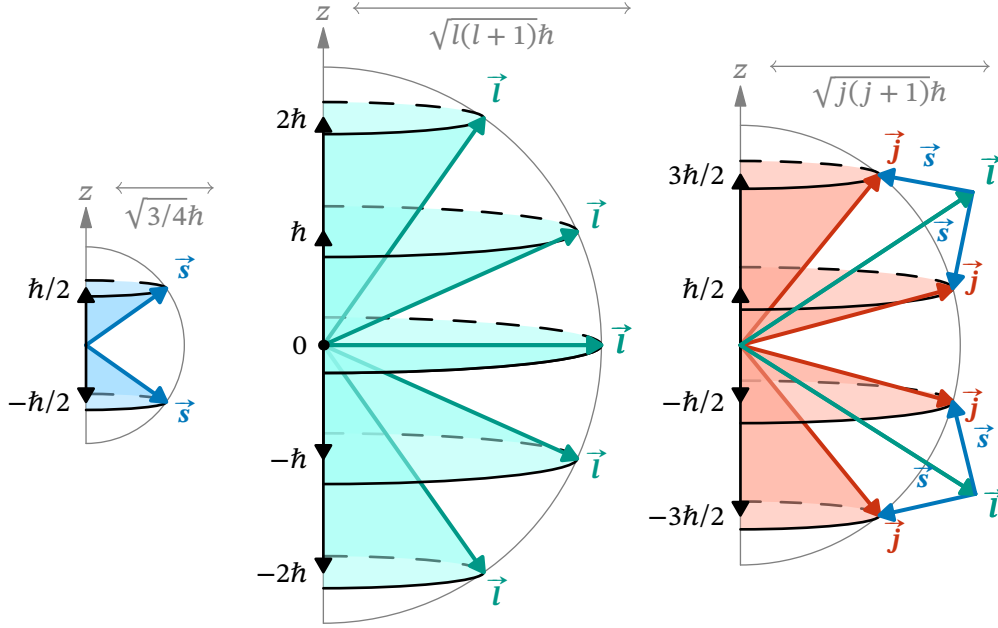


Figure 3.6: Vector model of the angular momentum: spin \vec{s} , orbital \vec{l} and total \vec{j} angular momentum vectors, for $l = 2$ and $j = l - s = 3/2$. The undefined value of the x and y components of the momenta is represented as the precession of the vectors at fixed latitudes $m_s\hbar$, $m_l\hbar$ and $m_j\hbar$.

The spin constitutes an independent degree of freedom, that we describe in the basis $\{|s, m_s\rangle\}$. Since they act on a different vector space, the spin operators \hat{S}^2 and \hat{S}_z commute with \hat{L}^2 , \hat{L}_z and \hat{H} . We can then form a new set of basis states spanning both real space and spin space, called spinorbitals: $\{|n, l, s, m_l, m_s\rangle\} = \{|n, l, m_l\rangle \otimes |s, m_s\rangle$. The explicit form of a specific spinorbital $|\psi\rangle$ is $\psi(\vec{r}, m_s) = \varphi(\vec{r})\zeta(m_s) = (\langle \vec{r} | \langle m_s |) (|n, l, m_l\rangle \otimes |s, m_s\rangle)$, with φ and ζ describing respectively the orbital and spin parts of a wavefunction.

Finally, the total angular momentum operator is $\hat{J} = \hat{L} \otimes \hat{I}_s + \hat{I}_l \otimes \hat{S}$, where \hat{I} is the identity operator. Since it is implicitly understood that each operator acts on its own space, we will from now on omit the tensor product and simply write $\hat{J} = \hat{L} + \hat{S}$. The component \hat{J}_z commutes with \hat{L}_z and \hat{S}_z , leading to:

$$\begin{aligned} \hat{J}_z|\psi\rangle &= \hat{L}_z|\varphi\rangle + \hat{S}_z|\zeta\rangle \\ &= (m_l + m_s)(|\varphi\rangle \otimes |\zeta\rangle) = m_j|\psi\rangle. \end{aligned} \quad (3.21)$$

The three magnitudes \hat{J}^2 , \hat{L}^2 and \hat{S}^2 commute as well. However, \hat{J}^2 does not commute with \hat{L}_z and \hat{S}_z , so that we cannot construct a basis in which the electron has well-defined values of j , m_l and m_s simultaneously. For example, an electron in the 3d subshell ($n = 3$, $l = 2$) with the quantum numbers $m_l = -1$ and $m_s = 1/2$ has a total angular momentum of $m_j = -1/2$, but j could be either $l + s = 5/2$ or $l - s = 3/2$. Reciprocally, Fig. 3.6

shows that when the magnitude of the three momenta is fixed, the projections of \vec{l} and \vec{s} along the z axis are undefined. This is pictured in the vector model as \vec{l} and \vec{s} precessing around $\vec{j} = \vec{l} + \vec{s}$.

Instead of describing electronic wavefunctions in the basis $\{|n, l, s, m_l, m_s\rangle\}$, we can use the coupled basis $\{|n, l, s, j, m_j\rangle\}$. The eigenvectors of each basis are linear combinations of eigenvectors in the other basis, related by the Clebsch–Gordan coefficients. In our example, the wavefunction of the 3d electron is:

$$|\psi\rangle = \begin{cases} \left|3, 2, \frac{1}{2}, -1, \frac{1}{2}\right\rangle, & \text{(uncoupled basis)} \\ \sqrt{\frac{2}{5}} \left|3, 2, -1, \frac{5}{2}, -\frac{1}{2}\right\rangle - \sqrt{\frac{3}{5}} \left|3, 2, -1, \frac{3}{2}, -\frac{1}{2}\right\rangle. & \text{(coupled basis)} \end{cases} \quad (3.22)$$

All operators so far commute with the Hamiltonian in Eq. (3.18), so that the two representations are equivalent. When we later include the spin-orbit coupling contribution to the Hamiltonian (see Section 3.2.2.3), the uncoupled basis will not anymore represent eigenstates of \hat{H} , that is to say will not represent steady states of the electron, and we will prefer characterizing the system by its total angular momentum.

3.2.1.2 Understanding spatial quantization

There are only a limited number of values that m_l and m_s or m_j can take, but we know that the magnetization of a material can take an arbitrary direction in space. Due the simplicity of its matrix representation, we consider the transition between the quantum and classical angular momentum for the case of the spin.

In the $\{|m_s\rangle\}$ basis, the operators for each component of the spin angular momentum are expressed by the Pauli spin matrices:

$$\hat{S}_x = \frac{\hbar}{2} \begin{bmatrix} 0 & 1 \\ 1 & 0 \end{bmatrix}, \quad \hat{S}_y = \frac{\hbar}{2} \begin{bmatrix} 0 & -i \\ i & 0 \end{bmatrix}, \quad \hat{S}_z = \frac{\hbar}{2} \begin{bmatrix} 1 & 0 \\ 0 & -1 \end{bmatrix}. \quad (3.23)$$

The quantization axis being z , only \hat{S}_z is diagonal. For reasons that will become apparent in the next sections, we define its eigenvectors $|m_s\rangle$ as “spin down” and “spin up”:

$$\left|+\frac{1}{2}\right\rangle = |\downarrow\rangle = \begin{bmatrix} 1 \\ 0 \end{bmatrix}, \quad \left|-\frac{1}{2}\right\rangle = |\uparrow\rangle = \begin{bmatrix} 0 \\ 1 \end{bmatrix}. \quad (3.24)$$

In this basis, the respective eigenvectors of the three operators have the same vector representation as the polarization states of light: the eigenvectors of \hat{S}_z are the Jones vectors for linear horizontal and vertical polarization, those of \hat{S}_x linear diagonal polarization, and \hat{S}_z circular polarization. We thus know that, like any polarization state, any spin state of the electron can be expressed by a superposition of the up and down states:

$$|\zeta\rangle = a|\uparrow\rangle + b|\downarrow\rangle, \quad (3.25)$$

where a and b are complex coefficients. Finally, we define the observable spin angular momentum vector as:

$$\vec{\mathbf{S}} = \left[\langle \hat{\mathbf{S}}_x \rangle, \langle \hat{\mathbf{S}}_y \rangle, \langle \hat{\mathbf{S}}_z \rangle \right], \quad (3.26)$$

using the expectation values $\langle \hat{\mathbf{S}}_i \rangle = \langle \zeta | \hat{\mathbf{S}}_i | \zeta \rangle$. If we measure an ensemble of electrons in the same state, for example $|\zeta\rangle = 1/\sqrt{2}|\uparrow\rangle + 1/\sqrt{2}|\downarrow\rangle$, their observable angular momentum is $\vec{\mathbf{S}} = \hbar/2[1, 0, 0]$ and in the absence of orbital contribution, the magnetization is aligned with the x axis. For individual electrons, a measurement along the x axis always returns $m_s = +1/2$, while a measurement along the y or z axis has a probability of 50% to return each value. In the vector model, $\vec{\mathbf{S}}$ can be seen as a time average of the precessing vector $\vec{\mathbf{s}}$, with a reduced magnitude of $\hbar/2$ instead of $\sqrt{3/4}\hbar$.

3.2.1.3 Magnetic moments

Finally, we arrive at the subject of magnetic properties. Since the electron is a charged particle that, in a classical picture, orbits the nucleus and spins around its own axis, it forms current loops that produce magnetic moments as described in [Section 3.1.2](#). The magnetic moment of a particle of charge q and mass m is related to its angular momentum by the gyromagnetic ratio $\gamma = qg/(2m)$, where the g -factor is a dimensionless proportionality constant. The magnetic moment operators have the same properties as the angular momentum operators: only their z component is determined, and the observable vector is $\vec{\boldsymbol{\mu}} = [\langle \hat{\boldsymbol{\mu}}_x \rangle, \langle \hat{\boldsymbol{\mu}}_y \rangle, \langle \hat{\boldsymbol{\mu}}_z \rangle]$. Due to the sign of its charge $q = -e$, the magnetic moment of an electron is opposed to its orbital momentum. Its smallest unit is the Bohr magneton $\mu_B = e\hbar/2m_e = 9.274 \times 10^{-24} \text{ A m}^2$.

For orbital motion, we always have $g = g_l = 1$. The orbital magnetic moment operator is thus:

$$\hat{\boldsymbol{\mu}}_l = \gamma \hat{\mathbf{L}} = -\frac{\mu_B}{\hbar} \hat{\mathbf{L}}, \quad (3.27)$$

with magnitude $\sqrt{l(l+1)}\mu_B$ and z component $-\mu_B m_l$. Similarly, the spin magnetic moment operator is $\hat{\boldsymbol{\mu}}_s = \gamma \hat{\mathbf{S}}$. The g -factor for spin is $g_s = 2 + \alpha/\pi \approx 2$, where α is the fine-structure constant. Thus $\hat{\boldsymbol{\mu}}_{s_z}$ has the eigenvalues $-\mu_B g_s m_s \approx \mp \mu_B$. Because of this sign reversal, our definition of “spin up” corresponds to a moment $+\mu_B$.

Since the spin contributes twice as much to the magnetic moment as the orbital angular momentum, the operator for the total moment is:

$$\hat{\boldsymbol{\mu}}_j = \hat{\boldsymbol{\mu}}_l + \hat{\boldsymbol{\mu}}_s = -\frac{\mu_B}{\hbar} (\hat{\mathbf{L}} + g_s \hat{\mathbf{S}}) \approx -\frac{\mu_B}{\hbar} (\hat{\mathbf{L}} + 2\hat{\mathbf{S}}). \quad (3.28)$$

The total magnetic moment is not parallel to the total angular momentum. In the vector model, $\vec{\boldsymbol{\mu}}_j \propto \vec{\mathbf{l}} + 2\vec{\mathbf{s}} = \vec{\mathbf{j}} + \vec{\mathbf{s}}$ and thus it also precesses around $\vec{\mathbf{j}}$. If we are working in the coupled basis where $\vec{\mathbf{l}}$ and $\vec{\mathbf{s}}$ are not known, their effective contribution thus

depends on their average projection on \vec{j} , given by the Landé g-factor [100]:

$$g_j = g_l \frac{j(j+1) - s(s+1) + l(l+1)}{2j(j+1)} + g_s \frac{j(j+1) + s(s+1) - l(l+1)}{2j(j+1)} \quad (3.29)$$

$$\approx 1 + \frac{j(j+1) + s(s+1) - l(l+1)}{2j(j+1)},$$

which allows us to define the total magnetic moment operator as:

$$\hat{\mu}_j = \gamma \hat{J} = -\frac{\mu_B g_j}{\hbar} \hat{J}. \quad (3.30)$$

Depending on whether the coupled or uncoupled basis is the best representation of the wavefunction, we can thus calculate the moment with Eq. (3.28) or Eq. (3.30).

3.2.1.4 The Zeeman effect

Until now, the choice of the z axis was arbitrary and the atom effectively isotropic; since states in the same subshell with different values of m_l and m_s are degenerate in field-free space, the electron can be found in any combination of those states. The application of a magnetic field breaks the full rotational symmetry of the Hamiltonian and lifts this degeneracy. As written in Eq. (3.2), the magnetic field exerts a torque on each magnetic moment. We must add a new term to the Hamiltonian:

$$\hat{H}_Z = -\hat{\mu}_l \cdot \vec{B} - \hat{\mu}_s \cdot \vec{B} = -\hat{\mu}_j \cdot \vec{B}. \quad (3.31)$$

To simplify the expression of the magnetic moment, we choose the quantization axis z to be along the direction of \vec{B} , in which case $\hat{H}_Z = -B_z \hat{\mu}_{j_z}$. While the field is small, \hat{H}_Z is treated as a small perturbation of the energy of well-defined orbitals. The energy shift for an electron in the state $|\psi\rangle = |n, l, s, j, m_j\rangle$ is given by the expectation value of the Hamiltonian [101]:

$$E_Z = \langle \psi | \hat{H}_Z | \psi \rangle = -B_z \langle \hat{\mu}_{j_z} \rangle = \frac{\mu_B g_j}{\hbar} B_z \langle \hat{J}_z \rangle = \mu_B g_j m_j B_z. \quad (3.32)$$

The magnetic field splits the fine-structure spectroscopy lines of hydrogen into $2j+1$ lines with the energy difference $\mu_B g_j B_z$ [101], which is called the Zeeman effect. The splitting in the case of $s \neq 0$ was historically called the anomalous Zeeman effect, because of the unexpected factor $g_s \approx 2$. The ground state has $m_j = -j$, so that the total momentum becomes aligned along the magnetic field. This corresponds necessarily to $m_l = -l$ and $m_s = -1/2$, which we have called the spin up direction.

As we did for FeBO₃ in Section 2.3.2, it is often possible to express the internal forces influencing the magnetization of a material as effective magnetic fields, with the caveat that some only act on the spin component. A Zeeman-like Hamiltonian $-\hat{\mu}_j \cdot \vec{B}_{\text{eff}}$ or $-\hat{\mu}_s \cdot \vec{B}_{\text{eff}}$ can then be used to represent all of them.

3.2.2 Magnetic moment of an isolated atom

Now that we have seen the mechanics leading to the formation of the magnetic moment of an hydrogen-like atom, we can generalize the same principles to atoms containing multiple electrons. We will first introduce the atomic quantum numbers, then explain what leads to the formation of these states.

3.2.2.1 Multi-electron quantum numbers

We start again with a multi-electron Hamiltonian composed of the kinetic and potential energy of each electron:

$$\hat{H} = \sum_i^N \left(\frac{\hat{\mathbf{p}}_i^2}{m_e} - \frac{Ze^2}{4\pi\epsilon_0|\mathbf{r}_i|} + \sum_{j>i} \frac{e^2}{4\pi\epsilon_0|\mathbf{r}_i - \mathbf{r}_j|} \right). \quad (3.33)$$

Compared to Eq. (3.18), we have added the electrostatic repulsion between the electrons. Because of this term, the Schrödinger equation has no exact solution describing simultaneously all the electrons. To get around this problem, we approximate it by an average spherical potential V and assume in a first time that the electrons are otherwise independent from each other. In this central field approximation, the Hamiltonian becomes:

$$\hat{H}_{\text{cf}} = \sum_i^N \left(\frac{\hat{\mathbf{p}}_i^2}{m_e} - \frac{Ze^2}{4\pi\epsilon_0|\mathbf{r}_i|} - eV(\mathbf{r}_i) \right), \quad (3.34)$$

and the atomic wavefunction is decomposed into the product of independent electronic wavefunctions: $|\Psi\rangle = |\psi_1\rangle \otimes |\psi_2\rangle \otimes \cdots \otimes |\psi_N\rangle$, which are each described in terms of the spinorbitals defined in the previous section.

As we have seen, a subshell contains $2(2l + 1)$ different spinorbitals, and can thus contain at most as many electrons. The number of electrons N in each subshell, indicated as nl^N , forms the configuration of the atom. For example, the ground state of a neutral carbon atom corresponds to the electronic configuration $1s^2 2s^2 2p^2$. For a given configuration, there are $\prod_i (4l_i + 2)! / (N_i! (4l_i + 2 - N_i)!)$ possible arrangement of the electrons in the available spinorbitals, with the index i referring to each subshell. For carbon, we get $1 \times 1 \times 15$ possibilities. Electrons being indistinguishable, filled subshells do not contribute to the product. In addition, they have an equal amount of electrons with opposite values of m_l and m_s and have thus no net angular momentum from either orbit nor spin. For this reason, magnetic properties only arise from partially filled subshells, and we usually do not need to consider the rest of the electrons outside of their contribution to the mean Coulomb potential.

The angular momentum of an ensemble of electrons is quantified by the quantum numbers L, S, J, M_L, M_S and M_J , which have the same meaning as their lowercase counterparts. This applies both to individual subshells and the whole atom. We will generally assume that there is a single partially filled subshell, to simplify the calculation

of the magnetic moment of an atom. The arithmetic of angular momentum operators is the same as in the previous section. The operators for the net orbital, spin and total angular momentum for an ensemble of N electrons are simply:

$$\hat{\mathbf{L}} = \sum_i^N \hat{\mathbf{L}}_i, \quad \hat{\mathbf{S}} = \sum_i^N \hat{\mathbf{S}}_i, \quad \hat{\mathbf{J}} = \sum_i^N \hat{\mathbf{J}}_i, \quad (3.35)$$

where it is implicit that each operator only acts on the vector space of the corresponding electron. Again, we do not use these operators directly, but instead their squares and z components. Similarly to Eq. (3.21), we have for a two-electron configuration where $|\Psi\rangle = |\psi_1\rangle \otimes |\psi_2\rangle$:

$$\begin{aligned} \hat{\mathbf{S}}_z |\Psi\rangle &= \hat{\mathbf{S}}_{z_1} |\psi_1\rangle + \hat{\mathbf{S}}_{z_2} |\psi_2\rangle \\ &= (m_{s_1} + m_{s_2}) (|\psi_1\rangle \otimes |\psi_2\rangle) = M_S |\Psi\rangle. \end{aligned} \quad (3.36)$$

The quantum numbers describing the projections on the z axis are thus given by $M_L = \sum_i m_{l_i}$, $M_S = \sum_i m_{s_i}$ and $M_J = \sum_i m_{j_i}$. This is not the case for L , S and J , as similarly to what we saw for when adding the angular momenta of one electron, the squared atomic operators $\hat{\mathbf{L}}^2$, $\hat{\mathbf{S}}^2$ and $\hat{\mathbf{J}}^2$ do not commute with the electronic $\hat{\mathbf{L}}_{z_i}$, $\hat{\mathbf{S}}_{z_i}$ and $\hat{\mathbf{J}}_{z_i}$, respectively. In general, many arrangements of the electrons result in the same M_L and M_S , and each projection quantum number can be associated with several magnitudes of the corresponding angular momentum. Describing the spin of the atom in the coupled basis $\{|S, M_S\rangle\}$ thus involves the loss of information regarding the spin of individual electrons, and likewise for the bases $\{|L, M_L\rangle\}$ and $\{|J, M_J\rangle\}$. In the vector model, this is represented by the vectors \vec{l}_i and \vec{s}_i precessing around their resultants $\vec{L} = \sum_i \vec{l}_i$ and $\vec{S} = \sum_i \vec{s}_i$, respectively.

Since $-S \geq M_S \geq S$, the largest S achievable for a given electronic configuration is obtained by maximizing the number of electrons with $m_s = +1/2$. Assuming a single partially filled subshell, this means:

$$0 \leq S \leq \begin{cases} N/2, & (N \leq 2l+1) \\ 2l+1 - N/2, & (N > 2l+1) \end{cases} \quad (3.37)$$

Similarly, the largest L is obtained by maximizing m_l when filling the orbitals. This leads to:

$$0 \leq L \leq N(l+1/2) - N^2/4 - \begin{cases} 0, & (N \text{ even}) \\ 1/4, & (N \text{ odd}) \end{cases} \quad (3.38)$$

The two filling strategies are incompatible, so that L and S are not independent from each other. The allowed pairs are called terms and written ^{2S+1}L , where L is represented by the letters S, P, D, F, etc., and $2S+1$ indicate their multiplicity. Continuing with our example of a carbon atom with a $2p^2$ configuration, the 15 possible arrangements

of electrons give rise to a 1S term ($M_S = 0$ and $M_L = 0$), a 3P term ($M_S = -1$ to 1 and $M_L = -1$ to 1) and a 1D term ($M_S = 0$ and $M_L = -2$ to 2). Although electrons arrangements contribute to several terms, we still have a basis $\{|L, S, M_L, M_S\rangle\}$ containing 15 orthogonal states. Finding all existing terms and their decomposition into electronic orbitals is computationally heavy, but we will see in [Section 3.2.2.4](#) that finding the ground term is trivial using Hund's rules.

3.2.2.2 Intra-atomic exchange coupling

Two-electron exchange

We now examine the full electrostatic interactions between the electrons. For simplicity, let us consider an atom with only two electrons. Its Hamiltonian is:

$$\begin{aligned}\hat{H} &= \frac{\hat{\mathbf{p}}_1^2}{m_e} + \frac{\hat{\mathbf{p}}_2^2}{m_e} - \frac{Ze^2}{4\pi\epsilon_0|\mathbf{r}_1|} - \frac{Ze^2}{4\pi\epsilon_0|\mathbf{r}_2|} + \frac{e^2}{4\pi\epsilon_0|\mathbf{r}_1 - \mathbf{r}_2|} \\ &= \hat{H}_{01} + \hat{H}_{02} + \hat{H}_C,\end{aligned}\quad (3.39)$$

where \hat{H}_0 is the one-electron Hamiltonian and \hat{H}_C is the Coulomb repulsion. The latter cannot in general be simply expressed in terms of one-electron spinorbitals, but its expectation value can be approximated as a perturbation of them.

Let us consider first the wavefunction of the unperturbed atom $|\Psi\rangle = |\psi_1\rangle \otimes |\psi_2\rangle$, describing independent electrons on separate spinorbitals. Explicitly, its wavefunction is:

$$\Psi = \psi_1(\mathbf{r}_1, m_{s_1})\psi_2(\mathbf{r}_2, m_{s_2}) = \varphi_a(\mathbf{r}_1)\zeta(m_{s_1})\varphi_b(\mathbf{r}_2)\zeta(m_{s_2}),\quad (3.40)$$

where φ_a and φ_b are the initial orbitals of each electron, \mathbf{r}_i the space coordinates associated to each electron, and ζ the spin function. The expectation value $\langle\hat{H}_C\rangle$ is called the Coulomb integral:

$$\begin{aligned}C_{ab} &= \langle\Psi|\hat{H}_C|\Psi\rangle = \langle\varphi_a\varphi_b|\hat{H}_C|\varphi_a\varphi_b\rangle \\ &= \int \varphi_a^*(\mathbf{r}_1)\varphi_b^*(\mathbf{r}_2)\frac{e^2}{4\pi\epsilon_0|\mathbf{r}_1 - \mathbf{r}_2|}\varphi_a(\mathbf{r}_1)\varphi_b(\mathbf{r}_2)d\mathbf{r}_1d\mathbf{r}_2.\end{aligned}\quad (3.41)$$

It represents the Coulomb repulsion between the unperturbed electronic density distributions of the electrons. The spin does not enter the Hamiltonian, but it influences the allowed atomic states. The Pauli exclusion principle requires a many-electrons wavefunction to be antisymmetric under exchange, that is to say to change its sign when the space and spin coordinates of any two electrons are exchanged. For this, either the spatial part of Ψ can be antisymmetric and the spin part symmetric, or the other way around. In terms of the permutation operator \hat{P} , both must be eigenvectors with the eigenvalues ± 1 :

$$\hat{P}|\Psi\rangle = -|\Psi\rangle = \begin{cases} -|\varphi^a\rangle \otimes +|\zeta^s\rangle \\ +|\varphi^s\rangle \otimes -|\zeta^a\rangle, \end{cases}\quad (3.42)$$

where the subscript denotes a symmetric or antisymmetric function of both electrons.

Let us consider first the spin. The state of the atom, characterized by the quantum numbers S and M_S , must be a linear combination of the four possible two-spin states:

$$\begin{aligned} |S, M_S\rangle &= \sum_{m_{s_1}, m_{s_2}} c_{12} |m_{s_1}\rangle \otimes |m_{s_2}\rangle \\ &= c_1 |\uparrow\uparrow\rangle + c_2 |\uparrow\downarrow\rangle + c_3 |\downarrow\uparrow\rangle + c_4 |\downarrow\downarrow\rangle. \end{aligned} \quad (3.43)$$

If the electrons have the same spin, it is easy to see that $\hat{P}|\uparrow\uparrow\rangle = |\uparrow\uparrow\rangle$ and the two parallel spin states are symmetric. The antiparallel spin states are neither symmetric nor antisymmetric, as we can see from calculating the 2×2 matrix representation of $|m_{s_1}\rangle \otimes |m_{s_2}\rangle$ using Eq. (3.24): we obtain $\hat{P}|\uparrow\downarrow\rangle = |\uparrow\downarrow\rangle^T \neq \pm|\uparrow\downarrow\rangle$. The simplest symmetric state we can build is their equal superposition, since $\hat{P}(|\uparrow\downarrow\rangle + |\downarrow\uparrow\rangle) = |\downarrow\uparrow\rangle + |\uparrow\downarrow\rangle$. The general symmetric spin wavefunction is thus composed of three possible states, which form the $S = 1$ triplet:

$$\begin{aligned} |\zeta^s\rangle &= c_1 |\uparrow\uparrow\rangle + c_2 |\downarrow\downarrow\rangle + \frac{c_3}{\sqrt{2}} (|\uparrow\downarrow\rangle + |\downarrow\uparrow\rangle) \\ &= c_1 |1, +1\rangle + c_2 |1, -1\rangle + c_3 |1, 0\rangle, \end{aligned} \quad (3.44)$$

and is degenerate in the absence of magnetic field. The component $|1, 0\rangle$ corresponds to the spins being parallel in the xy plane. The corresponding antisymmetric wavefunction is the $S = 0$ singlet:

$$|\zeta^a\rangle = |0, 0\rangle = \frac{1}{\sqrt{2}} (|\uparrow\downarrow\rangle - |\downarrow\uparrow\rangle). \quad (3.45)$$

Similarly, we build the symmetric and antisymmetric spatial wavefunctions:

$$|\varphi^s\rangle = \frac{|\varphi_a\varphi_b\rangle + |\varphi_b\varphi_a\rangle}{\sqrt{2}}, \quad (3.46a)$$

$$|\varphi^a\rangle = \frac{|\varphi_a\varphi_b\rangle - |\varphi_b\varphi_a\rangle}{\sqrt{2}}. \quad (3.46b)$$

Let us now examine the consequences. If the atom is in the ground state ($1s^2$ configuration), the electrons are filling the lowest orbital, with $n = 1$, $l = 0$ and $m_l = 0$. The spatial part of the wavefunction $\varphi_{100}(\vec{r}_1) \varphi_{100}(\vec{r}_2)$ is symmetric, so the spin wavefunction must be antisymmetric and the electrons have as expected the opposite spin. In this case, there is no change and we can use Eq. (3.41) to calculate the Coulomb repulsion.

If the atom is in an excited state, or if we are considering two electrons in a higher shell that may occupy different orbitals, the uncoupled state $\varphi_a(\vec{r}_1) \varphi_b(\vec{r}_2)$ is not allowed, as it is not an eigenvector of \hat{P} . For any $\varphi_b \neq \varphi_a$, the atom can take two distinct orbital

configurations:

$$\Psi^S = \varphi^s \zeta^a = \frac{1}{\sqrt{2}} (\varphi_a(\vec{r}_1) \varphi_b(\vec{r}_2) + \varphi_a(\vec{r}_2) \varphi_b(\vec{r}_1)) \zeta^a, \quad (3.47a)$$

$$\Psi^T = \varphi^a \zeta^s = \frac{1}{\sqrt{2}} (\varphi_a(\vec{r}_1) \varphi_b(\vec{r}_2) - \varphi_a(\vec{r}_2) \varphi_b(\vec{r}_1)) \zeta^s. \quad (3.47b)$$

These two states are respectively called the singlet Ψ^S and triplet Ψ^T states, according to their spin degeneracy. Because the orbit of the electrons is modified, so is the expectation value of the Coulomb repulsion:

$$\begin{aligned} \langle \Psi | \hat{H}_C | \Psi \rangle &= \int \frac{1}{2} (\varphi_a^*(\vec{r}_1) \varphi_b^*(\vec{r}_2) \pm \varphi_a^*(\vec{r}_2) \varphi_b^*(\vec{r}_1)) \frac{e^2}{4\pi\epsilon_0 |\vec{r}_1 - \vec{r}_2|} \\ &\quad \times (\varphi_a(\vec{r}_1) \varphi_b(\vec{r}_2) \pm \varphi_a(\vec{r}_2) \varphi_b(\vec{r}_1)) d\vec{r}_1 d\vec{r}_2 \\ &= C_{ab} \pm J_{ab}, \end{aligned} \quad (3.48)$$

where C_{ab} is the Coulomb integral given by Eq. (3.41), and $J_{ab} = \langle \varphi_a \varphi_b | \hat{H}_C | \varphi_b \varphi_a \rangle > 0$ is called the exchange integral. There are three possible energies for two electrons: $E(\Psi^T) = 2E_0 + C_{ab} - J_{ab}$ when the electrons have the same spin, $E(\Psi^S) = 2E_0 + C_{ab} + J_{ab}$ when they have the opposite spin and occupy different orbitals, and $E(\Psi^S) = 2E_0 + C_{aa}$ when they occupy the same orbital. While C_{ab} and J_{ab} vary depending on the orbitals involved, the intra-orbital Coulomb integral $C_{aa} = C$ is identical for all orbitals in the same subshell. The Pauli exclusion principle, by preventing electrons with parallel spin to occupy the same space, lowers their Coulomb repulsion, thereby making triplet states more favorable.

We can rewrite the Hamiltonian as an explicit function of the spin, using the fact that $\hat{S}^2 = \hat{S}_1^2 + \hat{S}_2^2 + 2\hat{S}_1 \cdot \hat{S}_2$. The expectation values of the operators are $\langle \hat{S}_1^2 \rangle = \langle \hat{S}_2^2 \rangle = 3\hbar^2 / 4$, and $\langle \hat{S}^2 \rangle = S(S+1)\hbar^2 = 0$ in the singlet and $2\hbar^2$ in the triplet state. Thus:

$$\langle 2\hat{S}_1 \cdot \hat{S}_2 \rangle = \begin{cases} -3\hbar^2 / 2, & \text{(singlet)} \\ +\hbar^2 / 2, & \text{(triplet)} \end{cases} \quad (3.49)$$

and we can redefine $\hat{H}_C = C_{12} - J_{12} / 2 - 2J_{12} / \hbar^2 \times \hat{S}_1 \cdot \hat{S}_2$, so that its expectation value is preserved. We are assuming that the spin alignment can change, that is to say the electrons are in different orbitals. The spin part of the interaction is represented by the Heisenberg exchange Hamiltonian:

$$\hat{H}_{\text{ex}} = -2 \frac{J_{12}}{\hbar^2} \hat{S}_1 \cdot \hat{S}_2, \quad (3.50)$$

where $J_{12} > 0$, which is always the case for exchange integrals, favors the parallel alignment of the spins. The same expression will also be used to represent the exchange interaction between the spins of two atoms, or the macroscopic spins representing the two sublattices of an antiferromagnetic material, in which case $J_{12} < 0$ favors the antiparallel alignment.

Many-electron exchange

For more than two electrons, it is not possible to antisymmetrize the spin part of the wavefunction with respect to all possible permutations. Unless all electrons have the same spin, we have to antisymmetrize the orbital and spin degrees of freedom jointly. The antisymmetric wavefunction corresponding to a specific combination of N spinorbitals is given by the Slater determinant:

$$\Psi(\psi_a^{\zeta_a}, \psi_b^{\zeta_b}, \dots, \psi_x^{\zeta_x}) = \frac{1}{\sqrt{N!}} \begin{vmatrix} \psi_a^{\zeta_a}(1) & \psi_b^{\zeta_b}(1) & \dots & \psi_x^{\zeta_x}(1) \\ \psi_a^{\zeta_a}(2) & \psi_b^{\zeta_b}(2) & \dots & \psi_x^{\zeta_x}(2) \\ \vdots & \vdots & \ddots & \vdots \\ \psi_a^{\zeta_a}(N) & \psi_b^{\zeta_b}(N) & \dots & \psi_x^{\zeta_x}(N) \end{vmatrix}, \quad (3.51)$$

where $\psi_n^{\zeta_n}(i) = \varphi_n(\vec{r}_i) \zeta_n(m_{s_i})$ is the original spinorbital of electron i . The initial unperturbed state as a product of the wavefunctions of independent electrons is given by the diagonal of the matrix. Each Slater determinant describes an antisymmetric wavefunction in the decoupled basis, where all electrons have well-defined quantum numbers. The atomic states in the $\{|L, S, M_L, M_S\rangle\}$ basis are then obtained by the linear superposition of several Slater determinants, similarly to Eq. (3.22). For our previous case of two electrons, the determinants $\Psi(\psi_a^\uparrow, \psi_b^\uparrow)$ and $\Psi(\psi_a^\downarrow, \psi_b^\downarrow)$ are the wavefunctions of the two states with $M_S = \pm 1$, and we find the remaining two wavefunctions for $M_S = \pm 0$ using $\Psi(\psi_a^\uparrow, \psi_b^\downarrow) \pm \Psi(\psi_a^\downarrow, \psi_b^\uparrow)$.

The interactions between many electrons can be reduced to the sum of their pairwise interactions. Computing them implies that the state of the electrons is known. We can thus calculate the energy of an atomic state $|L, S, M_L, M_S\rangle$ when it consists of a single Slater determinant. In this case, each pair of electrons with parallel spins contributes an energy $\mathcal{C}_{ij} - \mathcal{J}_{ij}$, and each pair of electrons with antiparallel spins contributes \mathcal{C}_{ij} . The energy of the determinantal wavefunction Ψ is thus:

$$\langle \Psi | \hat{H} | \Psi \rangle = \sum_{i=1}^N \left(E_{0i} + \sum_{j>i}^N \mathcal{C}_{ij} - \delta(m_{s_i}, m_{s_j}) \mathcal{J}_{ij} \right). \quad (3.52)$$

With this, we can obtain the term energies of an atom. For a p^3 configuration for example, the possible terms are 4S , 2P and 2D . For simplicity, let us assume that all inter-orbital integrals are identical. The determinant $\Psi(\psi_{-1}^\uparrow, \psi_0^\uparrow, \psi_{+1}^\uparrow)$ gives $M_S = 3/2$ and thus contributes only to the 4S term. In the absence of magnetic field, the energy of all states in the term is thus $E(^4S) = 3\mathcal{C}_{ij} - 3\mathcal{J}_{ij}$. Similarly, the determinant $\Psi(\psi_0^\uparrow, \psi_{+1}^\uparrow, \psi_{+1}^\downarrow)$ with $M_L = 2$ contributes only to the 2D term, which has then the energy $E(^2D) = 2\mathcal{C}_{ij} + \mathcal{C} - \mathcal{J}_{ij}$. There is no determinant contributing only to the 2P term. We find its energy by observing that the three determinants $\Psi(\psi_{-1}^\downarrow, \psi_0^\uparrow, \psi_{+1}^\uparrow)$, $\Psi(\psi_{-1}^\uparrow, \psi_0^\downarrow, \psi_{+1}^\uparrow)$ and $\Psi(\psi_{-1}^\uparrow, \psi_0^\uparrow, \psi_{+1}^\downarrow)$ give $|M_L, M_S\rangle = |0, 1/2\rangle$, which appears once in each of the three terms. The sum of their

energies being conserved, we have $E(^4S) + E(^2D) + E(^2P) = 9C_{ij} - 3J_{ij}$, and thus $E(^2P) = 4C_{ij} - C + J_{ij}$. Fitting these formula to the term energies of a nitrogen atom, where $E(^2D) - E(^4S) = 2.38 \text{ eV}$ and $E(^2P) - E(^4S) = 3.57 \text{ eV}$ [102], we obtain $J_{ij} = 0.66 \text{ eV}$, and $C = C_{ij} + 2J_{ij} / 5$. The Coulomb repulsion and the exchange interactions lift the degeneracy of the terms, encouraging the parallel alignment of the spins in different orbitals and thus the maximization of L and S .

3.2.2.3 Spin-orbit coupling

We now add a contribution that we neglected so far: the spin-orbit coupling. It can be interpreted as the effect of the movement of the nucleus in the rest frame of each electron. In the classical current loop model, the current creating the orbital moment of the electron is given by Eq. (3.6): $I_e = \hat{\mu}_l / 2\pi r^2$. The current loop created by the orbiting nucleus in the rest frame of the electron is $I_n = -ZI_e$. According to Eq. (3.7), it generates on the electron the magnetic field:

$$\vec{B}_n = \frac{\mu_0 Z e}{4\pi m_e r^3} \hat{L}_z. \quad (3.53)$$

A rigorous derivation using the Dirac equation results in an additional factor 1/2. It is commonly explained by the relativistic rotation of the rest frame of the electron, called the Thomas precession [103], producing an opposing magnetic field. Including this factor, the net magnetic field experienced by the electron is $\vec{B} = -\vec{v} \wedge \vec{E} / 2c^2$, where $E = -\vec{\nabla} V(r)$. With the potential of the nucleus $V(r) = Ze / 4\pi\epsilon_0 r$, we find $\vec{B} = \vec{B}_n / 2$. A more recent semi-classical model explains the spin-orbit coupling in the rest frame of the nucleus as the force exerted by the electric field of the latter onto the relativistic electric dipole moment created by the spin of the moving electron. The factor 1/2 arises from a change in kinetic energy of the electron when its spin is flipped, which compensates half of the change in electrostatic energy [104]. Staying with the first theory, the spin-orbit coupling Hamiltonian represents the energy of the electron, which in its own frame has only a spin moment, in the magnetic field of the nucleus:

$$\hat{H}_{\text{so}} = -\hat{\mu}_s \cdot \vec{B} = -\frac{g_s e}{2m_e^2 c^2 r} \frac{dV}{dr} \hat{S} \cdot \hat{L} = \frac{g_s \mu_0 e^2}{8\pi m_e^2 r^3} \hat{S} \cdot \hat{L}. \quad (3.54)$$

Since the expectation value $\langle 1/r^3 \rangle$ only depends on the radial part $R_{n,l}$ of the wavefunction, we can simplify the Hamiltonian as [105, chapter 4]:

$$\begin{aligned} \hat{H}_{\text{so}} &\approx \frac{\mu_0 e^2}{4\pi m_e^2} \left\langle \frac{1}{r^3} \right\rangle \hat{S} \cdot \hat{L} \\ &= \frac{Z^4 m_e c^2 \alpha^4}{\hbar^2 n^3 l(l+1/2)(l+1)} \hat{S} \cdot \hat{L} = \lambda_{n,l} \hat{S} \cdot \hat{L}, \end{aligned} \quad (3.55)$$

where α is the fine-structure constant. The spin-orbit constant $\lambda_{n,l} > 0$ is the same for all electrons in the same subshell, and the coupling between the spin of one electron and

the orbit of another is negligible. This allows us to define the multi-electron spin-orbit coupling Hamiltonian as:

$$\hat{H}_{\text{so}} = \lambda \hat{\mathbf{L}} \cdot \hat{\mathbf{S}}, \quad (3.56)$$

where $\lambda = \pm \lambda_{n,l} / 2S$, with a negative sign when the subshell is more than half-filled. We will see the reason for this change of sign in Section 3.2.2.4. Because of the dependency of the spin-orbit constant on the nuclear potential, this coupling is stronger for heavy elements: $\lambda_{n,l} \hbar^2 = 53 \text{ meV}$ for Fe ($Z = 26$) but 556 meV for Pt ($Z = 78$) [105, chapter 4].

The Hamiltonian of a multi-electron atom becomes:

$$\hat{H} = \hat{H}_{\text{cf}} + \hat{H}_{\text{ex}} + \hat{H}_{\text{so}}. \quad (3.57)$$

The spherical central field Hamiltonian is responsible for creating well-defined electronic orbitals in the form of spherical harmonics characterized by n and l , and is always the largest term. The exchange Hamiltonian couples the angular momenta of the electrons, forming $\hat{\mathbf{L}} = \sum_i \hat{\mathbf{L}}_i$ and $\hat{\mathbf{S}} = \sum_i \hat{\mathbf{S}}_i$, while the spin-orbit Hamiltonian couples the two types of angular momenta to form $\hat{\mathbf{J}} = \hat{\mathbf{L}} + \hat{\mathbf{S}}$. Whether the latter should be modeled as a perturbation of the atomic state or the electronic states depends on which of \hat{H}_{ex} or \hat{H}_{so} is expected to dominate. We thus have two possible approximations to model the total angular momentum of an atom, called the L - S and j - j coupling schemes:

$$\hat{\mathbf{J}} = \begin{cases} \hat{\mathbf{L}} + \hat{\mathbf{S}} = \sum_i \hat{\mathbf{L}}_i + \sum_i \hat{\mathbf{S}}_i & (L\text{-}S \text{ coupling}) \\ \sum_i \hat{\mathbf{J}}_i = \sum_i (\hat{\mathbf{L}}_i + \hat{\mathbf{S}}_i) & (j\text{-}j \text{ coupling}) \end{cases} \quad (3.58)$$

j-j coupling

If $\hat{H}_{\text{so}} > \hat{H}_{\text{ex}}$, the spin-orbit coupling of each electron needs to be considered before the exchange interaction. This is the case in heavy atoms, typically with $Z > 75$. As we discussed in Section 3.2.1.1, the state of each electron is described in the basis $\{|n, l, s, j, m_j\rangle\}$. In the vector model, $\vec{\mathbf{l}}_i$ and $\vec{\mathbf{s}}_i$ are represented as precessing around $\vec{\mathbf{j}}_i = \vec{\mathbf{l}}_i + \vec{\mathbf{s}}_i$.

The electron–electron exchange interactions are then treated as a perturbation on the orientation of the $\vec{\mathbf{j}}_i$, which now precess around the total angular momentum of the atom $\vec{\mathbf{J}} = \sum_i \vec{\mathbf{j}}_i$. The state of the subshell is described by $|L, S, J, M_J\rangle$. This coupling is thus called the j - j coupling (Fig. 3.7a).

L-S coupling

For lighter elements, $\hat{H}_{\text{ex}} > \hat{H}_{\text{so}}$ and the atom is best described with the Russell–Saunders or L - S coupling. This is for example the case for Fe^{2+} , whose energy levels are plotted in Fig. 3.8.

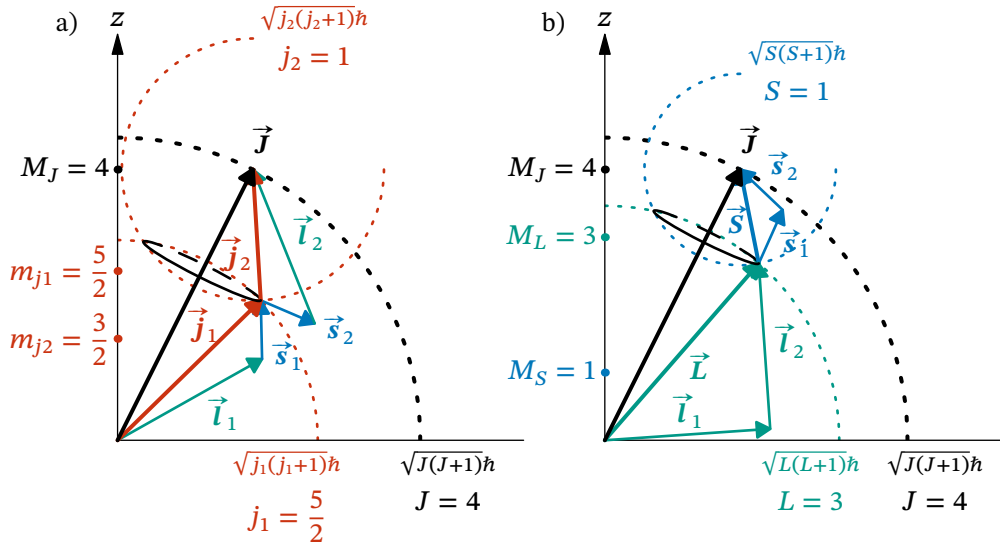


Figure 3.7: Vector model for the a) j - j and b) L - S coupling schemes, describing the coupling of two electrons with $l = 2$, $m_s = +1/2$, $m_l = 0$ and 2. \vec{J} is quantized with respect to z around which it precesses with the fixed component $M_J\hbar$. The coupled vectors conserve their magnitude (dotted circles) but not their orientation. They precess together around their resultant (black ellipse around \vec{J}) and thus have no defined projection along z anymore.

The exchange interaction couples the orbital angular momenta of individual electrons into \vec{L} and their spin angular momenta into \vec{S} , around which the original angular momenta are represented as precessing (Fig. 3.7b). The spin-orbit interaction is then added as a perturbation. It causes the Hamiltonian to stop commuting with \hat{L}_z and \hat{S}_z , making M_L and M_S bad quantum numbers. In the same way as for electrons, the new quantum numbers follow:

$$|L - S| \leq J \leq L + S \quad (3.59a)$$

$$-J \leq M_J \leq J. \quad (3.59b)$$

For a given atomic term, J defines the level or multiplet written $^{2S+1}L_J$, and M_J the unique atomic state. With this coupling as well, states are described in the basis $\{|L, S, J, M_J\rangle\}$. The spin-orbit coupling causes, with other relativistic effects such as the Zitterbewegung and corrections to the kinetic energy, the fine structure splitting of the hydrogen energy levels, removing the degeneracy of the multiplets. In most cases, the energy difference between adjacent multiplets is $E_J - E_{J-1} = \lambda J$.

When several subshells are incomplete, they couple in a single atomic state. For example, Pt has the electronic configuration $[\text{Xe}]4f^{14}5d^96s^1$. The latter two subshells, each missing one electron, couple to form the ground multiplet 3D_3 , in which $S = S_d + S_s = 1/2 + 1/2 = 1$, $L = L_d + L_s = 2$, and $J = L + S$. As we will now see, this can

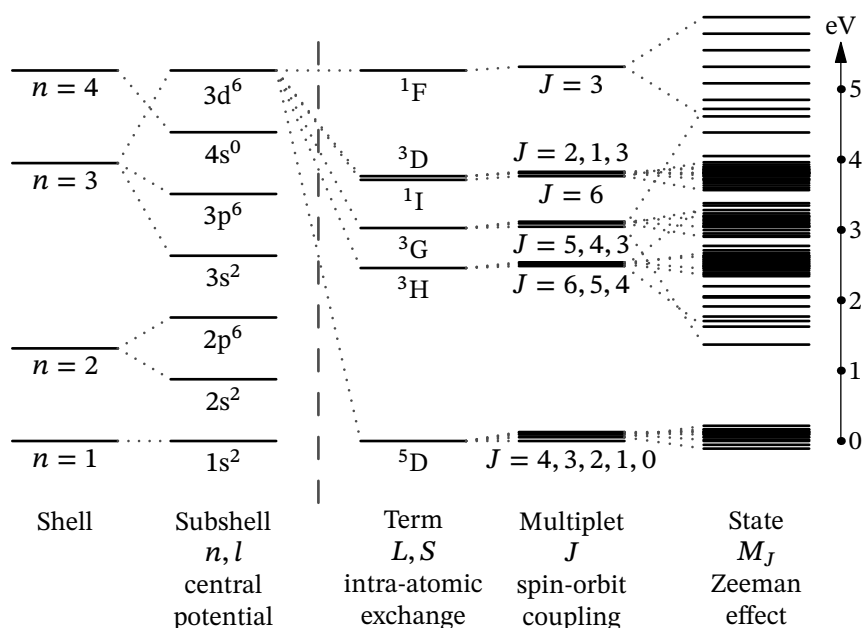


Figure 3.8: Lowest energy levels of an isolated Fe^{2+} ion in the electronic configuration $[\text{Ar}]3d^6$, following the L – S coupling model. The labels under each column indicate their characteristic quantum numbers and the mechanism responsible for their splitting. Only the incomplete $3d^6$ subshell can organize into several different terms. The ground multiplet is $5D_4$. The energies of the terms and their splitting are taken from Kramida and Ralchenko [102], while the shells and subshells (left of the dashed line) are only schematized. The gap between multiplets is small compared to the gaps between terms, indicating that the L – S coupling is a good model.

be determined using Hund’s rules, avoiding the need to calculate the expectation value of the Hamiltonian.

3.2.2.4 Finding the ground state: Hund’s rules

We have seen the contributions to the energy of an isolated atom: Coulomb repulsion, exchange interaction and spin-orbit coupling. Instead of calculating the expectation value of the Hamiltonian to find the lowest-energy level, Hund’s rules offer a simple way to deduce it from the electronic configuration of atoms satisfying the L – S coupling, given the set of existing terms. The rules only strictly apply to finding the ground multiplet of an atom or ion with a unique incomplete subshell. While generalizations to atoms with several incomplete subshells are generally successful, as we have seen for Pt, those to atoms in excited states fail in many cases [106, 107]. In addition, they apply to isolated atoms: we will see in Section 3.2.3 that the presence of a crystal field may prevent their application.

- The first rule, named the rule of maximum multiplicity, states that the spin quantum number S is maximized. The ground term then contains the electron configuration leading to the highest possible value of $|M_S|$, when the subshell is filled with as many electrons with parallel spin as possible. This rule allows the minimization of \hat{H}_{ex} .
- The second rule states that if several of the allowed terms satisfy the first rule, then the orbital quantum number L is maximized. The ground term then contains the highest possible value of $|M_L|$, which allows the minimization of \hat{H}_{so} .
- The third rule states that the lowest-lying multiplet within the ground term minimizes the total quantum number J if the subshell is less than half-filled, and maximizes J if it is more than half-filled. This rule is linked to the change of sign of the spin-orbit constant λ : since $\lambda_{n,l} > 0$, the spin-orbit coupling encourages m_l and m_s for each electron to have opposite signs. If the subshell is less than half full and the spins align to maximize M_S according to the first rule, then M_L and M_S will have the opposite sign as well, which decreases J and leads to the minimization of \hat{H}_{so} for $\lambda > 0$. If the subshell is more than half full, the majority spin electrons have no net contribution to M_L but determine the sign of M_S , so M_L and M_S have the same sign and J is maximized.

For the $2p^2$ configuration with the three allowed terms 1S , 3P and 1D that we found in Section 3.2.2.1, the first rule is enough to determine that the lowest-energy term is 3P . Hund's rules give no information to order the energy of the other allowed terms, and a quantitative ordering can only be obtained by calculating the wavefunction of each term. The 3P term corresponds to $L = S = 1$ and contains thus three multiplets with $J = 0, 1$ and 2 according to Eq. (3.59). Since the subshell contains two out of the possible six electrons, the ground multiplet is 3P_0 . In this case, there is only one possible orientation of the angular momentum in a magnetic field: $M_J = 0$, and this atom is non-magnetic. The Fe^{2+} ion in Fig. 3.8 exhibits the opposite behavior: it has six of the possible ten electrons in the $3d$ subshell, so its ground multiplet is 5D_4 . This fairly large value of J gives rise to the large magnetic moment of Fe^{2+} ions.

Once the ground term of an atom is determined, we can calculate its magnetic moment. The formulas in Section 3.2.1.3 for single electrons can be generalized without any change:

$$\hat{\boldsymbol{\mu}}_J = \gamma \hat{\mathbf{J}} = -\frac{\mu_B g_J}{\hbar} \hat{\mathbf{J}}. \quad (3.60)$$

The magnetization of a material is a macroscopic average of the magnetic moment per unit volume:

$$\vec{\mathbf{M}} = \frac{1}{V} \sum_i \langle \hat{\boldsymbol{\mu}}_J \rangle_i. \quad (3.61)$$

It is thus maximized if all atoms in the sample have $M_J = -J$.

We are now in the capacity to calculate the magnetic moment of an atom and understand why a certain element has magnetic properties. However, the magnetic moment

of a single atom does not tell us whether a material is, for example, paramagnetic or ferromagnetic. These properties, encoded in the susceptibility of the material, come from the collective behavior of all atoms.

3.2.3 Influence of the crystal field

As isolated atoms, the majority of elements have $J \leq 0$ and carry a magnetic moment in their ground state. The only exceptions are elements with only full subshells, elements with a p^2 configuration whose ground multiplet we calculated above, as well as tungsten and samarium whose ground multiplets are 5D_0 and 7F_0 , respectively. In the solid state however, most pure elements are paramagnetic or diamagnetic. Only the 3d transition metals Fe, Co and Ni and the 4f rare earth elements Gd, Tb, and Dy can be ferromagnetic, under some conditions of temperature, pressure, and other parameters; a few others are ferrimagnetic or antiferromagnetic. Most elements lose their magnetic moment as soon as they belong to a polyatomic substance. In materials consisting of several types of atoms, it is hard to predict whether the magnetic moment will be conserved and what the magnetic behavior will be. We will concentrate in this section on the influence of neighboring atoms on the magnetic properties of 3d and 4f elements in particular.

3.2.3.1 Orbital localization

As we have seen, the solutions to the Schrödinger equation for the single-electron Hamiltonian in Eq. (3.18) are the orbitals $\varphi(r, \theta, \phi) = R_{n,l}(r) Y_l^{m_l}(r, \theta, \phi)$. The radial part depends on the quantum numbers n and l : n describes the energy of an electron in the potential of the nucleus, and l describes the centrifugal part of its kinetic energy. These two radial contributions can be considered as an effective potential energy:

$$E_{\text{eff}}(r) = \frac{Z^* e^2}{4\pi\epsilon_0 r} + \frac{l(l+1)\hbar^2}{2m_e r^2}, \quad (3.62)$$

where Z^* is the atomic number reduced by a screening parameter, to account for the average Coulomb repulsion between electrons in the central field approximation (see Section 3.2.2.1). The kinetic contribution creates a potential barrier at a finite distance to the nucleus, of height increasing with l . For $Z^* = 1$, this term dominates and creates a repulsive potential for all except s subshells. As Z^* increases, the Coulombic contribution creates a potential well which becomes deeper, narrower and shifts towards the nucleus. However, the reduced atomic number is not constant for a given element, but depends on r : Z^* is maximal near the nucleus, while outside the outer shells $Z^* \approx 1$. For heavy enough atoms, this creates two distinct potential wells, separated by the remaining hydrogen-like centrifugal barrier. At $Z = 21$, the charge density of the 3d orbitals moves from the hydrogen-like outer well to the inner well, which leads to the beginning of the 3d transition metal series (see Fig. 3.9). Similarly, at $Z = 57$ the 4f charge density moves into the inner well, which corresponds to the beginning of the 4f rare earth series.

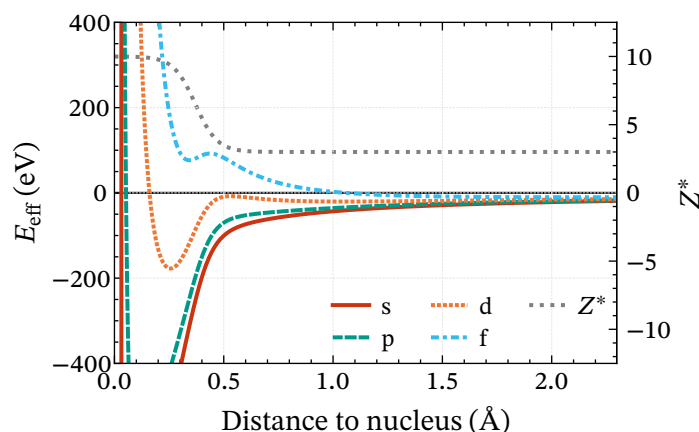


Figure 3.9: Qualitative representation of the effective potential for the outer orbitals of 3d transition metals. The centrifugal barrier near 0.5 Å is caused by the decrease of Z^* , and creates distinct inner and outer potential wells.

For both types of elements, the electrons responsible for their magnetic properties are thus localized in deep inner wells, and shielded from external influences by the largely delocalized 4s or 6s electrons. This allows 3d and 4f elements to retain in the solid state many of the properties of their isolated atoms. However, the height of the centrifugal barrier causes a critical difference in behavior. The barrier is very pronounced for the 4f subshell, strongly localizing the wavefunctions orbitals inside the atom. As a consequence, 4f elements can be modeled as isolated atoms subject to a small perturbation. The barrier is almost absent for the 3d subshell, allowing the orbitals to extend and overlap with neighboring atoms. The 3d elements have thus a hybrid behavior, and whether isolated atoms or fully delocalized electrons are the best approximation depends on the situation. As metals, Fe, Co and Ni achieve a balance which allows them to conserve most of their magnetic moment, while also participating in the collective behaviors that give rise to ferromagnetism (see [Section 3.2.4](#)).

3.2.3.2 Crystal field levels

The Hamiltonian of an isolated atom is given by [Eq. \(3.57\)](#), with $\hat{H}_{cf} \gg \hat{H}_{ex} \gg \hat{H}_{so}$ for both 3d and 4f elements. When the orbitals carrying a magnetic moment are localized and do not interact directly with surrounding atoms, it is possible to model the influence of the latter by a static electric field: the crystal field. With this approximation, we neglect the effects of covalent bonding, charge overlap, and conduction electrons. It however explains the origin of several phenomenon relevant notably to magnetic insulators such as FeBO_3 .

Weak crystal field: the Stark effect

The crystal field surrounding an atom modifies the electrostatic potential of the electrons, breaking its spherical symmetry. However, in the weak field limit $\hat{H}_{\text{ex}} \gg \hat{H}_{\text{so}} \gg \hat{H}_{\text{cry}}$, where $\hat{H}_{\text{cry}} = -e \sum_i^N V_{\text{cry}}(\vec{r}_i)$, it can be treated as a perturbation of the state of an isolated atom. This is most appropriate for 4f rare earth compounds, as the 4f subshell is shielded by the more delocalized outer electrons. In this limit, we only need to consider the splitting of the ground multiplet. The unperturbed atom is characterized by $|L, S, J\rangle$, and the M_J are degenerate in the absence of magnetic field.

The potential of the crystal field has the same point symmetry as the atom. It can be expanded in terms of spherical harmonics:

$$-e V_{\text{cry}}(r, \theta, \phi) = \sum_n \sum_{m_n=-n}^{+n} r^n A_n^{m_n} Y_n^{m_n}(\theta, \phi), \quad (3.63)$$

where the $A_n^{m_n}$ are crystal field parameters, whose sign indicates the sign of the charges of the surrounding atoms. The relevant non-zero values of n and m_n depend on the symmetry. Because the product of two electronic wavefunctions is spatially symmetric and can be expanded into spherical harmonics with $n \leq 2l$, only terms with n even and $n \leq 6$ for 4f atoms will remain when evaluating the perturbation energy $E_{\text{cry}} = \langle \Psi | \hat{H}_{\text{cry}} | \Psi \rangle$. The $n = 0$ term corresponds to a constant energy offset and is neglected. We are particularly interested in the octahedral symmetry, where the atom is at the center of the coordinate system and negative charges are placed on the Cartesian axes at positions $(\pm a, 0, 0)$, $(0, \pm a, 0)$ and $(0, 0, \pm a)$. The only remaining terms are $n = 4$ and $m_n = 0$ and ± 4 .

Since both orbitals and the crystal field are expanded as spherical harmonics, evaluating E_{cry} is straightforward if $|\Psi\rangle$ is decomposed into combinations of electronic orbitals. However, this is often unpractical: the electrons of an atom such as Tb with the configuration $4f^9$ can form 2002 different Slater determinants, only 76 of which are not entering into the ground multiplet ${}^6\text{H}[15/2]$ because they have $|M_L| > 5$. Instead, the new eigenstates of the Hamiltonian and their degeneracy are calculated using group theory [108]. Wavefunctions with a given angular momentum quantum number, whether J, L, S or their electronic counterparts, always decompose in the same irreducible representations in a given point symmetry group. Where a set of wavefunctions is formed by the tensor product of several vector spaces, for example when combining several electrons, the corresponding irreducible representations are given by the direct product of the irreducible representations of the electrons.

To allow the evaluation of the perturbation energy in the basis $\{|J, M_J\rangle\}$, we transform the crystal field Hamiltonian using the Stevens operator equivalents, which are dimensionless combinations of \hat{J} operators [109]. In the case of $n = 2$ and $m_n = 0$ for example, the term $r^2 A_2^0 Y_2^0$ becomes $\alpha_2 \langle r^2 \rangle A_2^0 \hat{O}_2^0$, where the dimensionless constant α_n and the mean radial distribution $\langle r^n \rangle$ depend on the atom, and the Stevens operator is

$\hat{O}_2^0 = 3\hat{J}_z^2 - \hat{J}^2$. The crystal field energy is then simply $\alpha_2 \langle r^2 \rangle A_2^0 (3M_J^2 - J(J+1))$ and the degeneracy of the angular momentum projection M_J is partially lifted.

Since the wavefunction of the resulting energy levels may be a complicated combination of angular momentum eigenstates, the states and their degeneracy are calculated using group theory [108]. The crystal field levels are labeled as $|\Gamma\rangle$, where Γ is the irreducible representation of \hat{J} in the given point symmetry group. Eigenstates with the same angular momentum quantum number, whether J , L , S or their electronic counterparts, decompose in the same irreducible representations. Where a set of wavefunctions is formed by the tensor product of several vector spaces, for example when combining several electrons, the corresponding irreducible representations are given by the direct product of the irreducible representations of the electrons. Each time the symmetry of the Hamiltonian is reduced, some irreducible representations become reducible, and the corresponding energy levels are split.

This splitting of the energy levels according to their electric dipole moment under the effect of an electric field is called the Stark effect. It is the electric equivalent to the Zeeman effect. Contrarily to \hat{H}_Z however, \hat{H}_{cry} preserves the time-reversal symmetry of the Hamiltonian, which means that every energy eigenstate $|\Psi\rangle$ is degenerate with $\hat{T}|\Psi\rangle$. The time-reversal operator reverses magnetic dipole moments, so that $\hat{T}|M_J\rangle = i^{2M_J}|-M_J\rangle$. Because of this, singlet states under the crystal field must be $|0\rangle$ or a mixed state of the form $|+M_J\rangle \pm |-M_J\rangle$. As the symmetry of the crystal potential lowers, more degeneracies are lifted, and thus more levels have no magnetic moment.

Medium crystal field

When the strength of the crystal field increases so that $\hat{H}_{\text{ex}} \gg \hat{H}_{\text{cry}} \gg \hat{H}_{\text{so}}$, J is no longer a good quantum number, while to the first order L and S still are. The same procedure can be applied to calculate the splitting of the ground term, by expressing the Stevens operator equivalents as functions of \hat{L} operators [110].

For FeBO_3 , where the oxygen ions form an octahedral environment around each Fe^{3+} ion:

$$\begin{aligned} -eV_{\text{cry}} &= r^4 A_4^0 Y_4^0 + r^4 A_4^4 Y_4^4 + r^4 A_4^{-4} Y_4^{-4} \\ &= r^4 A_4^0 \left(Y_4^0 + \sqrt{5/14} (Y_4^4 + Y_4^{-4}) \right). \end{aligned} \quad (3.64)$$

After replacing the spherical harmonics by the Stevens operator equivalents, we can express the octahedral crystal field Hamiltonian in the basis $\{|M_L\rangle\}$, here for $L = 2$ [111]:

$$\hat{H}_{\text{cry}} = Dq \begin{bmatrix} 1 & 0 & 0 & 0 & 5 \\ 0 & -4 & 0 & 0 & 0 \\ 0 & 0 & 6 & 0 & 0 \\ 0 & 0 & 0 & -4 & 0 \\ 5 & 0 & 0 & 0 & 1 \end{bmatrix}, \quad (3.65)$$

with $Dq = \alpha_4 \langle r^4 \rangle A_4^0 / 21$. The states $|0\rangle$ and $|\pm 1\rangle$ are eigenvectors of the Hamiltonian with eigenvalues $6Dq$ and $-4Dq$, respectively. The states $|\pm 2\rangle$ are coupled by the crystal field due to the non-diagonal matrix elements. New eigenstates are given by their linear combinations $|+2\rangle \pm |-2\rangle$, with eigenvalues $6Dq$ and $-4Dq$, respectively, as well. From a group theory perspective, the $L = 2$ term is split in octahedral symmetry into two irreducible representations, labeled using Mulliken symbols as the triplet T_{2g} , which contains the states of energy $-4Dq$, and the doublet E_g of energy $6Dq$.

Using the same procedure, we find the crystal field splitting of Fe^{3+} ions with configuration $3d^5$. The ground term is 6S . Since it has no orbital angular momentum, it does not split and results in a single representation ${}^6A_{1g}$, where the superscript indicates the unchanged spin multiplicity. The first excited term is 4G , with $L = 4$ and thus an orbital multiplicity of 9. It is split, in order of increasing energy, in the triplets ${}^4T_{1g}$ and ${}^4T_{2g}$, and the degenerate singlet ${}^4A_{1g}$ and doublet 4E_g [112].

Strong crystal field: low spin state

As the crystal field increases in strength and $\hat{H}_{\text{ex}} \gtrsim \hat{H}_{\text{cry}}$, the perturbation of the potential becomes too large for L to stay a good quantum number and we consider the splitting of the orbitals directly. The same mathematical formalism applies to the orbitals as to the atomic terms. Since $l = 2$, the d orbitals are split into three t_{2g} and two e_g orbitals, whose energy is again given by Eq. (3.65). The strength of the crystal field is measured by their splitting $\Delta_o = 10Dq$, which is 1.57 eV in FeBO_3 [113].

Rather than spherical harmonics, it is more appropriate to use an alternative basis in which the orbitals are time-reversal symmetric and can thus exist as singlet states. We transform the complex spherical harmonics, which have spherical symmetry and are characterized by their angular momentum, into the real cubic harmonics, which have a fixed direction in space and no net angular momentum [114]:

$$Z_l^0 = Y_l^0 \quad (3.66a)$$

$$Z_l^{m_l+} = \frac{1}{\sqrt{2}} (Y_l^{-m_l} + (-1)^{m_l} Y_l^{+m_l}) \quad (3.66b)$$

$$Z_l^{m_l-} = \frac{i}{\sqrt{2}} (Y_l^{-m_l} - (-1)^{m_l} Y_l^{+m_l}). \quad (3.66c)$$

For d electrons, this corresponds to the standard set $d_{z^2} = Z_2^0$, $d_{x^2-y^2} = Z_2^{2+}$, $d_{xy} = Z_2^{2-}$, $d_{xz} = Z_2^{1+}$ and $d_{yz} = Z_2^{1-}$. The electronic density of the first two is concentrated along the axes of the Cartesian coordinate system (e_g symmetry), and the last three in between the axes (t_{2g} symmetry). This alternative basis allows to easily see that negative charges on the axes raise the energy of the e_g orbitals.

Neglecting spin-orbit coupling, we can use Eqs. (3.52) and (3.65) to estimate the energy of known arrangements of the electrons for FeBO_3 . The ground level 6S corresponds to the

unique configuration $t_{2g\uparrow}^3 e_{g\uparrow}^2$. The lower and upper crystal field levels of the first excited term, ${}^4T_{1g}$ and ${}^4A_{1g}$, have the configurations $t_{2g\uparrow}^3 t_{2g\downarrow}^1 e_{g\uparrow}^1$ and $t_{2g\uparrow}^3 e_{g\uparrow}^1 e_{g\downarrow}^1$, respectively. Of interest is also the ${}^2T_{2g}$ level of the 2I term, with the configuration $t_{2g\uparrow}^3 t_{2g\downarrow}^2$. Their energies are given by:

$$E({}^6A_{1g}) = 5E_0 + 10C - 10J, \quad (3.67a)$$

$$E({}^4T_{1g}) = 5E_0 + 10C - 6J - \Delta_o, \quad (3.67b)$$

$$E({}^4A_{1g}) = 5E_0 + 10C - 6J, \quad (3.67c)$$

$$E({}^2T_{2g}) = 5E_0 + 10C - 4J - 2\Delta_o, \quad (3.67d)$$

where E_0 is the energy of a 3d electron in the central potential approximation, and C and J are the Coulomb and exchange integrals given by Eq. (3.41), approximated as identical for all orbitals. The ground level ${}^6A_{1g}$ and the upper level ${}^4A_{1g}$, which differ by the spin-flip of an e_g electron, have an energy difference of $4J$, since the spin-flip involves four electron pairs. With $C = 1.15$ eV and $J = 0.7$ eV [113], the unperturbed 4G and 2I terms lie respectively 2.8 eV and 4.2 eV above the ground state.

As Δ_o increases, the energy levels reorder. The ${}^2T_{2g}$ level is the only one whose energy evolves as $-2\Delta_o$, and drops thus the fastest. In an FeBO_3 crystal, it is approximately degenerate with ${}^4T_{1g}$. If Δ_o increases further until $\hat{H}_{\text{cry}} > \hat{H}_{\text{ex}}$, above ~ 2.6 eV, ${}^2T_{2g}$ drops below ${}^6A_{1g}$ and becomes the ground level. This is called the low-spin state, as Hund's first rule is broken and it becomes more advantageous to fill the t_{2g} orbitals with antiparallel spins. When $\hat{H}_{\text{cry}} \gg \hat{H}_{\text{ex}}$ and the energy is dominated by Δ_o , the energy levels merge according to their electron configuration: $E(t_{2g}^5 e_g^0) \approx -2\Delta_o$, $E(t_{2g}^4 e_g^1) \approx \Delta_o$ and $E(t_{2g}^3 e_g^2) \approx 0$.

3.2.3.3 Quenching and one-ion magnetic moment

One of the consequences of the crystal field is the quenching of the orbital angular momentum. On one hand, the lifting of the orbital degeneracy caused by the crystal field coupled with time-reversal symmetry favors the formation of atomic eigenstates with an expectation value $\langle \hat{L}_z \rangle = 0$. On the other hand, the spin-orbit coupling favors the formation of states with a large spin and orbital angular momentum. The exact wavefunction of an atom will have a hybrid quality. In 4f elements, we have seen that $\hat{H}_{\text{so}} \gg \hat{H}_{\text{cry}}$ and the orbital angular momentum is essentially unchanged. In 3d elements however, $\hat{H}_{\text{cry}} \gg \hat{H}_{\text{so}}$ and the orbital angular momentum is significantly reduced.

In the case of FeBO_3 , although the unperturbed ground term of Fe^{3+} ions has $L = 0$, the covalent Fe–O bonds lead in practice to the presence of an additional electron, so that the configuration is close to $3d^6$ and we expect from Hund's rules $L = 2$ and $S = 2$. The measured spin angular momentum, as defined by Eq. (3.26), is indeed $|\vec{S}| = 2\hbar$, but the measured orbital-to-spin ratio is $|\vec{L}| / |\vec{S}| = 0.03$ [115]: the orbital angular momentum

is almost completely quenched. The same is true for bulk iron metal, which consists of Fe^{2+} ions as well and exhibits $|\vec{\mathbf{L}}|/|\vec{\mathbf{S}}| \approx 0.04$ [116].

When the ground state is an orbital singlet, $\langle \hat{\mathbf{L}}_z \rangle = 0$ and to the first order, the orbital angular momentum is fully quenched. We expect to find a total angular momentum $\hat{\mathbf{J}} \approx \hat{\mathbf{S}}$.

When the orbital degeneracy is not fully lifted, we expect a reduced but finite orbital angular momentum and further splitting of the state. Let us consider as example the ${}^2\text{T}_1$ term of Fe^{3+} ions. We have seen that its lowest level is the ${}^2\text{T}_{2g}$ triplet, which becomes the ground state of the ion in an strong octahedral crystal field. Since $S = 1/2$, the irreducible representation of the spin angular momentum is E' . The spin-orbit coupling will generate the direct product ${}^2\text{T}_{2g} \otimes E' = E'' \oplus U'$ [117, appendix C]. The basis functions of such so-called double groups are tabulated, and we find that E'' is a doublet with $J = 1/2$, while U' is a quadruplet with $J = 3/2$.

The value of J in this case qualifies the transformation properties of the angular momentum, but does not represent its measurable magnitude. It corresponds to a fictitious angular momentum [118]. Predicting the magnetic moment of the atom necessitates to evaluate the Hamiltonian and find the full wavefunctions. Different models are used for 4f rare earth elements, 3d transition insulators [119] and itinerant transition metals [116, 120, 121]. Since the orbital angular momentum is significantly quenched in 3d transition materials, and since as we will see in Section 3.2.4.6 the magnetic ordering of a material depends on its spin, we assume that only the spin is present and include the orbital influence in an effective g-factor. The spin-orbit coupling, Zeeman, and potentially further Hamiltonians are treated by non-degenerate perturbation theory and transformed into an effective operator that only depend on the spin, and is thus called spin Hamiltonian [118, 122]. The Zeeman energy shift in a magnetic field of an atom in the ground state $|\Gamma, S\rangle$ with unperturbed energy $E_\Gamma^{(0)}$ becomes:

$$\begin{aligned} E_Z &= E_Z^{(1)} + E_Z^{(2)} \\ &= \langle \Gamma, S | \frac{\mu_B}{\hbar} g_s \hat{\mathbf{S}}_z B_z | \Gamma, S \rangle + \langle S | \left(\frac{\mu_B}{\hbar} \right)^2 \vec{\mathbf{B}} \cdot \mathbf{\Lambda} \cdot \vec{\mathbf{B}} + 2\lambda \frac{\mu_B}{\hbar} \vec{\mathbf{B}} \cdot \mathbf{\Lambda} \cdot \hat{\mathbf{S}} | S \rangle, \end{aligned} \quad (3.68)$$

where the spatial dependency of the orbit appears in the tensor:

$$\mathbf{\Lambda} = - \sum_{\Gamma' \neq \Gamma} \frac{\langle \Gamma | \hat{\mathbf{L}} | \Gamma' \rangle \langle \Gamma' | \hat{\mathbf{L}} | \Gamma \rangle}{E_{\Gamma'}^{(0)} - E_\Gamma^{(0)}}. \quad (3.69)$$

Neglecting the spin-independent second-order term in Eq. (3.68) which will be discussed in Section 3.2.4.3, the effective spin Zeeman Hamiltonian is:

$$\hat{\mathbf{H}}_{\text{so}} = \frac{\mu_B}{\hbar} \vec{\mathbf{B}} \cdot \mathbf{g} \cdot \hat{\mathbf{S}}, \quad (3.70)$$

where the tensor g-factor is $\mathbf{g} = g_s \mathbf{1} + 2\lambda \mathbf{\Lambda}$, with λ the spin-orbit coupling constant. Because $\mathbf{\Lambda}$ is negative, the g-factor is reduced and is less than $g_s \approx 2$. The effective magnetic moment is thus $\mu = -\mu_B \mathbf{g} \cdot \hat{\mathbf{S}} / \hbar$.

3.2.3.4 Magnetocrystalline anisotropy

A second consequence of the spin-orbit coupling is the magnetocrystalline anisotropy, that is to say the difference in free energy of a material as a function of the direction of its magnetization. The collective behaviors of magnetic atoms that lead to the spontaneous magnetization of a material will be discussed in Section 3.2.4.6. We typically assume that the magnetization acts as a single macroscopic magnetic moment with a constant magnitude, which rotates when a magnetic field is applied on the material. For rare earth atoms, whose magnetic moment is perturbed by a small crystal field, the anisotropy energy is given by the crystal field energy; for 3d transition materials, it is given by the spin-orbit coupling.

Up to the second order of perturbation, the energy shift of a given state is:

$$E_{\text{so}} = E_{\text{so}}^{(1)} + E_{\text{so}}^{(2)} = \lambda \langle \Gamma, S | \hat{\mathbf{L}} \cdot \hat{\mathbf{S}} | \Gamma, S \rangle + \lambda^2 \sum_{\Psi' \neq \Psi} \frac{|\langle \Psi | \hat{\mathbf{L}} \cdot \hat{\mathbf{S}} | \Psi' \rangle|^2}{E_{\Psi} - E_{\Psi'}}. \quad (3.71)$$

Its first-order energy vanishes, as the perturbation theory assumes a non-degenerate orbital ground state so that $\langle \hat{\mathbf{L}} \rangle = 0$. We define an arbitrary spin quantization direction s , in which the spin-up state is $|\uparrow_s\rangle = e^{i\phi/2} \cos \theta |\uparrow_z\rangle / 2 + e^{-i\phi/2} \sin \theta |\downarrow_z\rangle / 2$. The spin-orbit coupling matrix then represent the energy shift of a given orbital state as a function of the orientation of the spin quantization axis. The direction of magnetization corresponds to the spin quantization direction:

$$\vec{\mathbf{M}} = \frac{\langle \hat{\boldsymbol{\mu}}_s \rangle}{V} = M_s (\sin \theta \cos \phi \vec{\mathbf{x}} + \sin \theta \sin \phi \vec{\mathbf{y}} + \cos \theta \vec{\mathbf{z}}), \quad (3.72)$$

where z is the orbital quantification axis and the main anisotropy axis.

The second-order spin-orbit coupling perturbation leads to a uniaxial anisotropy. Higher orders are added as necessary to describe the symmetry of the material, using the anisotropy constants:

$$K_n \propto \frac{1}{V} \frac{\lambda^{2n}}{\Delta E^{2n-1}}. \quad (3.73)$$

The uniaxial anisotropy has an energy density of the form:

$$U_{\text{mca}} = K_1 \sin^2 \theta + K_2 \sin^4 \theta. \quad (3.74)$$

If the second and fourth-order anisotropy constants K_1 and K_2 are positive, U_{mca} is minimized for $\theta = 0$ and z is an easy axis, which means that the magnetization will tend to spontaneously align parallel to this axis. If both constants are negative, z is a hard axis and xy an easy plane. A large magnetic field would typically be needed in order to align the magnetization along z . A secondary anisotropy axis in the xy plane is added with $K'_1 \sin^2 \theta \cos 2\phi$.

In cubic lattices such as bulk ferromagnetic iron, the lowest contributions are of the fourth and sixth order:

$$U_{\text{mca}} = K_1^c \sin^2 \theta (\sin^2 \theta \cos^2 \phi \sin^2 \phi + \cos^2 \theta) + K_2^c \sin^4 \theta \cos^2 \theta \sin^2 \phi \cos^2 \phi. \quad (3.75)$$

Iron has three easy axes along the directions $[100]$, $[010]$ and $[001]$, with $K_1^c = 4.8 \times 10^4 \text{ J m}^{-3}$ and $K_2^c = -1.5 \times 10^4 \text{ J m}^{-3}$ at room temperature, and hard axes along the directions of type $\langle 111 \rangle$.

The magnetocrystalline anisotropy in FeBO_3 has the rhombohedral form [105, chapter 3]:

$$U_{\text{mca}} = K_1 \sin^2 \theta + K_2 \sin^4 \theta + K_2' \sin^3 \theta \cos \theta \cos 3\phi + K_3 \sin^6 \theta + K_3' \sin^6 \theta \cos(6\phi) + K_3'' \sin^3 \theta \cos^3 \theta \cos 3\phi, \quad (3.76)$$

where θ is the polar angle of the sublattice magnetization with respect to the c axis, which is a hard axis, and ϕ is the azimuthal angle with respect to one of the three axes of symmetry in the basal plane, which are easy axes.

In magnetic problems such as finding the direction of the magnetization in [Section 2.3.2](#), we are often only interested in a small region of the sphere, in which the angle between the magnetization and an anisotropy axis is small. To the first order, the magnetocrystalline anisotropy can then be approximated as uniaxial: $U_{\text{mca}} \approx K_1 \sin^2 \theta$ or, equivalently, $U_{\text{mca}} \approx -K_1 \cos^2 \theta = -K_1 M_z^2 / M_s^2$.

3.2.4 Collective behaviors of magnetic atoms

For a long time, two competing families of models tried to describe the origin of ferromagnetism in 3d transition metals. On one end of the spectrum, there is the model of localized ions carrying a magnetic moment, that we have used so far. On the other end, there is the band model of nearly free conduction electrons whose behavior emerges from Fermi-Dirac statistics. As described in [Section 3.2.3.1](#), the 3d electrons of Fe, Co and Ni are at the threshold between both behaviors. To this day, the interplay of the different mechanisms in iron raises questions [123, 124].

This section introduces the band description of solids, which will enable us to use both types of models to describe the collective behaviors emerging from the interactions between atoms or free electrons. We will see the origins of the response of materials to a magnetic field, giving rise to their classification as described in [Section 3.1.4](#), as well as the formation of a spontaneous ordering.

3.2.4.1 From orbitals to the band structure

We have seen how the crystal field potential distorts orbitals. When two atoms are sufficiently close to each other, the potential energy due to both nuclei has the same

order of magnitude and the orbitals become shared. Orbitals that spatially extend over an entire molecule are called molecular orbitals. Let us consider again the single-electron Hamiltonian of Eq. (3.18), but adding a second nucleus at short distance:

$$\hat{H} = \frac{\hat{\mathbf{p}}^2}{m_e} - \frac{Ze^2}{4\pi\epsilon_0|\vec{\mathbf{r}} - \vec{\mathbf{R}}_A|} - \frac{Ze^2}{4\pi\epsilon_0|\vec{\mathbf{r}} - \vec{\mathbf{R}}_B|}. \quad (3.77)$$

As we did when perturbing the orbitals with the crystal field, we can find approximate eigenstates of the Hamiltonian as linear combinations of atomic orbitals. If φ_A and φ_B are the 1s orbital from the atom A and B respectively, the molecular orbitals are:

$$|\psi^b\rangle = \frac{|\varphi_A\rangle + |\varphi_B\rangle}{\sqrt{2(1 + \mathcal{O}_{AB})}}; \quad |\psi^a\rangle = \frac{|\varphi_A\rangle - |\varphi_B\rangle}{\sqrt{2(1 - \mathcal{O}_{AB})}}, \quad (3.78)$$

where we defined the overlap integral $\mathcal{O}_{AB} = \langle\varphi_A|\varphi_B\rangle = \int \varphi_A^*(\vec{\mathbf{r}})\varphi_B(\vec{\mathbf{r}})d\vec{\mathbf{r}}$ to renormalize the wavefunctions. The bounding orbital $|\psi^b\rangle$ is the overlap of two wavefunctions with the same sign, and shows an increased charge density where they overlap. The antibounding orbital $|\psi^a\rangle$ is composed of two wavefunctions with a different sign, which interfere destructively and form a so-called node between the atoms where the charge density vanishes.

The atomic orbitals $|\varphi_A\rangle$ and $|\varphi_B\rangle$ are eigenstates of their respective one-nucleus Hamiltonian, with the same eigenvalue $E_{1s} = E_p - eV_0$. The energy of the molecular orbitals is given by the expectation value:

$$E = \langle\psi|\hat{H}|\psi\rangle = \frac{\langle\varphi_A|\hat{H}|\varphi_A\rangle \pm \langle\varphi_A|\hat{H}|\varphi_B\rangle}{1 \pm \mathcal{O}_{AB}} = E_{1s} + \frac{\mathcal{C}_A \pm t_{AB}}{1 \pm \mathcal{O}_{AB}}. \quad (3.79)$$

Because φ_A is not an eigenstate of the potential energy of atom B and reciprocally, some terms remain unevaluated. The integral $\mathcal{C}_A = \langle\varphi_A|-eV_B|\varphi_A\rangle < 0$ represents the potential energy of the orbital $|\varphi_A\rangle$ in field of the atom B . It is generally small compared to the other terms and thus neglected. The hopping integral $t_{AB} = \langle\varphi_A|-eV_A|\varphi_B\rangle$ couples the two atomic orbitals in the potential of the atom A . Its sign depends on the relative sign of the orbitals in their overlapping region. In this case, $t_{AB} < 0$ and it represents an additional attraction due to the increased charge density where the orbitals overlap, which reduces the energy of $|\psi^b\rangle$.

Let us add a third proton to our hypothetical linear molecule. We combine again three 1s atomic orbitals into three molecular orbitals. Neglecting the overlap renormalization:

$$\begin{aligned} |\psi^b\rangle &= (|\varphi_A\rangle + \sqrt{2}|\varphi_B\rangle + |\varphi_C\rangle) / 2, \\ |\psi^n\rangle &= (|\varphi_A\rangle - |\varphi_C\rangle) / \sqrt{2}, \\ |\psi^a\rangle &= (-|\varphi_A\rangle + \sqrt{2}|\varphi_B\rangle - |\varphi_C\rangle) / 2. \end{aligned} \quad (3.80)$$

The $|\psi^b\rangle$ and $|\psi^a\rangle$ orbitals are fully bounding and antibounding, respectively, and have by the same arguments as above the lowest and the highest energies. The charge density

of $|\psi^b\rangle$ extends uninterrupted over the three atoms, while $|\psi^a\rangle$ exhibits two nodes. The orbital $|\psi^n\rangle$ is non-bounding, as it has no charge density on the middle atom. Since all integrals are zero, its energy is the same as that from an atomic orbital.

We can generalize this process to form a basis of $N + 1$ molecular orbitals extending along a 1D chain of $N + 1$ identical atoms. Their energy increases with the number n of nodes they form along the axis of the molecule, ranging from $n = 0$ to N . As previously, the fully bounding and antibounding orbitals are $|\psi^b\rangle = \sum_j |\varphi_j\rangle$ and $|\psi^a\rangle = \sum_j \cos j\pi |\varphi_j\rangle$, respectively. A reasonable choice to construct the rest of the basis is to distribute the nodes of each molecular orbital evenly along the chain. We thus define $|\psi^n\rangle = \sum_j \cos(j\pi n / N) |\varphi_j\rangle$, in which the coefficient changes sign every N / n atoms. If the distance between adjacent atoms is the constant a , we can express the coefficient as a function of the atomic position $z = aj$, and the spacing of the nodes becomes characterized by a wavevector $k = \pi n / Na$. The molecular orbitals have become Bloch wavefunctions: the product of a plane wave with a periodic function.

As the number of atoms in the chain increases, so does the number of molecular orbitals. In an infinite lattice, k becomes a continuous function and the molecular orbitals form a band. In three dimensions, k can also take an arbitrary direction. The Bloch wavefunctions found by this tight-binding approach are defined as:

$$\psi_{m,\vec{k}}(\vec{r}) = \frac{1}{\sqrt{2}} \sum_{\vec{R}} e^{i\vec{k}\cdot\vec{R}} \varphi_m(\vec{r} - \vec{R}), \quad (3.81)$$

where the lattice vector \vec{R} is the position of the nuclei and m indexes the atomic orbitals. Neglecting the overlap and the Coulomb integral, the energy is:

$$E_m(\vec{k}) = E_m + \sum_{\vec{R}} \sum_n e^{i\vec{k}\cdot\vec{R}} t_{mn}(\vec{R}) \quad (3.82a)$$

$$\approx E_m + 2e^{ika} t(\vec{R}), \quad (3.82b)$$

where in the second line we considered only first neighbor in the relevant direction ($R = \pm a$) and a single type of orbitals ($m = n$). The first term is the atomic energy of φ_m . The second is the sum of the hopping integrals between the m orbital of an atom and any orbital n on another atom, which generally vanishes after the first few neighbors. The value $k = \pi / 2a$ marks the limit between bounding and antibounding orbitals, where the band energy is equal to the atomic energy. Bounding orbitals are thus energetically favored, which is referred to as the kinetic energy gain.

So far, we have only considered spherically symmetrical s orbitals. With different types, we have to take into account that the sign of the wavefunction depends on the direction. For example, $m = p_z$ orbitals have a positive and a negative lobe. At $k = 0$, the positive lobe of one orbital overlaps with the negative lobe of its immediate neighbor along the z axis, but with the positive lobe of its neighbors along the x and y axes. The charge density of the $|\psi_{p_z,0}\rangle$ orbital is thus distributed into sheets of approximately constant charge,

separated by nodal planes. The sign of the hopping integral and thus the dispersion curve of the p_z band depends on the direction. For $\vec{k} = \pi/2\vec{z}$, the orbitals are bonding with all neighbors. The energy is thus at its lowest point. For $\vec{k} = \pi/2\vec{x} + \pi/2\vec{y}$, the orbitals are anti-bonding in all directions, and the energy of the band reaches its maximum.

3.2.4.2 Electron conduction

We have seen the formation of the band structure as one orbital becomes delocalized throughout the material. Whether that process happens for a particular orbital depends on its overlap with the neighboring atoms. The lower shells are filled and shielded by the outer electrons, and thus form a non-interacting core of localized orbitals. The outer shells then delocalize. If all atoms in the lattice are the same, there will be the same amount of electrons per atom as previously. However, where the subshells had before well-separated energies, the bands now generally overlap. Electrons will occupy the orbitals with the lowest energy, which as we have seen might have a large k . The Fermi level, or chemical potential μ , marks the limit between occupied and empty states. To a first approximation, a material is conductive if the Fermi level falls within a band, as it allows a small electric field to polarize the movement of the electrons.

The Bloch waves $|\psi_{m,\vec{k}}\rangle$ are not eigenstates of the momentum operator and the relation $\vec{p} = \hbar\vec{k}$ for free electrons is not valid. Instead, electrons in a lattice must be treated as waves, with a group velocity $\vec{v}_m(\vec{k}) = \partial E_m(\vec{k})/\partial \vec{k}$. It is proportional to the hopping integral, which explains its name. In the absence of electric field, the electrons near the Fermi level move at a Fermi velocity of $\sim 10^6$ m s⁻¹ in random directions, by hopping from atom to atom, and there is no net current. As they scatter elastically on quasi-particles or impurities after a mean free path in the order of a few tens of nanometers, they move to a free orbital of similar energy with a different wavevector. The application of an electric field $\vec{E} = -\vec{\nabla}V$ changes the chemical potential by $-eV$. This spatial dependency skews slightly the energy of the bands, so that scattering electrons relax preferentially into states with $\vec{k} \parallel -\vec{E}$. The net velocity of the charge distribution \vec{v}_d is then only in the order of micrometers per second. It is related to the conductivity of the medium by $\sigma = e\vec{v}_d / \vec{E}V$, giving a current density $\vec{j} = \sigma\vec{E} = -e\vec{v}_d / V$.

The current density can also be expressed as a function of the gradient of the chemical potential: $\vec{j} = \sigma\vec{\nabla}\mu / e$. In addition to electric fields, which change the energy of the bands, a chemical potential gradient can be caused by a change in the distribution of electrons, such as induced by a temperature gradient [125] or a localized excess of electrons.

In Chapter 4, we will be interested in the transport of spin by the conduction electrons. This occurs when the Fermi velocity or mean free path of the electrons are spin-dependent, so that there is a net angular momentum carried by the current.

Bands usually have a parabolic shape near the $k = 0$ point or other high-symmetry points of the Brillouin zone, which is reminiscent of the dispersion of free electrons and

allows conduction electrons to be approximated as such with a reduced effective mass. They carry their spin through the material, until they undergo spin-flip scattering. Their behavior is thus best described by statistical methods. In the absence of spontaneous organization of the magnetic moments, their paramagnetic and diamagnetic properties dominate the response of metallic materials to a magnetic field.

3.2.4.3 Susceptibility of materials

We start our exploration of the collective behavior of magnetic moments with the origins of the magnetic susceptibility. Paramagnetism and diamagnetism describe the appearance of a net magnetization in a material subject to a magnetic field, respectively due to a small positive or negative susceptibility. The material may be initially non-magnetic due either to the absence of magnetic moments or to their random orientation.

We will first consider the effect of a magnetic field on conducting materials, modeled as consisting of free, non-interacting electrons. Then we will see the analogous effects on ions, leading to the appearance of the Curie law, which will be used in the next section to model the appearance of ferromagnetism.

Pauli paramagnetism

The Hamiltonian of a free electron in a magnetic field is:

$$\hat{H} = \frac{(\hat{\mathbf{p}} + e\hat{\mathbf{A}})^2}{2m_e} - \hat{\boldsymbol{\mu}}_s \cdot \hat{\mathbf{B}}, \quad (3.83)$$

where $\hat{\mathbf{p}} = -i\hbar\hat{\nabla}$ is the momentum operator and $\hat{\mathbf{A}}$ is the vector potential of the magnetic field $\hat{\mathbf{B}} = \hat{\nabla} \wedge \hat{\mathbf{A}}$. Since free electrons have no fixed orbit, only their spin contributes to their magnetic moment. In addition to m_s , they are otherwise characterized only by their momentum $\hbar\vec{\mathbf{k}}$, which in this case is the eigenvalue of $\hat{\mathbf{p}}$.

In momentum space, electrons with the same kinetic energy $E = \hbar^2|\vec{\mathbf{k}}|^2 / (2m_e)$ are distributed on a sphere of radius $|\vec{\mathbf{k}}|$. The density of states (DOS) $g(E) = dn(E)/dE$, with $n(E)$ the volumic density of electrons, characterizes the amount of states of this sphere. While, as we saw in Section 3.2.4.1, the amount of allowed values of $\vec{\mathbf{k}}$ increases with the volume of the material, its density is a constant of the latter. As illustrated in Fig. 3.10, $g(E)$ grows with the circumference of the sphere, so that $g(E) \propto \sqrt{E}$.

At zero temperature, the Fermi energy E_F marks the sharp limit between occupied and empty states. At finite temperatures, the limit is characterized by the chemical potential μ . The probability for a state of energy E to be occupied is given by Fermi-Dirac statistics:

$$f(E) = \frac{1}{1 + \exp\left(\frac{E-\mu}{k_B T}\right)}, \quad (3.84)$$

where by definition $f(\mu) = 1/2$. The ratio $\mu / k_B T \approx E_F / k_B T$ determines how much the distribution deviates from its zero-temperature value. As the Fermi temperature E_F / k_B

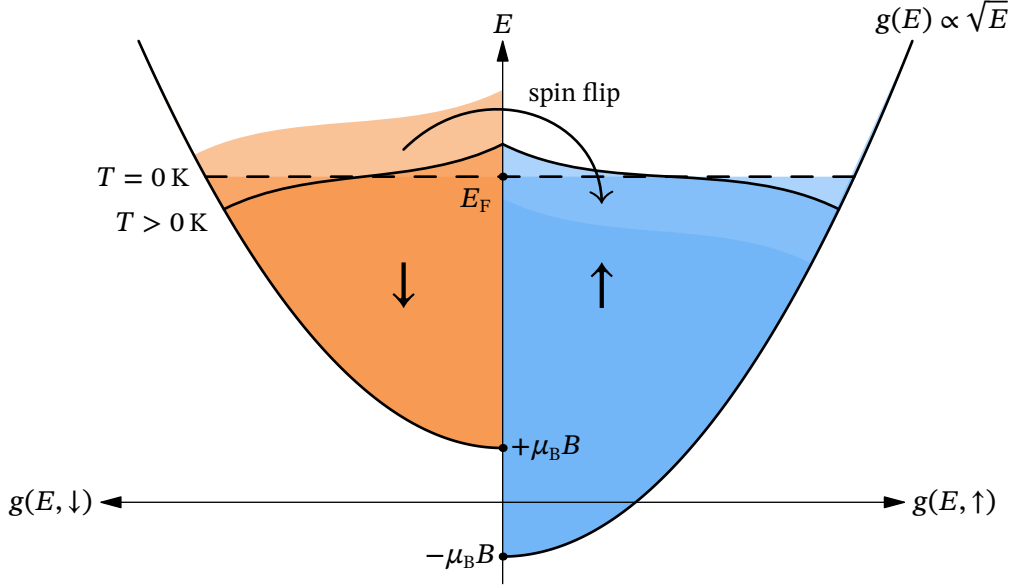


Figure 3.10: Parabolic density of states of free electrons in a magnetic field, shifted by the Zeeman effect. The colored surfaces represent the occupied states. The electrons occupy all states of energy $E < E_F$ at $T = 0$ K (dashed line), while some states with higher energy are occupied at $T > 0$ K (full line).

is in the order of tens of thousands of Kelvin, we can generally neglect the effects of the temperature on the DOS. The use of a Fermi-Dirac distribution, rather than a classical Boltzmann distribution, thus leads to temperature independence.

When a magnetic field with induction $\hat{\mathbf{B}}$ is applied, the energy levels of the electrons are shifted by $\pm\mu_B B_z$ due to the Zeeman effect. The DOS becomes asymmetric in spin [99, chapter 5]:

$$g(E, \uparrow\downarrow) = \frac{1}{2} g(E \pm \mu_B B) \approx \frac{1}{2} \left(g(E) \pm \mu_B B_z \frac{dg(E)}{dE} \right). \quad (3.85)$$

The spin up electrons, which have $m_s = -1/2$ and thus their magnetic moment aligned along the field, have a lower energy than the spin down electrons of the same momentum. When the magnetic field turns on, some spin down electrons see their energy raised above the Fermi level, while unoccupied spin up states are lowered under it. To reach thermal equilibrium again, the spin down electrons flip their spin, creating a net positive moment in the material.

Each flipped electron adds μ_B to the net moment. The induced magnetization is thus given by the difference in electronic density between both directions of spin:

$$\begin{aligned} M &= \mu_B \int_0^{E_F} (g(E, \uparrow) - g(E, \downarrow)) dE \\ &= \mu_B^2 B_z g(E_F). \end{aligned} \quad (3.86)$$

Remembering that $M = \chi H$, we obtain the Pauli susceptibility of free electrons:

$$\chi_P = \mu_0 \mu_B^2 g(E_F) = \mu_0 \mu_B^2 \frac{3n}{2E_F}. \quad (3.87)$$

This expression can be adapted for real materials by correcting the DOS. Since only the electrons near the Fermi level participate, χ_P is typically small – for most metals, in the order of 10^{-5} . It is the strongest for localized bands with little dispersion, as their occupation is the most sensitive to a shift in the band energy.

Landau diamagnetism

In addition to Pauli paramagnetism, spinless free electrons also exhibit a small diamagnetic response [126]. Classically, a magnetic field curves the trajectory of an electron according to the Lorentz equation, Eq. (3.1). This results in the formation of a small orbital magnetic moment.

We concentrate on the first term of the Hamiltonian in Eq. (3.83). The vector potential $\hat{\mathbf{A}}$ does not have a unique description; we can choose $\hat{\mathbf{A}} = \hat{\mathbf{B}} \wedge \hat{\mathbf{r}} / 2$, which for $\hat{\mathbf{B}}$ along z is $\hat{\mathbf{A}} = B / 2[-\hat{\mathbf{y}}, \hat{\mathbf{x}}, 0]$. The Hamiltonian becomes:

$$\begin{aligned} \hat{H} &= \frac{1}{2m_e} \left(\left(\hat{\mathbf{p}}_x - \frac{eB}{2} \hat{\mathbf{y}} \right)^2 + \left(\hat{\mathbf{p}}_y - \frac{eB}{2} \hat{\mathbf{x}} \right)^2 + \hat{\mathbf{p}}_z^2 \right) \\ &= \frac{m_e \omega_c}{4} \left((\hat{\mathbf{y}}_0 - \hat{\mathbf{y}})^2 + (\hat{\mathbf{x}}_0 - \hat{\mathbf{x}})^2 \right) + \frac{1}{2m_e} \hat{\mathbf{p}}_z^2, \end{aligned} \quad (3.88)$$

where we defined the operators $\hat{\mathbf{x}}_0 = 2\hat{\mathbf{p}}_y / (eB)$, $\hat{\mathbf{y}}_0 = 2\hat{\mathbf{p}}_x / (eB)$, and the cyclotron frequency:

$$\omega_c = \frac{eB}{m_e}. \quad (3.89)$$

This Hamiltonian describes an unmodified momentum along z and two harmonic oscillators along x and y , which oscillate at the cyclotron frequency, and whose potential minima are given by $\hat{\mathbf{x}}_0$ and $\hat{\mathbf{y}}_0$ (which do not commute). The presence of the magnetic field confines the trajectory of the electron in the xy plane into cyclotron orbits.

The harmonic oscillator part of the Hamiltonian has the eigenvalues $E_l = \hbar\omega_c(l + 1/2)$: the electron orbits with a discrete number of allowed energy levels called Landau levels, characterized by the quantum number $l \geq 0$. As the angular frequency is constant, l corresponds to an increase in the radius of the orbit. The free electron thus gains an orbital angular momentum $\hbar l$. In momentum space, the allowed states lie on concentric cylinders centered on the k_z axis, inside the Fermi sphere (see Fig. 3.11a). Instead of a purely parabolic DOS, it forms an energy comb with peaks at E_l and a decreasing tail above them due to the remaining momentum. The Fermi level shifts to accommodate the same number of electrons.

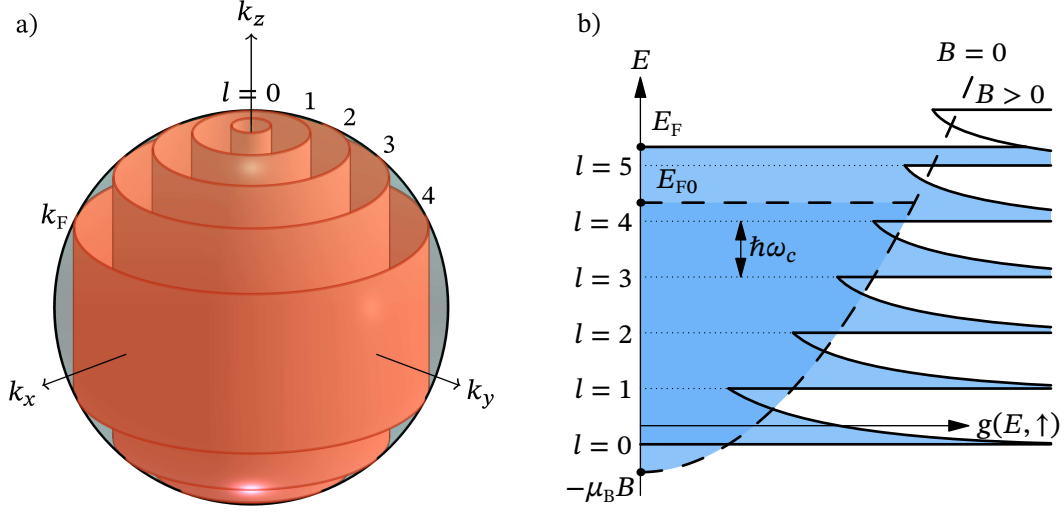


Figure 3.11: a) Landau levels in momentum space formed by electrons with a momentum quantized in the xy plane. b) Modified DOS (represented only for electrons with spin up).

Following the approach of Blundell [127, chapter 7.6], we then calculate the magnetization resulting from the orbital moment of the electrons:

$$M = - \left(\frac{d\phi}{dB} \right)_T, \quad (3.90)$$

where $\phi = U - TS - BM$ is the Gibbs free energy density of the system. We assume that $T = 0$ K and the internal energy $U = 0$ as the electrons are non-interacting [128], so that $\phi = -BM$ is the energy added to the system by the magnetic field [127]:

$$\phi = \int_0^{E_F} g(E) E dE - \int_0^{E_{F0}} g_0(E) E dE = \frac{k_F e^2 B^2}{24\pi^2 m_e}. \quad (3.91)$$

We then obtain the susceptibility:

$$\begin{aligned} \chi_{Ld} &= \mu_0 \frac{d^2\phi}{dB^2} = -\frac{1}{3} \mu_0 \left(\frac{e\hbar}{2m_e} \right)^2 \left(\frac{m_e k_F}{\pi^2 \hbar^2} \right) \\ &= -\frac{1}{3} \chi_P. \end{aligned} \quad (3.92)$$

For a free electrons gas, the contribution of the Landau diamagnetism is exactly a third of the one of Pauli paramagnetism. The resulting total susceptibility of the gas is $2\chi_P / 3$. Because of this, metals, except those dominated by exchange interactions, are paramagnetic. In other solids however, the contribution of the Landau diamagnetism may dominate when the effective mass m^* of the free electrons is small, as the Landau susceptibility becomes:

$$\chi_{Ld} = -\frac{1}{3} \left(\frac{m_e}{m^*} \right)^2 \chi_P. \quad (3.93)$$

This is for example the case for graphite, in which $m^* \approx 0.01m_e$ for electrons moving perpendicularly to the basal plane, resulting in a large diamagnetic susceptibility of $\chi = -6 \times 10^{-4}$ at room temperature [129].

Langevin diamagnetism

The same phenomena of paramagnetism and diamagnetism also occur in bound electrons. The semi-classical Langevin theories were their first successful descriptions [130]. All bound electrons exhibit a diamagnetic behavior, but its contribution is small and only relevant for closed shells that have no net magnetic moment.

Similarly to the Landau diamagnetism, the Langevin diamagnetism is caused by the $(e\hat{\mathbf{A}})^2 / 2m_e$ component of the Hamiltonian, shown in Eq. (3.83). The electrons being bound, they do not describe cyclotron orbits; the field results in a small perturbation of their atomic orbitals. We express the vector potential as an additional angular momentum $\hat{\mathbf{L}}_p = \hat{\mathbf{r}} \wedge e\hat{\mathbf{A}} = \hat{\mathbf{r}} \wedge \hat{\mathbf{B}} \wedge \hat{\mathbf{r}}e / 2$, whose z component is $\hat{L}_{p_z} = (\hat{x}^2 + \hat{y}^2)eB / 2$.

In a classical description, the Langevin diamagnetism is caused by the Larmor precession of the orbital angular momentum of individual electrons. We have seen an example of Larmor precession in Section 2.3.2, as the precession of the magnetization of FeBO_3 . When the magnetic moment of an electron is subjected to the field $\vec{\mathbf{B}}$, it experiences a torque given by Eq. (3.2):

$$\vec{\tau} = \frac{d\vec{\mathbf{L}}}{dt} = \gamma\vec{\mathbf{L}} \wedge \vec{\mathbf{B}}, \quad (3.94)$$

where $\vec{\mathbf{L}} = [\langle \hat{\mathbf{L}}_x \rangle, \langle \hat{\mathbf{L}}_y \rangle, \langle \hat{\mathbf{L}}_z \rangle]$ is the classical angular momentum. The solution of Eq. (3.94) is a precession around the magnetic field: $\vec{\mathbf{L}} = [R \cos(\omega_L t), R \sin(\omega_L t), \langle \hat{\mathbf{L}}_z \rangle]$, where $\omega_L = -\gamma_l B = \omega_c / 2$ is the Larmor frequency and $R = x + y$ is the distance between

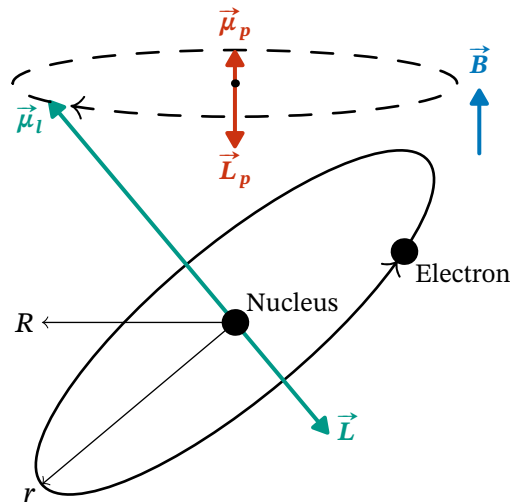


Figure 3.12: Larmor precession of the orbital angular momentum of an electron in a magnetic field, creating an additional magnetic moment $\vec{\mu}_p$.

the electron and the nucleus projected in the plane normal to the field. As shown in Fig. 3.12, the in-plane components of the additional angular momentum average to zero, and we obtain $\vec{L}_p = e\vec{B}\langle R^2 \rangle / 2 = m_e\omega_L\langle R^2 \rangle\vec{z}$. The resulting magnetic moment is thus opposed to the field:

$$\vec{\mu}_p = \gamma\vec{L}_p = -\frac{e^2\langle R^2 \rangle}{4m_e}\vec{B}. \quad (3.95)$$

Assuming the orbits of all Z electrons in an atom to be spherically symmetric so that $\langle R^2 \rangle = 2\langle r^2 \rangle / 3$, where r is the radius of the orbit, the total additional magnetic moment of the atom is:

$$\vec{\mu}_p = \sum_{i=1}^Z \vec{\mu}_{p_i} = -\frac{e^2 Z \langle r^2 \rangle}{6m_e} \vec{B}. \quad (3.96)$$

Multiplied by the atomic density n , this gives the magnetization of the material. The diamagnetic susceptibility is thus [99, chapter 3]:

$$\chi_{Lg} = -\frac{e^2 Z n \langle r^2 \rangle}{6m_e}. \quad (3.97)$$

This contribution exists in all materials but is very small: for example, $\chi_{Lg} = -9 \times 10^{-6}$ for water and -2×10^{-10} for H_2 .

Langevin or Brillouin paramagnetism

The Langevin model of paramagnetism was among the earliest successes of statistical mechanics. The Brillouin model is the quantum formulation of the same phenomenon, which we will use here. It is the temperature-dependent paramagnetic susceptibility at the origin of Curie's law (introduced in Section 3.1.4). Contrarily to Langevin diamagnetism, this component applies only to atoms that exhibit a magnetic moment.

As shown in Section 3.2.1.4, the Zeeman energy of the atom subjected to a magnetic field is $\hat{H}_Z = -\hat{\mu}_J \cdot \hat{B} = \mu_B g_J M_J B_z$. At $T = 0$ K, the atom adopts the state with the lowest energy. But at finite temperature, the thermal energy partially counters this alignment. Contrarily to electrons, the ions follow Boltzmann statistics. The expectation value of the moment is found using the thermodynamic average over all states [96, chapter 4]:

$$\langle \hat{\mu}_z \rangle = \frac{\sum_i \hat{\mu}_{z_i} \exp\left(-\frac{\hat{H}_{z_i}}{k_B T}\right)}{\sum_i \exp\left(-\frac{\hat{H}_{z_i}}{k_B T}\right)} = \mu_B g_J J \mathcal{B}_J(r), \quad (3.98)$$

where:

$$\mathcal{B}_J(r) = \frac{2J+1}{2J} \coth\left(r \frac{2J+1}{2J}\right) - \frac{1}{2J} \coth\left(r \frac{1}{2J}\right) \quad (3.99)$$

is the Brillouin function and $r = \mu_B g_J J B_z / (k_B T)$ is the ratio of the magnetic and thermal energy. The Brillouin function represents the average alignment of the magnetic moments on the field: $J \mathcal{B}_J(r) = \langle M_J \rangle$. If the field is small, $r \ll 1$ and $\mathcal{B}_J(r) \approx r(J+1)/3J$.

The thermal average of the atomic magnetic moment is thus:

$$\langle \vec{\mu}_z \rangle \approx \frac{\mu_B^2 g_j^2 B_z J(J+1)}{3k_B T}. \quad (3.100)$$

Consequently, the susceptibility of the material with atomic density n is:

$$\chi_B = \frac{\mu_0 \mu_B^2 g_j^2 n J(J+1)}{3k_B T} = \frac{C}{T}, \quad (3.101)$$

where C is the Curie constant. Curie's law was first observed in oxygen, for which he measured $C = 118 \text{ K}$ and $\chi_B = 4 \times 10^{-7}$ [131].

Van Vleck paramagnetism

Since the energy of the diamagnetic moment in the field $\hat{\mu}_p \vec{B}$ is of the second order in \vec{B} , the paramagnetic moment should also be considered up to the same order. We thus finally examine the second-order Zeeman perturbation that we neglected in Eq. (3.68). The mixing of the ground term Γ and excited terms Γ' induced by the magnetic field leads to an energy correction [96, chapter 4]:

$$E_Z^{(2)} = \sum_{\Gamma' \neq \Gamma} \frac{|\langle \Gamma | \hat{\mu}_j \cdot \vec{B} | \Gamma' \rangle|^2}{E_{\Gamma'}^{(0)} - E_{\Gamma}^{(0)}}. \quad (3.102)$$

The resulting susceptibility is:

$$\chi_V = \frac{2n\mu_0 E_Z^{(2)}}{B^2} = 2n\mu_0 \gamma_j^2 \sum_{\Gamma' \neq \Gamma} \frac{|\langle \Gamma | \hat{\mu}_{jz} | \Gamma' \rangle|^2}{E_{\Gamma'}^{(0)} - E_{\Gamma}^{(0)}}, \quad (3.103)$$

and has the same order of magnitude as the diamagnetic component. When the crystal field splitting is small ($|E_{\Gamma'}^{(0)} - E_{\Gamma}^{(0)}| = \Delta E \ll k_B T$), the second-order contribution is negligible and the susceptibility follow Curie's law. This is the case for paramagnetic gases such as O_2 and NO_2 , and rare earth elements. When the separation between all levels is large, the material can only magnetize via this mixing process and the susceptibility is fully temperature-independent [132].

We have now reviewed the different phenomena that contribute to produce a net magnetic moment in paramagnetic or diamagnetic materials subject to a magnetic field. One effect remains unexplained: the existence of a spontaneous magnetization in some materials.

3.2.4.4 The molecular field model of ferromagnetism

So far, we have assumed that the orientation of the magnetic moments of atoms are independent from each other and randomly aligned in the absence of a magnetic field.

This is however not always the case, as shown by the existence of a spontaneous magnetic order in some materials: ferromagnetic, antiferromagnetic or ferrimagnetic.

This spontaneous magnetization was first explained by postulating the existence of an internal magnetic field proportional to the magnetization: the Weiss molecular field $\vec{H}_W = n_W \vec{M}$. Contrarily to the actual dipolar field described in Section 3.1.3 that opposes the magnetization, this hypothetical field ensures that the parallel alignment of the magnetic moments is energetically favorable. To result in a spontaneous magnetization of the whole material, the Weiss coefficient n_W needs to be as large as ~ 100 . Although the molecular field does not exist, such a mean-field theory remains a useful approximation of the many-body problem of interacting magnetic moments, allowing to extend the Brillouin model of paramagnetism to magnetically ordered materials.

In the absence of external magnetic field, the material is subject to the molecular field $\vec{B} = \mu_0 n_W \vec{M}$. According to Eq. (3.98), the resulting magnetization is $M = M_0 \mathcal{B}_J(r)$, where $M_0 = \mu_B g_j n J$ is the maximum magnetization, corresponding to all magnetic moments being fully aligned on the field ($M_J = -J$). At finite temperature, the spontaneous magnetization is thus given by:

$$\frac{M}{M_0} = \mathcal{B}_J(r), \quad (3.104)$$

where as before $r = \mu_B g_j J n_W M / (k_B T)$. Since $\mathcal{B}_J(r) \propto r$, we also have:

$$\frac{M}{M_0} = \frac{\mathcal{B}_J(r)}{\mathcal{B}_J(r_0)} = \frac{r}{r_0} = r \frac{T(J+1)}{3CJn_W}, \quad (3.105)$$

where we inserted the Curie constant defined in Eq. (3.101). Given that the molecular field needs to be larger than the thermal fluctuations in order to magnetize the material, the approximation $r \ll 1$ is not valid and $\mathcal{B}_J(r)$ is given by Eq. (3.99). Under a critical temperature $T_C = n_W C$, there exists a value of r that satisfies both Eqs. (3.104) and (3.105), from which we obtain the spontaneous magnetization as shown on Fig. 3.13. T_C is the Curie temperature mentioned in Section 3.1.4, which is the highest temperature at which a material is ferromagnetic. It is for example 1043 K for iron, associated with a molecular field of $\mu_0 H_W = 1553$ T [133, chapter 11]. For $0 < T < T_C$, the net magnetization in the material is lowered by thermal fluctuations, which slightly deviate each atomic spin from its equilibrium position, creating a random background of thermal spin waves. Above T_C , the thermal energy randomizes the spins and the material becomes paramagnetic. Its susceptibility then follows the Curie–Weiss law:

$$\chi_{CW} = \frac{C}{(T - T_C)}. \quad (3.106)$$

One of the challenges of models attempting to explain the origin of ferromagnetism, notably in 3d transition metals, is to reproduce their measured Curie temperature. The Heisenberg model of interacting localized ions, which we will introduce in Section 3.2.4.6, is successful on this point. However, it fails to reproduce the non-integer magnetic moment of those materials. This in turn is well-reproduced by the Stoner model of nearly free electrons.

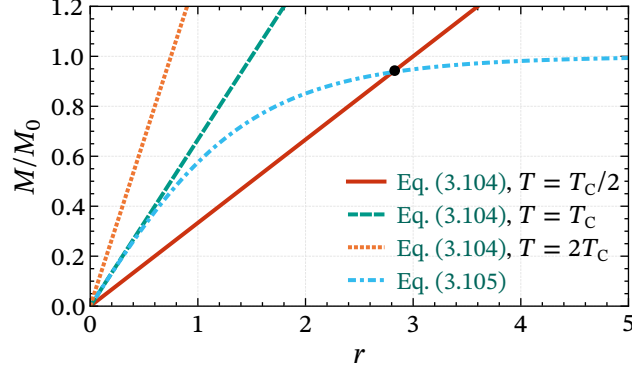


Figure 3.13: Spontaneous magnetization created by the molecular field for $J = 1$, $g_j = 2$ and $n_w = 100$ in the absence of external magnetic field. The magnetization is defined by the crossing of the two curves.

3.2.4.5 The Stoner model of ferromagnetism

To describe the ferromagnetism of conduction electrons, the same self-consistent approach as above is applied using the Pauli paramagnetism model. The bands are split as shown in Fig. 3.10 by the molecular field $n_w M$. The Weiss coefficient is given by [96, chapter 5]:

$$n_w = \frac{ID(E_F, \uparrow\downarrow)}{\chi_P} = \frac{I}{2n\mu_0\mu_B^2}, \quad (3.107)$$

where $D(E_F, \uparrow\downarrow) = g(E_F) / 2n$ is the DOS per atom and per spin at the Fermi energy.

In the Stoner model, the origin of the band splitting is the Coulomb repulsion between electrons of the opposite spin, of energy $I \approx 1$ eV. The DOS of the free electrons is assumed to be sufficiently low for the repulsion between electrons of the same spin to be comparatively negligible, due to the Pauli exclusion principle. The Coulomb interaction increases the energy of each band according to the number N of electrons having the opposite spin: $E_m(k, \uparrow) = E_m^{(0)}(k) + IN_\downarrow$. The corresponding potential energy of the material is $IN_\uparrow N_\downarrow$.

With the magnetization given by $M = \mu_B(n_\uparrow - n_\downarrow)$, a splitting of the bands by:

$$\delta E = 2\mu_0\mu_B n_w M = I \frac{(n_\uparrow - n_\downarrow)}{n} \quad (3.108)$$

causes the flip of $\delta N = D(E_F, \uparrow\downarrow)\delta E$ electrons, lowering the potential energy by $I(\delta N)^2$. At the same time, the flipped electrons have moved into states with a higher band energy $E_m^{(0)}(k)$, which for bands with free electron-like dispersion corresponds to states with a larger k . The corresponding kinetic energy increase of the material is $\delta N\delta E$. The total energy change is thus:

$$\begin{aligned} \Delta E &= \delta N\delta E - I(\delta N)^2 \\ &= D(E_F, \uparrow\downarrow)(\delta E)^2 (1 - ID(E_F, \uparrow\downarrow)). \end{aligned} \quad (3.109)$$

We need $\Delta E < 0$ for the splitting of the bands to be favorable. This leads to Stoner's criterion for the existence of ferromagnetism in a material:

$$ID(E_F, \uparrow\downarrow) > 1. \quad (3.110)$$

Materials with a large DOS, that is to say narrow flat bands in which electrons have a small velocity, thus favor ferromagnetism. Among the 3d transition elements, only Fe, Co and Ni satisfy this criterion. Their spontaneous magnetic moments at room temperature are respectively $2.216\mu_B$, $1.715\mu_B$ and $0.616\mu_B$ per atom.

We saw that in these materials, the orbital angular momentum is nearly fully quenched. The contribution of each electron to the magnetic moment of the atom is thus $\pm\mu_B$ due to its spin alone. In localized models, the number of electrons in the incomplete subshells of each atom is well defined, so that their magnetic moment and thus the saturated moment of a material is expected to be an integer multiple of the Bohr magneton. This is however far from the case. In a band model, the 3d, 4s and 4p bands generally overlap, so that their average occupation per atom is not integral. Ferrimagnetic iron has for example 7.4 electrons per atom in the 3d bands, leading to its non-integer magnetic moment.

On one hand, an itinerant model of ferromagnetism is then necessary to predict the magnetic moment of transition metals. On the other hand, the Stoner model is unable to reproduce the Curie–Weiss law describing their temperature dependence. Its predicted susceptibility is $\chi = \chi_P / (1 - ID(E_F, \uparrow\downarrow))$, and is increased by the presence of the Coulomb repulsion I compared to a purely paramagnetic metal. The Curie temperature is defined as the temperature at which $ID(E_F, \uparrow\downarrow) = 1$ and the susceptibility diverges. The DOS and the Fermi level being only weakly temperature-dependent, the Stoner model predicts Curie temperatures almost an order of magnitude too large: for example, depending on the model used to calculate the band structure, 5300 K [134] or 2560 K [135] for Fe, whose experimental Curie temperature is 1034 K.

An accurate description of those materials needs elements from both theories. The reason for this is the energy-dependency of the localization of 3d electrons. We have shown in Section 3.2.3.1 the localized nature of the charge density of atomic 3d orbitals, and the presence of a small centrifugal barrier. Because of the latter, the radial part of the wavefunction for $l = 3$ is very sensitive to the energy of the electrons. When considering wavefunctions that are Bloch-like between atoms but strongly influenced by the nucleus at short distances, this sensitivity is carried over to the metallic state. Low-energy electrons are able to spread out and delocalize, while the wavefunction of high-energy electrons at the top of the 3d band is slightly more localized than the one of a free atom [136]. This results in the large difference in the structure of e_g and t_{2g} bands in iron, the former being narrow and weakly dispersive and the latter broad and delocalized. Because of this, different types of exchange interactions and correlations effects, such as the spatial separation of electrons of the same spin due to the Pauli exclusion principle, or the Coulomb repulsion between opposite spins characterized by the Stoner constant I , are at the origin of the magnetic order.

3.2.4.6 Exchange interactions

The real phenomena modeled by the molecular field are ultimately Coulomb repulsion and the Pauli principle. The ordering of the magnetic moments in ferromagnetic materials stems from the exchange interactions between atoms or electrons, whose spins appear to interact with each other. In [Section 3.2.2.2](#), we have derived the intra-atomic Heisenberg exchange Hamiltonian, from which Hund's first rule originates. Although the Heisenberg model originally describes only direct inter-atomic exchange between atoms with overlapping orbitals, it can be used to model other isotropic exchange interactions. It can also represent the coupling between the magnetization vectors of different domains or AFM sublattices, which we will use in [Section 3.3.3](#) to model the dynamics of FeBO₃.

Direct exchange

Let us consider two electrons in a H₂ molecule, sharing the bonding orbital $|\psi^b\rangle = |\varphi_A\rangle + |\varphi_B\rangle$ constructed from the 1s subshells. Neglecting any interaction between them, the naive wavefunction of the molecule is:

$$|\Psi\rangle = |\psi^b\rangle|\psi^b\rangle = |\varphi_A\rangle|\varphi_A\rangle + |\varphi_A\rangle|\varphi_B\rangle + |\varphi_B\rangle|\varphi_A\rangle + |\varphi_B\rangle|\varphi_B\rangle. \quad (3.111)$$

As before, the Coulomb potential part of the Hamiltonian contains the interactions of each electron with the nucleus A , B , and each other. In order to express the energy as a function of the hopping integral $t = \langle\varphi_A|\hat{H}_A|\varphi_B\rangle = \langle\varphi_B|\hat{H}_B|\varphi_A\rangle$, it is helpful to separate the operators that act separately on each electron:

$$\hat{H} = (\hat{H}_A + \hat{H}_B) \otimes \hat{I} + \hat{I} \otimes (\hat{H}_A + \hat{H}_B) + \hat{H}_C. \quad (3.112)$$

We can thus evaluate $\langle\Psi|\hat{H}|\Psi\rangle$:

$$\langle\varphi_A\varphi_A|\hat{H}|\varphi_A\varphi_A\rangle = \begin{cases} \langle\varphi_A|\hat{H}_A|\varphi_A\rangle \otimes \langle\varphi_A|\varphi_A\rangle \\ + \langle\varphi_A|\hat{H}_B|\varphi_A\rangle \otimes \langle\varphi_A|\varphi_A\rangle \\ + \langle\varphi_A|\varphi_A\rangle \otimes \langle\varphi_A|\hat{H}_A|\varphi_A\rangle \\ + \langle\varphi_A|\varphi_A\rangle \otimes \langle\varphi_A|\hat{H}_B|\varphi_A\rangle \\ + \langle\varphi_A\varphi_A|\hat{H}_C|\varphi_A\varphi_A\rangle \end{cases} = \begin{cases} E_{1s} \\ + C_{CF} \\ + E_{1s} \\ + C_{CF} \\ + \mathcal{U} \end{cases} \quad (3.113a)$$

$$\langle\varphi_A\varphi_B|\hat{H}|\varphi_B\varphi_B\rangle = \begin{cases} \langle\varphi_A|\hat{H}_A|\varphi_B\rangle \otimes \langle\varphi_B|\varphi_B\rangle \\ + \langle\varphi_A|\hat{H}_B|\varphi_B\rangle \otimes \langle\varphi_B|\varphi_B\rangle \\ + \langle\varphi_A|\varphi_B\rangle \otimes \langle\varphi_B|\hat{H}_A|\varphi_B\rangle \\ + \langle\varphi_A|\varphi_B\rangle \otimes \langle\varphi_B|\hat{H}_B|\varphi_B\rangle \\ + \langle\varphi_A\varphi_B|\hat{H}_C|\varphi_B\varphi_B\rangle \end{cases} = \begin{cases} t_0 \\ + 0 \\ + 0 \\ + 0 \\ + C_t \end{cases} \quad (3.113b)$$

where \mathcal{U} is the on-site Coulomb repulsion, \mathcal{C}_{CF} is analogous to the crystal field potential, and \mathcal{C}_t couples the electrons during a hop. We also define the exchange integral $\mathcal{J}_d = \langle \varphi_A \varphi_B | \hat{\mathbf{H}}_{\text{C}} | \varphi_B \varphi_A \rangle = \langle \varphi_A \varphi_A | \hat{\mathbf{H}}_{\text{C}} | \varphi_B \varphi_B \rangle$ and the net hopping energy $t = t_0 + \mathcal{C}_t$. By this process, we find the matrix of the interaction Hamiltonian [96, chapter 5]:

$$\hat{\mathbf{H}} = \underbrace{E_{1s} + \mathcal{C}_{\text{CF}}}_{E_0} + \begin{bmatrix} \mathcal{U} & t & t & \mathcal{J}_d \\ t & 0 & \mathcal{J}_d & t \\ t & \mathcal{J}_d & 0 & t \\ \mathcal{J}_d & t & t & U \end{bmatrix} \begin{matrix} AA \\ AB \\ BA \\ BB \end{matrix} \quad (3.114)$$

Neglecting the normalization factors, its eigenstates are:

$$\begin{aligned} |\Psi_{\text{cov}}\rangle &= |\varphi_A\rangle|\varphi_B\rangle - |\varphi_B\rangle|\varphi_A\rangle; & E_{\text{cov}} &= E_0 - \mathcal{J}_d, \\ |\Psi_{\text{ion}}\rangle &= |\varphi_A\rangle|\varphi_A\rangle - |\varphi_B\rangle|\varphi_B\rangle; & E_{\text{ion}} &= E_0 + \mathcal{U} - \mathcal{J}_d, \\ |\Psi_{\pm}\rangle &= |\varphi_A\rangle|\varphi_A\rangle + |\varphi_B\rangle|\varphi_B\rangle + \frac{E_{\mp}^0}{2t} (|\varphi_A\rangle|\varphi_B\rangle + |\varphi_B\rangle|\varphi_A\rangle) \\ & & E_{\pm} &= E_0 + \mathcal{J}_d + E_{\pm}^0 = E_0 + \mathcal{J}_d + \frac{\mathcal{U}}{2} \pm \frac{\sqrt{\mathcal{U}^2 + 16t^2}}{2}. \end{aligned} \quad (3.115)$$

The states $|\Psi_{\text{cov}}\rangle$ and $|\Psi_{\text{ion}}\rangle$ have antisymmetric spatial wavefunctions, and thus correspond to a FM alignment. The former is as usual a spin triplet, but the ionic configuration can only have the spin state $|\uparrow\downarrow, 0\rangle + |0, \uparrow\downarrow\rangle$. The mixed states $|\Psi_{\pm}\rangle$ are the superposition of two Slater determinants, both spatially symmetric, and are thus both singlets with antiparallel spins.

In order to use the Heisenberg Hamiltonian from Eq. (3.50), we define an effective exchange constant $\mathcal{J} = \mathcal{J}_d + \mathcal{U} / 4 - \sqrt{t^2 + \mathcal{U}^2 / 16}$ to describe the energy difference between the lowest two states, $|\Psi_{\text{cov}}\rangle$ and $|\Psi_{-}\rangle$. Although $\mathcal{J}_d > 0$, it is now possible to find $\mathcal{J} < 0$ due to the kinetic contribution, which favors an antiparallel alignment of individual spins and thus no net magnetic moment.

Stoner limit:

In the itinerant limit $t \gg \mathcal{U} \gg \mathcal{J}_d$, the exchange constant becomes $\mathcal{J} = \mathcal{J}_d + \mathcal{U} / 4 - |t|$. This corresponds to the independent-electron Stoner model, whose constant is $I = \mathcal{J}_d + \mathcal{U} / 4$.

For $\mathcal{U} = 0$, the mixed orbitals become $|\Psi_{+}\rangle = |\psi^a\rangle|\psi^a\rangle$ and $|\Psi_{-}\rangle = |\psi^b\rangle|\psi^b\rangle$, of energy $\mathcal{J}_d \pm 2|t|$. Since the hopping integral is the one-electron level splitting between the bounding, non-bounding and antibounding orbitals as shown in Eq. (3.82), it is proportional to the width $W = 2Zt$ of the resulting band, where Z is the number of nearest neighbors. It is thus inversely proportional to the DOS $D(E_{\text{F}}, \uparrow\downarrow)$ and opposes the fulfillment of the Stoner criterion. A large mobility of the electrons prevents the formation of a magnetic moment by direct exchange.

Heisenberg limit:

In the strongly correlated limit $\mathcal{U} \gg t$, the exchange constant becomes $\mathcal{J} = \mathcal{J}_d - 2t^2 / \mathcal{U}$. For $t = 0$, we find that $|\Psi_+\rangle$ is a purely ionic state of energy $E_0 + \mathcal{U} + \mathcal{J}_d$, and $|\Psi_-\rangle$ a purely covalent state of energy $E_0 + \mathcal{J}_d$. The covalent and ionic groups of states form the lower and upper Hubbard sub-band, respectively. Within each sub-band, we recover the same picture as in Section 3.2.2.2, with two energy levels separated by $2\mathcal{J}_d$.

When the energy cost of adding an electron on an atom becomes larger than the bandwidth, that is to say $\mathcal{U} > W = 2Zt$, a band gap forms between the Hubbard sub-bands. The correlation of the electrons prevents the formation of ionic states, and the material becomes a Mott insulator with each electron localized on a different atom. Transition metal oxides are often Mott insulators, due to the decreased overlap of the orbitals of the metallic ions which results in a smaller bandwidth compared to the pure element. This is the case in FeBO_3 , where the Fe^{3+} ions are surrounded by O^{2-} ions, resulting in small values of $t \approx 0.05$ eV and $W \approx 0.4$ eV, while $\mathcal{U} \approx 3$ eV [113].

The Heisenberg model is suited to represent localized spins on a lattice. The Hamiltonian of the system is:

$$\hat{\mathbf{H}}_{\text{ex}} = -2 \sum_{i>j} \frac{\mathcal{J}_{ij}}{\hbar^2} \hat{\mathbf{S}}_i \cdot \hat{\mathbf{S}}_j, \quad (3.116)$$

where \mathcal{J}_{ij} is the exchange constant per atom. If it is positive and homogeneous, the material has a fully ferromagnetic ground state. The exchange constant is then related to the Weiss constant of the molecular field theory by $n_W = 2Z\mathcal{J} / \mu_0 n g^2 \mu_B^2$.

If some \mathcal{J}_{ij} are negative, the different couplings compete. The simplest configuration producing an AFM material is that of a bipartite lattice, where $\mathcal{J}_{ij} > 0$ between atoms belonging to the same sublattice and $\mathcal{J}_{ij} < 0$ between the sublattices. This is the case for FeBO_3 , whose atoms are distributed into two sublattices of antiparallel magnetizations. Since the magnetization originates entirely from the spin, we can express the macroscopic exchange energy density between magnetization sublattices as:

$$U_{\text{ex}} = n \hat{\mathbf{H}}_{\text{ex}} = -\frac{2Z\mathcal{J}}{ng^2\mu_B^2} \vec{\mathbf{M}}_1 \cdot \vec{\mathbf{M}}_2, \quad (3.117)$$

where $\vec{\mathbf{M}}_i = n \langle \hat{\boldsymbol{\mu}}_S \rangle$. For FeBO_3 , $Z = 6$ and the inter-sublattices exchange constant is $\mathcal{J} = -7.5$ meV [137].

Other exchange couplings

Neither in Fe nor FeBO_3 is the direct exchange responsible for the formation of the magnetic order. We will here summarize the main effects contributing to the sign of \mathcal{J} in these two materials.

Superexchange:

The superexchange interaction is the interaction of two localized spins mediated by a non-magnetic ion, and is at the origin of the AFM order of the sublattices of FeBO_3 .

As illustrated in Fig. 2.21, the Fe^{3+} ions are found in layers parallel to the basal plane, interspersed with layers of O^{2-} and B^{3+} . There is a small FM direct exchange between Fe^{3+} ions in the same plane. Along the c axis of the crystal, there is no direct overlap between the orbitals of adjacent Fe^{3+} ions. The Fe^{3+} 3d orbitals however overlap with the 2p orbitals of O^{2-} , which donates its electrons to form covalent bonds. If a Fe–O–Fe group of atoms is aligned along the z axis, the 3d orbitals of both cations overlap with the same $2p_z$ orbital of the central oxygen, each bounding with a different electron. When the 3d subshell is half-full, the Pauli exclusion principle ensures that the direct exchange occurring at the bonds is antiferromagnetic, and thus the superexchange is antiferromagnetic as well. Depending on the bond angle, there is either a strong AFM exchange or a weak FM exchange.

In FeBO_3 , the nearest-neighbor exchange with 120° bonds, which couples ions in adjacent planes, is AFM. The two sublattices thus correspond to the alternating Fe^{3+} layers. The inter-sublattices next nearest-neighbor exchange with 180° bonds and the intra-sublattice nearest-neighbor exchange are AFM as well, but are an order of magnitude weaker [138].

Double exchange:

The double exchange interaction is another exchange between localized spins, that occurs in conductors between magnetic ions having a different ionization state. The hopping of an electron to the ion carrying the hole is only possible if it satisfies Hund's rules. The resulting exchange is FM, with an amplitude dependent on the relative direction of the spin quantization axes of the ions.

In ferromagnetic iron, the e_g electrons are localized and interact by a combination of double exchange and superexchange. The resulting exchange constant is ferromagnetic, with $\mathcal{J}_{e_g e_g} = 8$ meV. They interact with the t_{2g} electrons as well, with $\mathcal{J}_{e_g t_{2g}} = 19$ meV [124].

RKKY interaction:

Since conduction electrons have a maximal wavevector determined by the Fermi surface of the material, they are not able to respond to point-like disturbances. This includes the atomic magnetic moments. The truncated magnetization response of a free electrons gas in momentum spaces creates diffraction-like oscillations of the magnetization in real space, which is known as the Ruderman-Kittel-Kasuya-Yosida (RKKY) interaction. The exchange is ferromagnetic at the center, and its sign oscillates with the distance with a period of π / k_F .

In Fe, such a phenomenon couples the delocalized t_{2g} electrons. This leads to a long-range exchange, which is AFM between nearest neighbors with $\mathcal{J}_{t_{2g}-t_{2g}} = -14$ meV. It opposes the ferromagnetic exchange of the e_g electrons, resulting in a total exchange constant of 13 meV [124], which makes iron a ferromagnet.

Dzyaloshinski–Moriya interaction:

Finally, the Dzyaloshinskii–Moriya (DM) interaction is an anisotropic component of the superexchange interaction, that arises when taking into account the spin-orbit coupling [139]. It is relevant in FeBO₃. We discussed a similar anisotropy of the Zeeman Hamiltonian in Section 3.2.3.3. The Heisenberg Hamiltonian is generalized by replacing the scalar exchange constant between atoms i and j by a tensor:

$$\hat{H}_{\text{ex}} = -\frac{2}{\hbar^2} \sum_{i>j} \hat{\mathbf{S}}_i \cdot \mathcal{J}_{ij} \cdot \hat{\mathbf{S}}_j. \quad (3.118)$$

It can be decomposed into a symmetric component \mathcal{F}_{ij} , from which we extract the isotropic part, and an antisymmetric component \mathcal{D}_{ij} :

$$\begin{aligned} \mathcal{J}_{ij} + \mathcal{F}_{ij} &= (\mathcal{J}_{ij} + \mathcal{J}_{ij}^{\top}) / 2 \\ \mathcal{D}_{ij} &= (\mathcal{J}_{ij} - \mathcal{J}_{ij}^{\top}) / 2. \end{aligned} \quad (3.119)$$

The latter represents the DM interaction. Its Hamiltonian is usually expressed in the form:

$$\hat{H}_{\text{DM}} = -\frac{2}{\hbar^2} \sum_{i>j} (\hat{\mathbf{S}}_i \cdot \mathcal{D}_{ij} \cdot \hat{\mathbf{S}}_j) = -\frac{2}{\hbar^2} \sum_{i>j} \vec{\mathcal{D}} \cdot (\hat{\mathbf{S}}_i \wedge \hat{\mathbf{S}}_j), \quad (3.120)$$

where the components of the DM vector $\vec{\mathcal{D}}$ are defined by:

$$\mathcal{D}_{ij} = \frac{1}{2} \begin{bmatrix} 0 & \mathcal{J}_{xy} - \mathcal{J}_{yx} & \mathcal{J}_{xz} - \mathcal{J}_{zx} \\ \mathcal{J}_{yx} - \mathcal{J}_{xy} & 0 & \mathcal{J}_{yz} - \mathcal{J}_{zy} \\ \mathcal{J}_{zx} - \mathcal{J}_{xz} & \mathcal{J}_{zy} - \mathcal{J}_{yz} & 0 \end{bmatrix} = \begin{bmatrix} 0 & \mathcal{D}_z & -\mathcal{D}_y \\ -\mathcal{D}_z & 0 & \mathcal{D}_x \\ \mathcal{D}_y & -\mathcal{D}_x & 0 \end{bmatrix}. \quad (3.121)$$

In FeBO₃, $\vec{\mathcal{D}}$ is normal to the basal plane, along the [001] axis, and $\mathcal{D} = 0.24$ meV [137]. The DM interaction is responsible for the canting of the sublattice magnetizations away from the pure antiferromagnetic alignment. This creates the weak net ferromagnetic moment that we studied in Section 2.3.2.

We have now finished our review of the quantum origins of the macroscopic phenomena that we discussed in Section 3.1: from the magnetic moment of an electron, to the collective behavior of atoms. We have seen some of the effects contributing to the susceptibility of paramagnetic and diamagnetic materials, and some of the forms of exchange interactions creating the ferromagnetic and antiferromagnetic order of spontaneously magnetized materials. To complete this chapter, we will now look into the manipulation of the magnetization, and use the models of the different phenomena that we have discussed in order to predict the equilibrium position and precession frequency of the magnetization in FeBO₃.

3.3 Manipulation of the magnetization

In a ferromagnetic material, or a canted antiferromagnet with a net magnetic moment such as FeBO_3 , the direction of magnetization is determined by the interplay between the anisotropy and the applied magnetic fields. We will first look at the main sources of anisotropy, and how they influence the hysteresis curve of a sample. Finally, we will discuss the time evolution of the magnetization, and derive the equations for its precession in FeBO_3 that we used in [Section 2.3.2.1](#).

3.3.1 Shape anisotropy

The anisotropy of a material refers to the strength of the magnetic field necessary in order to magnetize it in a given direction. We have discussed in [Section 3.2.3.4](#) the intrinsic magnetocrystalline anisotropy, which depends on the crystalline structure of the material. The shape anisotropy is the other main contribution, and depends on the shape of a specific sample. While at atomic scales the orientation of the magnetic moments is dominated by the exchange interactions, at large distances the magnetostatic interactions take over. This results in the formation of domains, which have a local magnetic order but result in no net magnetization at the macroscopic scale.

As introduced in [Section 3.1.3](#), a uniformly magnetized body generates a demagnetizing field $\vec{H}_d = -\mathbf{N}_d \cdot \vec{M}$. Its magnetostatic self-energy is [[96](#), chapter 3]:

$$U_{\text{ms}} = -\frac{\mu_0}{2} \vec{M} \cdot \vec{H}_d. \quad (3.122)$$

If the sample is an ellipsoid with axial symmetry along z , \mathbf{N}_d is zero except for the components $N_{xx} = N_{yy} = N_{\perp}$ and $N_{zz} = N_{\parallel}$, where $N_{xx} + N_{yy} + N_{zz} = 1$. The magnetostatic energy simplifies to:

$$U_{\text{ms}} = \frac{\mu_0 M^2}{2} (N_{\parallel} + (N_{\perp} - N_{\parallel}) \sin^2 \theta), \quad (3.123)$$

which corresponds to a uniaxial anisotropy, as defined in [Section 3.2.3.4](#). The anisotropy constant K_{sa} is given by the energy difference between the hard and easy directions, $\theta = 0$ and $\pi / 2$. We obtain:

$$K_{\text{sa}} = U_{\text{ms}}(\pi / 2) - U_{\text{ms}}(0) = \frac{\mu_0 M^2}{2} (1 - 3N_{\parallel}). \quad (3.124)$$

If $N_{\parallel} < 1 / 3$, which is the case when the longest axis of the ellipsoid is along z , K_{sa} is positive and z is the easy direction.

The behavior of thin films is of particular interest, as it describes the FeBO_3 samples and the spintronic THz emitters of [Chapter 4](#). For an ideal thin film in the xy plane, approximated as an infinite flattened ellipsoid, $N_{\perp} = 0$ and $N_{\parallel} = 1$, giving $K_{\text{sa}} = -\mu_0 M^2 / 2 < 0$. The same anisotropy tends to align the magnetization in the plane of the sample. However, it competes with the other sources of anisotropy. The effective

anisotropy constant can be separated into a surface and a volume contribution [140]:

$$K_{\text{eff}} = K_v + \frac{2K_s}{d}, \quad (3.125)$$

where d is the thickness of the sample. The volume anisotropy K_v include the magnetocrystalline and shape anisotropies, as well as the magneto-elastic anisotropy caused by the strain due to lattice mismatch when the film is deposited on a substrate. We assume that the magnetocrystalline anisotropy axis is normal to the film. The surface anisotropy K_s includes Néel's interface anisotropy, which results from the symmetry breaking at the interfaces, as well as surface strain. Under the critical thickness $d_{\perp} = -2K_s / K_v$, the surface anisotropy dominates and it is possible to find $K_{\text{eff}} > 0$, leading to the equilibrium magnetization being tilted out of the plane of very thin samples.

The saturation magnetization for polycrystalline Fe is $\mu_0 M_s = 2.14$ T. We then find $K_{\text{sa}} = -1.86 \times 10^6 \text{ J m}^{-3}$ [140], two orders of magnitude larger than its magnetocrystalline anisotropy constant K_1 given in Section 3.2.3.4. The volume anisotropy is thus dominated by the shape anisotropy. The order of magnitude of the Néel contribution to the surface anisotropy is $K_s = 10^{-3} \text{ J m}^{-3}$ [141], which gives a typical critical thickness for iron of $d_{\perp} = 1.5$ nm. The exact value of K_s depends on the materials on each side of the interface and their orientation. For Fe|W and Fe|Pt interfaces such as the ones found in the samples that will be discussed in Chapter 4, $K_s < 0$ [140, table 3] and the surface anisotropy contributes to confining the magnetization in the plane. To model these samples and the $35 \mu\text{m}$ -thick FeBO_3 sample, we thus use $K_{\text{eff}} \approx K_1 + K_{\text{sa}}$.

3.3.2 Stoner-Wohlfarth model of the hysteresis

The anisotropy energy of a sample is used to calculate its hysteresis curve. We assume that the sample is formed of a single ferromagnetic domain, so that its magnetization is always saturated. When an external magnetic field is applied on the sample, the additional Zeeman energy density is:

$$U_Z = -\vec{M} \cdot \vec{B}_{\text{app}} = -\mu_0 M_s H_{\text{app}} \cos(\theta_H - \theta), \quad (3.126)$$

where θ and θ_H are the polar angles of the magnetization and the external field respectively, and we assume that both \vec{M} and \vec{H}_{app} are contained in the xz plane. The total energy density includes the anisotropy and Zeeman contributions:

$$U = U_a + U_Z = K_{\text{eff}} \sin^2 \theta - \mu_0 M_s H_{\text{app}} \cos(\theta_H - \theta). \quad (3.127)$$

The hysteresis curve of the material can be calculated using Eq. (3.127), by finding the orientation of the magnetization minimizing the energy. This behavior originates in its tendency to stay trapped in local energy minima until the external field reaches a threshold amplitude.

Fig. 3.14a shows the dependence of the energy on the direction of magnetization, for several orientations and magnitudes of the external field. The easy axis is defined so that

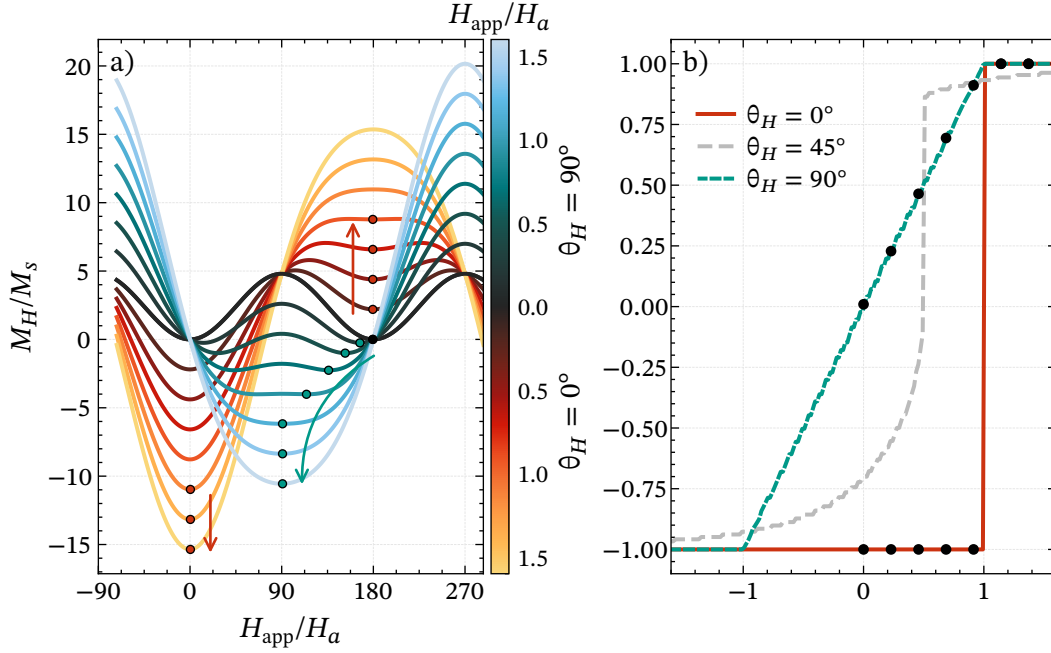


Figure 3.14: a) Energy density of a single-domain ferromagnet with positive uniaxial anisotropy, for different amplitudes and orientations of the external field \vec{H}_{app} : along the easy axis ($\theta_H = 0^\circ$, red lines) and within the hard plane ($\theta_H = 90^\circ$, blue lines). Markers indicate the local energy minimum when the field is increased, with $\theta = 180^\circ$ initially. We use $\mu_0 M_s = 2.14$ T and $K_{eff} = 4.8 \times 10^4$ J m $^{-3}$. b) Corresponding hysteresis curves, with the magnetization projected along the direction of \vec{H}_{app} .

in the absence of external field, the energy is minimized when $\theta = 0^\circ$ or 180° . Let us assume that the initial orientation of the magnetization is 180° . When an external field is applied with $\theta_H = 0^\circ$, the energy of the $\theta = 180^\circ$ magnetization increases. However, the magnetization is trapped in a local energy minimum until H_{app} becomes larger than the anisotropy field:

$$H_a = \frac{2K_{eff}}{\mu_0 M_s}. \quad (3.128)$$

When it reaches this value, the Zeeman effect overcomes the anisotropy and the orientation of the magnetization switches suddenly. When instead the external field is applied along the hard direction $\theta_H = 90^\circ$, the location of the energy minimum shifts smoothly. The magnetization rotates progressively until $H_{app} > H_a$, at which points the energy is minimum for $\theta = \theta_H$.

We can recognize in Fig. 3.14b the hysteresis curves for ferromagnetic materials that we saw in Section 3.1.4. The hard or soft nature of a ferromagnet, and thus the value of their intrinsic coercivity H_c , depends on whether the field is applied along an easy or

hard axis, respectively. The coercivity is the field necessary to reverse the direction of the magnetization. It decreases nonlinearly from $H_c = H_a$ at $\theta_H = 0^\circ$ to $H_c = 0$ at 90° , with $H_c = H_a / 2$ at 45° .

3.3.3 Dynamics of the magnetization

Our last subject is the dynamics of the magnetization subjected to a magnetic field. We have assumed in the previous section that the magnetization switches direction by instantaneously realigning on the applied field, staying saturated at all times. In real samples, the material is usually divided into domains, that each have a direction of magnetization minimizing the local energy. When the applied field is small, it is able to move the domain walls, progressively increasing the size of the domains whose magnetization has the correct alignment. In strong fields, the Zeeman effect dominates over the anisotropy and the magnetization of the domains rotates. This last effect is the one resulting in the precession we measured in FeBO_3 .

3.3.3.1 Landau-Lifshitz-Gilbert equation

The equation of motion of the magnetization vector is described by the Landau-Lifshitz-Gilbert (LLG) equation:

$$\frac{d\vec{M}}{dt} = -\mu_0\gamma|\vec{M} \wedge \vec{H}_{\text{eff}} + \frac{\alpha}{|\vec{M}|} \left(\vec{M} \wedge \frac{d\vec{M}}{dt} \right), \quad (3.129)$$

where γ is the gyromagnetic ratio of the material and α the Gilbert damping parameter. The latter being a constant implies that the magnetization amplitude is constant. The effective magnetic field \vec{H}_{eff} is introduced to include the effect of anisotropy, exchange, etc., on the orientation of the magnetization.

At equilibrium, $\vec{M} \wedge \vec{H}_{\text{eff}} = 0$ and the magnetization is parallel to the effective field. When the field changes, for example by the application of an external field, the first term of Eq. (3.129) describes the right-handed precession of \vec{M} around the new orientation of \vec{H}_{eff} . The second term expresses the progressive dissipation of the excitation, until the magnetization reaches the equilibrium again.

When a material is composed of several sublattices, the magnetization of each of them follows Eq. (3.129). Since they are linked by the exchange interaction, their precessions can only take a limited number of relative phase, shape, orientation, etc. FeBO_3 has two such modes, whose frequencies we will calculate in Section 3.3.3.3.

The same exchange phenomenon is also responsible for the propagation of spin waves. Neglecting the damping part, Eq. (3.129) is linear and thus applies to the magnetization as well as to the underlying magnetic moments. When a localized excitation triggers the precession of a magnetic moment, the exchange interaction spreads the precession to its neighbors. Thus a spin wave travels with its wavelength corresponding to the distance

between two moments with the same phase of precession, and its amplitude to the radius of the cone traced by \vec{M} .

3.3.3.2 Steady state of FeBO₃

FeBO₃ has two sublattices, with the magnetizations \vec{M}_1 and \vec{M}_2 of equal magnitude M_0 , neglecting the effect of temperature. As a canted antiferromagnet, its magnetic state is characterized by the ferromagnetic vector $\vec{M} = \vec{M}_1 + \vec{M}_2$ and the antiferromagnetic vector $\vec{L} = \vec{M}_1 - \vec{M}_2$. Since an applied field of $H_{\text{app}} > 1.59 \text{ kA m}^{-1}$ (2 mT) is sufficient to remove the magnetic domain structure of the crystal [82], we assume that the crystal is homogeneously magnetized and the magnitude of the net magnetization vector \vec{M} is the saturation magnetization M_s . We define the coordinate system so that the out-of-plane axis c is along z and one of the easy axes in the basal plane is along x . The external magnetic field is applied in-plane along the y axis. The energy density is:

$$U = U_{\text{ex}} + U_{\text{DM}} + U_{\text{mca}} + U_{\text{sa}} + U_Z, \quad (3.130)$$

where the isotropic exchange energy U_{ex} is given by Eq. (3.117), the anisotropic exchange U_{DM} by Eq. (3.120), the magnetocrystalline anisotropy U_{mca} by Eq. (3.76), the shape anisotropy U_{sa} by Eq. (3.124), and the Zeeman energy U_Z by Eq. (3.126). Each of these effects can be expressed as an effective magnetic field by taking its gradient with respect to each magnetization: $\vec{H}_{\text{eff}_i} = -\vec{\nabla}_{\vec{M}_i} U / \mu_0$. After this, the energy acting on the magnetization of each sublattice can be represented by the single Zeeman-like component $U_i = -\mu_0 \vec{M}_i \cdot \vec{H}_{\text{eff}_i}$.

The isotropic exchange and the DM interaction energies are:

$$U_{\text{ex}} + U_{\text{DM}} = -\frac{2Z}{\mu_B^2 g_j^2 n} \left(j \vec{M}_1 \cdot \vec{M}_2 + \vec{\mathcal{D}} \cdot (\vec{M}_1 \wedge \vec{M}_2) \right), \quad (3.131)$$

from which we get the effective magnetic fields on the magnetization \vec{M}_i :

$$\vec{H}_{\text{ex}_i} = H_{\text{ex}} \frac{\vec{M}_j}{M_0} \quad \text{with} \quad H_{\text{ex}} = \frac{2ZjM_0}{\mu_0 \mu_B^2 g_j^2 n} \quad (3.132)$$

$$\vec{H}_{\text{DM}_i} = \pm H_{\text{DM}} \frac{\vec{M}_j}{M_0} \wedge \vec{e}_z \quad H_{\text{DM}} = \frac{2Z\mathcal{D}_z M_0}{\mu_0 \mu_B^2 g_j^2 n}. \quad (3.133)$$

Using these, we can express the energy as:

$$\begin{aligned} U_{\text{ex}} + U_{\text{DM}} &= -\mu_0 \vec{M}_1 \cdot (\vec{H}_{\text{ex}_1} + \vec{H}_{\text{DM}_1}) = -\mu_0 \vec{M}_2 \cdot (\vec{H}_{\text{ex}_2} - \vec{H}_{\text{DM}_2}) \\ &= -\mu_0 H_{\text{ex}} M_0 (\sin \theta_1 \sin \theta_2 \cos(\phi_1 - \phi_2) + \cos \theta_1 \cos \theta_2) \\ &\quad + \mu_0 H_{\text{DM}} M_0 \sin \theta_1 \sin \theta_2 \sin(\phi_1 - \phi_2), \end{aligned} \quad (3.134)$$

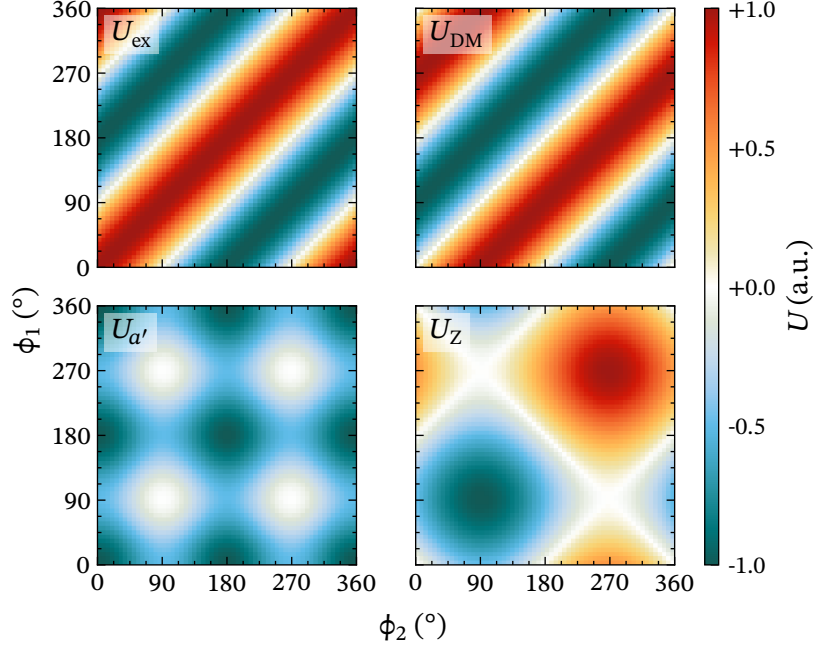


Figure 3.15: Normalized exchange (U_{ex}), Dzyaloshinskii–Moriya (U_{DM}), in-plane anisotropy ($U_{a'}$) and Zeeman U_Z energy densities in FeBO_3 depending on the azimuthal angle of the sublattice magnetizations. The easy axis is x ($\phi_i = 0$ or 180°) and the external magnetic field is applied along the y axis ($\phi_H = 90^\circ$).

where θ_i and ϕ_i are respectively the polar and azimuthal angles of $\vec{\mathbf{M}}_i$. The DM vector $\vec{\mathcal{D}}$ is directed along the c axis [137]. Since $\vec{\mathbf{M}}_1 \wedge \vec{\mathbf{M}}_2 = -\vec{\mathbf{M}}_2 \wedge \vec{\mathbf{M}}_1$, the sign of $\vec{\mathcal{D}}$ defines the relative orientation of the two sublattices. With $\mathcal{D}_z < 0$ [142] and thus $H_{\text{DM}} < 0$, the energy U_{DM} is minimized for $0 < \phi_1 - \phi_2 < \pi$. As shown in Fig. 3.15, U_{ex} and U_{DM} are respectively minimized when $\phi_1 - \phi_2 = \pm 180^\circ$ and $+90^\circ$, irrespective of the absolute orientation of the magnetizations in the basal plane.

Then, we separate the magnetocrystalline and shape anisotropy into the large out-of-plane component and a smaller in-plane component. We further approximate the latter, which is normally six-fold and proportional to $\cos^2 3\phi_i$ [143], as a two-fold component in $\cos^2 \phi_i$. For this reason, we chose the coordinate system so that $\phi_i \approx 0$ or 180° . We thus obtain:

$$\begin{aligned} U_{\text{mca},i} + U_{\text{sa},i} &= -(K_1 + K_{\text{sa}}) \frac{M_{iz}^2}{M_0^2} - K_{\parallel} \frac{M_{ix}^2}{M_0^2} \\ &= -(K_1 + K_{\text{sa}}) \cos^2 \theta_i - K_{\parallel} \sin^2 \theta_i \cos^2 \phi_i, \end{aligned} \quad (3.135)$$

with $K_1 < 0$, $K_{\text{sa}} < 0$ and $K_{\parallel} > 0$. The amplitude of the in-plane $\vec{\mathbf{H}}_a$ and out-of-plane $\vec{\mathbf{H}}_{a'}$,

Table 3.2: Effective magnetic fields characterizing FeBO₃ at room temperature. Values taken from Schober [83], Kurtzig et al. [91], and Tarakanov et al. [93].

	kA m ⁻¹	mT
H_{ex}	-206.9×10^3	-260×10^3
H_{DM}	-4.9×10^3	-6.16×10^3
H_a	-135	-170
$H_{a'}$	21×10^{-3}	26.4×10^{-3}
H_{me}	55×10^{-3}	70.0×10^{-3}
M_0	303	381
M_s	9.15	11.5

effective fields on the magnetization \vec{M}_i are the same as in Eq. (3.128):

$$\vec{H}_{a_i} = H_a \frac{M_{iz}}{M_0} \vec{e}_z \quad \text{with} \quad H_a = \frac{2(K_1 + K_{\text{sa}})}{\mu_0 M_0} \quad (3.136)$$

$$\vec{H}_{a'_i} = H_{a',i} \frac{M_{ix}}{M_0} \vec{e}_x \quad H_{a',i} = \frac{2K_{\parallel}}{\mu_0 M_0}. \quad (3.137)$$

As shown in Fig. 3.15, the energy density $U_{a'}$ for the in-plane anisotropy is minimized when ϕ_1 and ϕ_2 are multiples of π , which means that both magnetizations are aligned along the x axis.

Finally, including the Zeeman term due to the external field, the total magnetic energy of the FeBO₃ sample is [83]:

$$\begin{aligned} U = & -\mu_0 \left(\frac{H_{\text{ex}}}{M_0} (\vec{M}_1 \cdot \vec{M}_2) + \frac{H_{\text{DM}}}{M_0} \vec{e}_z \cdot (\vec{M}_1 \wedge \vec{M}_2) \right. \\ & + \frac{H_a}{2M_0} (M_{1z}^2 + M_{2z}^2) + \frac{H_{a'}}{2M_0} (M_{1x}^2 + M_{2x}^2) \\ & \left. + (\vec{M}_1 + \vec{M}_2) \cdot \vec{H}_{\text{app}} \right). \end{aligned} \quad (3.138)$$

The amplitudes of the effective fields are given by Table 3.2. To preserve the generality of Eq. (3.138) independently of the sign of the exchange and anisotropy constants, we allow the amplitudes to take a negative sign.

The effective field $\vec{H}_{\text{eff}_i} = \vec{H}_{\text{app}} + \vec{H}_{\text{ex}_i} + \vec{H}_{\text{DM}_i} + \vec{H}_{a_i} + \vec{H}_{a'_i}$ acts on each sublattice via Eq. (3.129). To obtain the equilibrium angle of the magnetization vectors, we can solve the LLG equation, assuming that the magnetization is at rest: $\vec{M}_i \wedge \vec{H}_{\text{eff}_i} = 0$.

Alternatively, we can solve $dU/d\phi_i = 0$. Both equations simplify to the same expression, which is easy to solve analytically when the external field is applied along the x or y axis, as this preserves the symmetry of the magnetization vectors with respect to the easy axis (see Hagedorn and Gyorgy [144] for a treatment with an arbitrary field direction).

For this reason, we assume that the external field is applied along the y axis. If its amplitude is small enough to preserve the quasi-AFM configuration of the two sublattices, this allows their magnetization vectors to remain near the easy axis, while the net magnetization \vec{M} aligns on \vec{H}_{app} . We set $\phi_1 = \pi - \alpha$ and $\phi_2 = \alpha$, where α is the canting angle. Because of the large value of H_a and because we apply the external field in the plane, we also assume that the magnetization is confined in the plane of the sample, leading to $\theta_1 = \theta_2 = \theta_H = \pi / 2$. We thus have:

$$\begin{aligned} \frac{dU}{d\phi_i} &= \pm M_0 \mu_0 \left(\left(\frac{H_{a'}}{2} - H_{\text{ex}} \right) \sin 2\alpha + H_{\text{DM}} \cos 2\alpha - H_{\text{app}} \cos \alpha \right) \\ &\approx \pm M_0 \mu_0 \left((H_{a'} - 2H_{\text{ex}}) \alpha + H_{\text{DM}} - H_{\text{app}} \right) = 0, \end{aligned} \quad (3.139)$$

where we assume that the canting angle is small and the magnetic order stays close to antiferromagnetic. Solving the equation gives:

$$\alpha = \frac{H_{\text{app}} - H_{\text{DM}}}{H_{a'} - 2H_{\text{ex}}}. \quad (3.140)$$

Inserting this result into Eq. (3.138), we find that $d^2U/d(\phi_i)^2 > 0$ for both sublattices, and this corresponds indeed to an energy minimum.

In the absence of external field, $\alpha = 0.68^\circ$. With H_{app} up to 400 mT as we used in Section 2.3.2, the canting increases to 0.72° . We can estimate that the net magnetization $M_S \approx 2M_0 \sin \alpha$ should be found in the range of 7.2 kA m^{-1} to 7.6 kA m^{-1} , which is comparable to the experimental value presented in Table 3.2.

In our experiments, we do not know the angle of the easy axis of the FeBO_3 crystals. However, $H_{a'}$ is very small compared to H_{app} and can be neglected. Then, we find the same expression for α as given by Schober [83] and Gurevich and Melkov [145, chapter 3].

3.3.3.3 Ferromagnetic resonance

Finally, we derive the equations for the frequency of the uniform magnetization precession modes in FeBO_3 , which are the spin wave modes with a wavevector $k = 0$. Since the spin is a quantized quantity, so are spin waves. The associated quasi-particles are magnons, that correspond to the delocalized flip of the spin of a single electron. They thus carry an angular momentum $\pm \hbar$ and an energy $\hbar\omega$, where ω is the angular frequency of the precession of the magnetic moments. Their energy, and thus their frequency, can be separated into several contributions [94, 138]:

$$\omega^2 = \omega_H^2 + \omega_k^2 + \omega_\Delta^2. \quad (3.141)$$

The angular frequency ω_H comes from the energy due to the presence of an external magnetic field, while ω_k comes from the exchange energy between neighboring atoms during the propagation of the spin wave and is thus proportional to the wavevector k . Since we only consider the uniform precession modes, this contribution disappears. Finally, ω_Δ is the gap energy that provides a finite magnon energy at $H_{\text{app}} = 0$ and $k = 0$, and can originate from in-plane anisotropy, magneto-elastic coupling, or the hyperfine interaction with the spin of the nuclei [94].

As before, we assume that the FeBO_3 sample is a thin planar crystal with the hard axis out of plane and parallel to the z axis, and that the external magnetic field is applied along the y axis. In this geometry, the equations for the frequency of the quasi-ferromagnetic resonance (qFMR) and quasi-antiferromagnetic resonance (qAFMR) modes that we found in the literature are:

$$\left(\frac{\omega_{\text{qFMR}}}{\mu_0|\gamma|}\right)^2 \approx \begin{cases} H_{\text{app}}(H_{\text{app}} + H_{\text{DM}}) & = 22.2 \text{ GHz} \quad [145, 146] \quad (3.142a) \\ H_{\text{app}}(H_{\text{app}} + H_{\text{DM}}) + 2H_{\text{ex}}H_{a'} & = 22.4 \text{ GHz} \quad [83, 86] \quad (3.142b) \\ H_{\text{app}}(H_{\text{app}} + H_{\text{DM}}) + 2H_{\text{ex}}H_{\text{me}} & = 22.8 \text{ GHz} \quad [93] \quad (3.142c) \\ H_{\text{app}}(H_{\text{app}} + H_{\text{DM}}) + H_{\Delta_1}^2 & \quad [94, 147] \quad (3.142d) \\ H_{\text{app}}(H_{\text{app}} + M_S + H_a) & = 3.0 \text{ GHz} \quad [29] \quad (3.142e) \\ (H_{\text{app}} + H_{a'})(H_{\text{app}} + H_{a'} + M_S + H_a) & = 4.7 \text{ GHz}, \quad [148] \quad (3.142f) \end{cases}$$

$$\left(\frac{\omega_{\text{qAFMR}}}{\mu_0|\gamma|}\right)^2 \approx \begin{cases} H_{\text{DM}}(H_{\text{app}} + H_{\text{DM}}) + 2H_{\text{ex}}H_a & = 316 \text{ GHz} \quad [83, 86] \quad (3.143a) \\ H_{\text{DM}}(H_{\text{app}} + H_{\text{DM}}) + 2H_{\text{ex}}H_a + H_{\Delta_2}^2 & \quad [147] \quad (3.143b) \\ H_{\text{app}}H_{\text{DM}} + 2H_{\text{ex}}H_a & = 264 \text{ GHz}, \quad [146] \quad (3.143c) \end{cases}$$

where the numerical values are calculated using Table 3.2 and assuming $\mu_0 H_{\text{app}} = 100$ mT. Most sources agree that $\omega_H = \mu_0|\gamma|\sqrt{H_{\text{app}}(H_{\text{app}} + H_{\text{DM}})} = 22.2$ GHz for the qFMR frequency. Schober [83] names $H_{\Delta_1}^2 = 2H_{\text{ex}}H_{a'}$ as the isotropic energy gap, while Jantz and Wettling [94] and Velikov et al. [147] attribute the gap to magneto-elastic coupling. The measured value of $\omega_{\Delta_1} = 3$ GHz [94, 138] agrees better with Eq. (3.142b), where $\omega_{\Delta_1} = 3.3$ GHz, than with Eq. (3.142c), where $\omega_{\Delta_1} = 5.3$ GHz. The impact on the qFMR frequency is however minimal. Expressions of the qAFMR frequency are rarer and do not converge to the same numerical value.

Eq. (3.142f) and presumably Eq. (3.142e) model FeBO_3 as a ferromagnet. Although the LLG equation applies to the net magnetic moment as well as the two sublattice magnetizations, so that all three vectors precess at the same frequency, the removal of H_{ex} and H_{DM} has a major influence on the energy of the material and thus on the precession frequency. To understand the difference between the different models, and

which order of magnitude we should expect for the qAFMR frequency, we now calculate the precession frequencies.

As we have seen in Section 3.3.3.2, both magnetization vectors at equilibrium are in the xy plane and canted away from the x axis by an angle α given by Eq. (3.140). We follow the method of Herrmann [149] to find their precession frequency. We will solve the LLG equation for each sublattice, neglecting the damping:

$$\frac{d\vec{M}_i}{dt} = -\mu_0|\gamma|\vec{M}_i \wedge \vec{H}_{\text{eff}i}. \quad (3.144)$$

To simplify the computation, we express the equation in the coordinate system attached to each magnetization at rest. We obtain each transformed vector \vec{M}'_i by rotating \vec{M}_i by an angle of $-\phi_i$, so that at equilibrium:

$$\begin{bmatrix} M'_{ix} \\ M'_{iy} \\ M'_{iz} \end{bmatrix} = \begin{bmatrix} \cos \phi_i & \sin \phi_i & 0 \\ -\sin \phi_i & \cos \phi_i & 0 \\ 0 & 0 & 1 \end{bmatrix} \begin{bmatrix} M_{ix} \\ M_{iy} \\ M_{iz} \end{bmatrix} = \begin{bmatrix} M_0 \\ 0 \\ 0 \end{bmatrix}. \quad (3.145)$$

We also express the effective fields $\vec{H}'_{\text{eff}i}$ in the coordinate system of the corresponding magnetization. For example, $\vec{H}_{\text{ex}1}$, which is given by Eq. (3.132), becomes $\vec{H}'_{\text{ex}1} = H_{\text{ex}}[-\cos 2\alpha, -\sin 2\alpha, 0]$.

In addition to the DC external field, we use a short THz pulse to perturb the magnetization and trigger spin oscillations. This can be modeled by separating the fields and magnetizations into a steady-state and a small dynamic component:

$$\begin{aligned} \vec{H}_{\text{app}}(t) &= \vec{H}_{\text{DC}} + \vec{h}_{\text{THz}}(t) \\ \vec{H}_{\text{eff}i}(t) &= \vec{H}_{\text{eff}i}^0 + \vec{h}_{\text{eff}i}(t) \\ \vec{M}_i(t) &= \vec{M}_i^0 + \vec{m}_i(t). \end{aligned} \quad (3.146)$$

Since the amplitude of the precession is small, we assume that the x' component of each magnetization is constant, so that:

$$\vec{M}'_i(t) = \begin{bmatrix} M_0 \\ 0 \\ 0 \end{bmatrix} + \begin{bmatrix} 0 \\ m'_{iy} \\ m'_{iz} \end{bmatrix}, \quad (3.147)$$

and assuming that the THz excitation has passed ($\vec{h}_{\text{THz}} = 0$):

$$\vec{H}'_{\text{eff}_i}(t) = \begin{bmatrix} H_{a'} - H_{\text{ex}} + \alpha(H_{\text{DC}} - 2H_{\text{DM}}) \\ \mp H_{\text{DC}} \pm H_{\text{DM}} \pm \alpha(H_{a'} - 2H_{\text{ex}}) \\ 0 \end{bmatrix} \quad (3.148)$$

$$+ \frac{1}{M_0} \begin{bmatrix} \mp H_{\text{DM}} m'_{jy} \pm \alpha(H_{a'} m'_{iy} + 2H_{\text{ex}} m'_{jy}) \\ -2\alpha H_{\text{DM}} m'_{jy} - H_{\text{ex}} m'_{jy} \\ H_a m'_{iz} + H_{\text{ex}} m'_{jz} \end{bmatrix}.$$

Eq. (3.144) becomes:

$$\frac{d\vec{M}_i^0}{dt} + \frac{d\vec{m}_i}{dt} = -\mu_0|\gamma| (\vec{M}_i^0 \wedge \vec{H}_{\text{eff}_i}^0 + \vec{m}_i \wedge \vec{H}_{0\text{eff}_i} + \vec{M}_i^0 \wedge \vec{h}_{\text{eff}_i} + \vec{m}_i \wedge \vec{h}_{\text{eff}_i}). \quad (3.149)$$

The first right-hand term disappears by definition, and we neglect the last term since both \vec{m}_i and \vec{h}_{eff_i} are small. Without loss of generality, we replace the dynamic components by their complex amplitudes \vec{m}_i and \vec{h}_{eff_i} , which are defined by:

$$\vec{h}_{\text{eff}}(t) = \frac{1}{2} (\vec{h}_{\text{eff}} e^{i\omega t} + \vec{h}_{\text{eff}}^* e^{-i\omega t}) \quad (3.150)$$

$$\vec{m}(t) = \frac{1}{2} (\vec{m} e^{i\omega t} + \vec{m}^* e^{-i\omega t}).$$

This leaves us with an equation linear in \vec{m}_i :

$$\frac{d\vec{m}_i e^{i\omega t}}{dt} = -\mu_0|\gamma| (\vec{m}_i e^{i\omega t} \wedge \vec{H}_{\text{eff}_i}^0 + \vec{M}_i^0 \wedge \vec{h}_{\text{eff}_i} e^{i\omega t}) \quad (3.151)$$

$$i\omega \vec{m}_i = -\mu_0|\gamma| (\vec{m}_i \wedge \vec{H}_{\text{eff}_i}^0 + \vec{M}_i^0 \wedge \vec{h}_{\text{eff}_i}).$$

Since we neglect the x' components, we arrive at two systems of two coupled equations:

$$\frac{i\omega m'_{1y}}{\mu_0|\gamma|} = H_a m'_{1z} + H_{\text{ex}} m'_{2z} - m'_{1z} (H_{a'} + H_{\text{app}}\alpha - 2H_{\text{DM}}\alpha - H_{\text{ex}}) \quad (3.152a)$$

$$\frac{i\omega m'_{2y}}{\mu_0|\gamma|} = H_a m'_{2z} + H_{\text{ex}} m'_{1z} - m'_{2z} (H_{a'} + H_{\text{app}}\alpha - 2H_{\text{DM}}\alpha - H_{\text{ex}}) \quad (3.152b)$$

$$\frac{i\omega m'_{1z}}{\mu_0|\gamma|} = 2H_{\text{DM}}\alpha m'_{2y} + H_{\text{ex}} m'_{2y} + m'_{1y} (H_{a'} + H_{\text{app}}\alpha - 2H_{\text{DM}}\alpha - H_{\text{ex}}) \quad (3.152c)$$

$$\frac{i\omega m'_{2z}}{\mu_0|\gamma|} = 2H_{\text{DM}}\alpha m'_{1y} + H_{\text{ex}} m'_{1y} + m'_{2y} (H_{a'} + H_{\text{app}}\alpha - 2H_{\text{DM}}\alpha - H_{\text{ex}}) \quad (3.152d)$$

We transform the system into a matrix equation of the form:

$$\frac{i\omega}{\mu_0|\gamma|} \begin{bmatrix} m'_{1y} \\ m'_{2y} \\ m'_{1z} \\ m'_{2z} \end{bmatrix} = \begin{bmatrix} 0 & 0 & a & b \\ 0 & 0 & b & a \\ c & d & 0 & 0 \\ d & c & 0 & 0 \end{bmatrix} \begin{bmatrix} m'_{1y} \\ m'_{2y} \\ m'_{1z} \\ m'_{2z} \end{bmatrix}. \quad (3.153)$$

The possible values of the precession frequency ω are given by the four eigenvalues of the matrix, two of which will be positive:

$$\frac{i\omega}{\mu_0|\gamma|} = \begin{cases} \pm \sqrt{(a+b)(c+d)} \\ \pm \sqrt{(a-b)(c-d)}, \end{cases} \quad (3.154)$$

where:

$$\begin{aligned} a - b &= H_a - H_{a'} - \frac{(H_{\text{DC}} - 2H_{\text{DM}})(H_{\text{DC}} - H_{\text{DM}})}{H_{a'} - 2H_{\text{ex}}}, \\ a + b &= H_a - H_{a'} + 2H_{\text{ex}} - \frac{(H_{\text{DC}} - 2H_{\text{DM}})(H_{\text{DC}} - H_{\text{DM}})}{H_{a'} - 2H_{\text{ex}}}, \\ c - d &= H_{a'} - 2H_{\text{ex}} + \frac{-H_{\text{DC}}H_{\text{DM}} + (H_{\text{DC}} - 2H_{\text{DM}})^2}{H_{a'} - 2H_{\text{ex}}}, \\ c + d &= \frac{H_{a'}^2 - 2H_{a'}H_{\text{ex}} + H_{\text{DC}}^2 - H_{\text{DC}}H_{\text{DM}}}{H_{a'} - 2H_{\text{ex}}}. \end{aligned} \quad (3.155)$$

After numerical evaluation, we obtain the frequency of the two precession modes of FeBO_3 . For $H_{\text{DC}} = 100$ mT:

$$\begin{aligned} \omega_{\text{qFMR}} &= -i\mu_0|\gamma|\sqrt{(a+b)(c+d)} = 22.4 \text{ GHz} \\ \omega_{\text{qAFMR}} &= -i\mu_0|\gamma|\sqrt{(a-b)(c-d)} = 362 \text{ GHz}. \end{aligned} \quad (3.156)$$

As shown in Fig. 3.16, our equation exactly matches the approximation of Schober [83] in Eq. (3.142b) for the qFMR frequency, with however a 46 GHz difference for the qAFMR frequency in Eq. (3.143a).

The eigenvector of Eq. (3.153) associated with each frequency gives us the relative amplitude of the components of \vec{m}'_1 and \vec{m}'_2 , which are plotted in Figs. 3.16c and 3.16d. In the qFMR mode, the sublattice magnetizations precess in phase while preserving the angle between them. The precession is mainly in the plane of the sample, with an ellipticity ratio $|m'_y / m'_z| = 650$ at $H_{\text{DC}} = 100$ mT.

Setting $H_{\text{DM}} = 0$, so that the material becomes a pure antiferromagnet ($\alpha \approx 0^\circ$) and the two magnetization vectors precess as one, significantly reduces the energy as it removes the conflict between the isotropic and anisotropic exchange. When this is the case, the frequency converges towards the result of Eq. (3.142e), where only the precession of

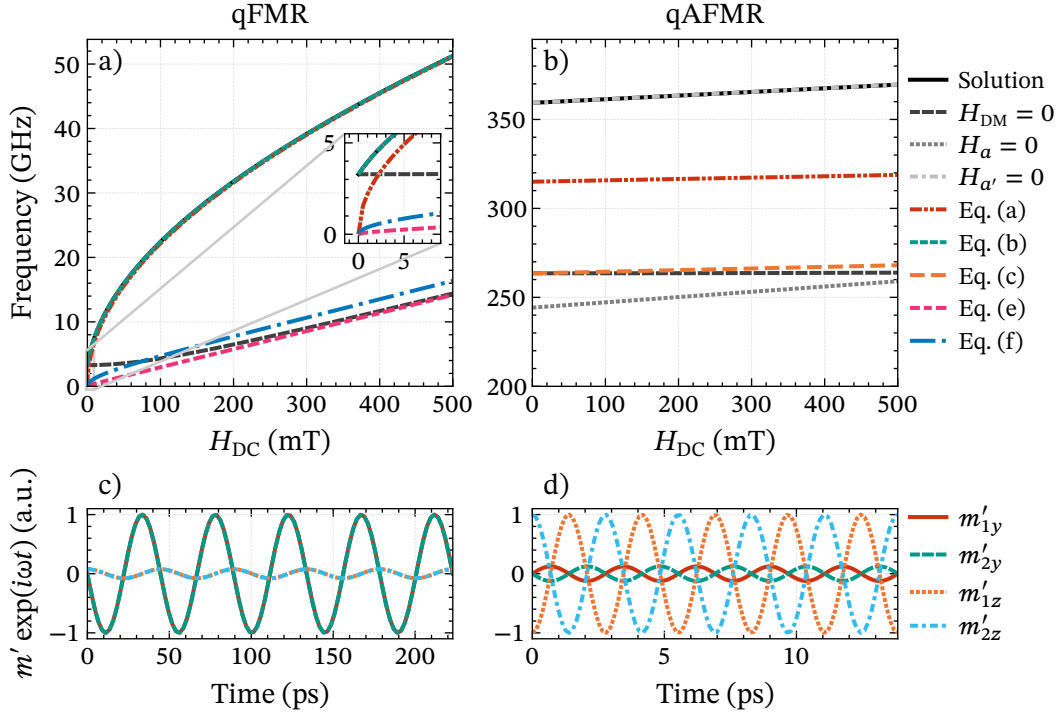


Figure 3.16: Comparison of the a) qFMR and b) qAFMR frequencies obtained with Eq. (3.156) and with the different models found in the literature. The legend refers to the formulas in a) Eq. (3.142) and b) Eq. (3.143). c) qFMR and d) qAFMR oscillations of the magnetization components, assuming $H_{DC} = 100$ mT. The m'_{iz} in c) and m'_{iy} in d) are scaled up by a factor 50 and 5, respectively.

the net magnetic moment was modeled. As expected from Eq. (3.142b), setting $H_{a'} = 0$ leads to the disappearance of the gap at $H_{DC} = 0$, with as predicted a gap frequency $\omega_{\Delta_1} = 3.3$ GHz, and our equation then follows the gapless Eq. (3.142a). The offset caused by the gap becomes negligible above ~ 20 mT. Because of the large ellipticity of the precession, removing the out-of-plane anisotropy H_a has no visible effect. Finally, changing the sign of H_{ex} to simulate a ferromagnet is not possible without modifying Eq. (3.139), as it would violate our assumptions about the canting angle α : that the equilibrium position of the magnetization vectors is symmetrical around the y axis, and that the small angle approximations are valid.

In the qAFMR mode, the sublattice magnetizations precess in the opposite direction compared to the qFMR mode around their equilibrium position, and with the opposite phase to each other. The net magnetization oscillates along the y axis and the canting angle oscillates around its equilibrium value. This mode of precession frustrates the isotropic exchange, which is the largest contributor to the magnetic energy. This leads

to a high precession frequency with a small dependency on H_{DC} . The exchange energy is minimized by precessing mainly out of plane, where the configuration becomes purely antiferromagnetic. The ellipticity ratio is $|m'_z / m'_y| = 40.4$ at $H_{\text{DC}} = 100$ mT. This is smaller than in the qFMR mode, because both HA^* and Hdm^* favor the in-plane component of the precession.

Setting $H_{\text{DM}} = 0$ reduces the precession frequency by a third, and has for consequence to increase the ellipticity by a similar proportion. The frequency then matches the result of Eq. (3.143c) for low applied fields, although the model of Borovik-Romanov and Kreines [146] includes the DM interaction. Setting $H_a = 0$ has a similar effect. Only with $H_a = H_{\text{DC}} = 0$ is the precession almost completely out-of-plane. The frequency then drops to 3.3 GHz at $H_{\text{DC}} = 0$, the same gap frequency as the qFMR mode. Because of small in-plane component of the precession, removing the in-plane anisotropy $H_{a'}$ has no visible effect.

3.4 Conclusion

With this overview of the theory of magnetism, we have seen from the ground up the origins of the phenomena discussed in this manuscript in the context of our measurements of FeBO₃. Starting from the spin of electrons, we have discussed how the presence of a magnetic moment in an atom depends of its electronic configuration, and how the presence of a spontaneous magnetization in a material depends on the exchange interactions between neighboring atoms. We have seen how the anisotropy of a ferromagnetic sample determines the direction and magnitude of its magnetization, and calculated its hysteresis curve. Finally, using the particular case of FeBO₃, we have calculated the dependency of the energy of a material on its magnetization, and derived its equilibrium configuration as well as its precession modes when the magnetization has been disturbed.

In the next chapter, we will use our knowledge of magnetism to look deeper into the dynamics of the spin. Instead of considering a single classic magnetization vector, we will look at the magnetic moment carried by electrons as they travel through different materials, and we will attempt to experimentally control this spin current to form spintronic THz emitters.

Spintronic THz emitters

After using THz radiation to excite spin waves in [Section 2.3.2](#), we now look into the complementary process of using spintronic processes to generate THz radiation. Spintronic emitters are an efficient and straightforward THz source consisting of a stack of alternating magnetic and nonmagnetic materials, which emit a transient THz pulse when they absorb an ultrafast laser pulse. Their bandwidth can reach up to 30 THz [21], which would allow to excite magnons in different materials. We decided to use a deposition technique that produces a large shape anisotropy on the magnetic layers, which confines the magnetization along a chosen axis and allows us to experiment with the geometry of the layers. In addition to exploring the parameters leading to a better THz output, we aimed to contribute to a deeper understanding of the physics of the spintronic emitters.

[Section 4.1](#) explains the current understanding of the physical processes behind the THz emission and how we modeled the output of the samples. [Section 4.2](#) details the design of our emitters and the experimental setup. [Sections 4.3.1 to 4.3.3](#) shows the effect of the deposition of simple samples, while [Sections 4.3.4 and 4.3.5](#) shows different geometries with which we experimented.

4.1 Theory and model

The mechanisms of ultrafast demagnetization and the associated THz emission are still a subject of discussion. The emission of THz radiation in the context of the ultrafast demagnetization [4] of ferromagnetic thin films induced by femtosecond lasers was first reported in 2004 [150, 151]. The first discovered mechanism to explain this emission was the radiation by a time-dependent magnetic dipole in the ferromagnetic layer, following $E \propto dM/dt$. This direct link between the magnetization dynamics and the THz field sparked interest in THz emitters as probes to study the out-of-equilibrium magnetization.

A particular area of focus was the question of angular momentum conservation during the ultrafast demagnetization [152]. In multilayer structures, it was found that a factor contributing to the demagnetization is the transfer of angular momentum out of the ferromagnetic layer by a spin current [153]. This current takes the form of a

superdiffusive transport of the spin-majority electrons [11, 154], which are able to leave the ferromagnetic layer due to their increased mobility compared to the spin-minority electrons. In 2013, a THz emission one order of magnitude stronger than the magnetic dipole radiation was discovered [155], which is the electric dipole radiation of these electrons when they are injected in a non-magnetic layer.

To increase our understanding of the experimental results of this chapter (Section 4.3), we implemented a numerical model of spintronic THz emitters, which we will detail step by step in the following sections.

4.1.1 Spin current

The material that we use as source of the spin current is a ferromagnetic film of pure iron with a typical thickness of 3.5 nm. As we have seen in the previous chapter, the valence bands of iron contain seven electrons per atom, among which in average 3.9 and 2.32 are found in the t_{2g} and e_g bands respectively [156]. An average of 0.91 spin-minority (down) electron is found in the former, leading to a net magnetic moment of $2.2\mu_B$ at room temperature.

Thermodynamical models are used to simplify the description of the dynamics of ultrafast demagnetization and the generation of a spin current. The three-temperature model describes the heat distribution between three coupled reservoirs: the lattice with temperature T_l , the net charge of 3d and 4sp electrons with temperature T_e , and their net spin with temperature T_s [4, 152]. The coupling values used in this work are given in Table 4.1. The diffusion of the hot electrons is modeled phenomenologically by a gradient of chemical potential. The spin voltage $V_s = (\mu_\uparrow - \mu_\downarrow)/e$, which is the difference between the chemical potential of both spins, quantifies the local spin polarization.

When a laser pulse is absorbed by the ferromagnetic (FM) layer, it leads to its demagnetization within ~ 100 fs. The photoexcitation of electrons near the Fermi level by 1.55 eV photons creates an out-of-equilibrium electronic distribution. Although the temperature of the excited electrons reaches well above the Curie energy, the average thermal energy is an order of magnitude lower than the exchange splitting and does not destroy the short-range magnetic order of Fe [157]. While spin-majority electrons decay without change of spin, spin-flip scattering accompanied by magnon emission dominate the decay of the spin-minority electrons [158], which is the main channel of ultrafast demagnetization in iron. Since spin waves are carried by the localized electrons, they in turn cause an increase of the orbital angular momentum via the spin-orbit coupling, which is quenched by the crystal field and leads to the further transfer of angular momentum to the lattice [159, 160].

At the same time, the excited electrons propagate at the Fermi velocity in a superdiffusive motion [11, 154], undergoing regular elastic scatterings that randomize their momentum. Through the inelastic scattering events mentioned above, they decay to less mobile bands and eventually stop contributing to the transport. Above the Fermi level,

the spin-majority bands have a free electron-like dispersion, while most of the spin-minority bands are narrow. Consequently, the group velocity of spin-majority electrons is significantly higher [161]. They reach an homogeneous density within ~ 100 fs [162], which ends the demagnetization. The slow transport of the spin-minority electrons persists for ~ 500 fs until they thermalize [11]. If the demagnetizing FM layer is in contact with a non-magnetic (NM) metallic layer, electrons can travel from one material to the other. The diffusing wavefront of fast spin-majority electrons leads to a sharp peak of net spin-polarized current into the NM layer. It is followed by a longer, weaker current of the opposite spin polarization, as the spin-majority electrons back-flow towards the FM layers [155] and finally the slow spin-minority electrons take over.

The extent of the angular momentum transport depends on the relative quantity and velocity of the spin-majority and minority electrons. The spin polarization of the ensemble of conduction electrons is $\sigma = (n_{\uparrow} - n_{\downarrow}) / (n_{\uparrow} + n_{\downarrow})$, where n is the density of electrons of the given spin. The charge and spin currents are respectively defined as:

$$\vec{j}_c = \vec{j}_{\uparrow} + \vec{j}_{\downarrow}, \quad (4.1)$$

$$\vec{j}_s = \vec{j}_{\uparrow} - \vec{j}_{\downarrow}, \quad (4.2)$$

where $\vec{j} = \sigma_0 \vec{E} - eD\nabla n = D\nabla\mu$ is the current density of electrons of one spin, D their diffusion coefficient and μ their chemical potential. The initial population difference of the electrons near the Fermi level, coupled with the higher diffusion velocity of spin-majority electrons, make iron efficient for generating spin currents.

To simulate spintronic THz emitters, we calculated the amplitude of the spin current following the model of Rouzegar et al. [163]:

$$j_s(t) \propto \Phi(t) (A_{es} \exp(-\Gamma_{es}t) - A_{el} \exp(-\Gamma_{el}t)) \otimes P(t), \quad (4.3)$$

with:

$$A_{es} = (\Gamma_{es} - R\Gamma_{el}) / (\Gamma_{es} - \Gamma_{el}), \quad (4.4a)$$

$$A_{el} = (\Gamma_{el} - R\Gamma_{el}) / (\Gamma_{es} - \Gamma_{el}), \quad (4.4b)$$

$$\Gamma_{el} = (G_{el}^F + G_{el}^N) / (C_e^F + C_e^N), \quad (4.4c)$$

$$R = \frac{C_e^F + C_e^N}{C_e^F + C_e^N + C_l^F + C_l^N}. \quad (4.4d)$$

$\Phi(t)$ is the Heaviside step function representing the instantaneous illumination by the infrared (IR) pump at $t = 0$; the convolution by the pump profile $P(t)$ produces the actual distribution of the pumping in time. The decay of the spin current is controlled by the electron-spin (τ_{es}) and electron-lattice (τ_{el}) relaxation times, with $\Gamma = 1/\tau$. The relaxation constant Γ_{es} was fitted to match the peak frequency of an experimental THz spectrum, while Γ_{el} is calculated in Eq. (4.4c) from the electron and lattice heat capacities and

Table 4.1: Input parameters for Eq. (4.3). The values of C_e , and G_{el} are taken at $T_e = 5000$ K for Fe, 4000 K for Pt and 7000 K for W.

	Unit	Fe	Pt	W
C_e	$10^6 \text{ J m}^{-3} \text{ K}^{-1}$	2.25 [167]	3 [168]	0.7388 [169]
C_l	$10^6 \text{ J m}^{-3} \text{ K}^{-1}$	2.2 [165]	2.85 [168]	2.4554 [169]
G_{el}	$10^{17} \text{ W m}^{-3} \text{ K}^{-1}$	38 [170]	1.3 [170]	1.3 [170]
λ	10^{-9} m	-	1.2 [19]	1.4 [19]
ϑ_H	1	-	0.051 [171]	-0.33 [172]

their couplings, using the values given in Table 4.1. Those values are heavily dependent on the actual electronic temperature, which we previously calculated using the three-temperature model, following a system of equations adapted from Kirilyuk, Kimel, and Rasing [164] and Chimata et al. [165]:

$$\begin{aligned}
 dT_e/dt &= \frac{1}{C_e} (-G_{el}(T_e - T_l) - G_{es}(T_e - T_s) + P(t)), \\
 dT_s/dt &= \frac{1}{C_s} (-G_{es}(T_s - T_e) - G_{sl}(T_s - T_l)), \\
 dT_l/dt &= \frac{1}{C_l} (-G_{el}(T_l - T_e) - G_{sl}(T_l - T_s) - h\pi\omega_0^2(T_l - T_{BG})),
 \end{aligned} \tag{4.5}$$

where h represents the losses to the environment, $P(t)$ the instantaneous laser power, ω_0 the beam radius and T_{BG} the environment temperature, considered equal to the steady-state temperature of the samples. We published the values we used in this model in Ref. [166].

4.1.2 Inverse spin Hall effect and THz emission

In the bulk of the NM material, the spin current is converted into a transverse charge current by the inverse spin Hall effect (ISHE) [173–175]. In materials with strong spin-orbit coupling, electrons scatter preferentially in one direction or the other depending on their spin. While the spin Hall effect transforms a spin-neutral charge current into a spin current by deviating electrons of both spins in opposite directions, the inverse effect transforms the spin-polarized current coming from the FM layer into a net charge current in the plane of the NM layer (see Fig. 4.1)

The spin Hall angle ϑ_H quantifies the efficiency of the conversion between the two currents according to:

$$\vec{j}_c = \vartheta_H \vec{j}_s \wedge \vec{\sigma} \tag{4.6}$$

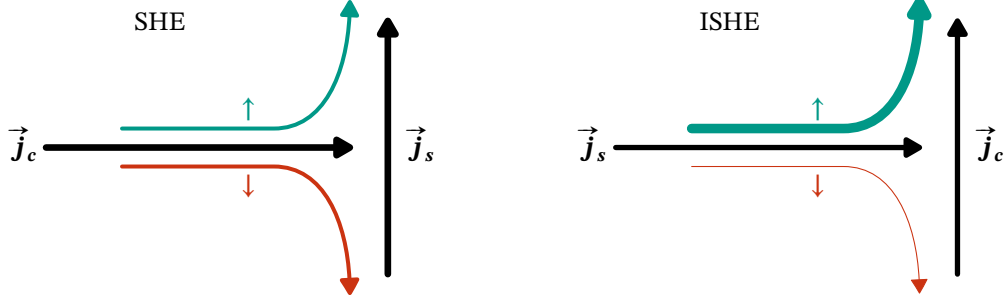


Figure 4.1: Spin Hall effect (left) and inverse spin Hall effect (right).

where $\vec{\sigma} = \vec{M} / M_s$ is the spin polarization vector of the spin current. The best THz emission is thus obtained when the spin current is fully polarized ($\sigma = 1$) and for NM materials with a high ϑ_H .

While the FM layer also has a non-zero spin Hall angle [176], the effect is negligible due to the quenching of its angular momentum: $\vartheta_{Fe} \approx -1.36 \times 10^{-3}$ [155] and $\vartheta_{Py} \approx 3.4 \times 10^{-4}$ [177], while, taking the average of the values compiled for room temperature in Refs. [178, table 1, 179, table 14.1], $\vartheta_W \approx -33\%$ and $\vartheta_{Pt} \approx 4.2 \pm 2.9\%$. Hence we only consider the spin-to-charge current conversion in the bulk of the NM layer.

However, the FM|NM interface is not transparent and the transmission of the spin current into the NM layer is highly dependent on the materials and on the preparation of the sample [180]. The breaking of the lattice symmetry at the interface causes scattering, creating an interfacial spin-mixing resistance that reduces the spin polarization of the transmitted spin current by a significant fraction, for example by 60% for Co|Pt [181, 182]. In addition, structural imperfections at the interface influence the local spin-orbit coupling, possibly inverting the sign of the interfacial spin-to-charge conversion [183]. To take these different effects into account, we assume that as our spintronic THz emitters are manufactured identically (with the exception of the deposition incidence, see Section 4.2.1.1), the interfacial transmission only depends on the materials.

To model the THz emission, we thus replace Eq. (4.6) by:

$$j_c = t_{Fe|x} \vartheta_H j_s \quad (4.7)$$

where $t_{Fe|x}$ contains the interfacial emission and current transmission from the Fe layer to the NM layer x . We extract the relative values of $t_{Fe|W}$ and $t_{Fe|Pt}$ in Section 4.3.3.

The transient current in the NM layer emits THz radiation, which can be calculated using the inhomogeneous 1D Helmholtz equation:

$$\begin{aligned} \vec{\nabla} \wedge (\vec{\nabla} \wedge \vec{E}(\omega)) + k^2(\omega) \vec{E}(\omega) &= -\frac{Z_0 \omega}{ic} j_c(z, \omega) \\ \left(\frac{\partial^2}{\partial z^2} + k^2 \right) E_y(\omega) + k^2(\omega) E_y(\omega) &= -\frac{Z_0 \omega}{ic} j_c(z, \omega) = -\delta(z) q(\omega) \end{aligned} \quad (4.8)$$

where $\delta(z)$ is the Dirac delta function and $q(\omega)$ is the spectrum of the point source at $z = 0$. The solution for the electric field emitted by the point source is its convolution

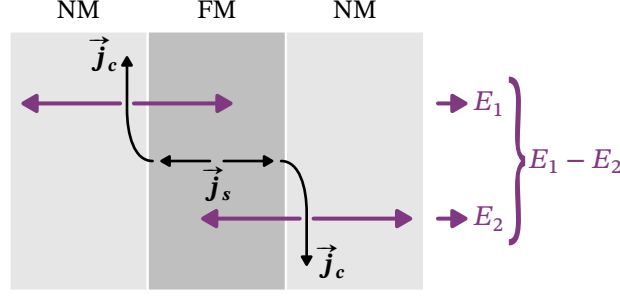


Figure 4.2: Schematic representation of the field addition: the THz field emitted by each current \vec{j}_c is propagated from the interface where it is generated until outside the sample. Then all fields are superposed, with a sign matching the orientation of the current.

with the Green function $G(z)$:

$$E(z, \omega) = G(z) \otimes \delta(z) q(\omega) = \frac{i \exp(-ik|z|)}{2k} \frac{\omega}{i\epsilon_0 c^2} j_c(z=0, \omega), \quad (4.9)$$

or at the location of the point source:

$$E(\omega) = j_c(\omega) / (2nc\epsilon_0). \quad (4.10)$$

To take into account the spacial dependency of the emission, we consider that the inverse spin Hall effect (ISHE) depletes the spin current following an exponential decay law, using as constant the electron mean free path λ [184]: $j_c(z, \omega) = j_c(z_0, \omega)e^{-(z-z_0)/\lambda}$ where z_0 is the location of the interface. The integrated emission in the NM layer of thickness L is then:

$$\begin{aligned} E(\omega) &= \int_{z_0}^{z_0+L} \frac{j_c(z_0, \omega)}{2nc\epsilon_0} e^{-(z-z_0)/\lambda} dz = \frac{j_c(z_0, \omega)}{2nc\epsilon_0} \lambda (1 - \lambda e^{-L/\lambda}) \\ &= \frac{t_{\text{Fe}|x}^{\text{SH}}}{2nc\epsilon_0} j_s(\omega) \lambda (1 - \lambda e^{-L/\lambda}). \end{aligned} \quad (4.11)$$

4.1.3 THz propagation and EOS

After calculating the emitted THz field in the previous section, we now address its propagation through the sample. To take into account the many reflections of the field on the multiple layers, we use a transfer-matrix method, adapted to the transmission of a field which is not incident on the sample but has its source inside. The modifications of the standard transfer-matrix model are detailed in [Appendix C](#). After propagating the field from each individual THz sources to outside the sample, the total field is added up, taking into account the relative direction of the charge currents (see [Fig. 4.2](#)).

To allow the use of the transfer-matrix method, in which the electric field is only known at the interfaces, we consider that the full THz emission given by [Eq. \(4.11\)](#) is

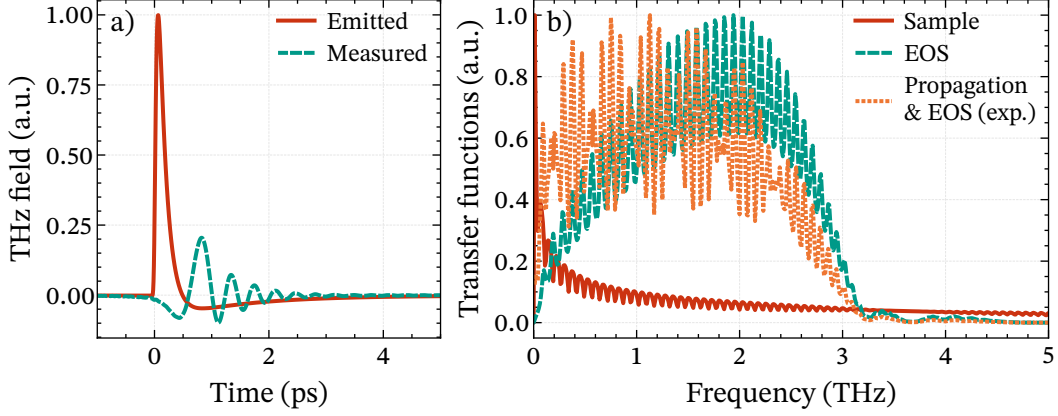


Figure 4.3: a) Comparison between the THz waveforms of the sample Fe*|Pt at the emission point (calculated) and outside the sample (measured). b) Transfer functions of the propagation in the sample T_{SE} and of the EOS crystal used in the measurement T_{EOS} (both simulated), as well as the experimental total transfer function of the setup $T_{prop}T_{EOS}$. The fringes in the transfer functions come from the internal reflections in the materials.

located at the FM|NM interface. We verified that this approximation does not influence the calculated field by approximating the exponentially distributed emission using fictitious NM|NM interfaces within the NM layer. Due to the transparency of the layers for THz radiation, the difference was negligible.

The propagation of the emitted THz field through the setup is then calculated following the transfer functions given by Faure et al. [185], taking into account the transmission through the IR filter, the frequency-dependence of the collection and refocusing, as well as the electro-optic sampling (EOS) setup, which is detailed in Section 4.2.2.4. The refractive indices of the relevant materials are listed in Appendix A.

Fig. 4.3 shows the effect of different transfer functions distorting the initial THz field. The lower end of the spectrum is better transmitted by the sample. Most of the propagation through the setup has a low impact, until the THz pulse reaches the EOS crystal, where it is sampled by the probe. While the spectrum of the simulated THz field reaches 10 THz, the 5.3 THz phonon of ZnTe is responsible for a smaller measured bandwidth of 3 THz.

The total equation describing the THz emission is thus:

$$S(\omega) = E(\omega) T_{SE}(\omega) T_{prop}(\omega) T_{EOS}(\omega) \quad (4.12)$$

with $E(\omega)$ given by Eqs. (4.3), (4.7) and (4.11), and where $T_{SE}(\omega)$ is the transfer function of the propagation out of the sample; $T_{prop}(\omega)$ the propagation of the THz radiation from the position of the sample to the one of the EOS crystal, and $T_{EOS}(\omega)$ the measurement by electro-optic sampling.

To ensure the best comparison between the measurements and the simulations of different samples, we measured experimentally the value of $T_{\text{prop}}(\omega) T_{\text{EOS}}(\omega)$ as the ratio of an experimental signal $S(\omega)$ by the corresponding simulated $E(\omega) T_{\text{SE}}(\omega)$. As the distortion of the THz waveform during EOS is sensitive on the exact mounting of the crystal, this ensures that simulated waveforms look similar to the measured waveforms if the modeling of the sample is correct.

4.2 Experimental setup

One of the aspirations of this project was to experiment with emitters containing several FM layers and control their relative magnetization, with the objectives of increasing the efficiency of the THz generation and observing the consequences on the spin current. This experimental uncoupling of the FM layers was achieved by changing the conditions during their fabrication. We now describe the design and fabrication method of the spintronic THz emitters, then the measurement setup.

4.2.1 Sample design and fabrication

Several approaches exist to control the relative magnetization of two FM layers: using the Ruderman-Kittel-Kasuya-Yosida interaction where the sign of the exchange constant depends on the distance between them [186], using exchange-coupled layers [187], or pinning the magnetization of a single layer by contact with an antiferromagnet [188]. These three approaches limit the flexibility of designing the emitters as they place constraints on the width or material of the NM layers.

As an alternative, it has long been known that the deposition of FM materials such as iron [189] and Permalloy [190] at a non-normal angle of incidence induces uniaxial anisotropy in the film plane. In 2016, Schlage et al. [191] introduced a new method to control the magnetization of a FM layer based on oblique incidence deposition (OID). By depositing these layers at oblique incidence, they can be given a tunable anisotropy independently of the other layers, allowing to control the magnetization of each FM layer individually without restricting the design of the sample.

4.2.1.1 Magnetron sputtering deposition

All spintronic THz emitters we prepared by magnetron sputtering deposition, on $25\text{ mm} \times 25\text{ mm}$, $635\text{ }\mu\text{m}$ -thick (0001)-plane double-polished Al_2O_3 wafer substrates. A strong voltage is applied on the sputtering gas, typically argon, until it ionizes into a plasma. Above the breakdown voltage, it generates a self-sustaining current as plasma ions free new electrons, which in turn ionize new atoms of the gas. The sputtering target is placed in front of the cathode, from which accelerated ions knock out atoms. In magnetron sputtering, alternating magnet poles behind the target create a magnetic

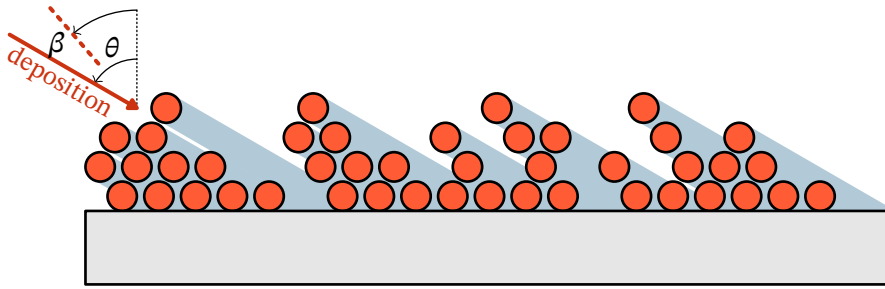


Figure 4.4: Self-shadowing creating peaks and valleys during the sputtering at oblique incidence. The angle θ represents the deposition angle and β the growth angle.

field which traps the plasma above it, while the neutral atoms flying out from the target are unaffected. The atomic vapor then condensates on the substrate, where it is adsorbed [192, chapter 1]. The substrate is usually parallel to the target to equalize the distribution on the surface (normal incidence).

The adsorbed atoms are named ad-atoms and arrive on the surface at random positions. Depending on their interactions with other atoms and the surface, they will tend to either cluster into 3D islands or grow into 2D layers. Their mobility depends on the sputtering conditions, particularly the deposition rate and the substrate temperature. A typical deposition rate for magnetron sputtering is $10^7 \text{ m}^{-2} \text{ s}^{-1}$, equivalent to 10^{-2} monolayer/s [192, chapter 8]. As iron is deposited under its melting point at room temperature and the deposition rate is relatively high, ad-atoms have a low mobility, which prevents them from diffusing towards sites with low energy and forming a monocrystalline film. In this island regime, nucleation starts instead at many points on the film, leading to a polycrystalline structure. They grow and coalesce laterally, forming a porous network on the surface, as illustrated in Fig. 4.4. Above a thickness of 10 nm to 20 nm, vertical growth takes over and the islands start forming fibrous columns, each with a random crystallographic texture.

If the deposition is made at oblique incidence, the ad-atoms tend to be intercepted by the highest structures, which shadow lower structures behind them, leading to a self-perpetuating order. As they mostly attach to the front of the structures, the columns grow tilted towards the deposition direction [193, 194]. Under $\theta = 60^\circ$ of incidence [195], the growth angle β of the columns mostly follows the empirical relation $2 \tan \beta = \tan \theta$ [196]. Above 60° , no accurate universal empirical rule exists [197].

Except when otherwise indicated, the polar angle of deposition is $\phi = 0^\circ$, defined with respect to an edge of the square substrate. The sample is then rotated in-plane by 180° halfway through the deposition of each FM layer to prevent the formation of a thickness gradient.

4.2.1.2 Formation of the magnetic anisotropy

Low pressure reduces the scattering rate of the sputtered atoms, increasing the directionality of OID. Our samples are deposited with a base pressure under 7×10^{-7} mbar. Details about the deposition chamber can be found in [198, section 4.1]. For most samples, the FM layers consist of a 3.5 nm-thick layer of iron. At this thickness, the columns are not yet formed. Instead, one can observe grains that stretch in the direction transverse to the incident plane, as they are free to grow laterally but are affected by self-shadowing in the deposition direction [199, 200]. The iron is in a polycrystalline α -Fe phase, although lattice defects are expected due to the low thickness.

As shown in Fig. 4.5, this surface roughness causes the apparition of a stray and demagnetizing field (see Section 3.1.3) when the magnetization is in the incidence plane. This additional magnetostatic energy adds an in-plane component to the initial

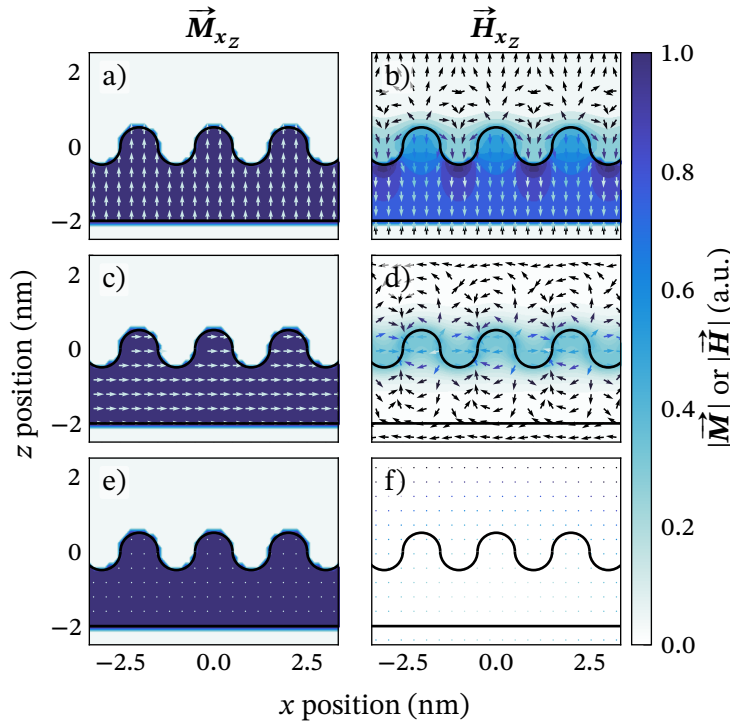


Figure 4.5: Simulated [201] dipolar field (right column) in the deposition plane for a given uniform magnetization (left column), calculated at the center of a $200 \text{ nm} \times 200 \text{ nm}$ magnetic layer. The thickness of the layer varies between 1.5 nm to 2.5 nm in a pattern of waves parallel to the y axis on the upper surface. The arrows and colors represent respectively the direction and magnitude of the fields. The situation where \vec{M} is perpendicular to the deposition plane (e) produces no stray field ($|\vec{H}| < 3 \times 10^{-4}$) compared to when $M \parallel z$ (a) and $M \parallel x$ (c), and is thus privileged: y is the easy axis.

additional shape anisotropy. Similarly to Eq. (3.124), the in-plane uniaxial anisotropy constant is $K = \mu_0 M^2 (N_{xx} - N_{yy}) / 2$, where the demagnetization tensor components are a function of the average correlation length of the surface thickness [199]. As the grains elongate laterally, N_{yy} decreases, while the self-shadowing increases N_{xx} . The anisotropy is weak for low incidence angles, then increases continuously in the range of 45° to 85° [191]. To be able to switch the relative magnetization of two ferromagnetic layers in the same sample, we thus typically deposited the first one at 60° and the second at 80° .

4.2.1.3 Sample design

To increase the THz output, most samples have more layers than the minimal structure of substrate|FM|NM. Seifert et al. [21] showed that the performance of the emitter is increased when a second NM layer is added to make use of the spin current flowing through both interfaces. In this situation, $\vec{j}_s \wedge \vec{\sigma}$ in Eq. (4.6) has the opposite sign. To avoid that \vec{j}_c also reverses its sign and the THz emission from both interfaces superpose destructively, we need to choose two NM layer with opposite spin Hall angles ϑ , as shown in Fig. 4.6a.

We make use of this principle to design samples with a second FM layer, with a substrate|NM|FM|NM|FM|NM structure. We alternate the NM materials as described before, which ensures the coherent emission within each NM|FM|NM substructure. However, within the central FM|NM|FM substructure, spin currents with opposite signs enter the same NM layer. Here, to compensate the change of sign of \vec{j}_s , the only free parameter is $\vec{\sigma}$. In other words, for the two FM layers to emit THz radiation coherently, they must be magnetized in opposite directions, as shown by Fig. 4.6b. This is achieved by imparting them different surface anisotropies, so that their magnetizations switch under the application of different magnetic fields and there is a range in which they have an antiferromagnetic (AFM) alignment.

The ISHE does not occur in MgO, which is an insulator. In some samples, we inserted a MgO layer between FM and NM layers to prevent the transmission of the spin current,

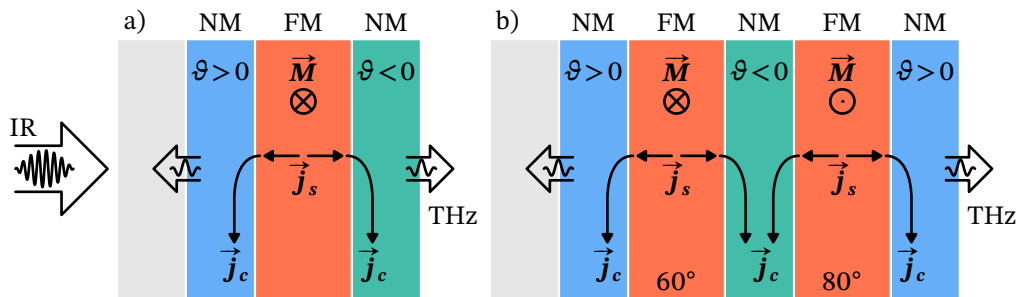


Figure 4.6: Scheme of a) a trilayer sample and b) a five-layer sample. The adjacent NM layers have opposite spin Hall angles ϑ to ensure a coherent THz emission.

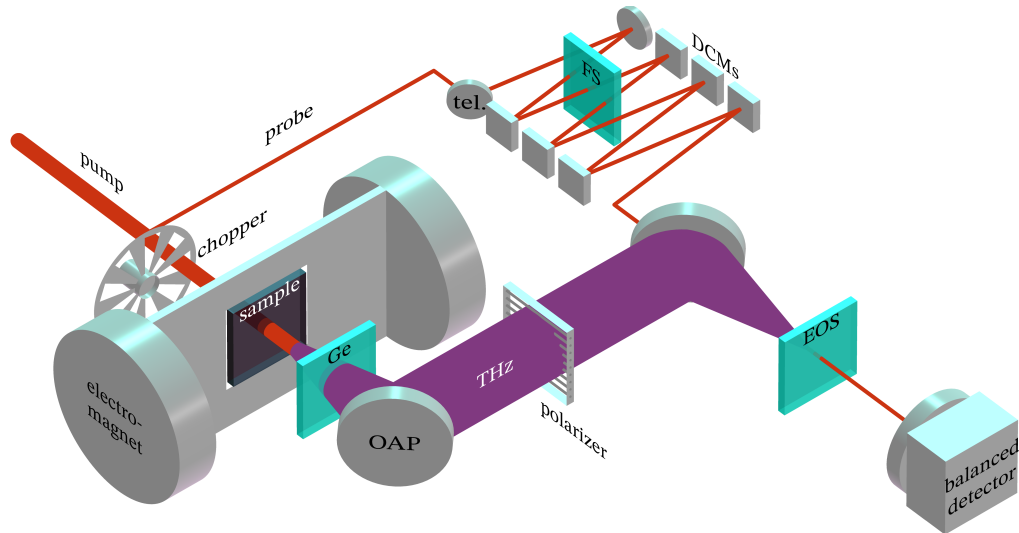


Figure 4.7: Schematized setup for the measurement of the spintronics emitters. The pump arm is chopped from 3 kHz to 1.5 kHz and generates THz radiation in the sample before being separated by the germanium filter (Ge). The probe arm is reduced to a smaller beam diameter in a double telescope (tel.) and compressed in several steps by cascaded stages of SPM in a fused silica (FS) window and recompression by dichroic mirrors (DCMs). The THz is filtered from its horizontal polarization and is focused by a pair of off-axis parabolas (OAP) into the electro-optics sampling crystal (EOS). The probe is there superposed to the THz and its polarization rotation is measured by a balanced detector.

but kept the NM layer in order to maintain a similar heat profile in the sample. We additionally used MgO layers to match the thickness of samples whose output we wanted to compare, so the propagation length of the IR and THz beams would be similar from sample to sample. The structure of all samples used in this chapter is detailed in [Table 4.2](#). The names used to refer to the samples indicate the materials of their metallic layers, excluding the substrate and other insulating layers. In the case of the five-layer samples, for which the structure is symmetrical, we indicate the lower half. Layers deposited at oblique incidence are identified with an asterisk.

4.2.2 Laser setup

The spintronic emitters setup uses the 800 nm, 35 fs, 3 kHz Ti:sapphire laser system as the tilted pulse front THz setup described in [Chapter 2](#). A combination of a half waveplate and a thin film polarizer (TFP) is used to split the beam into a pump and a probe beams, such that 200 μJ are always available for the probe arm. The setup is schematized in [Fig. 4.7](#).

Table 4.2: Structure of the spintronic THz emitters fabricated for this work. The substrate of all samples is $365 \mu\text{m Al}_2\text{O}_3$. The numbers in brackets indicate the incidence angle θ of deposition of the FM layers. The polar deposition angle is always $\varphi = 0$, except in the case of $[\text{Fe}^{90^\circ}|\text{W}]_2$ ($\varphi = 45^\circ$ and -45°).

Sample	Material [$\theta(^{\circ})$], thickness (nm)										Figs.				
W Py Pt	W	2.2	Py[0]	2.4	Pt	2.1						4.12			
W Py* Pt	W	2.0	Py[60]	1.8	Pt	2.1						4.12			
Fe* Pt	MgO	2.0	Fe[60]	3.5	Pt	2.0						4.12, 4.18			
Fe* W	MgO	2.0	Fe[60]	3.5	W	2.0						4.12, 4.14, 4.17–4.19			
Fe W	MgO	2.0	Fe[0]	3.5	W	2.0						4.14			
[Pt Fe*] ₂	Pt	2.0	Fe[60]	3.5	MgO	4.0	Fe[80]	3.5	Pt	2.0		4.12, 4.16, 4.17, 4.19			
[Pt Fe* W] ₂	Pt	2.0	Fe[60]	3.5	W	4.0	Fe[80]	3.5	Pt	2.0		4.16, 4.17, 4.19			
[W Fe* Pt] ₂	W	2.0	Fe[30]	3.5	Pt	5.0	Fe[80]	3.5	W	2.0		4.16			
MgO Fe* MgO	MgO	2.0	Fe[60]	3.5	MgO	2.0						4.17			
[Fe* W] ₂	MgO	2.0	Fe[60]	3.5	W	4.0	Fe[80]	3.5	MgO	2.0		4.17			
[Pt MgO Fe* W] ₂	Pt	2.0	MgO	2.0	Fe[60]	3.5	W	4.0	Fe[80]	3.5	MgO	2.0	Pt	2.0	4.17
[Fe ^{90°} W] ₂	MgO	2.0	Fe[60]	3.5	W	4.0	Fe[80]	3.5	MgO	2.0				4.22	

4.2.2.1 Magnetic field

To control the magnetic field on the spintronic THz emitters, the samples were mounted on a copper holder at the center of the gap of an electromagnet. Because the iron core of the electromagnet has a certain hysteresis, the electrical current that drives it should always be adjusted by following the same path in order to reproducibly reach the same magnetic field. Before each measurement, the electromagnet is systematically driven to ± 4 A, the largest one delivered by the power supply, to saturate its magnetization. Its current is then monotonically decreased or increased, respectively, to adjust the magnetic field.

For these two paths along the hysteresis curve to the electromagnet, we calibrated the correspondence between the current and the horizontal component of the magnetic field at the center of the sample holder. A range of -40 mT to 40 mT is sufficient to switch the magnetization of all samples. In this range, the relationship is linear with an offset depending on the direction of the current swipe. The calibration is displayed in Fig. 4.8.

4.2.2.2 IR pump

After the separation of the laser beam into a pump arm and a probe arm, the collimated pump beam is propagated by the distance needed to match the path length of the probe, and chopped to a repetition rate of 1.5 kHz to improve the detection of the THz signal. In order to illuminate the sample homogeneously, the center of the beam profile, which is approximately Gaussian, is truncated to a diameter of ~ 5 mm by an iris immediately before the sample. This ensures the illuminated region is always the center of the sample,

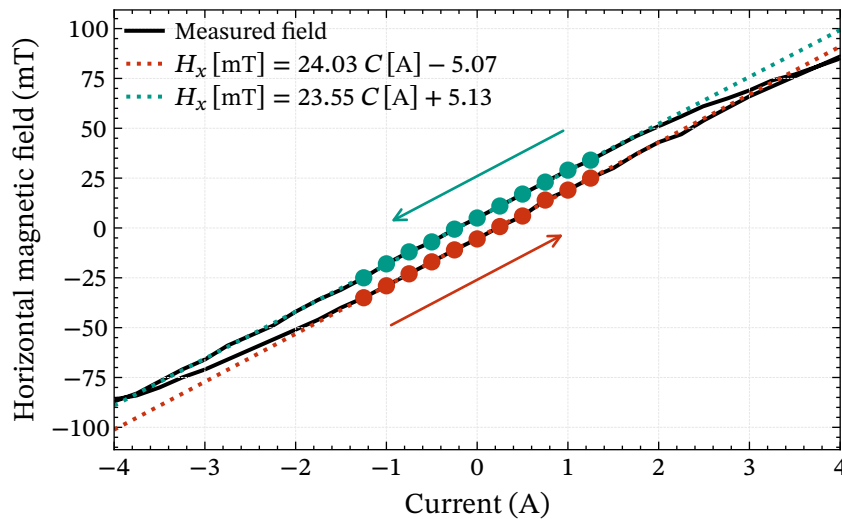


Figure 4.8: Correspondence between the chosen current in the electromagnet and the magnetic field at the center of the sample holder. The linear fits (dotted lines) are calculated from the corresponding points with markers.

where we calibrated the magnetic field.

During most measurements, the energy in the pump was in the order of 1 mJ. Typically 50 % to 75 % of it are absorbed by the metallic layers of the sample. We calculated the relative power absorbed in each layer m from the difference of the Poynting vectors at its interfaces [202]:

$$P_m(t) = S_m - S_{m+1} \quad (4.13)$$

$$S_m = \text{Re} \left(\frac{n_m}{\mu_m} (E_{\rightarrow}^* + E_{\leftarrow}^*) (E_{\rightarrow} - E_{\leftarrow}) \right) \quad (4.14)$$

where E is the complex left- or right-propagating IR electric field at the beginning of the layer m , and is obtained from a transfer-matrix calculation. Since the spin current is generated by the heat of the absorbed pump and the samples are not birefringent, the polarization of the beam has no influence.

After the sample, the transmitted part of the pump copropagates with the generated THz field. To remove it, a 5 mm-thick germanium filter is placed before the THz collection optics.

4.2.2.3 IR probe

The probe arm of the laser system is used to sample the emitted THz radiation. We designed the setup to be able to resolve a spectrum potentially extending up to 30 THz [21]. The probe pulses, which are 35 fs long in the best conditions, can at most resolve half of this bandwidth and thus require further compression.

The compression setup was published in Calendron et al. [203]. Its concept is to increase the bandwidth of the beam by self-phase modulation (SPM), then recompress the pulse on chirped mirrors. For more efficiency, this is repeated three times. To avoid introducing dispersion on the beam between the compressor of the laser system and the additional compression setup, the probe arm is the one reflected on each TFP splitting the beam. Its energy is maintained at 200 μJ .

Before the compression, the beam diameter d is reduced from 6 mm \times 7 mm to 1.5 mm by two successive telescopes to reach a sufficient intensity in the FS plate. These are made of 4 concave silver mirrors of focal length of respectively -1000 mm, $+300$ mm, -1500 mm and $+400$ mm. Modeling the input pulse as Gaussian with a FWHM duration of $\tau = 35$ fs and the energy $E = 200 \mu\text{J}$, the peak intensity of the probe beam is $I_0 = 8P_0 / \pi d^2 = 6.1 \times 10^{15} \text{ W m}^{-2}$, where $P_0 = 2E\sqrt{\ln(2)} / \pi / \tau$.

The nonlinear medium used for self-phase modulation is an uncoated 2 mm-thick fused silica plate. Self-phase modulation is a third-order nonlinear process, hence the refractive index changes with the square of the field amplitude:

$$n^2 = 1 + \chi^{(1)} + \chi^{(2)}E + \chi^{(3)}E^2. \quad (4.15)$$

Because of the inversion symmetry, the second-order susceptibility $\chi^{(2)}$ vanishes in centrosymmetric or noncrystalline materials such as fused silica. The refractive index

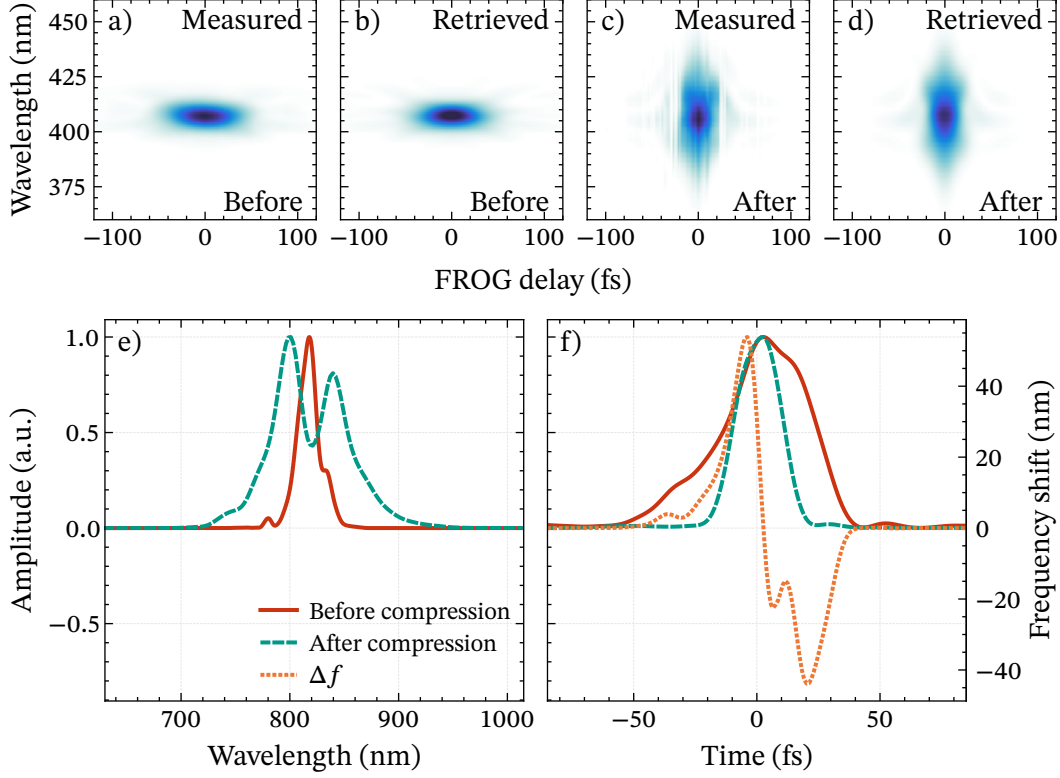


Figure 4.9: e) Spectrum and f) beam profile of the probe beam before and after the compression setup, retrieved from the FROG traces in a–d, as well as the corresponding instantaneous frequency shift Δf .

can thus be separated into its first-order component and intensity-dependent component: $n(t) = n_0 + n_2 I(t)$. For a complex index $n = n' - i\kappa$, the nonlinear refractive index n_2 is linked to the susceptibility $\chi^{(3)}$ by [204]:

$$\begin{aligned}
 n_2 &= \frac{3}{4n_0^2 c \epsilon_0} \chi^{(3)} \left(\left(\chi_R^{(3)} + \frac{\kappa_0}{n_0'} \chi_I^{(3)} \right) - i \left(\chi_I^{(3)} - \frac{\kappa_0}{n_0'} \chi_R^{(3)} \right) \right) \\
 &\approx \frac{3}{4n_0^2 c \epsilon_0} \chi^{(3)} \quad \text{in a lossless material } (\kappa = 0).
 \end{aligned}
 \tag{4.16}$$

In the case of fused silica, $n_2 = 2.43 \times 10^{-16} \text{ cm}^2 \text{ W}^{-1}$ [205]. Since the intensity of a laser pulse varies with time, the refractive index of the fused silica plate varies too, which induces a time-dependent phase shift. During the propagation of the pulse through a length $L = 2 \text{ mm}$, it accumulates a nonlinear phase $\delta_2 = n_2 I L \omega / c$. The induced frequency shift is then approximately:

$$\Delta f(t) \approx -\frac{\partial \delta_2}{\partial t} = -\frac{n_2 f_0 L}{c} \frac{\partial I(t)}{\partial t}.
 \tag{4.17}$$

As shown in Fig. 4.9, the initial pulse has in practice a full width half maximum (FWHM) duration of $\tau = 37.5$ fs and a FWHM bandwidth of 18.7 nm centered at $c / f_0 = 817$ nm. The corresponding instantaneous frequency shift reaches a maximum of 54 nm.

The peak intensity of the probe incident on the fused silica wafer is above the critical power for self-focusing, which is $P_{\text{crit}} = \alpha \lambda^2 / (4\pi n_0 n_2) = 2.8 \times 10^6$ W, with $\alpha = 0.148$ for a Gaussian beam. When the beam profile is inhomogeneous, this tends to split it into separate filaments and make the alignment of the probe fluctuate with its energy. It is therefore important for the measurements to maintain a clean beam profile. For this, we placed an almost-closed iris after the fused silica wafer, which removes the parasitic filaments.

Finally, the dispersed beam is recompressed by being reflected six times on five different dichroic chirped mirrors (DCMs). The first two of them are used after each of the three passes through the fused silica wafer. They compensate each a group delay dispersion of 54 fs^2 per bounce, equivalent to 1.5 mm of fused silica. The near-recompression allows the intensity to remain high for the next pass through the wafer, enabling the further broadening of the spectrum. The remaining dispersion after the third pass is balanced by three DCMs compensating 26 fs^2 per pair.

As shown in Fig. 4.9, we measure after recompression a bandwidth of 68.9 nm and duration of 21.3 fs FWHM. This would allow the resolution of frequencies reaching 23 THz.

4.2.2.4 THz measurement

As illustrated in Fig. 4.7, the THz emitted by the spintronic emitters on the side opposed to the incident pump is collected and focused by two off-axis parabolas (OAPs) with reflected focal lengths of 6" and 4", respectively. We measured the THz energy with the pyroelectric detector MPY-RS from WiredSense, with a sensitivity at 1.5 kHz of $14.6 \text{ V } \mu\text{J}^{-1}$. An additional 2 mm-thick polyethylene cover, measured to have a THz transmission of 60 %, was used to filter the remaining IR radiation, bringing the sensitivity down to $8.8 \text{ V } \mu\text{J}^{-1}$.

Our first samples were CoFeB|Pt bilayers, giving a THz signal in the range of 20 mV to 50 mV when pumped by 1 mJ IR pulses. The emitted THz energy was thus 4.0 ± 1.7 nJ. This indicates that IR-to-THz conversion efficiency of the setup is of the order of $\sim 4 \times 10^{-6}$.

Due to the low THz energy and our interest in measuring its spectrum, the rest of the measurements are done by electro-optic sampling (EOS). The second OAP has a centered hole with a 3 mm diameter on the reflecting surface, allowing the compressed probe to propagate collinearly to the converging THz beam and overlap with the THz focus.

As mentioned earlier, the intensity profile of the pump beam on the spintronic emitters

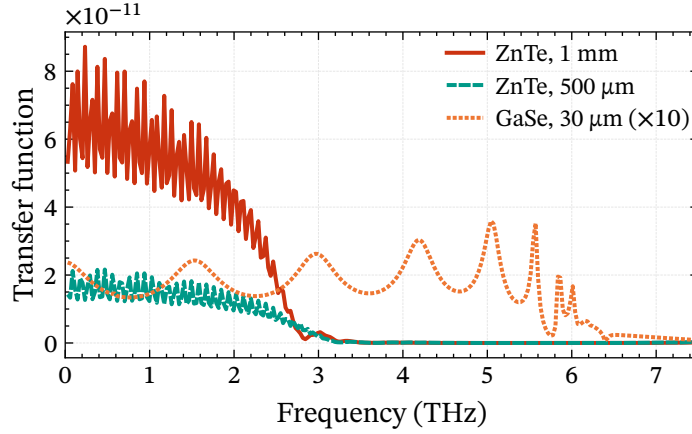


Figure 4.10: Amplitude transfer function of the available EOS crystals. The transfer function is $T = T_{\text{trans}} T_{\text{crystal}} T_{\text{env}} \chi_{\text{eff}}^{(2)}$ according to Eq. (B.4).

is cut to approximately 5 mm diameter by an iris. Since the THz is emitted proportionally to the absorbed pump energy as shown by Eq. (4.3), the emitted THz beam size can be approximated to have the same diameter. Assuming it has a M^2 of 1, its divergence is 2° and the OAPs should collect the entire beam. The estimated diameter of the THz focus on the EOS crystal is 3.3 mm. The compressed probe is not focused to avoid reintroducing dispersion.

The mechanisms of EOS and balanced detection are detailed in Appendix B. In the EOS crystal, the polarization of the probe rotates proportionally to the amplitude of the overlapping THz electric field. The delay of the probe is thus scanned to measure the complete THz waveform. The acquisition and control of the delay are made using Labview. The choice of EOS crystal controls the measurable THz bandwidth, as shown by Fig. 4.10 which compares the crystal that were available for the experiment. The measurements in Section 4.3 were performed with the 500 μm -thick ZnTe crystal, as we first thought that the resonance of GaSe at 0.6 THz would prevent the measurement of the low frequencies. The experimental waveforms shown in this chapter are not corrected to account for the frequency-dependency of $T_{\text{EOS}}(\omega)$, as this was not necessary to compare them.

4.3 Experimental results

We now present the different experiments we performed with spintronic THz emitters. In Sections 4.3.1 and 4.3.2, we look at the influence of the pump energy and other non-magnetic-related effects on the emitted THz field. In Section 4.3.3, we compare samples deposited with and without the OID method described in Section 4.2.1. We then introduce samples with several FM layers and study their behavior.

4.3.1 Influence of the pump energy

Since the spin current is triggered by the absorption of the pump in the FM layer, a higher pump energy is expected to lead to a higher THz amplitude according to Eq. (4.3). However, increasing the temperature of the FM layer might lead to a reduction of its magnetization (see Section 3.2.4.4). Using a W|Py*|Pt sample, we increased the fraction of the laser energy going into the pump beam while keeping the energy of the probe beam constant. The magnetization of the sample was saturated by applying a magnetic field of -3 mT at the center of the sample. For each pump energy, we measured the temperature of the sample using an IR camera and recorded 1 to 3 EOS traces of the emitted THz while the temperature stabilized.

Figs. 4.11a and 4.11b shows the THz peak-to-peak amplitude versus the pump fluence and the emitter temperature. The signal amplitude is better correlated with the fluence than with the lattice temperature, mainly due to the difficulty of accurately measuring the temperature of the FM layer at the pump location. We see that the signal initially increases linearly with the fluence as expected, but quickly saturates around $300 \mu\text{J cm}^{-2}$, above which the THz output decreases. The fluence is too low to attribute the output re-

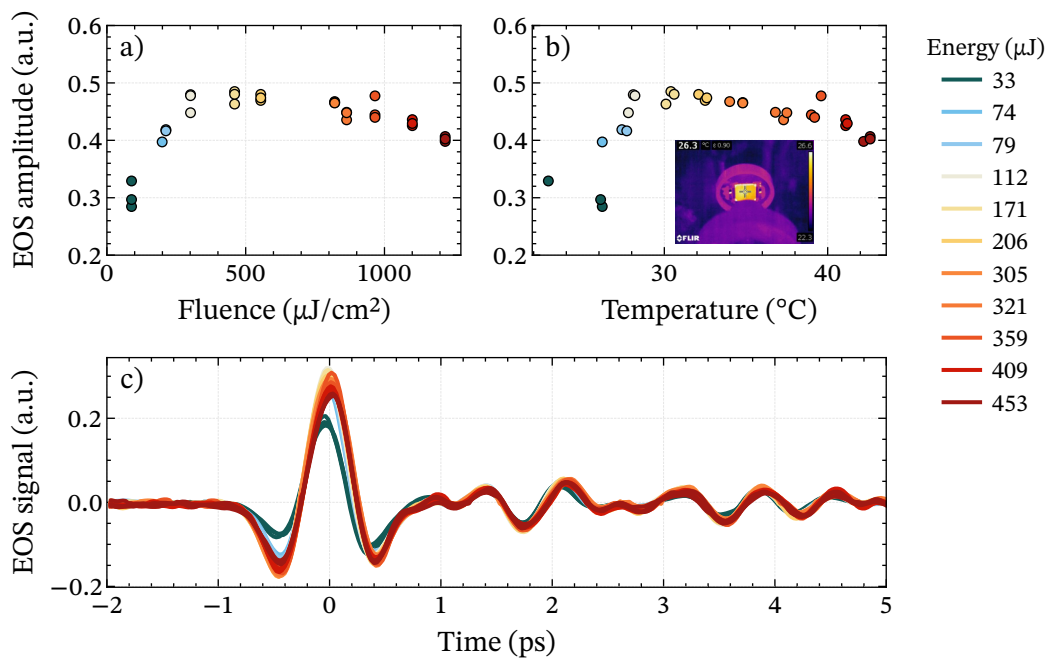


Figure 4.11: Influence of the pump fluence and spintronics emitters temperature on a–b) the THz amplitude and c) the THz waveform measured from a W|Py*|Pt sample. The colors indicate the corresponding energy in the pump pulse. The insert in b) is an example of an image from the infrared camera used to measure the temperature of the spintronic emitters (yellow square).

duction to optical damage [206] or the saturation of the ultrafast demagnetization [207]. Saturation was reported in different spintronic emitters by Zhang et al. [208] at fluences in the order of 1 mJ cm^{-2} to 1.5 mJ cm^{-2} , and attributed the saturation of the spin accumulation in the NM layer preventing the spin transport [155]. Their model does not reproduce the subsequent decrease of the THz amplitude in Fig. 4.11a. Since the Curie temperature of Py films is strongly reduced at low thicknesses [209], we suspect it is caused by the decrease of the saturation magnetization with the temperature of the sample.

Fig. 4.11c shows the corresponding THz waveforms measured by EOS, without compensating for the EOS-induced deformation. We can see that in addition to the amplitude, the change in energy is accompanied by a slight change in carrier-envelope phase (CEP). The total thermal expansion experienced by the 6.7 nm-thick sample for a 15°C heating is $9 \times 10^{-4} \text{ nm}$, which would delay a single-pass of the THz pulse by a negligible quantity. It appears more likely that the phase shift is caused by the rotation, which we did not quantify, of the two half-waveplates used to increase the pump energy while keeping the probe energy constant.

4.3.2 Identification of the origin of the signal

Considering the symmetry of the samples allows to isolate the parts of the THz signal that are of different origins. According to Eqs. (4.6) and (4.10), the polarity of a THz waveform generated by ISHE depends on the orientation of the magnetization and the direction of the spin current, which reflects the orientation of the FM|NM interface. The polarity of a THz waveform generated by magnetic dipole radiation in the FM layer depends only on the magnetization. Additionally, non-magnetic signals do not depend on the magnetization at all. Therefore, we can verify which phenomenon is at the origin of the THz field by inverting the direction of the magnetic field or changing which face of the sample is illuminated.

Fig. 4.12a shows an example of such a measurement for the sample $\text{Fe}^*|\text{Pt}$. As expected, when the magnetic field is inverted, the waveform follows. However, the amplitude and the pulse delay differ slightly. The same behavior was seen on all samples, pointing to a systematic non-magnetic component.

Fig. 4.12b shows the THz field emitted by $\text{W}|\text{Py}|\text{Pt}$, illuminating it from either the substrate side or the Pt side. The two waveforms are the inverse of each other, indicating that the THz signal originates from the ISHE and not from the demagnetization of the FM layer. The amplitude and phase difference can here be attributed to the displacement of the sample.

To investigate the origin of the non-magnetic component, we use the fact that according to the symmetry of the OI samples, rotating them by 180° in their plane should yield an identical result. This is shown for $[\text{Pt}|\text{Fe}^*]_2$ in Fig. 4.12c. As seen before, for both

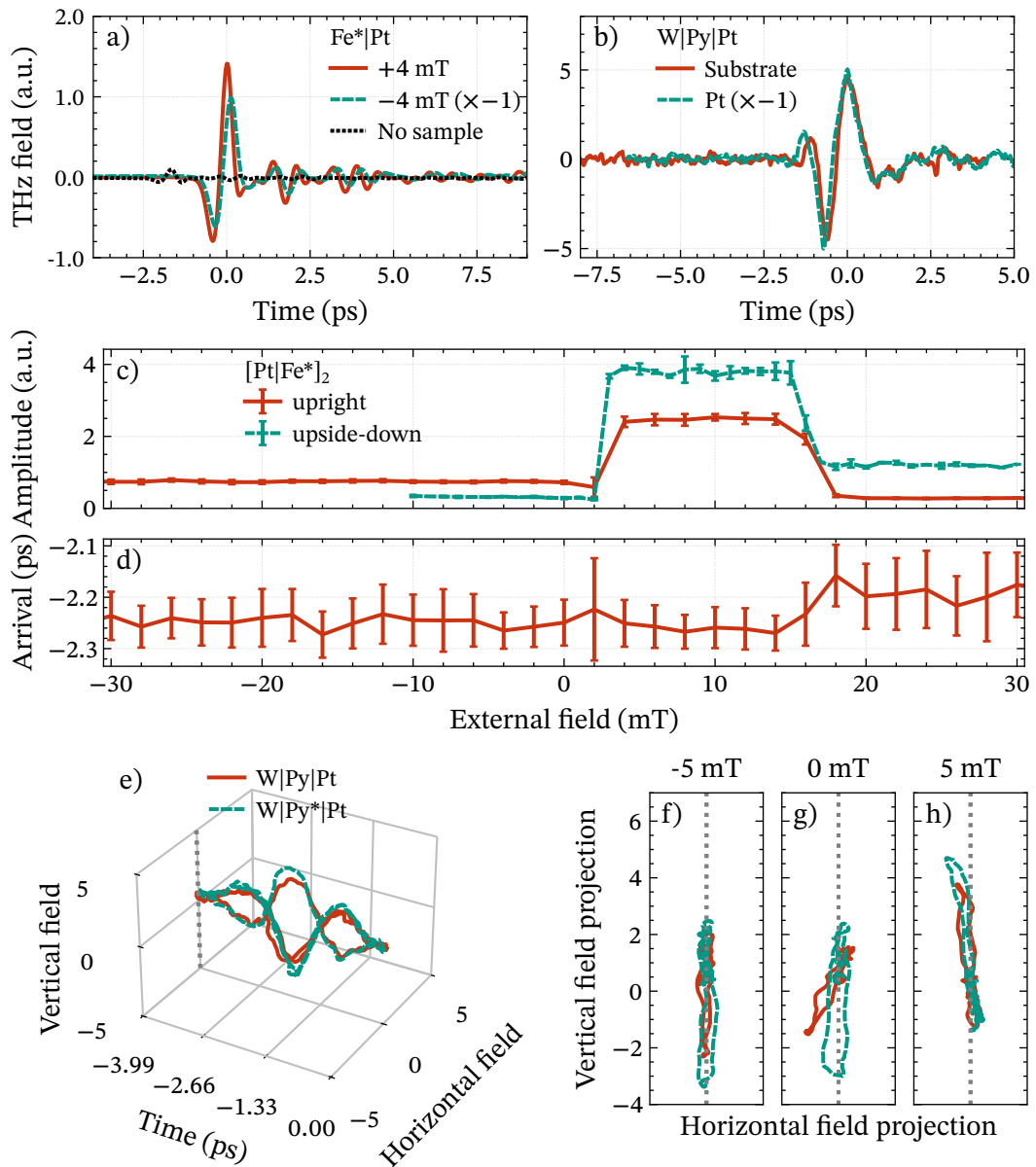


Figure 4.12: Asymmetry in the emitted THz. Amplitude difference when a) inverting the external magnetic field; b) changing the illuminated side; c) rotating the sample 180° along the laser propagation axis. d) Arrival time of the pulse, as defined by the peak of its envelope. e) Main part of the THz waveform of two samples only differing by the deposition method, taken at three different fields. f-h) Projection of the waveforms in e) on the surface normal to the propagation axis, showing a slightly elliptical polarization.

traces the THz amplitude is noticeably different when the magnetization direction is inverted. In addition, rotating the sample changes the overall THz amplitude and inverts the direction of the field for which the amplitude is higher. If the magnetic asymmetry was only due to the sample, the same amplitude should be seen at negative fields for the upright sample and at positive fields for the upside-down sample, and vice-versa. Hence, two effects seem to be at play: the THz output depends on the orientation of the magnetization along the easy axis, and the measured THz amplitude depends on the physical direction of the THz polarity.

The latter effect is linked to the polarization of the THz, as shown in [Figs. 4.12e to 4.12h](#) for W|Py*|Pt and W|Py|Pt. We measured the 3D shape of the THz waveforms by using a rotating polarizer to obtain both $\pm 45^\circ$ polarization components. The polarization is as expected mostly vertical (perpendicular to the magnetic field) and only weakly elliptical. At -5 mT, the main peak of the waveforms points down for both samples. At 0 mT, the polarization of W|Py|Pt is tilted, as the Py layer has no easy axis. At 5 mT, the main peak of the waveforms points up but with an additional tilt.

We found this behavior in all samples: the polarization is tilted when the main peak of the THz points up, regardless of the sign of the magnetic field for which this occurs. For trilayer samples, the tilt direction is always anticlockwise (as defined on the plot). It is this tilt that, when measured by EOS, results in a lower amplitude. The cause of the tilt is unknown, but is unrelated to the magnetic field and the sample direction, hence seems linked to the measurement setup.

Because each sample is glued on the copper holder, and the latter is manually reinstalled in the electromagnet before each new measurement, the easy axis of the sample can be tilted compared to the magnetic field. We aimed to mount the sample always in the same manner, with the help of a reference edge in the holder. By measuring on one occasion the angles on a photography of the mounted sample, we found a tilt of 1° between the sample and its holder, and using a spirit level a tilt of 2° in the opposite direction of the holder compared to the table. Assuming this was representative of the assembly of all samples, we expect only a $\sim 1^\circ$ bias in the THz polarization, which does not explain the systematic tilt.

Since the direction of the main peak depends on the direction of the current \vec{j}_c , it is possible that an initial difference in the path of the electrons leads to a difference in the propagation of the THz pulse. Due to the large difference in refractive index between the metallic layers and air, small deviations of the propagation direction inside the sample are then amplified in air, and can be transformed by the OAPs into a polarization rotation [210]. This hypothesis of a change in the beam path is supported by [Fig. 4.12d](#): the arrival time of the pulse, shown here for the upright [Pt|Fe*]₂ sample, changes by up to ~ 100 fs as the sample switches.

4.3.3 Influence of OID

We have established that the setup is able to produce and detect THz radiation, and that most of the signal originates from the ISHE. We now investigate the influence of the deposition methods employed for the FM layers, in order to demonstrate that the OID confines the magnetization and examine whether it affects the THz output.

We compare two samples identical except for the deposition method of the FM layer: $\text{Fe}^*|\text{W}$ ($\theta = 60^\circ$) and $\text{Fe}|\text{W}$ ($\theta = 0^\circ$). The surface roughness induced by OID is transmitted to the W layer deposited above it. Both samples emit THz at one interface only, as illustrated in Fig. 4.13.

The goal of the OID is to increase the anisotropy of the Fe layer so that the magnetization has only two states: aligned in either direction along the easy axis. Fig. 4.14a shows the hysteresis curves of both samples, with the magnetic field applied along the easy axis. We can see that without OID, the magnetization of $\text{Fe}|\text{W}$ switches progressively following the field. $\text{Fe}^*|\text{W}$ shows on the contrary a behavior close to an ideal hard magnet: it has a coercivity of 1 mT and retains its saturation magnetization until the field exceeds the OID-induced anisotropy, at which point it switches abruptly.

The effect is reflected in the THz polarization. As already mentioned in Section 4.3.2, it is linear and approximately vertical, but we observe a slight asymmetry with respect to the switching field. Fig. 4.14b shows the average linear fit of the tilt of the polarization. Excluding a step at ~ 2 mT when its magnetization switches, the polarization of the THz radiation emitted by $\text{Fe}^*|\text{W}$ is constant, indicating that the axis of the magnetization is stable. By contrast, the polarization of $\text{Fe}|\text{W}$ starts rotating as the field approaches 0 mT and reaches a maximum tilt of 15° at $+0.6$ mT, before realigning when the magnetization is again saturated. The large error bars around the switching point indicate that the average orientation of the magnetic domains in the absence of field is random.

Fig. 4.14c shows one measurement of the THz amplitude for both samples. That $\text{Fe}^*|\text{W}$ generates a higher THz amplitude than $\text{Fe}|\text{W}$ was not seen in all measurements of both samples and can be due to either an alignment difference or an actual difference in the thickness of theoretically identical samples. Both samples exhibits a dip in their emission at their switching field. There is an offset in the switching fields compared

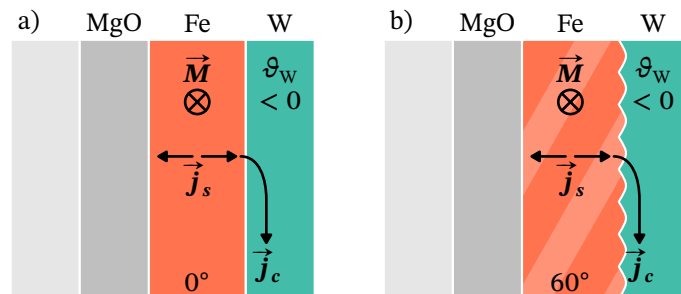


Figure 4.13: Schemes of a) $\text{Fe}|\text{W}$ and b) $\text{Fe}^*|\text{W}$.

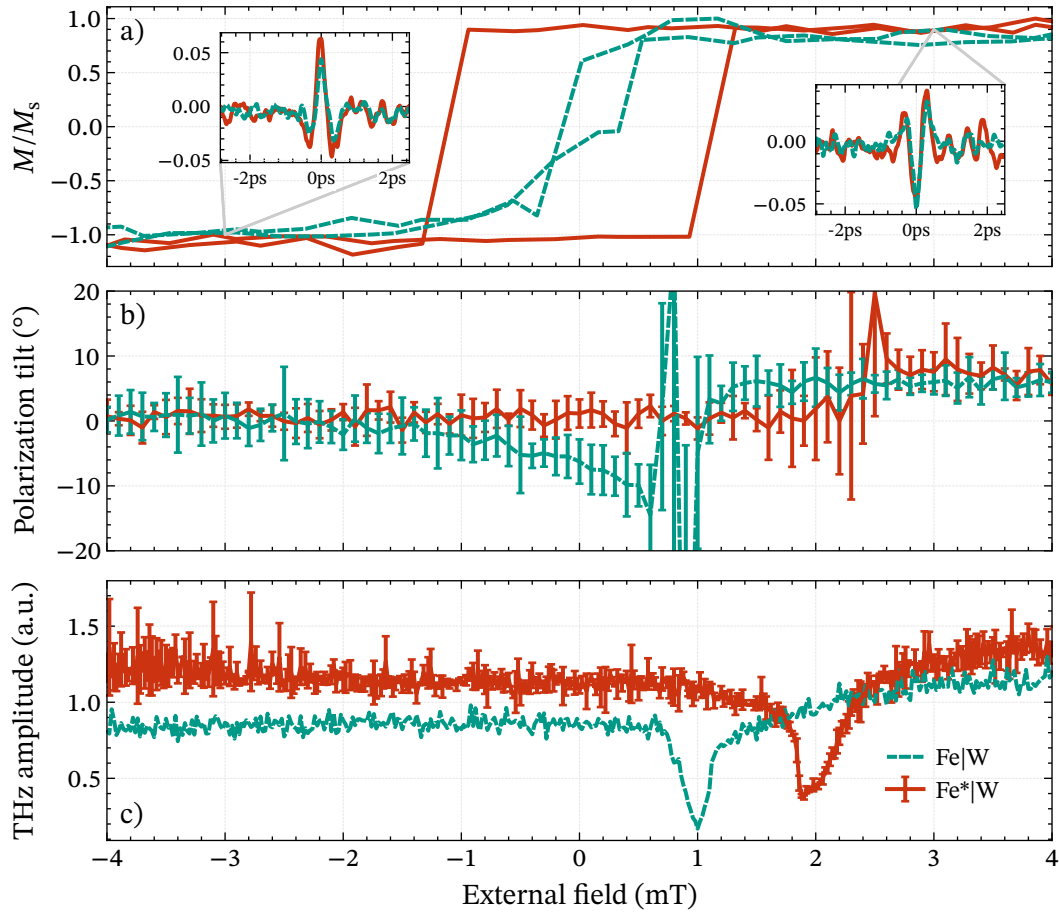


Figure 4.14: Measurements of Fe*|W (red) and Fe|W (blue). a) Hysteresis curves. Inserts: EOS traces taken at the indicated field. b) Fitted polarization tilt. The error bars denote the standard deviation of the resulting tilt for repeated measurements. c) Measured THz amplitude while increasing the external field.

to the magneto-optic Kerr effect (MOKE) measurement, which can be caused by the illuminated part of the sample not being exactly located where the magnetic field was measured (Section 4.2.2.1).

The decrease in THz amplitude of both samples shows the apparition of magnetic domains. As the external field approaches zero, the magnetization of each domain reverts to its own easy axis. In the case of Fe|W, since the layer is polycrystalline, the distribution of the domain orientations is isotropic in the plane of the sample, and can theoretically span half of the disk as the field is removed. With this model, the remanence magnetization of Fe|W is $M/M_s \approx 0.6$, which is difficult to confirm from the MOKE measurement. In the case of Fe*|W, the easy axes of the domains, at least on the

upper surface of the layers, are constrained by the OID anisotropy, thus its remanence magnetization is 1.

The THz polarization of each sample confirms the difference in behavior of the domains. We observe the center of the sample, where the magnetic field from the electromagnets is the weakest. In the case of Fe|W, the polarization starts to rotate before the change in amplitude, which indicates that as the magnetic field disappears, the average magnetization rotates, probably to align on a surrounding background field. Then as the field is increased, the Fe layer breaks into domains, whose magnetization rotates in a non-reproducible way to align again on the field from the electromagnet. In the case of Fe*|W, the decrease in THz amplitude is only accompanied by larger error bars in the polarization measurement, as domains are unable to tilt away from the OID axis. The domains on the edges of the sample near the electromagnet switch first, leading to a large frustration of the exchange interaction as domains have an antiparallel alignment. After a quick drop in THz amplitude, the observed domains realign as well.

4.3.4 AFM samples

We have seen that the magnetization of FM layers fabricated with the OID method is as expected confined to the easy axis imparted during the deposition. We now introduce the five-layer samples with two FM layers, that make use of this technique to control the relative orientation of their magnetizations. In [Section 4.3.4.1](#), we will observe this decoupling of the two FM layers, then in [Section 4.3.4.2](#) we will examine the THz generation efficiency of such samples. Finally, simulations of the spin current and THz generation are presented in [Section 4.3.4.3](#).

4.3.4.1 FM and AFM states

Trilayer samples are so thin that less than half of the pump power is absorbed. Following the same principle of alternating NM materials with opposite spin Hall angles (see [Section 4.2.1.3](#)), we expect to be able to enhance the THz output by stacking more layers to make use of the remaining pump power. As shown by [Fig. 4.15](#), because of the mirror symmetry of the sample structure, the charge currents from each half are parallel when the magnetizations are antiparallel, forming an artificial antiferromagnet. Other groups came to the same idea and achieved this using an antiferromagnetic exchange coupling between the FM layers [[187](#), [211](#)] to lock their relative magnetization, or two FM layers with respectively a free and a pinned magnetization [[188](#)]. Instead, we used the OID technique to give a different anisotropy to each FM layer and investigated the possible parameters to increase the range between the switching fields of both layers.

[Fig. 4.16](#) shows the measurements of two such samples, [Pt|Fe*|W]₂ and [Pt|Fe*]₂. During the sputtering of the samples, the polar deposition angle φ was kept constant so the FM layers have the same easy axis, but we used a different azimuthal angle for

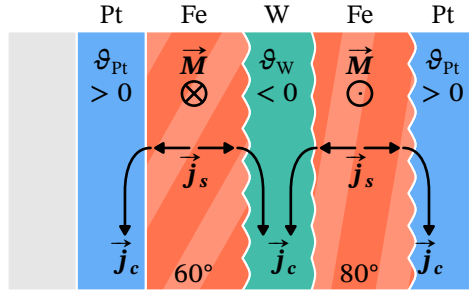


Figure 4.15: Scheme of $[\text{Pt}|\text{Fe}^*|\text{W}]_2$ in the antiferromagnetic configuration. In $[\text{Pt}|\text{Fe}^*]_2$, the central W layer is replaced by MgO, where no THz emission occurs.

the first ($\theta = 60^\circ$) and second ($\theta = 80^\circ$) FM layer to compel them to switch at different fields. Fig. 4.16a shows their hysteresis curves measured by MOKE along their easy axis. Similarly to simple trilayer OID samples presented in the last section, they have a high coercivity and a square-shaped hysteresis curve. In addition, they distinctively switch in two steps, one FM layer after the other. For comparison, a MOKE measurement along the hard axis of such a sample shows a smooth hysteresis curve with little structure.

The field at which the switching occurs depends on the anisotropy of each FM layer but also on the interlayer exchange coupling. In the absence of coupling, the layers can switch independently, which maximizes the range in which they are in an antiferromagnetic configuration. With the FM layers separated by a 4 nm insulating MgO layer, $[\text{Pt}|\text{Fe}^*]_2$ has a 17 mT-wide range. In the case of $[\text{Pt}|\text{Fe}^*|\text{W}]_2$, the interlayer exchange coupling transmitted by the 4 nm W layer reduces the antiferromagnetic range to 2.5 mT. The similar $[\text{W}|\text{Fe}^*|\text{Pt}]_2$ sample, despite having a thicker central 5 nm Pt layer, showed after several uses a reduced antiferromagnetic range of 0.2 mT. A more successful decoupling of the FM layers using W rather than Pt was also reported by Fix et al. [188].

Fig. 4.16b shows the corresponding THz amplitude when measuring the samples along the lower branch of the hysteresis curve. Both have a high emission in the range where the total magnetization is zero, namely in the antiferromagnetic configuration, due to the fact that all charge currents have the same sign. Outside of this range, the magnetizations are in a ferromagnetic configuration, and the THz radiation emitted from both halves of the samples partially cancel each other.

4.3.4.2 Efficiency of the samples

One interesting observation from Fig. 4.16b is that while $[\text{Pt}|\text{Fe}^*|\text{W}]_2$ has four interfaces at which the ISHE can happen and $[\text{Pt}|\text{Fe}^*]_2$ only two, the amplitude of their THz output in the antiferromagnetic configuration is similar. Comparing the absolute amplitude of the THz emitted by different samples proved difficult. Due to short-term fluctuations of the laser energy, measurements of the THz amplitude were typically repeated by scanning the magnetic field several times in a row. However these long measurements are sensitive

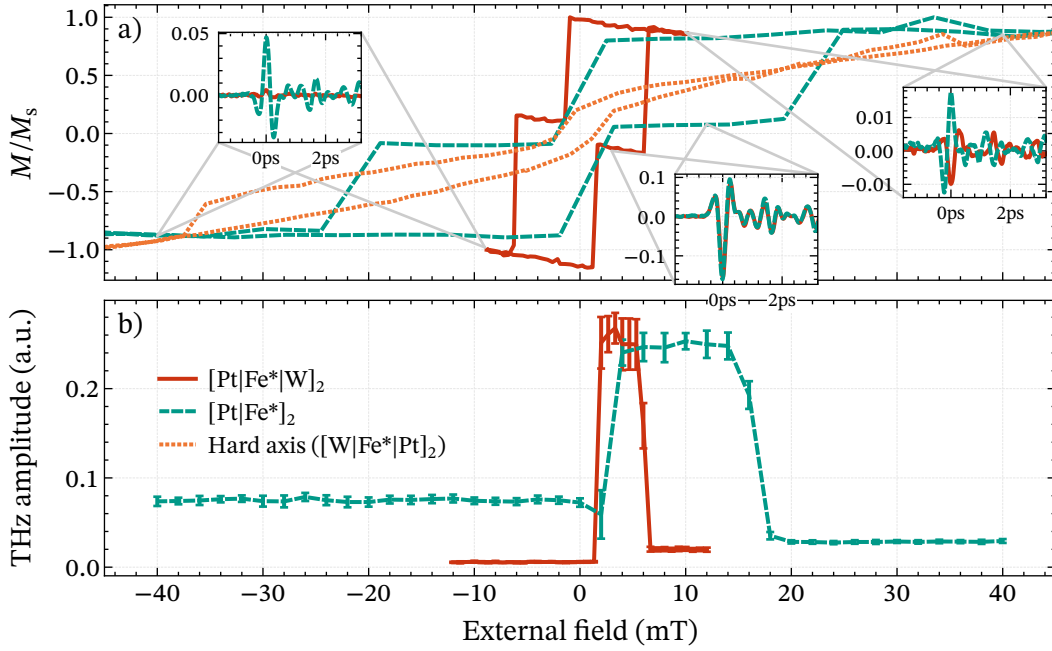


Figure 4.16: Measurements of $[\text{Pt}|\text{Fe}^*|\text{W}]_2$ (red) and $[\text{Pt}|\text{Fe}^*]_2$ (blue). a) Hysteresis curves of both samples along the easy axis, and for comparison one of a different sample along the hard axis. Inserts: EOS traces taken at the indicated fields for each magnetization configuration of the samples. b) Measured THz amplitude when increasing the external field.

to the slow drift of the laser energy. In addition, as mentioned in Section 4.2.2.4, the amplitude of the measured EOS signal was later found to depend on the probe alignment as well.

Fig. 4.17a shows the evolution of the THz amplitude emitted by $[\text{Pt}|\text{Fe}^*]_2$ with the increase of the pump energy. Two half waveplates were used to change the total energy entering the setup while keeping constant the energy going into the probe beam. As also seen in Fig. 4.16b and as found in all samples (see Section 4.3.2), the THz amplitude emitted by $[\text{Pt}|\text{Fe}^*]_2$ when its magnetization is saturated (in FM configuration) depends on the direction of the magnetic field. The amplitude ratio between the three magnetizations configurations is approximately constant over the whole plot. In both FM and AFM configurations, the THz amplitude increases at an average rate of $\sim 0.2\% \mu\text{J}^{-1}$ with respect to the amplitude at $180 \mu\text{J}$. A similar result was found by Yang et al. [212] for a sample consisting of the same materials, whose emitted peak THz field increases by $0.11\% \mu\text{J}^{-1}$ with respect to its amplitude at $200 \mu\text{J}$ between $200 \mu\text{J}$ to $360 \mu\text{J}$. This allows us to assume that the spin current responds linearly with the pump energy as given in Eq. (4.3).

Contrarily to the result for $\text{W}|\text{Py}^*|\text{Pt}$ in Fig. 4.11, whose THz emission started deca-

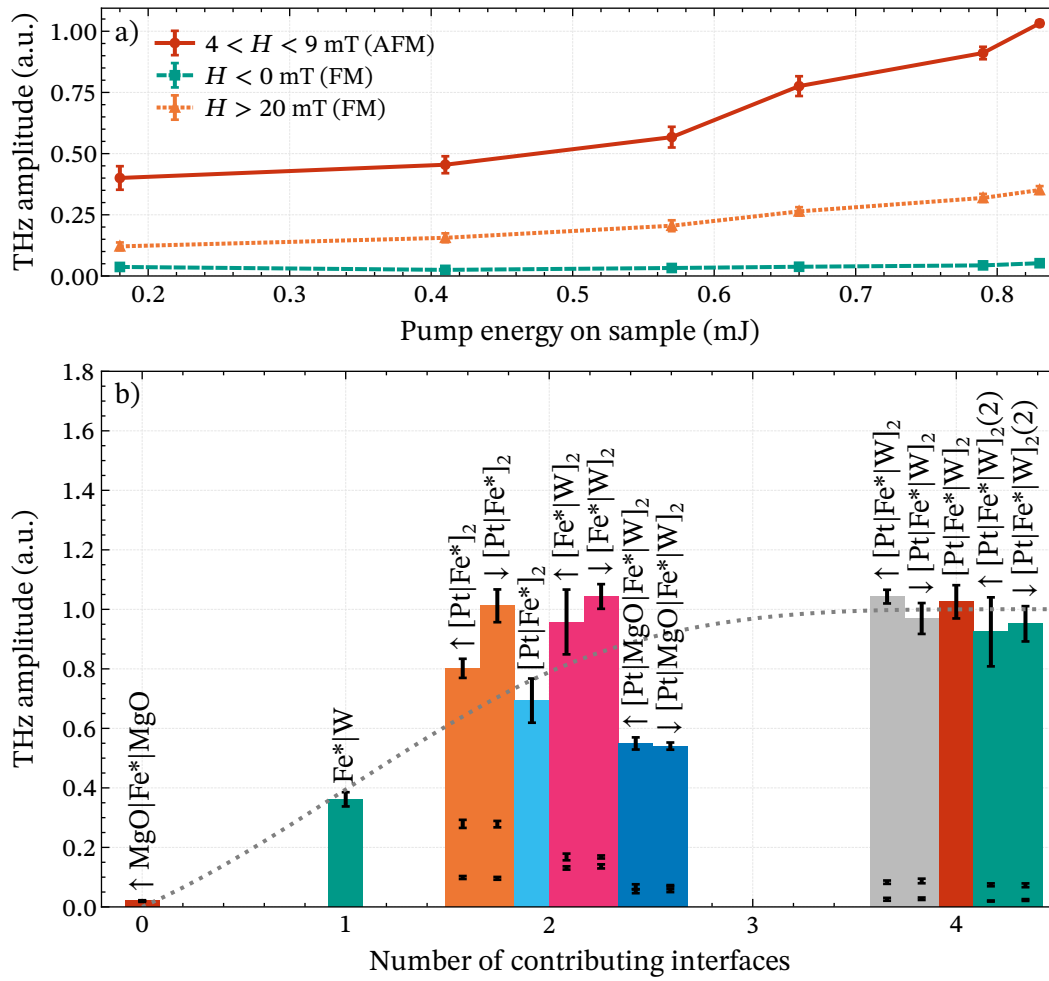


Figure 4.17: Factors contributing to the THz output. a) Amplitude of the THz field emitted by $[\text{Pt}|\text{Fe}^*]_2$ as a function of the pump energy and external magnetic field. b) Average THz amplitude generated by different samples as a function of their number of FM|NM interfaces. For five-layer samples, the bar represents the output in the AFM configuration, and errorbars inside the bar represent the two FM configurations. Arrows to the right (left) above the bars indicate amplitudes measured while increasing (decreasing) the magnetic field. These amplitudes were obtained during a single scan of the magnetic field by averaging over different fields. The absence of arrow indicate the amplitudes obtained by averaging successive measurements at a single field. The dotted line is a guide to the eye for the overall maximum output of each sample.

ing for a pump fluence around $300 \mu\text{J cm}^{-2}$, the output here shows no saturation as high as $830 \mu\text{J}$, or 8.4 mJ cm^{-2} . One of the reasons for this difference is the thickness and composition of the sample: at equal pump fluence, the two Fe layers of $[\text{Pt}|\text{Fe}^*]_2$ absorbs less energy each than the single Py layer of $\text{W}|\text{Py}^*|\text{Pt}$. Additionally, the current in Py has a greater spin polarization than in Fe, due to the larger difference in mean-free path between majority and minority electrons [11, 213]; this results in a quicker saturation of the spin-majority conduction bands in the NM layers [155].

Fig. 4.17b shows a comparison of the THz output of many different samples. A first set consists of $\text{MgO}|\text{Fe}^*|\text{MgO}$, $[\text{Pt}|\text{Fe}^*]_2$, $[\text{Fe}^*|\text{W}]_2$, $[\text{Pt}|\text{MgO}|\text{Fe}^*|\text{W}]_2$, $[\text{Pt}|\text{Fe}^*|\text{W}]_2$ and the nominally identical sample $[\text{Pt}|\text{Fe}^*|\text{W}]_2(2)$, which were measured in rapid succession one after the other. $[\text{Pt}|\text{Fe}^*|\text{W}]_2(2)$ was measured first and last to confirm that the sensitivity of the measurement was not impacted by any drift of the laser energy nor probe alignment during the measurement series. For each of these samples, we scanned the external field once in each direction. The plotted THz amplitudes are thus the average over the different fields for which the magnetization is in the same configuration. A second set of samples, consisting of $\text{Fe}^*|\text{W}$, and again $[\text{Pt}|\text{Fe}^*]_2$ and $[\text{Pt}|\text{Fe}^*|\text{W}]_2$ were measured later, after realignment of the laser. For each sample, we repeated several times the measurement of only one field, in the antiferromagnetic configuration. By coincidence, both measurements of $[\text{Pt}|\text{Fe}^*]_2$ and $[\text{Pt}|\text{Fe}^*|\text{W}]_2$ yielded an almost identical amplitude. It is thus assumed that the two sets of measurements are comparable, and their relative amplitudes are not corrected.

The ferromagnetic configuration of five-layer samples is shown as error bars inside to the main bar. As expected, we can see that for all samples, the THz amplitude when the samples are saturated is the same irrespective of along which branch of the hysteresis curve was the field scanned (full vs. empty markers). However, there is an offset between the THz amplitude depending on the direction of the saturating magnetic field. This offset, also visible in Fig. 4.17a and Fig. 4.16b, is the biggest for $[\text{Pt}|\text{Fe}^*]_2$.

The dotted line indicates the overall evolution of the maximal THz output compared to the number of emitting FM|NM interfaces. $\text{MgO}|\text{Fe}^*|\text{MgO}$ emits almost zero signal, confirming that, as expected from the study of the symmetry of the signal in Section 4.3.2, the THz emission come from the inverse spin Hall effect. The existing THz signal can be attributed to THz generation in the Ge filter reflecting the IR pump away from the EOS setup.

$\text{Fe}^*|\text{W}$ has a single interface, and reaches 40 % of the emitted field of an average five-layer sample. It will thus be necessary to investigate how much the sample thickness and materials are influencing the THz output.

Five-layer samples with two contributing FM|NM interfaces have a large variation of output amplitude, presumably because of their diversity of structure. The THz radiation in $[\text{Pt}|\text{Fe}^*]_2$ is generated in the outside layers, while for $[\text{Fe}^*|\text{W}]_2$ it is generated in the central layer. Both have a noticeable difference in measured amplitude depending on the branch of the hysteresis curve, explained in Section 4.3.2 by a difference in the THz

polarization. $[\text{Pt}|\text{MgO}|\text{Fe}^*|\text{W}]_2$ has an additional MgO layer inserted between the FM layers and the external NM layers, blocking the spin current. Compared to $[\text{Fe}^*|\text{W}]_2$, it is presumably the additional Pt layers that are responsible for reducing the THz amplitude by absorbing the pump.

Since $[\text{W}|\text{Fe}^*|\text{Pt}]_2$ was unable to maintain an antiferromagnetic configuration, the only samples with four contributing FM|NM interfaces are the nominally identical $[\text{Pt}|\text{Fe}^*|\text{W}]_2$ and $[\text{Pt}|\text{Fe}^*|\text{W}]_2(2)$. They have a very similar but not identical output, as can be expected from the difficulty of sputtering identical layers at the nm scale. Compared to $[\text{Pt}|\text{MgO}|\text{Fe}^*|\text{W}]_2$, which has the same metallic layers but half the number of contributing interfaces, they emit almost double the THz signal.

Overall, it seems that the gain from increasing the amount of contributing interfaces is partially canceled out by the losses from the additional metallic layers. The same behavior was seen by Yang et al. [212], who obtained a decreasing THz output with samples consisting of more than three stacked Pt|Fe|MgO structures.

4.3.4.3 Simulations of the THz emission

We have seen that the structure and materials of the samples influence heavily the THz generation. We are now interested in verifying whether the THz amplitude is entirely predicted by the optical properties of the samples, or whether the spin current is affected.

The relevant equations were described in Section 4.1. Given a stack of layers defined by a material and a thickness, we calculate the distribution of the absorbed IR power and deduce the strength of the generated spin currents. Estimating the efficiency of the spin-to-charge current conversion depending on the material, we then calculate the generated THz field at each interface and the total THz field exiting the sample.

Table 4.3 presents the fraction of pump energy absorbed in the samples previously shown in Fig. 4.17b, calculated for the pump incident on the substrate side. Because of the multiple internal reflections of the IR beam, the energy is well distributed throughout the samples and the FM layer on the substrate side absorbs at most 10% more energy than the other layer. The substrate and MgO layers are transparent for the IR, so that the absorption patterns in $[\text{Pt}|\text{MgO}|\text{Fe}^*|\text{W}]_2$ and $[\text{Pt}|\text{Fe}^*|\text{W}]_2$ are equivalent and their difference in THz emission is well explained by their different amount of contributing FM|NM interfaces. Within the samples with two contributing interfaces, the THz emission scales roughly with the absorption in the FM layers. However, the single iron layer of $\text{Fe}^*|\text{W}$ absorbs slightly more energy than the two irons layers combined of $[\text{Pt}|\text{MgO}|\text{Fe}^*|\text{W}]_2$, and yet has a significantly lower THz emission. As the spin current is proportional to the absorbed power (Eq. (4.3)) and the ISHE occurs for both samples at $\text{Fe}|\text{W}$ interfaces, we expect the total THz emission to be similar. There is thus another factor at play in these samples: the THz propagation.

As detailed in Appendix C, we use transfer matrices to calculate the propagation of the THz field from the FM|NM interface where it is emitted, to the output interface of the

Table 4.3: Fraction of pump power absorbed by full spintronic THz emitters and by each of their FM layers, and fraction of THz electric energy at the sample output, on the side opposed to the substrate, compared to the energy emitted by each THz source at an FM|NM interface. The values are given in the order of the interfaces in the sample, assuming that the pump is incident on the side of the substrate.

Sample	Pump power			THz energy output ($\times 10^{-3}$)			
	Total	In FM layers		In NM layers			
MgO Fe* MgO	37.6 %	37.6 %	-	-	-	-	-
Fe* W	48.8 %	32.7 %	-	3.49	-	-	-
Fe* Pt	54.3 %	29.6 %	-	4.17	-	-	-
[Pt Fe*] ₂	69.6 %	19.5 %	17.8 %	3.68	-	3.76	-
[Fe* W] ₂	67.3 %	22.9 %	22.3 %	4.76	-	4.89	-
[Pt MgO Fe* W] ₂	72.5 %	16.1 %	14.5 %	4.76	-	4.89	-
[Pt Fe* W] ₂	72.7 %	16.2 %	14.7 %	4.83	3.17	3.25	4.88

sample on the exterior side. The refractive index and absorption coefficient of the metals are two orders of magnitude higher for the THz frequencies than for the 800 nm pump (see TDS measurements in [Appendix A](#)), so it is heavily absorbed. The last four columns of [Table 4.3](#) shows the proportion of energy on the THz beam exiting the sample. Here too, the many internal reflections homogenize the THz field so that the output of all sources is similar, irrespective of their distance to the exit surface. The output of Fe*|W is about 25 % lower than the output of each THz source in [Pt|MgO|Fe*|W]₂, which is enough to compensate its stronger spin current and reduce the THz amplitude as observed in [Fig. 4.17b](#).

We now recall the two samples from [Fig. 4.16](#), [Pt|Fe*]₂ and [Pt|Fe*|W]₂: although their THz output is almost identical in the antiferromagnetic state, the waveforms and their amplitudes in the ferromagnetic states are very different. To understand this, we now need to simulate the THz output. For this, we are missing one last component: the values of the interface transmission coefficients $t_{\text{Fe|W}}$ and $t_{\text{Fe|Pt}}$ in [Eq. \(4.7\)](#).

The coefficients are fitted from measurements of reference samples, Fe*|W and Fe*|Pt. These samples have a single FM|NM interface each, are identical except for the material of the NM layers, and are measured in the same experimental conditions. As shown in [Fig. 4.18a](#), although the spin Hall angle of W is almost an order of magnitude larger

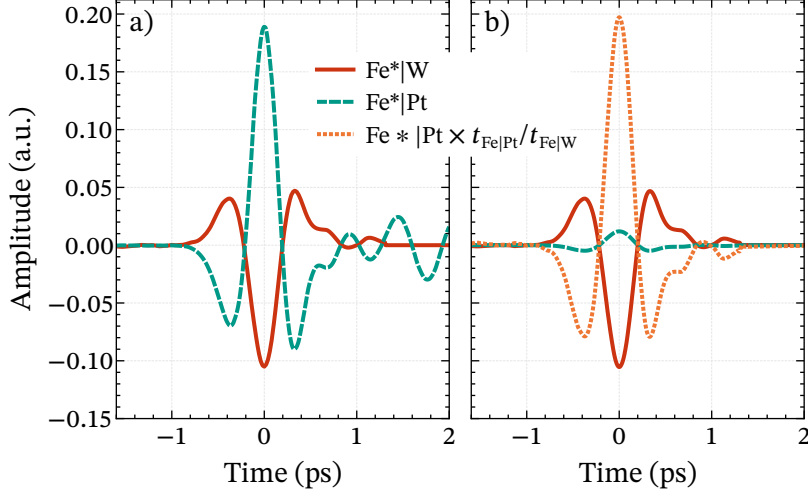


Figure 4.18: a) Experimental and b) simulated THz waveforms from the bilayer samples. The transfer function $T_{\text{prop}}(\omega) T_{\text{EOS}}(\omega)$ for the THz propagation after the samples was calculated from Fe*|W.

($\vartheta_{\text{W}} = -33\%$ and $\vartheta_{\text{Pt}} = 4.2 \pm 2.9\%$), the output of Fe*|Pt is twice higher. Light propagation is unable to explain the difference: according to Table 4.3, the FM layer of Fe*|W absorbs slightly more IR power, but the THz output of Fe*|Pt is slightly higher for equal emission, so the purely optical properties only account for the emission of Fe*|Pt being 8% higher. We assume that the discrepancy is caused by the material-dependent transmission of the spin current through the FM|NM interface.

From Eq. (4.7), the THz amplitude is proportional to the transmission factor $t_{\text{Fe}|x}$. The ratio of the amplitudes of both samples is thus:

$$R = \frac{E_{\text{W}}}{E_{\text{Pt}}} = \frac{t_{\text{Fe}|W} \vartheta_{\text{W}} j_{\text{s}}(\text{W}) T_{\text{W}}}{t_{\text{Fe}|Pt} \vartheta_{\text{Pt}} j_{\text{s}}(\text{Pt}) T_{\text{Pt}}} \quad (4.18)$$

where T_x is the transfer function of the THz field in the sample Fe*| x . The experimental ratio is $R_{\text{exp}} = 0.546$ (Fig. 4.18a). If we do not consider the interface transmission, $t_{\text{Fe}|W} = t_{\text{Fe}|Pt} = 1$ and we obtain $R_{\text{sim}} = 8.98$ (Fig. 4.18b). As expected from their spin Hall angles, the output of Fe*|Pt would be significantly smaller than that of Fe*|W. Using these two values, we have:

$$\frac{t_{\text{Fe}|Pt}}{t_{\text{Fe}|W}} = \frac{R_{\text{sim}}}{R_{\text{exp}}} = 16.4. \quad (4.19)$$

To take the interface transmission into account in the simulations, whose absolute amplitude is not calibrated, we simply use:

$$j_{\text{c}}(\text{Pt}) = \frac{t_{\text{Fe}|Pt}}{t_{\text{Fe}|W}} \vartheta_{\text{Pt}} j_{\text{s}}(\text{Pt}); \quad j_{\text{c}}(\text{W}) = \vartheta_{\text{W}} j_{\text{s}}(\text{W}), \quad (4.20)$$

so that the relative amplitudes of emissions from Fe|W and Fe|Pt interfaces match the measurements, as shown by the rescaled waveform in Fig. 4.18b. This process does not

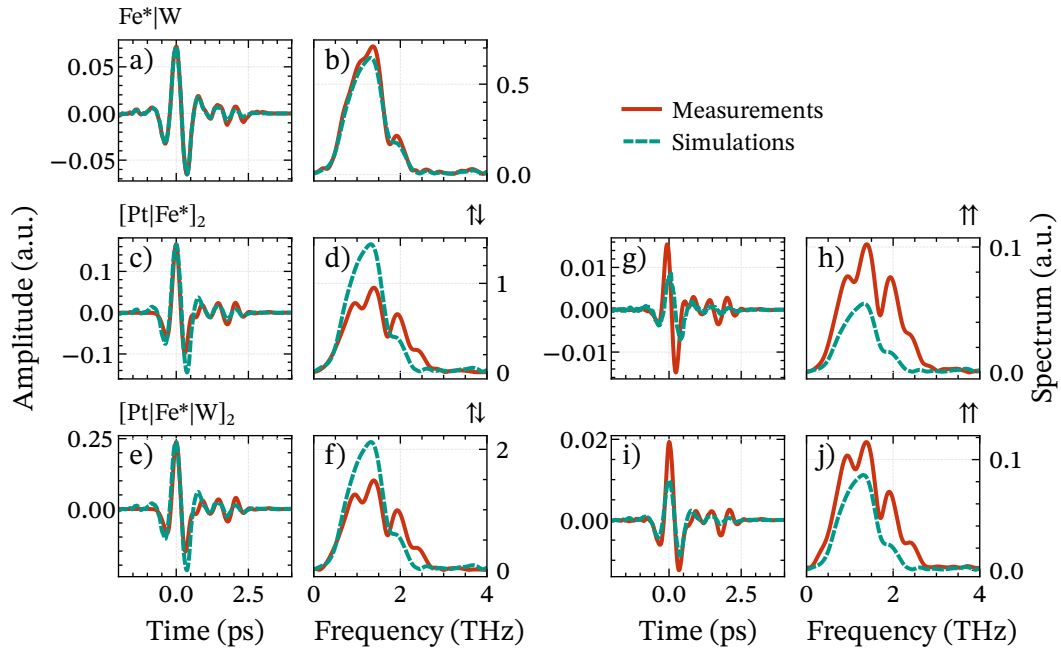


Figure 4.19: Comparison of measured and simulated samples. Each line corresponds to a sample. The arrows indicate the magnetization configuration: c–f) antiferromagnetic and g–j) ferromagnetic.

change the shape of the waveforms, thus we can now see that the CEP of $\text{Fe}^*|\text{Pt}$ is not perfectly reproduced.

With this value, we are now able to simulate samples with both types of interfaces as well as compare the THz output from different samples. Fig. 4.19 shows the THz waveforms and spectra for $[\text{Pt}|\text{Fe}^*]_2$ and $[\text{Pt}|\text{Fe}^*|\text{W}]_2$ as well as $\text{Fe}^*|\text{W}$ for reference. The measured waveforms are averaged over several successive measurements at the same magnetic field. Their amplitudes are the same as shown in Fig. 4.17b. The transfer function for the THz propagation and detection was calculated for $\text{Fe}^*|\text{W}$ by comparing the measured THz waveform and the simulated waveform at the output of the sample. The same transfer function was then applied to the simulated THz waveforms of the other samples. The difference in the experimental waveforms of $\text{Fe}^*|\text{W}$ between Figs. 4.18a and 4.19a is due to alignment differences in the experimental setup between both measurements. For this reason, the transfer function of the THz propagation is individual to each set of measurements.

For both five-layer samples in both of their configurations, we can see that the CEP of the simulated waveforms is similar to the CEP of the measured waveforms. The shape of the simulated pulses is entirely controlled by the propagation transfer function: at the output of the sample, the electric field of each THz emission looks like a single positive peak followed by a long negative tail (shown in Fig. 4.3a). The similarity of the waveforms

thus indicates that the propagation transfer function is adequate. The measured spectra have however a strong peak at 2 THz which is not as prominent in the simulated spectra, and which we presume to be due to a difference in the THz propagation due to the additional thickness of the five-layer samples.

In the AFM magnetization configuration (Figs. 4.19c to 4.19f), the simulated amplitude is too high for both samples, indicating that there are losses our model does not take into account, either in the samples themselves or in the THz propagation. In the FM magnetization configuration (Figs. 4.19g to 4.19j), it is the opposite. In this state, the THz fields of each half of the sample have the opposite polarity and should cancel each other, which means that there are differences between both halves that the model does not take into account. Since all THz waveforms have the same shape at the output of the sample, only their relative amplitudes and delays determine how efficiently they cancel out.

The simulations assume that each THz emission takes place when the IR pump is first reaching the relevant FM layer, and do not take into account the diffusion time of the currents. In $[\text{Pt}|\text{Fe}^*|\text{W}]_2$, this leads to a first 0.087 fs delay between the emissions of each half of the sample. Since the spin current is not saturated, the photoexcitation of electrons and the launch of the spin current is an ongoing process while the IR beam is reflected internally. This is thus an absolute upper bound on the IR-caused delay.

Then the internal propagation of the THz fields further delays each component: in $[\text{Pt}|\text{Fe}^*|\text{W}]_2$, the emission at the Fe|Pt interface on the output side is the first to arrive outside, followed by the emission of each interface in order, with delays of 3.05 fs, 4.58 fs and 5.34 fs. The THz propagation itself is thus the biggest contributor to the delay between the emissions of both halves of the sample, but this delay is nonetheless negligible compared to the duration of the THz pulse.

This model neglects any difference in the propagation speed of the spin current through the different FM|NM interfaces and in the NM layers. Since the samples are symmetrical, adding such a difference would impact the coherence of the emission within each half of the sample, but not contribute to the delay between both halves. It would thus decrease the THz amplitude in both magnetization configurations for $[\text{Pt}|\text{Fe}^*|\text{W}]_2$ but not $[\text{Pt}|\text{Fe}^*]_2$. In addition, any significant delay between the THz components would lead to a change in the shape of the final waveforms, which would not be corrected by the propagation transfer function calculated from $\text{Fe}^*|\text{W}$. This effect is thus unlikely to be the cause of the amplitude differences between the simulations and the measurements.

Having excluded all sources of timing mismatch between the THz emissions from each half of the samples, the remaining option is an amplitude mismatch. In the simulations, the THz field in the FM configuration is calculated by inverting the THz emission from the second half of the sample, thus assuming that the magnetization of the second FM layer is switched. Since the polarity of the measured waveforms is the same in FM and AFM configurations for both samples, we know that the second half of the sample emits less than the first.

A potential cause of imbalance is the magnetization of the FM layers. The relative

permeability $\mu_r = 1 + \chi_{\text{eff}}$ (see Section 3.1.4) is involved in the calculation of the Fresnel coefficients and the Poynting vector for the IR pump [214]. Fully magnetized FM layers have $\chi_{\text{eff}} = dM/dH = 0$, as a small magnetic field does not modify the magnetization. The partial demagnetization of Fe recovers after several picoseconds [215] and thus overlaps with the propagation of the THz pulses. We used $\mu_r = 1$ in the simulations, and obtain with it the best match for the proportion of IR energy transmitted by the samples: 24.8 % vs. 27.4 % for $[\text{Pt}|\text{Fe}^*]_2$ and 20.5 % vs. 15.8 % for $[\text{Pt}|\text{Fe}^*|\text{W}]_2$. Using $\chi_{\text{eff}} > 0$ reduces the absorption in the FM layers and thus decreases the THz amplitude in the AFM configuration, while increasing the proportion of remaining THz in the FM configuration, but it worsens our estimations of the pump transmission.

Another potential cause of imbalance is the fact that the FM layers are deposited on different materials, which was reported to influence their saturation magnetization [188]. This affects the spin polarization of the currents, and thus has a direct influence on the THz amplitude in each half of the sample. Finally, the difference in surface quality of the FM|NM interfaces likely plays a role: the first NM layer is deposited on the polished substrate, while the others are deposited above one or two OID layers, which have a rougher surface. As the surface quality influences the transmission of the spin current [216], this would reduce the amount of THz emitted by the second half of the sample.

While we can only conjecture which effects or combinations thereof are responsible for the mismatch in THz amplitudes, we estimate it is most likely that the latter two effects are impairing the extinction in the FM state. The THz emission is otherwise satisfactorily reproduced by the model.

4.3.5 Orthogonal magnetizations

As a final experiment, we investigated the consequences of a five-layer sample having FM layers with different easy axes. The $[\text{Fe}^{90}|\text{W}]_2$ sample has, like the others, two FM layers deposited with incidence angles of $\theta = 60^\circ$ and 80° , respectively. However, we now change the polar direction of deposition to $\varphi = \pm 45^\circ$, so that the easy axis is of each layer is now parallel to a diagonal of the sample, as shown in Fig. 4.20. The central layer is thickened to 4 nm to avoid any spin-transfer torque between the FM layers.

4.3.5.1 Expectations

With the sample mounted in the electromagnet, the magnetic field is now as a 45° angle from the easy axes of the sample. At high fields, we can expect that the OID anisotropy is not enough to maintain the magnetization of each layer in its easy axis. We used the equations in Section 3.3.2 to model the orientation of the magnetization of each FM layer when scanning the magnetic field. For iron, the assumed saturation magnetization is $\mu_0 M_s = 2.15 \text{ T}$ [99, table 7.3.1]. Since the FM layers of $[\text{Fe}^*|\text{W}]_2$ switch

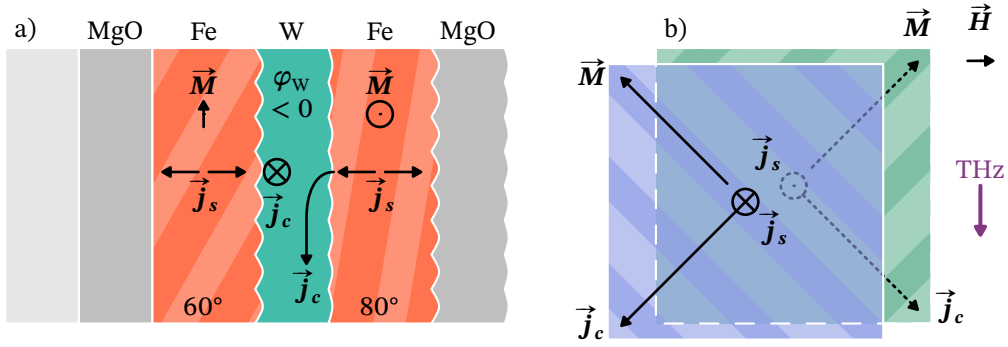


Figure 4.20: Scheme of $[\text{Fe}^{90}|\text{W}]_2$. a) Cut along the beam propagation axis and b) front view of the vectors in each half of the sample.

for $H_c = 1.2$ mT and 7.7 mT when the magnetic field is applied along the easy axis, and the samples are otherwise similar, we expect $[\text{Fe}^{90}|\text{W}]_2$ to switch at half these fields.

Although the labels of ferromagnetic and antiferromagnetic configurations are now technically incorrect, we will continue to refer to the two states of the sample as such, by analogy with the other five-layer samples from Section 4.3.4. Fig. 4.21a shows that we can expect that a small external field is sufficient to rotate the magnetizations, which are only lying in the easy axes for $H = 0$. The rotation of the magnetizations towards the field is however almost symmetrical, so that in the ferromagnetic configurations the THz polarization is almost constant (Fig. 4.21c). In the antiferromagnetic configuration, which is well-defined in Fig. 4.21b despite the hard-axis component, the THz polarization rotates by up to 90° .

If the magnetizations were confined to their easy axes, we would expect that contrarily to the previous samples, the total amplitude of the emitted THz is constant and only its polarization rotates (see Table 4.4). However, as shown by Fig. 4.21c, we can expect that the amplitude is reduced at high field because the magnetizations are almost parallel, as well as a jump in the amplitude when the second layer switches.

The sample can be mounted in two distinct orientations with respect to the magnetic field, which are distinguished by the angle of the two magnetization vectors with respect to the flow of the spin current. They are summarized as orientations A and B in Table 4.4. To change the orientation, we can equivalently rotate the sample 90° in its plane or change the illuminated face.

In the FM configurations, the magnetization of both layers are aligned on the field: $\angle(\vec{H}, \vec{M}) \leq \pm 45^\circ$. From Eq. (4.6), since both spin currents have the opposite sign when they cross the Fe|W interface, $\angle(\vec{M}, \vec{j}_c) = 90^\circ$ for the lower FM layer and -90° for the upper FM layer. Depending on the orientation of the sample, we thus have $\angle(\vec{H}, \vec{j}_c) = \pm 45^\circ$ or $\pm 135^\circ$. If the phase difference between the two components is negligible as we previously calculated in Section 4.3.4.3, the THz field has a linear polarization. In both cases, it is horizontally polarized, as expected from Fig. 4.21c,

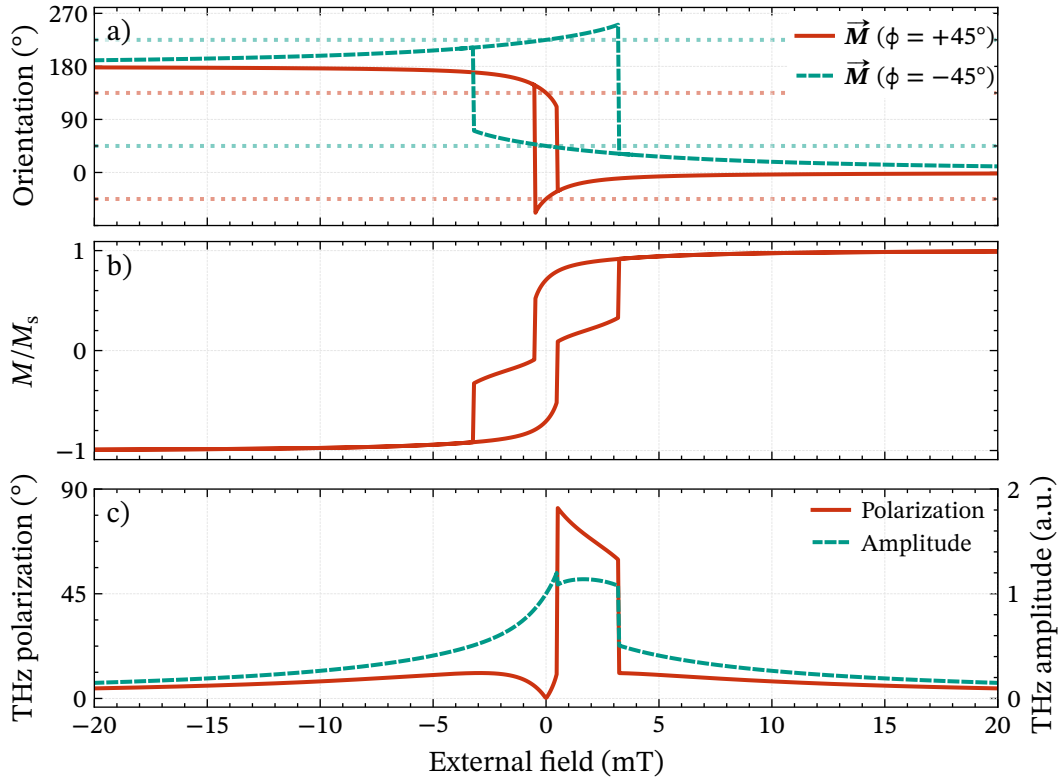


Figure 4.21: Simulated properties of $[\text{Fe}^{90^\circ}|\text{W}]_2$: a) orientation of the magnetization of each FM layer of $[\text{Fe}^{90^\circ}|\text{W}]_2$ with respect to the applied field. ϕ is the angle between the field and their respective easy axis, whose orientation is indicated by the horizontal lines. b) Corresponding hysteresis curve. c) THz polarization (left axis) and amplitude (right axis), assuming an emission with the same amplitude and phase from both layers.

although with a different polarity.

In the AFM configuration, the magnetization of the lower layer switches, leading to either $\angle(\vec{H}, \vec{M}) = 45^\circ$ and 135° or -45° and -135° . We thus have for both orientations $\angle(\vec{H}, \vec{j}_c) = -45^\circ$ and -135° , which means that in both cases, the resulting THz has a vertical polarization, with the same polarity. Table 4.4 summarizes the expected vector orientations.

4.3.5.2 Measurement

Since EOS is polarization-dependent, the measurement of the polarization must be done with two polarizers: the first one is adjusted to transmits the $\pm 45^\circ$ components of the THz polarization, while the second one transmits the remaining vertical component on the EOS crystal.

Table 4.4: Direction of the spin and charge currents in each FM layer as well as the THz polarization, in each magnetization configuration and for both orientations of the sample in the field.

Conf.	\vec{H}	Layer	Orientation A			Orientation B		
			\vec{M}	\vec{j}_c	THz	\vec{M}	\vec{j}_c	THz
FM	→	lower	↙	↘	←	↖	↗	→
		upper	↘	↙		↙	↘	
AFM	←	lower	↗	↘	↓	↘	↙	↓
		upper	↘	↙		↙	↘	
FM	←	lower	↗	↘	→	↘	↙	←
		upper	↘	↙		↗	↖	

From a field E polarized at an angle ϕ with respect to the vertical axis, the first polarizer transmits $E_{\pm 45^\circ} = E \cos(\pm 45 - \phi) = E \cos \phi \pm \sin \phi / \sqrt{2}$. The second polarizer transmits the vertical components of this, or $E_{0^\circ}^\pm = E(\cos \phi \pm \sin \phi)/2$. One can then reconstruct the vertical and horizontal components of the original polarization as $E_{\text{vert}} = E_{0^\circ}^+ + E_{0^\circ}^-$ and $E_{\text{hor}} = E_{0^\circ}^+ - E_{0^\circ}^-$, where $E = \sqrt{E_{\text{vert}}^2 + E_{\text{hor}}^2}$.

We measured the two diagonal components $E_{\pm 45^\circ}$ one after the other to minimize the change of experimental conditions. For each measurement, 57 EOS traces were acquired over a range from -7 mT to $+7$ mT. The measurements were noisy due to the low transmission of the second polarizer and the low amplitude of the original signal. To minimize the noise, each measurement was repeated 30 times in a row before repeating the same steps with the other orientation of the first polarizer. As each measurement took about 30 h, the measured THz energy was slowly fluctuating, probably because of the drifting of the probe, which adds another source of noise.

Accurately measuring the relative amplitude of the two diagonal components is crucial to retrieve the correct polarization. To remove the slow energy drift, we calculated the average THz amplitude of each scan (one EOS trace per value of the external field), then rescaled the measured waveforms so that the average THz amplitude of all scans made for one angle of the waveplate was the same. We used as reference the amplitude of the last scan for the first angle of the waveplate and the first scan for the second angle of the waveplate, which were done one after the other and are thus the least affected by the energy drift.

We then used the average THz waveform for each magnetic field and each polarization to retrieve E_{vert} and E_{hor} for each value of the external magnetic field.

4.3.5.3 Results

Fig. 4.22a shows the MOKE measurement of the sample. As we calculated, it has the two-step switching characteristic of five-layer samples, with an additional slope due to the mixing of the easy-axis and hard-axis magnetizations. The slope is however less pronounced than in Fig. 4.21b. In addition, the switching of the layers occur for an external field of 1.7 mT and 5 mT respectively, which is for both layers about 1.1 mT higher than expected. We thus slightly underestimated the coercivity of the FM layers.

The amplitude of the different THz components is shown in Fig. 4.22b. The total amplitude is approximately constant, with the same asymmetry described in Section 4.3.2. There is no clear jump in the total amplitude as we had expected from Fig. 4.21c. Between 1.5 mT and 4 mT, with a slight offset compared to the MOKE measurement, the E_{vert} component takes precedence on E_{hor} , as expected. We can however see that both polarization components are non-zero, indicating that the THz polarization is either tilted or elliptical. This is confirmed in Fig. 4.22c, which shows the tilt of the linear fit of the THz polarization. In the two FM configurations, the polarization has an average tilt of 33° and -4° , as well as 92° in the AFM configuration. This is noticeably off from the expected 5° and 65° to 80° in the FM and AFM configurations, respectively.

More insight can be gained from Fig. 4.22f, which shows the average polarization ellipses formed at each magnetic field by the projection of the THz electric field onto the plane of the sample. There are three distinct groups of ellipses, corresponding to the three magnetization configurations of the sample. Although the ellipses are noisy due to the low signal-to-noise ratio of the measurements, it is clear that the polarization is significantly elliptical, contrarily to all previous samples.

Figs. 4.22d and 4.22e show the measured $\pm 45^\circ$ components of the THz beam, which correspond to the individual emission of each FM layer. The increased pulse duration compared to the previous results was also shown by other samples and is due to the laser. There is a 0.5 ps offset between the pulses of the two plots, which causes the observed ellipticity. The pulses coming from the FM layer switching at 1.5 mT (Fig. 4.22d), that is to say the lowest layer, are delayed compared to the pulses coming from the upper layer.

We measured a linear THz polarization for $[\text{Pt}|\text{Fe}^*|\text{W}]_2$, $[\text{Pt}|\text{Fe}^*]_2$, as well as $[\text{Fe}^*|\text{W}]_2$, who has the same layer structure and thickness as $[\text{Fe}^{90^\circ}|\text{W}]_2$. We can thus assume that the timing offset is, directly or indirectly, caused by the change of orientation of the easy axes. In Section 4.3.4.3, we discussed potential causes of asymmetry between the two halves of the sample, and concluded that the impaired THz extinction was unlikely to be caused by a timing offset between the two emissions. This discussion excluded the birefringence of the sample, which is now relevant. The materials of all layers are isotropic; however a small birefringence is caused by the grating-like interfaces of the OID layers [217]. The refractive index at 1 THz of the first Fe|W interface, with $\theta = 60^\circ$, is 188.8 for the field emitted there, which is polarized along the deposition direction, and 194.1 for the THz field emitted by the other FM layer. The latter shows a slightly different

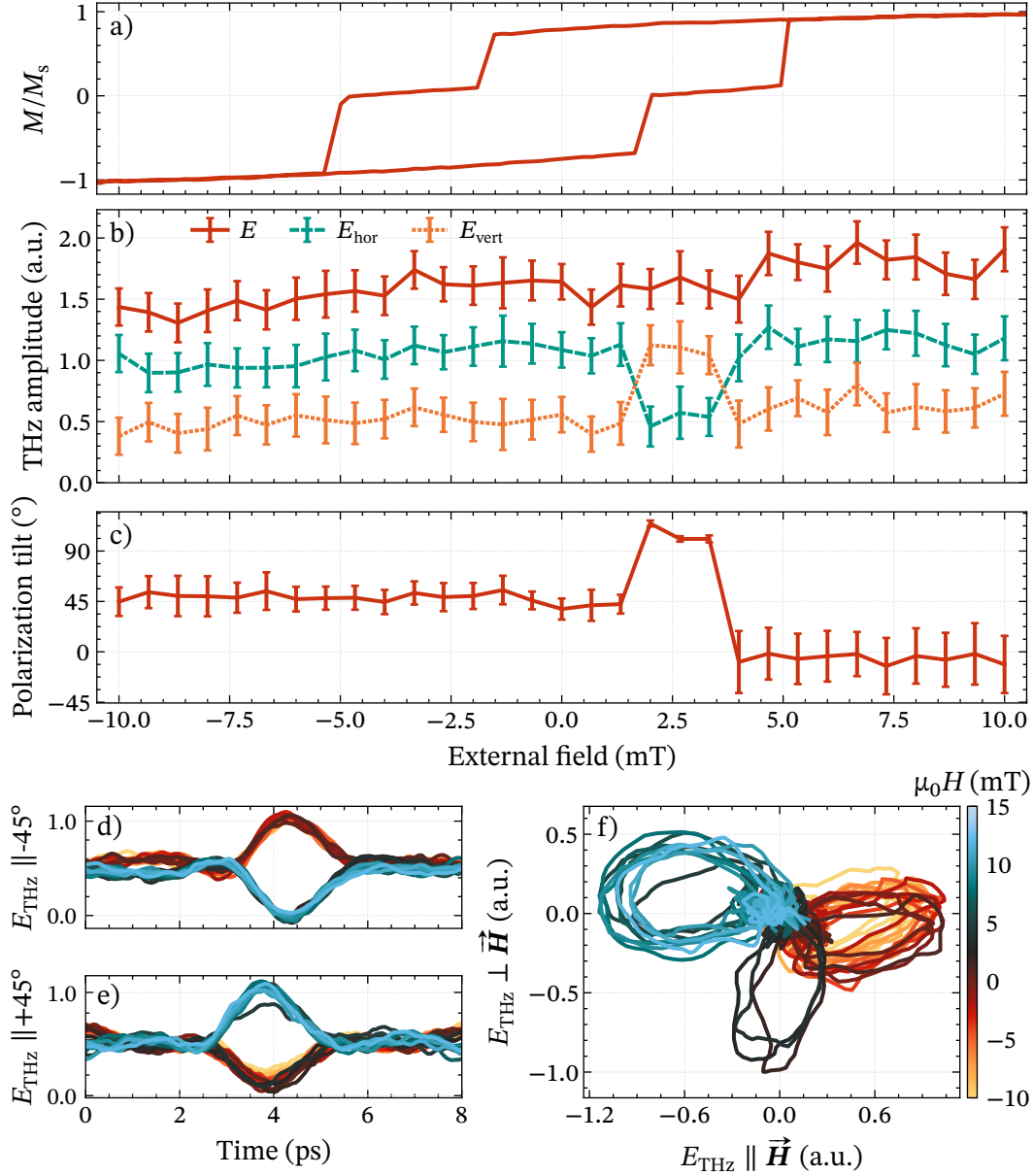


Figure 4.22: a) Hysteresis curve of $[\text{Fe}^{90}|\text{W}]_2$ measured at 45° between both easy axes. b) Peak-to-peak amplitude of the total THz field E and its retrieved components $E_{\text{hor}} \parallel \vec{H}$ and $E_{\text{vert}} \perp \vec{H}$. c) Fit of the orientation of the THz polarization extracted from f. d) Polarization-resolved EOS traces of the emission generated in the lower and e) upper halves of the sample. f) Projection of the THz electric field in the plane normal to the propagation direction. Each ellipse represents the average experimental waveform at a given magnetic field, indicated by the colors. The dotted lines represent the simulated polarization ellipses.

birefringence due to its 80° deposition angle, leading to a net delay. The inclusion of this effect in simulations of $[\text{Fe}^{90^\circ}|\text{W}]_2$, by inserting fictitious layers to represent these interfaces, doubles the delay between both THz components from 0.76 fs to 1.53 fs. The birefringence for the IR pump is negligible and does not contribute to the delay.

We thus deduce that the delay and the associated ellipticity is rather an artifact of the beam propagation in the measurement setup. In [Section 4.3.2](#), we showed the 0.1 ps magnetization-dependent delay that is seen in all samples, and attributed it to the amplification at the metal-air interface of small beam path differences in the samples. This offset is also visible in both of [Figs. 4.22d](#) and [4.22e](#). We argue that a similar mechanism is likely to be at play in the case of the two magnetization axes of $[\text{Fe}^{90^\circ}|\text{W}]_2$. Since the magnetic field of the electromagnet and the IR pulse are no longer parallel to the spin polarization of the electrons, it is expected that they affect the currents to some degree. A small effect is sufficient: the measured $150\ \mu\text{m}$ path difference over the propagation length of the THz beam can be caused by a deflection of just $\sim 2 \times 10^{-6}$ rad inside the sample, highlighting asymmetries that are otherwise negligible. For example, such a rotation of the expectation value of the spin polarization is obtained if 10 out of 10^6 electrons in the spin currents align on the magnetic field. This is the same order of magnitude as the induced magnetization of the W layer ($10^{-6}\mu_{\text{B}}$ / atom with a susceptibility of $\chi_m = 6.8 \times 10^{-5}$), which is caused by the same mechanism.

4.4 Conclusion

In this chapter, we aimed to study spintronic THz emitters as an efficient and easy-to-use THz source, experiment with the geometry of the sample and examine the impact on the emitted THz radiation. Through the innovative use of oblique incidence deposition to deposit FM layers with a controlled in-plane surface anisotropy, we are able to manipulate the behavior of the samples. The resulting remanence allows the magnetization of the FM layers to remain saturated in the absence of external magnetic field. Samples deposited with OID have the same THz emission as samples deposited without, and their additional surface roughness only plays a role when comparing the relative THz emission at opposite ends of the samples.

Our experiments demonstrated the ability of two FM layers with a different coercivity to switch between ferromagnetic and antiferromagnetic configurations, respectively minimizing and maximizing the THz emission as the radiation of individual layers superpose destructively or coherently. The additional thickness compensates the added interfaces, so that such five-layer samples have a similar THz output compared to trilayer samples. Minimizing the thickness of the sample conflicts with the need to maximize the rate of inverse spin Hall effect (ISHE) and avoid the coupling of ferromagnetic layers, leaving little room for optimization. Using FM layers with perpendicular easy axes, we demonstrated the control of the orientation of the THz polarization.

To simulate the samples, we drew on the work of Rouzegar et al. [163] to calculate the spin current, then implemented our own transfer-matrix algorithm to calculate the propagation of the THz fields inside the multilayer samples. This propagation algorithm proved largely accurate for reproducing the waveforms of the five-layer samples in the antiferromagnetic and ferromagnetic configurations, and provided valuable insights into the influence of the OI interface quality in obtaining a good extinction of the THz radiation.

Compared to sources such as phase matching in LiNbO_3 , THz generation using spintronic emitters allows a more compact and robust setup. From the IR-to-THz conversion efficiency of CoFeB|Pt samples, whose EOS amplitude was similar to that of W|Py*|Pt , we estimate the conversion efficiency of our samples to be 4×10^{-6} . This is close to the efficiency measured by Seifert et al. [22]. The measurement of the THz emission presented a few unexpected challenges. Despite an anticipated bandwidth of 10 THz for our pump duration, the available EOS crystals limited the measurable bandwidth to 3 THz. In addition, minor magnetization-dependent variations in alignment of the emitted THz radiation in the sample were amplified by the use of OAPs as collection optics, leading to measurements of tilted polarizations. This issue could potentially be mitigated by employing THz lenses instead.

Moving forward, further investigation would be needed into the cause of the measured changes in the beam path, in order to confirm their magnetic origin inside the sample. Understanding and mitigating this phenomenon is particularly important for samples such as $[\text{Fe}^{90^\circ}|\text{W}]_2$, to ensure a linear polarization of the THz emission.

Conclusion

The field of spintronics, which focuses on manipulating the spin degree of freedom, has led in the last decades to many advances in the development of electronic devices. Its potential to further enhance the energy efficiency and speed of applications such as memories and magnetic sensors remains promising. By integrating spintronics with ultrafast magnetism, it becomes possible to leverage the femtosecond speed of lasers to stimulate the launch of spin currents. The use of THz radiation, which corresponds to the timescale of low-energy processes in matter, presents an energy-efficient alternative to optical pulses. The resonant excitation of magnons with generates less heat in the sample, crucial for ensuring the stability of magnetic memories and increasing storage density.

In the first part of this thesis, we aimed to develop a high-energy THz source for resonantly exciting the spin dynamics of antiferromagnets. Two THz setups based on optical rectification in LiNbO_3 were built, yielding up to $19 \mu\text{J}$ and $2.6 \mu\text{J}$ with conversions efficiencies of 8.8×10^{-4} and 1.2×10^{-3} , respectively. A focusing horn was designed to amplify the THz electric field by a factor of 8.6. We employed the resulting THz radiation to trigger the uniform magnetization resonance modes in the model canted antiferromagnet FeBO_3 . The antiferromagnetic magnon mode, which has an order of magnitude higher frequency than the ferromagnetic mode, has applications for a faster magnetization switching, further highlighting the potential of THz radiation in spintronic applications.

In the second part of the thesis, we explored spintronic THz emitter designs to find novel approaches to manipulate spin currents for THz pulse emission. These devices, consisting of pairs of ferromagnetic and non-magnetic layers, convert the picosecond dynamics of spin currents into transient charge currents, emitting THz pulses via the inverse spin Hall effect. By employing oblique incidence deposition to induce surface anisotropy in the ferromagnetic layers, it became possible to maintain their magnetization without an external magnetic field, which is in an advantage in the pursuit of miniaturization. By controlling the relative orientation of magnetizations in the ferromagnetic layers in a spin valve-like structure, we demonstrated the ability to either enhance or suppress the THz emission. Such samples offers a practical way to

generate on-demand THz pulses. Additionally, imparting orthogonal anisotropies in the ferromagnetic layers enables the dynamic control of the THz polarization.

Looking ahead, the continued integration of spintronics, ultrafast magnetism, and THz technology holds great promise for advancing the efficiency and speed of electronic devices, paving the way for innovative applications in data storage, sensing, and communication systems. Further research and development in this interdisciplinary field are essential for unlocking the full potential of spintronics and THz technology in shaping the future of electronics.

Material characterization

To calculate the transfer function of electro-optic sampling (EOS), the propagation of THz radiation in LiNbO_3 as in [Chapter 2](#), or in spintronic THz emitters as in [Chapter 4](#), it is necessary to know the refractive index and absorption coefficient of the materials over the whole spectrum of the THz pulse. In many cases, this data is not available in the literature, or only for sporadic frequencies. To remedy to this problem, we measured the materials in question by time-domain spectroscopy (TDS).

A.1 Principle of time-domain spectroscopy

Our THz-time-domain spectroscopy (TDS) setup is a MenloSystems TERA K15 spectrometer. An antenna emits radiation with a spectrum spanning nominally 0 THz to 6 THz. Four TPX lenses with a focal length of 54 mm [218] form a double $4f$ telescope: the first pair collects and focuses the THz radiation in free space, while the second pair recollects the THz radiation and refocuses it on the detecting antenna. The transparent sample to be measured is placed in the first focus. A measurement can be done in a single-shot as the system records the time-dependent signal received by the detecting antenna. The properties of the material can then be deduced from its Fourier transform. To improve the resolution, the signal is averaged over typically 400 to 800 shots (50 s to 100 s of integration time). Nitrogen gas is injected in the measurement box until the relative humidity drops under 1 %, to avoid the absorption of the THz radiation by water vapor. The system is also equipped with a cryogenic chamber with TPX windows that can be inserted in the THz focus. The sample is then glued on a copper holder with a 5 mm-diameter hole, and cooled down to 77 K by liquid nitrogen.

To retrieve the complex refractive index of the material, we compare the Fourier spectrum of the field measured by the detecting antenna with the sample to a reference spectrum taken without the sample. The reference is taken in the same conditions than the measurement: low humidity and presence of the chamber or any other material. When the THz beam goes through the sample, assuming a single non-magnetic,

homogeneous layer of thickness d , its amplitude becomes:

$$\begin{aligned} E_s(\omega) &= E_0(\omega) t_{\text{in}}(\omega) t_{\text{out}}(\omega) e^{-ik(\omega)d} \\ &= E_0(\omega) \frac{4n}{(1+n)^2} e^{-in\omega d/c}, \end{aligned} \quad (\text{A.1})$$

where $t(\omega)$ are the Fresnel transmission coefficients and $n = n' - i\kappa$ is the complex refractive index of the material. Separating the real and complex part to express the absorption coefficient $\alpha = 2\omega\kappa / c$, we obtain:

$$E_s(\omega) = E_0(\omega) \frac{4n'}{(1+n')^2} e^{-in'\omega d/c} e^{-\alpha d/2}, \quad (\text{A.2})$$

where we neglected the contribution of the imaginary part of the refractive index in the Fresnel coefficients. Taking the Fourier transform of the measured signal, we thus have the amplitude and the phase of $E_s(\omega)$:

$$A_s(\omega) = E_0(\omega) \frac{4n'}{(1+n')^2} e^{-\alpha d/2}, \quad (\text{A.3a})$$

$$\phi_s(\omega) = \frac{n'\omega d}{c}, \quad (\text{A.3b})$$

while for the reference which propagates the same distance in air:

$$A_r(\omega) = E_0(\omega), \quad (\text{A.4a})$$

$$\phi_r(\omega) = \frac{\omega d}{c}. \quad (\text{A.4b})$$

The formula for the refractive index and the absorption can thus be retrieved by subtracting Eq. (A.4b) to Eq. (A.3b) and taking the ratio of Eq. (A.3a) by Eq. (A.4a) to obtain [219]:

$$n'(\omega) = 1 + \frac{c}{\omega d} (\phi_s(\omega) - \phi_r(\omega)) \quad (\text{A.5})$$

$$\alpha(\omega) = -\frac{2}{d} \ln \left(\frac{A_s(\omega)}{A_r(\omega)} \frac{(1+n'(\omega))^2}{4n'(\omega)} \right). \quad (\text{A.6})$$

Fig. A.1 shows an example of a measurement and retrieval of the refractive index and absorption for Al_2O_3 . To avoid oscillations in the spectrum when performing the Fourier transform, the time signal is truncated before analysis to remove the echoes occurring after the main signal. It then has to be padded or interpolated for the unwrapping of the phase to be correct. This however only works for samples thick enough that the echoes do not overlap with the main pulse.

This analytical method has disadvantages: it neglects the contribution of the complex part of the refractive index in the Fresnel coefficients, which modifies the phase of the beam, and it gives unreliable values when the noise level is too high. We can see in

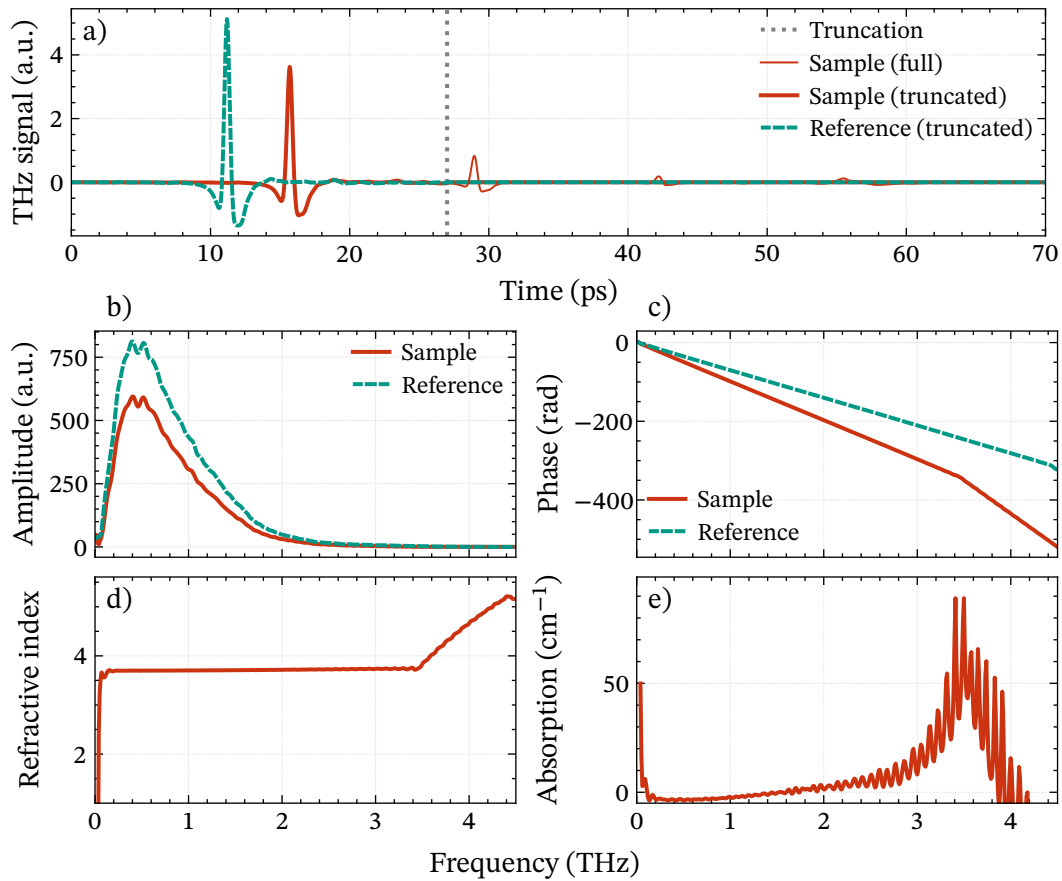


Figure A.1: Example TDS measurement of a wrongly assumed 500 μm -thick Al_2O_3 sample. a) Measured THz signal with and without sample, truncated before the Fourier transform. Calculated b) spectrum and c) phase of both signals. Resulting d) refractive index and e) absorption of Al_2O_3 .

Figs. A.1d and A.1e that the results become noisy above 3.5 THz when the amplitude of the measurement with sample becomes too low. This is clearly seen in the sudden change of trend of its unwrapped phase in Fig. A.1b. However, it is not as clear in the low-frequency end at which point the results become erroneous. In addition, this example shows a negative absorption coefficient under 1.6 THz, which is unphysical. This is due to an imprecise knowledge of the thickness of the sample: setting d too low results in both overestimating n' and underestimating α . While here the error is exaggerated for the sake of demonstration, it is easy for very thin or irregular samples to have a significant error in the expected thickness without having an obvious way of recognizing it.

Other sources of errors in the TDS data arise from the measurement itself. Figs. A.2a and A.2b shows the detected THz pulse immediately after starting the TDS and after letting it warm up overnight. The amplitude of the pulse increased by 2.2% and its

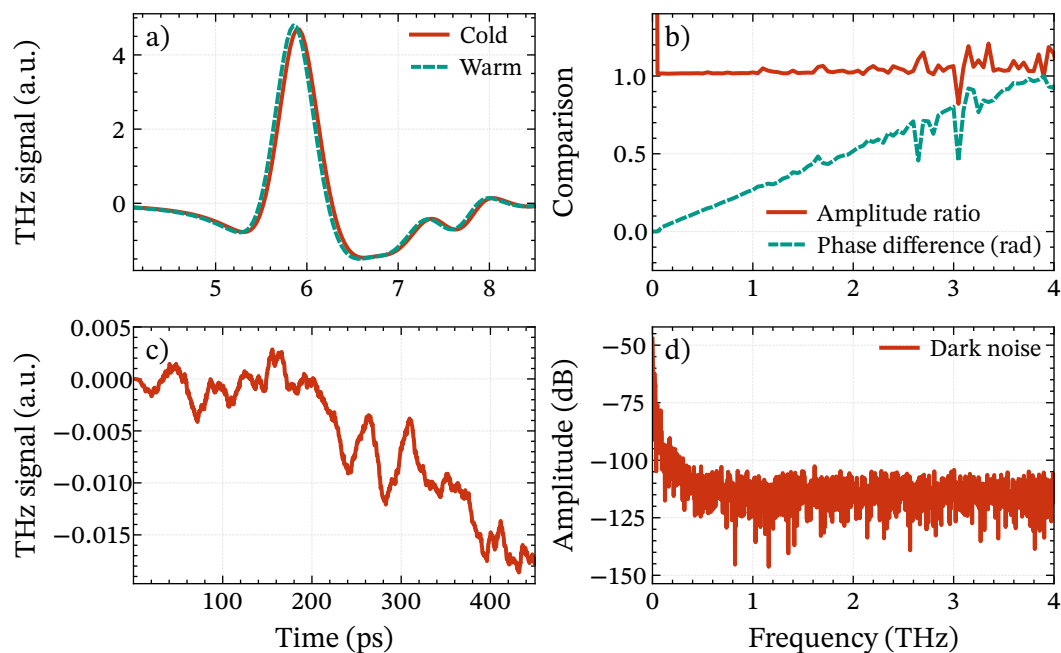


Figure A.2: Other sources of errors in the TDS data: a–b) the change of the pulse timing between immediately after starting the TDS and 16 h later (both measurements averaged over 500 pulses) and c–d) the additional low-frequency noise measured in the absence of a THz pulse (averaged over 17 000 measurements).

arrival time decreased by 67 fs, which would introduce an error principally on the refractive index if either the measurement or the reference is taken with a cold TDS. Fig. A.2d shows the spectrum of the dark noise measured while the THz pulse was blocked: there is a minor source of noise under 500 GHz measured by the detecting antenna. This contributes minimally to the error of the absorption coefficient on the low-frequency end of the measurement. A further source of error is the assumption of Eq. (A.1) that the THz radiation arrives at normal incidence on both surfaces of the sample, which necessitates that the latter is perfectly flat, sits in the focus of the beam, and is thinner than the Rayleigh length. When this is not the case, due to refraction, light rays that were focused at one point of the detecting antenna might be focused on another point or not reach the antenna. The issue is particularly problematic for thick transparent samples and is worse for higher frequencies.

A.2 Fit of the permittivity

To remedy to these problems, we use the Fit@TDS [220] software. We select one or several models for the complex refractive index such as the Drude, Lorentz or Debye

models, and the software fits their the parameters to the TDS data. This allows the relative permittivity $\epsilon_r = \epsilon'_r - i\epsilon''_r = n^2$ to satisfy the Kramers-Kronig relations linking its real and imaginary parts [33]:

$$\epsilon'_r(\omega) = 1 + \frac{2}{\pi} \int_0^\infty \frac{\omega' \epsilon''_r(\omega')}{\omega'^2 - \omega^2} d\omega' \quad (\text{A.7})$$

$$\epsilon''_r(\omega) = 1 + \frac{-2\omega}{\pi} \int_0^\infty \frac{\epsilon'_r(\omega')}{\omega'^2 - \omega^2} d\omega'. \quad (\text{A.8})$$

When the permittivity is constant over the THz range, this relationship reduces the refractive index and the absorption to a single unknown. The phase difference between the measurement with sample and the reference measurement depends only on the permittivity and the thickness of the sample. However, in practice, the thickness is usually known with some error, as was illustrated in Fig. A.1. In this case, the presence of an echo in the measurement supplies a second equation to fit both the permittivity and the actual thickness, as the phase of the main pulse and the x th echo are:

$$\phi_0 = \phi_t(\epsilon) + \frac{n'\omega d}{c}, \quad (\text{A.9})$$

$$\phi_x = \phi_t(\epsilon) + x\phi_r(\epsilon) + (2x + 1) \frac{n'\omega d}{c}, \quad (\text{A.10})$$

where ϕ_t and ϕ_r are the phases coming from the transmissions and internal reflections on both interfaces. For more complex models of the refractive index with an increasing number of variables, more echoes give a better result. The thickness of the sample should thus be chosen so that a sufficient number of echoes are visible. The measurement window must contain all echoes to avoid folding issues with the Fourier transform. In practice, Fit@TDS solves the equation [220]:

$$E_s(\omega) = \frac{4n}{(1+n)^2} \frac{\exp(-i(n-1)\omega d/c)}{\left(1 - \left(\frac{n-1}{1+n}\right)^2 \exp(-2in\omega d/c)\right)} E_r(\omega) \quad (\text{A.11})$$

where the denominator of the second factor is the Fabry-Pérot term.

The different components of the relative permittivity as they are defined in the software are:

- The constant permittivity at high frequency ϵ_∞ , which is always included.
- The Drude model:

$$\epsilon_{\text{Drude}}(\omega) = -\frac{\omega_p^2}{\omega^2 - i\gamma_p\omega} \quad (\text{A.12})$$

where ω_p is the plasma frequency and γ_p the damping rate. The Drude model is adapted to conducting materials and represents the contribution of free charges. It manifests as a refractive index diverging at $\omega = 0$ and, at low frequencies ($\omega < \gamma_p$), the absorption increasing with the frequency.

- The Lorentz model:

$$\epsilon_{\text{Lorentz}}(\omega) = \frac{\Delta\epsilon_i \omega_i^2}{\omega_i^2 - \omega^2 + i\gamma_i \omega} \quad (\text{A.13})$$

where $\Delta\epsilon_i$ is the oscillator strength, ω_i its angular frequency and γ_i its damping rate. Many materials have optical phonons in the THz range, which are represented by the Lorentz model a harmonic oscillators with exponential damping. Each oscillator is recognizable as an absorption peak accompanied by a step in the refractive index.

- The Debye model:

$$\epsilon_{\text{Debye}}(\omega) = \frac{\Delta\epsilon_j}{1 + i\omega / \gamma_j} \quad (\text{A.14})$$

where $\Delta\epsilon_j$ is the oscillator strength and γ_j its damping rate. The Debye model represents the slow thermal relaxation of polar molecules, and is adapted for materials such as liquids and polymers. It manifests as an rising absorption and falling refractive index with frequency.

- Scattering:

$$\epsilon_{\text{scatt}}(f) = \begin{cases} (-i\alpha f^3)^2 - 2i\alpha f^3 \sqrt{\epsilon_\infty + \epsilon_{\text{Drude}}} & \text{if } f_{\text{min}} < f < f_{\text{max}} \\ 0 & \text{otherwise.} \end{cases} \quad (\text{A.15})$$

where α is the scattering coefficient and $f_{\text{min/max}}$ is the minimum/maximum scattering frequency. Its formula is equivalent to adding $\delta\kappa = \alpha f^3$ to the existing imaginary part of the refractive index. Scattering represents additional losses of THz radiation due to defects in porous or textured materials, and results in featureless losses increasing with frequency.

The total function to fit the TDS data is thus:

$$\epsilon_r(\omega) = \epsilon_\infty + \epsilon_{\text{Drude}}(\omega) + \epsilon_{\text{scatt}}(\omega, \epsilon_r) + \sum_i \epsilon_{\text{Lorentz}}(\omega) + \sum_j \epsilon_{\text{Debye}}(\omega). \quad (\text{A.16})$$

Thin metallic samples have the difficulty that the permittivity depends on their thickness: few nm-thick samples have a lower contribution of the Drude model than bulk samples because of the smaller amount of conduction electrons decreasing the plasma frequency, and the decreased metallicity of the sample [221]. We are also assuming that the samples are not magnetic ($\mu_r = 1$), which influences the Fresnel coefficients [222].

In addition, we had access to a version of Fit@TDS able to fit a multilayer structure one unknown layer at a time, which was necessary for samples sputtered on a substrate. In the case of such samples, reference measurements taken with only the substrate have different Fresnel coefficients at the point of contact. This requires adapting Eq. (A.11) to the modified transfer functions describing the sample and reference.

A.3 Results

Table A.1 presents the fit parameters for the materials in this section. Unless written otherwise, the measurements were performed at room temperature and without mounting the sample in the vacuum chamber. We used Fit@TDS to fit the time-domain TDS data, selecting models and the constrains on their parameters according to the available literature.

A.3.1 Fused Silica

Fig. A.3 shows the measurement and fit of a fused silica wafer at room temperature in the TDS chamber. We based the starting parameters of the fit on the Lorentz oscillators identified by Komandin et al. [223] at 8.5 THz and 13.6 THz. Due to the amorphous nature of fused silica glass, the peaks are broad and the phonon at 13.6 THz has a large influence on the absorption we measure. The low-frequency features visible in the data from Chudpooti et al. [224] and Markelz [225] are reproduced by a small Debye oscillator.

A.3.2 KTP

Fig. A.4 shows the extraordinary z axis of a x -cut KTP sample measured at cryogenic temperature. The losses in the 2 mm-thick sample were too large to allow an accurate fit

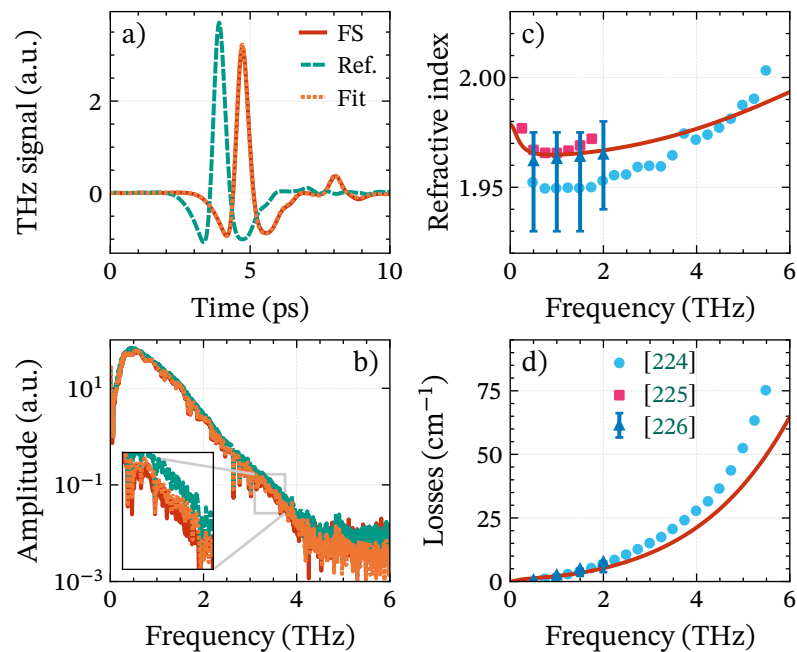


Figure A.3: Fit of fused silica at room temperature. Markers in c) and d): values from Refs. [224–226], the error bars indicating the distribution of other measurements compiled in [226, table 2].

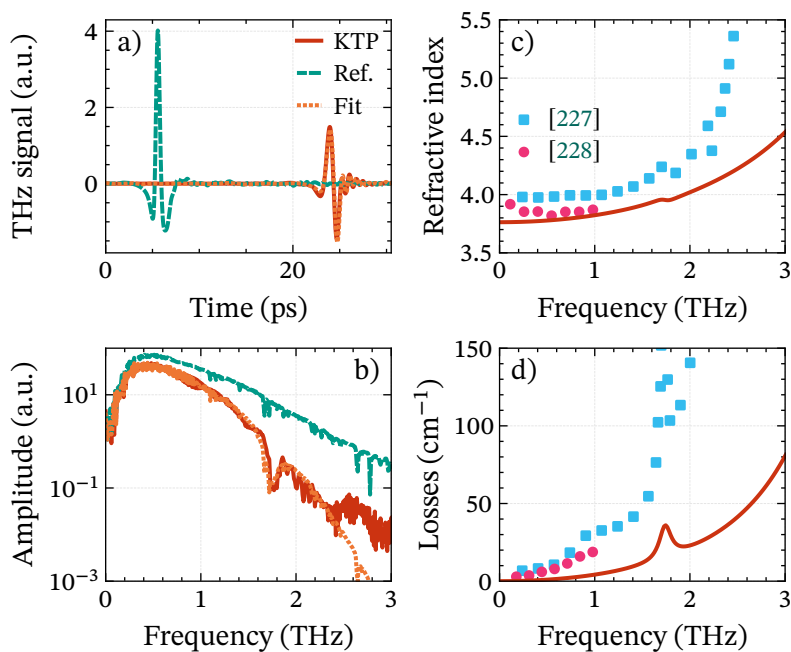


Figure A.4: Fit of the z axis of KTP at cryogenic (77 K) temperature. Markers in c) and d): room-temperature values from Refs. [227, 228].

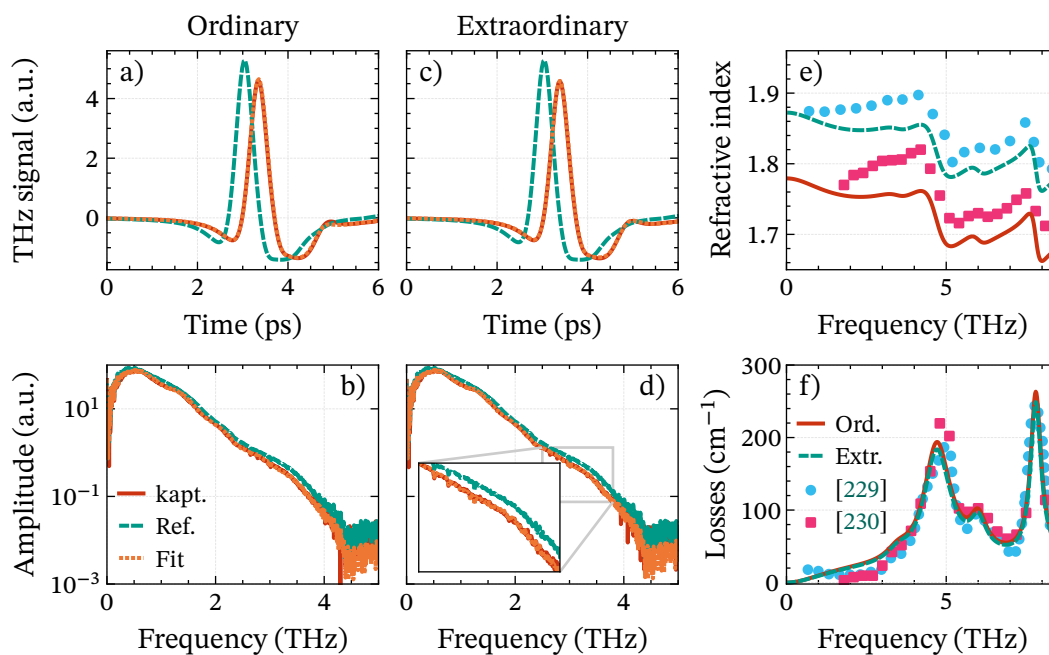


Figure A.5: Fit of Kapton along the ordinary and extraordinary axes. Markers in c) and d): values from Refs. [229, 230] along a unknown and mixed axis, respectively.

above 2 THz. Because of the limited bandwidth, the best fit was obtained with a strong peak at 4.7 THz. For comparison, the results of Antsygin et al. [227] and Mounaix et al. [228] at room temperature are shown, on which the same phonon at 1.74 THz is visible.

A.3.3 Kapton

We measured both the ordinary and extraordinary axes of a sheet of Kapton, which is a dielectric polymeric plastic. As the axes were not indicated, we identified the extraordinary axis as the angle at which the transmitted THz pulse has the largest delay. The precision of this method is however limited by the time resolution of the TDS (33.4 fs), which is as large as the 39.2 fs separation between the measured ordinary and extraordinary pulses.

The absorption under 3 THz is well reproduced by a Debye oscillator alone. Two Lorentz oscillators at 3.5 THz and 4.7 THz allow to fit the higher-frequency data. The further two Lorentz peaks provided in Table A.1 are estimates based on the data from Cunningham et al. [229], whose axis is not specified, and Smith and Loewenstein [230], which is an average of the two optical axes. We obtained a lower extraordinary refractive index than Ref. [229], which may indicate that our measurement underestimates the birefringence of Kapton.

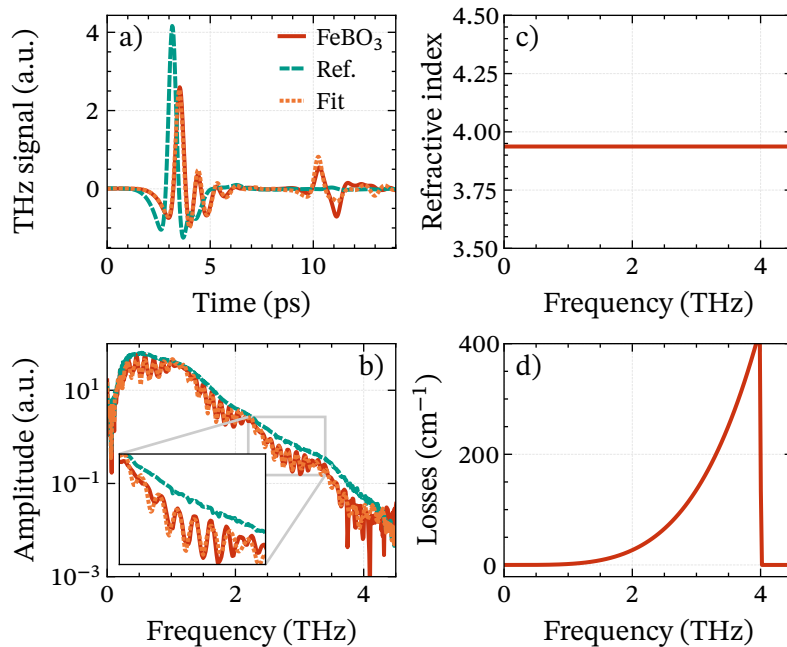


Figure A.6: Fit of FeBO₃ including back-reflection by the pinhole.

A.3.4 FeBO₃

Fig. A.6 shows our measurement of a (001)-plane multicrystalline FeBO₃ sample. To be able to manipulate the extremely brittle crystal, we glued it over a 4.5 mm-diameter hole between two Kapton sheets, which we then fixed loosely over a 3 mm-diameter metallic pinhole in the TDS focus.

The ~ 1 THz-wide oscillations in Fig. A.6b are due to internal reflections in FeBO₃, and are reproduced by a fit of ϵ_∞ and the sample thickness alone. Due to the irregular surface of the sample, we fitted the additional losses as scattering.

However, the ~ 0.13 THz-wide oscillations, corresponding to the reflection after 7.5 ps, cannot be reproduced by fitting the measurement. Because of the loose mounting of the FeBO₃ sample in front of the relatively small pinhole, we hypothesized that a part of the THz beam which is blocked by the latter during the reference measurement is reflected forward on the sample and passes through the pinhole, creating the second pulse. This process is modeled by an additional transfer function representing a reflection with 100 % efficiency on the pinhole of a variable proportion of a THz pulse, and its reflection on the sample at a variable distance to the pinhole. The fit in Fig. A.6 is obtained by multiplying the reference beam with this transfer function, before as usual applying the transfer function of the sample. We found that the timing of the additional reflection is reproduced for gap of 1.01 mm. To match the amplitude of the oscillations, we set that 100 % of the THz field that is passing through the pinhole during the reference measurement is still passing through in the presence of the sample, and that an additional 50 % of the field which is normally blocked can pass through the pinhole when it is reflected on the FeBO₃ crystal.

A.3.5 Al₂O₃

Fig. A.7 shows the measurement of a double-polished c-plane wafer of Al₂O₃, which is used as substrate for the spintronic THz emitters in Chapter 4. Based on the parameters given by Barker [233], we fitted the featureless increase in absorption as the side of a pair of strong Lorentz oscillators at 13.3 THz and 17.1 THz. To minimize the number of fit parameters, we neglected the smaller oscillators at 11.55 THz and 19.05 THz, which is compensated by a higher value of ϵ_∞ . While the results are close to other published experimental values [231, 232], all our measurements show a clear absorption peak at 3.55 THz not mentioned in the literature. We measured different samples from different manufacturers and found a similar peak in each one: at 3.4 THz in one and at 2.7 THz and 2.9 THz in a second, with one peak appearing and the other disappearing as the sample was rotated.

We assume that this peak corresponds to an additional IR-active phonon caused by the mechanical polishing of the surface [233]. This hypothesis is supported by the observed temperature dependence of the absorption peak. Fig. A.8 shows a succession of THz

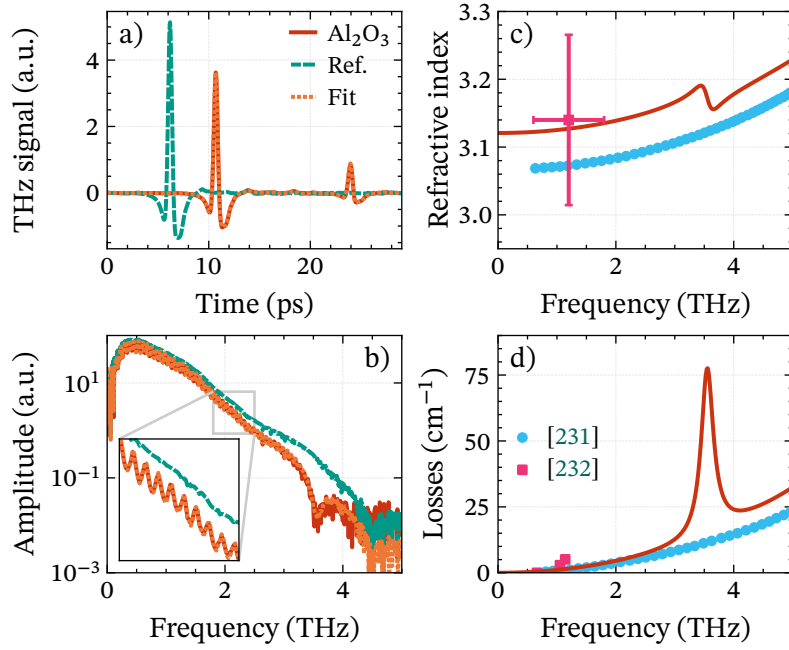


Figure A.7: Fit of Al_2O_3 along its ordinary axis. Markers in c) and d): values from Refs. [231, 232].

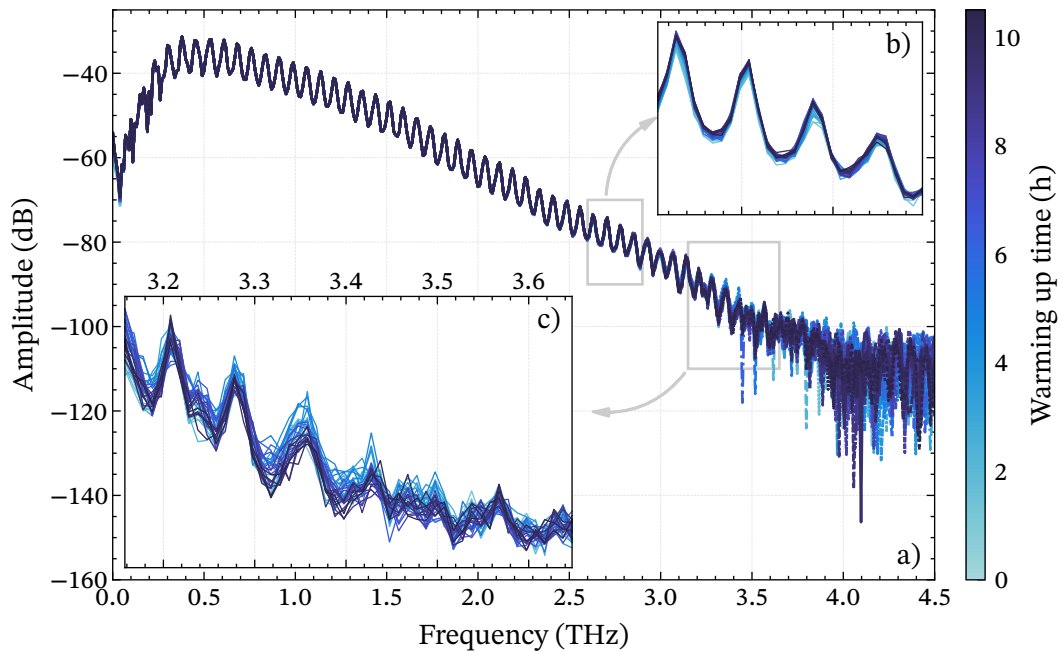


Figure A.8: Change in the absorption spectrum of Al_2O_3 as it warms up from 77 K to 230 K (estimated). Inserts: five-fold zoom from b) 2.6 THz to 2.9 THz and c) 3.15 THz to 3.65 THz.

spectra as an Al₂O₃ sample warms up from cryogenic temperatures. Due to the weight of the liquid nitrogen shifting the TDS chamber, it was not possible to take a reference measurement to retrieve the absorption coefficient. Over most of the frequency range, the spectrum is stable as shown in Fig. A.8b. However, around 3.4 THz, we see that the transmitted amplitude decreases progressively as the sample warms up, which is consistent with the hypothesis of a phonon.

A.3.6 MgO

We measured MgO as a 50 nm layer sputtered over the Al₂O₃ substrate, after determining the permittivity of the latter. Due to its small absorption and thickness, the influence of the MgO layer is however not distinguishable from the substrate by itself. We used the parameters of the Lorentz model given by Ren et al. [234] to describe MgO layers in Chapter 4.

A.3.7 Pt

We measured Pt as an Al₂O₃|Pt(50 nm) sample. With the permittivity of the substrate known, the one of the Pt layer can be determined. The delay of the transmitted pulse and its reflection come from the substrate, while its amplitude depends almost entirely on the Pt layer.

As a metal, Pt is described by the Drude model. We used as starting parameters for the fit those given by Seifert et al. [19], converting between conductivity and permittivity with:

$$\epsilon_r = \epsilon'_r - i\epsilon''_r = (\sigma'' - i\sigma') / \omega\epsilon_0, \quad (\text{A.17})$$

$$\omega_p = \sqrt{\sigma_{\text{DC}}\gamma_p / \epsilon_0}. \quad (\text{A.18})$$

Using Eq. (A.18), Eq. (A.12) simplifies to $\epsilon_{\text{Drude}}(\omega) = -i\sigma_{\text{DC}} / \epsilon_0\omega$ when $\gamma_p \gg \omega$, making the fit insensitive to the relaxation rate. We thus retain its value from Ref. [19] and use σ_{DC} and ϵ_∞ as only variable parameters.

Fig. A.10a shows that the THz absorption is high enough that noise distorts the measured waveform, even after correcting for the dark noise of the TDS measured in Fig. A.2. Since the Pt layer is too thin to create visible internal reflections, Fit@TDS is unable to unambiguously determine its thickness, and thus the target absorption. Assuming that $\sigma_{\text{DC}} = 3.9 \times 10^6 \text{ S m}^{-1}$ as in Ref. [19] results in $d = 90 \text{ nm}$ instead of the nominal 50 nm, which is an unrealistic error on the thickness of the sample. We thus instead assume that $d = 50 \text{ nm}$, which results in $\sigma_{\text{DC}} = 7.5 \times 10^6 \text{ S m}^{-1}$.

The larger conductivity is explained by the thickness dependence of the conductivity of thin films, due to the increased contribution of electron scattering at the interfaces. Fig. A.11a compares our result with different values for the conductivity of polycrystalline

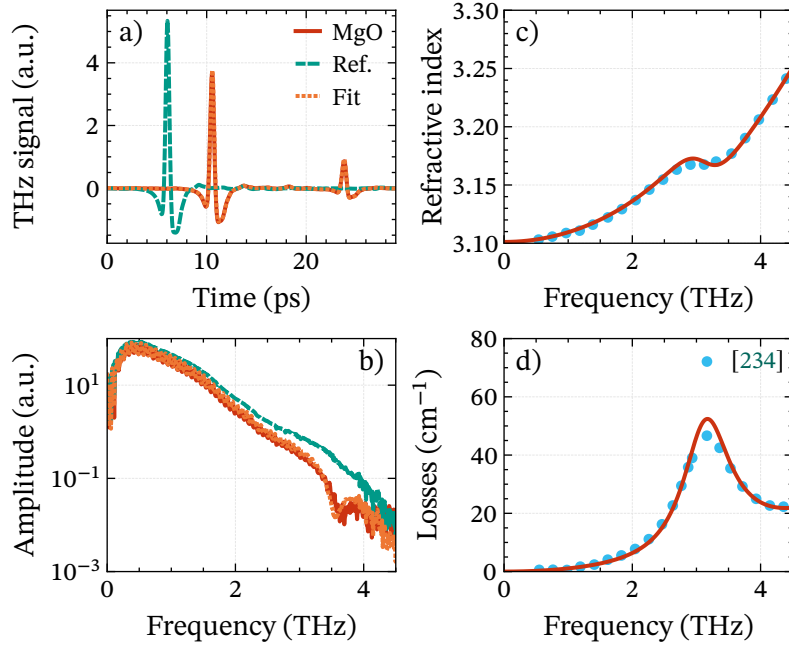


Figure A.9: Fit of MgO over an Al_2O_3 substrate. Markers in c) and d): values from Ref. [234]. The absorption peak at 3.6 THz is due to the substrate.

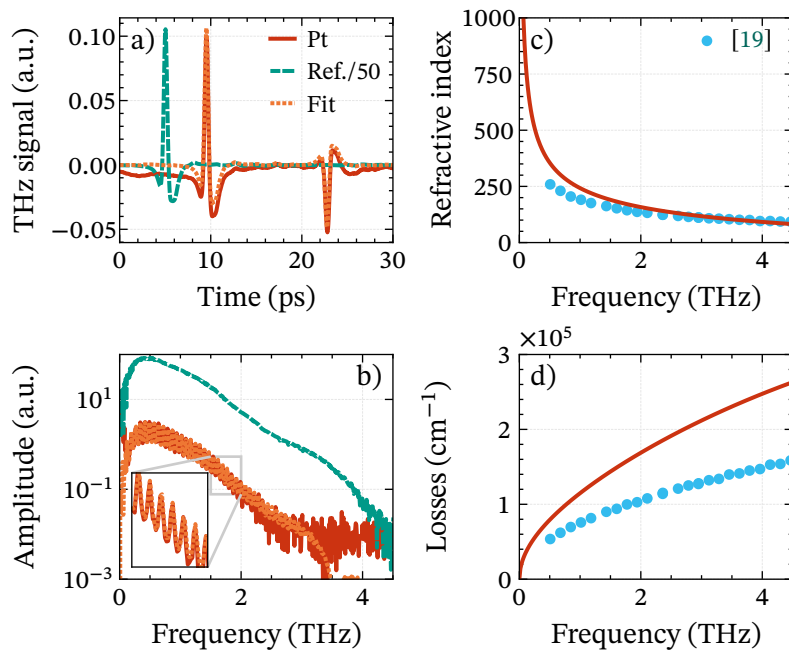


Figure A.10: Fit of Pt within an $\text{Al}_2\text{O}_3|\text{Pt}$ sample. Markers in c) and d): values calculated from the complex conductivity given in Ref. [19].

Pt films found in the literature. We fit the thickness dependency of σ_{DC} using the Fuchs–Sondheimer equation [235]:

$$\frac{\sigma}{\sigma_{\text{bulk}}} = 1 - \frac{3}{2k} \int_1^{\infty} \left(\frac{1}{t^3} - \frac{1}{t^5} \right) (1 - e^{-kt}) dt, \quad (\text{A.19})$$

where $k = d / \lambda$ and λ is the electron mean free path. The literature values of $\lambda = 22.4 \text{ nm}$ [236] and $\sigma_{\text{bulk}} = 9.27 \times 10^6 \text{ S m}^{-1}$ at room temperature [237] match the collected data. The fit shows that our estimation of σ_{DC} falls into the expected range for a 50 nm-thick layer. In the case of the spintronic THz emitters discussed in Chapter 4, we are interested in the absorption of 2 nm-thick Pt layers. In this case, we estimate $\sigma_{\text{DC}} = 1.8 \times 10^6 \text{ S m}^{-1}$.

A.3.8 Fe

Fe was measured within an $\text{Al}_2\text{O}_3|\text{Fe}(50 \text{ nm})|\text{Pt}(2 \text{ nm})$ sample. It was sputtered at normal incidence, to avoid the influence of oblique incidence deposition (OID) on its permittivity [244, 245]. The refractive indices of the external layers are fixed, with the one of Pt adapted for its reduced thickness as described above. As before, only the substrate contributes to the delay of the pulse, which makes the fit insensitive to d and ϵ_{∞} . We

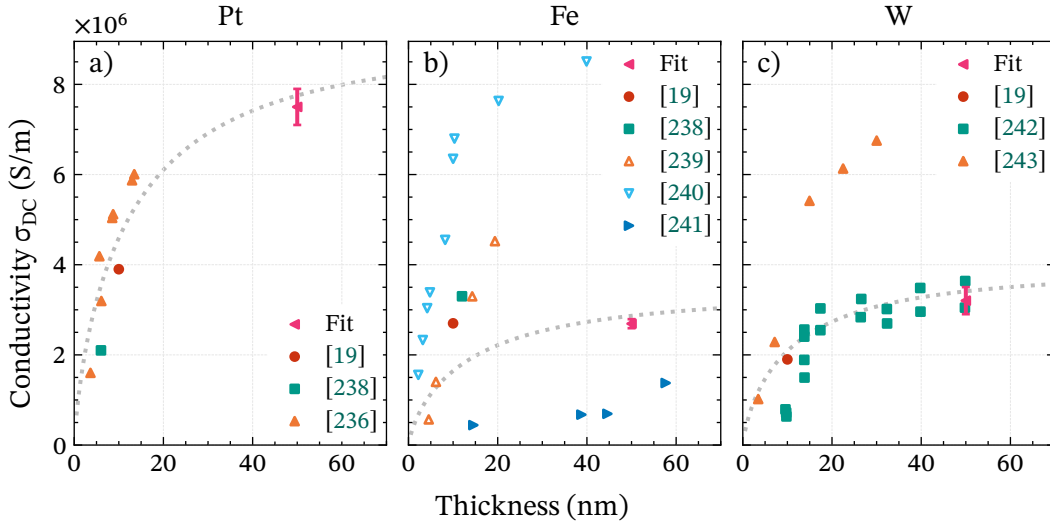


Figure A.11: Thickness-dependence of the conductivity of thin films at room temperature, comparing values from the literature fitted by Eq. (A.19) to the conductivity obtained with Fit@TDS. Empty markers denote values taken from epitaxial samples, whose conductivity is expected to be higher. The error bars indicate the range of values of σ_{DC} which give visually undistinguishable results in the reconstruction of the TDS measurement.

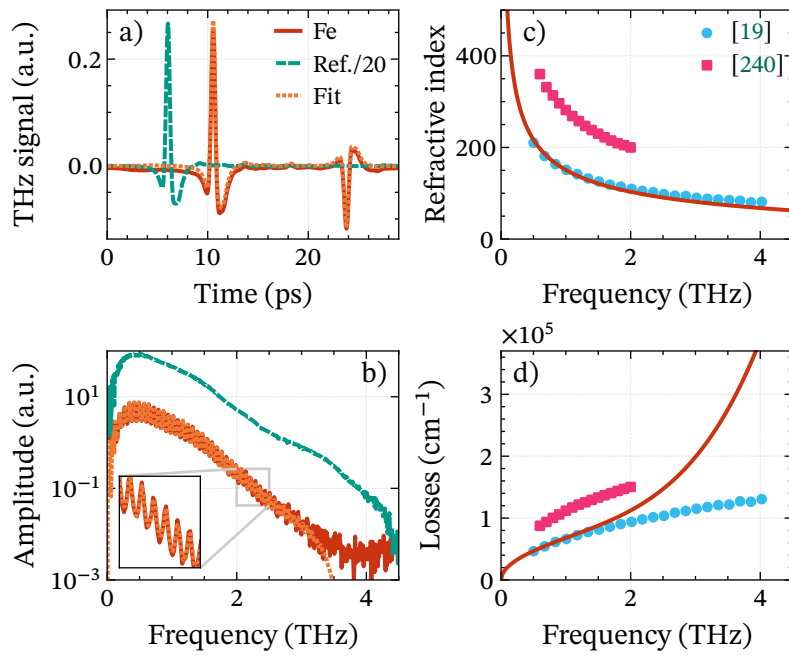


Figure A.12: Fit of Fe within an $\text{Al}_2\text{O}_3|\text{Fe}|\text{Pt}$ sample. Markers in c) and d): values calculated from the complex conductivity given in Refs. [19, 240].

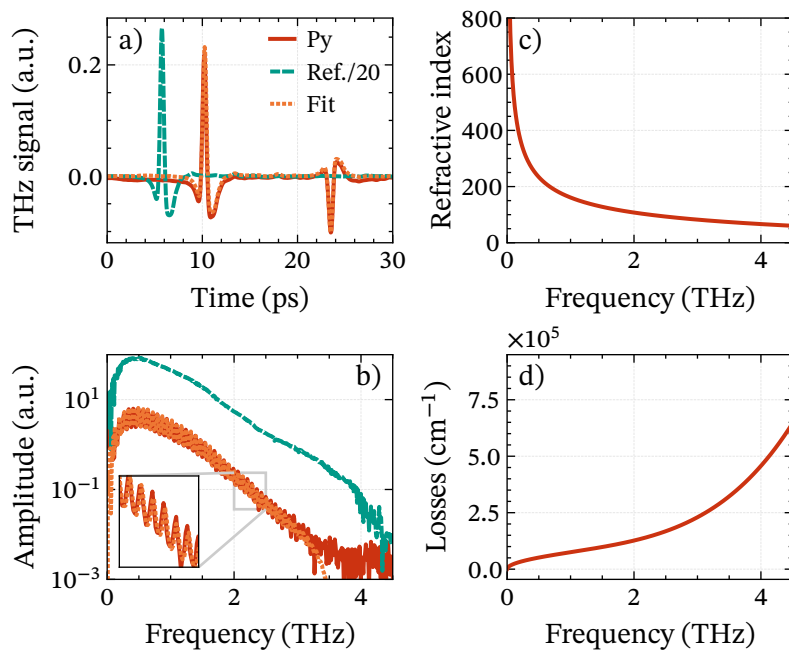


Figure A.13: Fit of Py within an $\text{Al}_2\text{O}_3|\text{Py}|\text{Pt}$ sample.

assume that, as was the case for Pt, the nominal thickness of $d = 50$ nm is a good approximation. The permeability of iron is neglected, which leads to a slight overestimation of the Fresnel coefficients. Since the internal reflections are absorbed in the thick Fe layer, the effect is negligible.

As shown in Fig. A.12, a fit with the Drude model alone reproduces the refractive index and absorption measured by Seifert et al. [19]. Strong scattering due to the rough interfaces of the sample is visible above 2 THz. We presume that the structural disorder of the layer is responsible for the low conductivity compared to what can be expected for a 50 nm-thick layer, as shown by Fig. A.11b. The measurements of Refs. [19, 238, 239] fall on a curve described by $\sigma_{\text{bulk}} = 10.3 \times 10^6 \text{ S m}^{-1}$ [239] and $\lambda \approx 50$ nm. The annealed epitaxial samples of Ref. [240] have a particularly large conductivity, while the sputtered polycrystalline samples of Ref. [241] have a lower conductivity than ours. We expect for the 3.5 nm-thick layers of the spintronic THz emitters a conductivity of $\sigma_{\text{DC}} \approx 10^6 \text{ S m}^{-1}$.

A.3.9 Py

Py was measured within an $\text{Al}_2\text{O}_3|\text{Py}(50 \text{ nm})|\text{Pt}(2 \text{ nm})$ sample and fitted with a Drude model and scattering as shown in Fig. A.13. The same concerns mentioned for Fe also apply to Py. The resulting plasma frequency is of the same order of magnitude as the one measured in the visible range by Tikuišis et al. [246].

A.3.10 W

Like the previous materials, W was measured within an $\text{Al}_2\text{O}_3|\text{W}(50 \text{ nm})|\text{Pt}(2 \text{ nm})$ sample and fitted with the Drude model and scattering, as shown in Fig. A.14. We find a relaxation rate and conductivity similar to the ones given by Seifert et al. [19], with σ_{DC} falling within the expected range for a 50 nm-thick layer based on the measurements of Petroff et al. [242], as shown by Fig. A.11c. Fitting the thickness dependency with $\lambda = 20$ nm, which is within the expected range [247], and $\sigma_{\text{bulk}} = 4 \times 10^6 \text{ S m}^{-1}$, we estimate $\sigma_{\text{DC}} = 0.84 \times 10^6 \text{ S m}^{-1}$ for a 2 nm-thick layer.

A.3.11 ZnTe

The permittivity of ZnTe, shown in Fig. A.15, is used in Chapter 4 to simulate the propagation of the THz pulse into the EOS crystal. It was not measured in the TDS, but instead is reconstructed from the Lorentz parameters fitted by Casalbuoni et al. [248] from the measurement of Gallot and Grischkowsky [249].

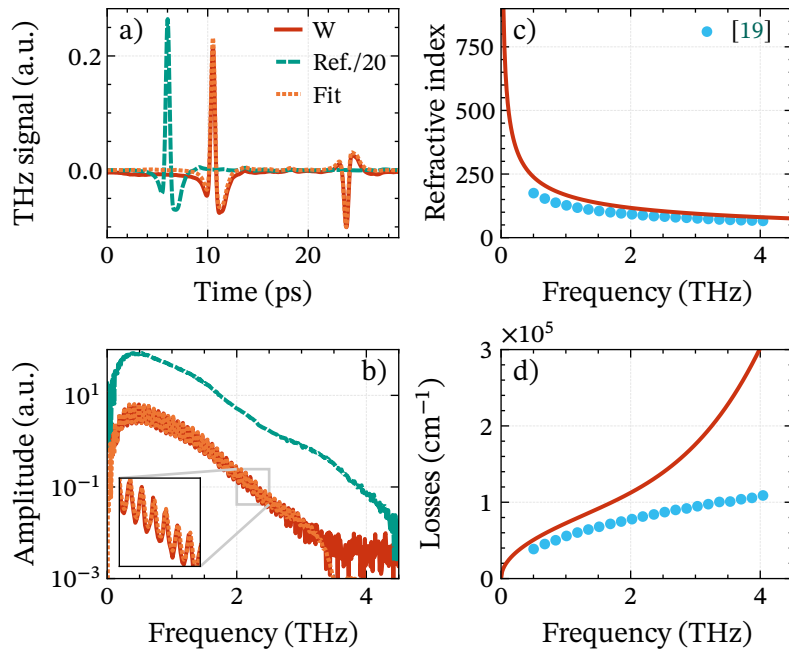


Figure A.14: Fit of W within an $\text{Al}_2\text{O}_3|\text{W}|\text{Pt}$ sample. Markers in c) and d): values calculated from the complex conductivity given in Ref. [19].

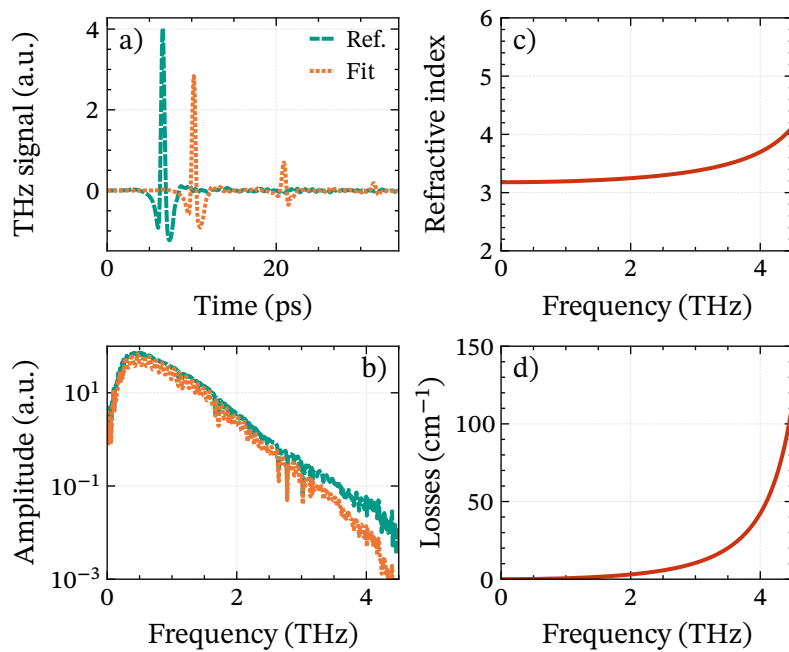


Figure A.15: Simulation of the propagation through a $500\ \mu\text{m}$ -thick ZnTe crystal, using the Lorentz model of Ref. [248].

Table A.1: Fit parameters for modeling the optical properties of the given materials under ~ 3 THz.

	Thickness (m)	ϵ_∞	Drude			Scattering	Lorentz			Debye	
			ω_p (Hz)	σ_{DC} (S m $^{-1}$)	γ_p (Hz)	α (Hz $^{-3}$)	$\Delta\epsilon_i$	ω_i (Hz)	γ_i (Hz)	$\Delta\epsilon_j$	γ_j (Hz)
fused silica	255.1×10^{-6}	3.32	-	-	-	-	0.0655 0.47	8.5×10^{12} 1.4×10^{13}	5.5×10^{12} 1.5×10^{12}	0.0592	1.9×10^{11}
KTP (77 K)	1.972×10^{-3}	4.74	-	-	-	-	0.02 9.4	1.7×10^{12} 4.7×10^{12}	1.5×10^{11} 1.6×10^{11}	-	-
ZnTe	500×10^{-6}	7.4	-	-	-	-	2.7	5.3×10^{12}	9×10^{10}	-	-
kapton (ord.) kapton (extr.)	122.1×10^{-6}	2.91 3.25	-	-	-	-	0.01 0.06 0.006 0.02	3.5×10^{12} 4.7×10^{12} 6×10^{12} 7.8×10^{12}	9×10^{11} 1×10^{12} 6×10^{11} 4×10^{11}	0.168	1.5×10^{12}
FeBO $_3$ (ord.)	34.89×10^{-6}	15.5	-	-	-	4×10^{-3}	-	-	-	-	-
Al $_2$ O $_3$ (ord.)	635.01×10^{-6}	4.02	-	-	-	-	0.019 2.7 3.0	3.6×10^{12} 1.3×10^{13} 1.7×10^{13}	2.5×10^{11} 3.5×10^{11} 1×10^{12}	-	-
MgO	50×10^{-9}	3.01	-	-	-	-	0.062 6.55	3.2×10^{12} 1.2×10^{13}	9×10^{11} 2×10^{11}	-	-
Pt	50×10^{-9}	6.53	6.6×10^{15}	7.5×10^6	5.1×10^{13}	-	-	-	-	-	-
Fe	50×10^{-9}	1	5.8×10^{15}	2.7×10^6	1.1×10^{14}	2.3	-	-	-	-	-
Py	50×10^{-9}	1	5.0×10^{15}	3.2×10^6	6.9×10^{13}	2.8	-	-	-	-	-
W	50×10^{-9}	1	9.8×10^{15}	3.2×10^6	2.7×10^{14}	1.4	-	-	-	-	-

Electro-optic sampling

Electro-optic sampling (EOS) is a technique allowing to measure the temporal shape of a signal that is too fast for an electronic detection, by transforming the temporal dependency of the signal into a spatial dependency. A probe pulse, short with respect to the sampled signal, is spatially superposed to the latter in a nonlinear material. Its polarization rotates in proportion to the instantaneous amplitude of the signal. Scanning their relative delay allows to reconstruct the whole pulse. In this work, we use it to characterize pulses with a bandwidth spanning 0.1 THz to 3 THz using near-infrared (IR) probes.

B.1 Theory

We introduced nonlinear optics in [Section 2.1.1.1](#). EOS uses a second-order effect, the linear electro-optic or Pockels effect, in which the electric field of the THz pulse $\mathcal{E}^{\text{DC}}(\Omega \approx 0)$, approximated constant, modulates the phase of the probe beam $\mathcal{E}^{\text{p}}(\omega)$ [56, 250]:

$$\mathcal{P}_i^{(2)}(\omega) = 2\epsilon_0 \sum_{jk} \chi_{ijk}^{(2)}(\omega; \omega, 0) \mathcal{E}_j^{\text{p}}(\omega) \mathcal{E}_k^{\text{DC}}. \quad (\text{B.1})$$

The effect is usually described using the electro-optic tensor $r_{ijk}(\omega) = -\chi_{ijk}^{(2)}(\omega; \omega, 0) / (\epsilon_{ii}^0(\omega) \epsilon_{jj}^0(\omega))$, where $\epsilon_{ii}^0 = 1 + \chi_{ii}^{(1)}$ is the linear dielectric constant in the coordinate system of the principal axes of the medium [251]. The electric field of the THz beam adds a nonlinear component to the refractive index tensor $n_{ij}(\omega) = \sqrt{1 + \chi_{ij}^{(1)} + 2\chi_{ijk}^{(2)} \mathcal{E}_k^{\text{DC}}}$, nearly instantaneously inducing birefringence in the plane of the crystal: $\Delta(1/n(\omega))_{ij} = r_{ijk}(\omega) \mathcal{E}_k^{\text{DC}}$. The polarization of the probe beam, initially linear, becomes elliptical and rotates proportionally to the instantaneous strength of the THz field.

The effect is alternatively described as a mixture of sum frequency generation (SFG) and difference frequency generation (DFG) [249]:

$$\begin{aligned} \mathcal{P}_i^{(2)}(\omega') &= \epsilon_0 \sum_{jk} \chi_{ijk}^{(2)}(\omega'; \omega, \Omega) \mathcal{E}_j^{\text{p}}(\omega) \mathcal{E}_k^{\text{THz}}(\Omega) \\ &= \epsilon_0 \sum_{jk} \chi_{ijk}^{(2)}(\omega'; \omega, \Omega) \hat{E}_j^{\text{p}}(\omega) \hat{E}_k^{\text{THz}}(\Omega) e^{-i(\hat{k}(\omega) \pm \hat{k}(\Omega))z}, \end{aligned} \quad (\text{B.2})$$

where $\omega' = \omega \pm \Omega$. As Ω is typically smaller than the bandwidth of the probe, $\omega' \approx \omega$ and the nonlinear polarization gives rise to a new wave $\mathcal{E}^{\text{EOS}}(\omega)$. After propagation through the crystal, this additional component of the probe beam is equivalent to an additional phase, proportional to the amplitude of the THz field [249]:

$$\mathcal{E}_i(\omega) = \mathcal{E}_i^{\text{p}} + \mathcal{E}_i^{\text{EOS}} = \mathcal{E}_i^{\text{p}} \left(1 + i \frac{(\mathcal{E}_i^{\text{SFG}} + \mathcal{E}_i^{\text{DFG}})}{i\mathcal{E}_i^{\text{p}}} \right) \approx \mathcal{E}_i^{\text{p}} e^{i\varphi_i}, \quad (\text{B.3})$$

where $\varphi_i = (\mathcal{E}_i^{\text{SFG}} + \mathcal{E}_i^{\text{DFG}}) / (i\mathcal{E}_i^{\text{p}})$.

We measure the modulation using a balanced detector, which consists of a half waveplate to rotate the polarization of the probe, a polarizer to separate the probe beam into two polarization components, and two detectors. The angle of the waveplate is chosen so that the probe intensity on both detectors is initially equal. We then record the difference in intensity as it is modulated by the THz beam: $S_{\text{EOS}}(\tau) \propto \int |E_x(t - \tau)|^2 - |E_y(t - \tau)|^2 dt \propto E^{\text{THz}}(\tau)$. Scanning the delay τ of the probe allows to sample the whole THz signal.

When it is only needed to compare the relative amplitude of EOS measurements done in the same conditions as we have done throughout this manuscript, considering S_{EOS} directly is sufficient. However, if the goal is to reconstruct the exact waveform of the THz pulse or the strength of its electric field, the frequency-dependent effects distorting the waveform must be corrected for. Most of these effects are linear with the THz amplitude, allowing us to model them as a transfer function in the frequency domain:

$$S_{\text{EOS}}(\Omega) = T_{\text{inter}} T_{\text{crystal}} T_{\text{env}} T_{\text{pol}} T_{\text{prop}} T_{\text{overlap}} \mathcal{E}_{\text{THz}}(\Omega), \quad (\text{B.4})$$

where each transfer function is explained in the following sections.

B.2 Interfaces and reflections: T_{inter}

When the THz pulse enters the detection crystal, and particularly if it is thin or has a thin substrate, it undergoes multiple reflections which give rise to a Fabry-Pérot effect. In the case of a single-layer EOS crystal of thickness L , the transfer function for the Fabry-Pérot effect is [185]:

$$T_{\text{FP}}(\Omega) = \sum_{n=0}^{\infty} (r_{\text{in}} r_{\text{out}} \exp(-2ikL))^n = \frac{1}{1 - r_{\text{out}}^2 \exp(-2ikL)} \quad (\text{B.5})$$

where $r_{\text{out}} = (Z_0 - Z) / (Z_0 + Z) = (n - 1) / (n + 1)$ is the Fresnel reflection coefficient at the output interface for a complex impedance Z and index n , assuming normal incidence and a non-magnetic material. For EOS, we are interested in the THz electric field near the input surface of the setup, where it can start interacting with the probe. The transfer function of the single layer is thus:

$$T_{\text{inter}}(\Omega) = \frac{t_{\text{in}}}{1 - r_{\text{out}}^2 \exp(-2ikL)}. \quad (\text{B.6})$$

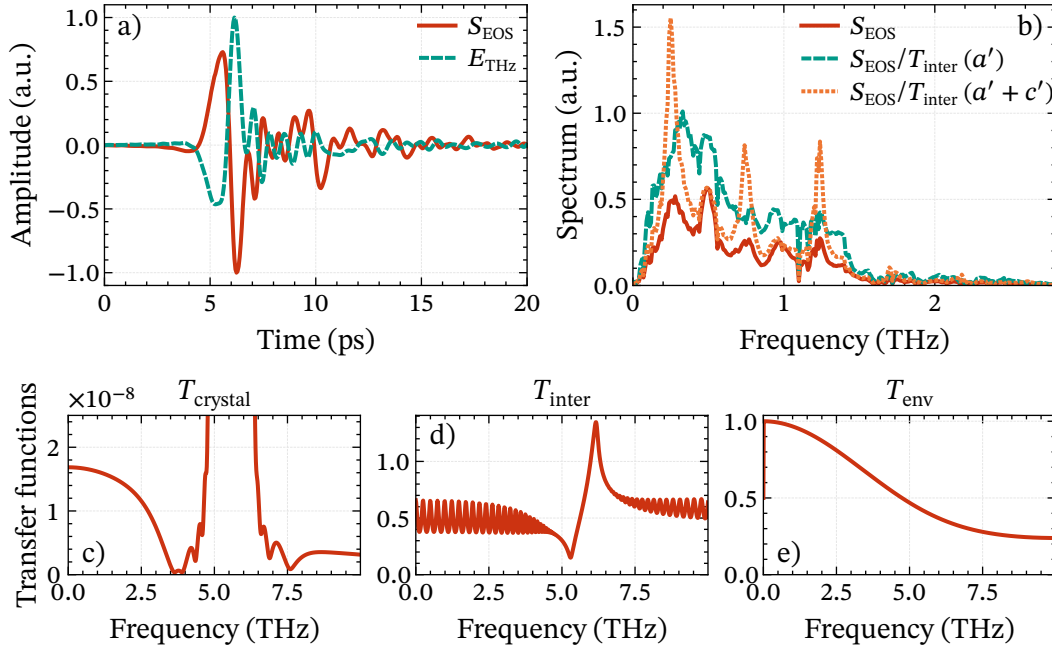


Figure B.1: Demonstration of the EOS deconvolution in a 190 μm -thick ZnTe crystal. a) Measured signal S_{EOS} and retrieved THz field E_{THz} . b) Spectrum before and after correction of the interference pattern by T_{inter} , including ($a' + c'$) or excluding (a') the back-propagating THz field. Transfer functions for c) the nonlinear process, d) the interference pattern and e) the time resolution of the probe.

Some EOS crystals are however mounted on a substrate. For the general case, one can use the transfer matrix method to calculate the transfer function of an arbitrary structure of M flat layers. We define a matrix linking the field at the beginning of each layer to field at the beginning of the next:

$$\begin{bmatrix} \mathcal{E}_{m-1}^+ \\ \mathcal{E}_{m-1}^- \end{bmatrix} = \mathbf{C}_m \begin{bmatrix} \mathcal{E}_m^+ \\ \mathcal{E}_m^- \end{bmatrix}. \quad (\text{B.7})$$

where \mathbf{C}_m is defined as per Eq. (C.1). In the case of EOS, we are interested in the THz field \mathcal{E}_N^+ entering the nonlinear layer N , as a function of the incoming field \mathcal{E}_0^+ . Multiplying the matrices of each layer, we can relate the field at the input and output of the whole structure:

$$\begin{bmatrix} \mathcal{E}_0^+ \\ \mathcal{E}_0^- \end{bmatrix} = \mathbf{C}_1 \mathbf{C}_2 \dots \mathbf{C}_{M+1} \begin{bmatrix} \mathcal{E}_{M-1}^+ \\ 0 \end{bmatrix}, \quad (\text{B.8})$$

and in the layer N to the output:

$$\begin{bmatrix} \mathcal{E}_N^+ \\ \mathcal{E}_N^- \end{bmatrix} = \mathbf{C}_{N+1} \mathbf{C}_{N+2} \dots \mathbf{C}_{M+1} \begin{bmatrix} \mathcal{E}_{M-1}^+ \\ 0 \end{bmatrix}. \quad (\text{B.9})$$

Defining the product of the matrices as:

$$\begin{bmatrix} a & b \\ c & d \end{bmatrix} = \mathbf{C}_1 \mathbf{C}_2 \dots \mathbf{C}_{M+1} \quad \text{and} \quad \begin{bmatrix} a' & b' \\ c' & d' \end{bmatrix} = \mathbf{C}_{N+1} \mathbf{C}_{N+2} \dots \mathbf{C}_{M+1}, \quad (\text{B.10})$$

the total field in the active nonlinear layer is then:

$$\mathcal{E}_N = \mathcal{E}_N^+ + \mathcal{E}_N^- = \frac{a' + c'}{a} \mathcal{E}_0^+. \quad (\text{B.11})$$

This includes the forward- and backward-propagating THz field. However, the backward-propagating field is usually poorly phase-matched with the probe and using the transfer function:

$$T_{\text{inter}}(\Omega) = \frac{a'}{a} \quad (\text{B.12})$$

is sufficient to completely remove the Fabry-Pérot oscillations in the measured spectrum. As shown in Fig. B.1b, including c' leads to overcompensating for the interference pattern. As the probe pulse is integrated in the detector and only its amplitude considered, the multiple reflections of the probe can be ignored.

B.3 Nonlinear process: T_{crystal} and T_{env}

As mentioned in Appendix B.1, the nonlinear polarization:

$$\begin{aligned} \mathcal{P}_i^{(2)}(\omega) &= \hat{P}_i^{(2)} e^{-i(\mathcal{K}(\omega \pm \Omega) \mp \mathcal{K}(\Omega))z}, \\ &= \epsilon_0 \sum_{jk} \chi_{ijk}^{(2)}(\omega; \omega \pm \Omega, \Omega) \hat{E}_j^{(2)}(\omega \pm \Omega) \hat{E}_k^{\text{THz}}(\Omega) e^{-i(\mathcal{K}(\omega \pm \Omega) \mp \mathcal{K}(\Omega))z} \end{aligned} \quad (\text{B.13})$$

gives rise to a new wave propagating according to the wave equation [33, chapter 2]:

$$(\nabla^2 - \mathcal{K}(\omega)) \mathcal{E}_i^{\text{EOS}}(\omega) = \frac{\omega^2}{\epsilon_0 c^2} \mathcal{P}_i^{(2)}(\omega), \quad (\text{B.14})$$

which simplifies to:

$$\frac{d}{dz} \hat{E}_i^{\text{EOS}}(\omega) = \frac{i\omega^2}{2\epsilon_0 c^2 \mathcal{K}} \hat{P}_i^{(2)}(\omega) e^{-i\Delta \mathcal{K} z}, \quad (\text{B.15})$$

where $\mathcal{K} = \omega \sqrt{1 + \chi_{ii}^{(1)}} / c$ is the complex wavevector and $\Delta \mathcal{K} = \mathcal{K}(\omega \pm \Omega) \mp \mathcal{K}(\Omega) - \mathcal{K}(\omega)$ the complex phase mismatch parameter. Integrating over the length L of the crystal, we get:

$$\hat{E}_i^{\text{EOS}}(\omega) = \frac{i\omega^2}{2\epsilon_0 c^2 \mathcal{K}} \hat{P}_i^{(2)}(\omega) \frac{e^{-i\Delta \mathcal{K} L} - 1}{i\Delta \mathcal{K}}. \quad (\text{B.16})$$

The real part of the factor $(e^{-i\Delta\kappa L} - 1) / i\Delta\kappa$ can be simplified to $L \text{sinc}(\Delta\kappa L / 2)$ and represents the loss of amplitude when the waves are mismatched. Its imaginary part accounts for the absorption of the waves as they go through the crystal, which is why it is important that T_{inter} is defined to give the THz field at the beginning of the layer.

The components due to SFG and DFG can be shown to be equivalent [249]. From Eqs. (B.3), (B.13) and (B.16), the modulation φ_i created by the new wave is thus:

$$\varphi_i(\omega) = \frac{\mathcal{E}_i^{\text{EOS}}(\omega)}{i\mathcal{E}_i^{\text{p}}(\omega)} = \frac{i\omega^2}{2\epsilon_0 c^2 \kappa} \chi_{ijk}^{(2)} \frac{\hat{E}_j^{\text{p}}(\omega - \Omega) \hat{E}_k^{\text{THz}}(\Omega)}{i\hat{E}_i^{\text{p}}(\omega)} \frac{e^{-i\Delta\kappa L} - 1}{i\Delta\kappa}. \quad (\text{B.17})$$

The EOS crystal we generally use is ZnTe, for which only the r_{41} coefficient is non-zero. In term of the nonlinear susceptibility, we thus have:

$$\varphi \propto \chi_{231}^{(2)} \left(\frac{\hat{E}_3^{\text{p}}(\omega - \Omega) \hat{E}_1^{\text{THz}}(\Omega)}{i\hat{E}_2^{\text{p}}(\omega)} + \frac{\hat{E}_2^{\text{p}}(\omega - \Omega) \hat{E}_1^{\text{THz}}(\Omega)}{i\hat{E}_3^{\text{p}}(\omega)} \right), \quad (\text{B.18})$$

where the directions 1, 2 and 3 refer to the crystal axes [1 0 0], [0 1 0] and [0 0 1], respectively.

We use the waveplate of the balanced detector to rotate the polarization of the probe so that the amplitude of both beams is identical in the absence of THz radiation [249]:

$$\mathcal{E}_x = \frac{1}{2}\mathcal{E}^{\text{p}} \left(1 + \frac{\varphi}{2} \right) \quad \text{and} \quad \mathcal{E}_y = \frac{1}{2}\mathcal{E}^{\text{p}} \left(1 - \frac{\varphi}{2} \right) \quad (\text{B.19})$$

where x and y refer to the coordinate system of the polarizer. For a given delay of the probe, the EOS signal is given by the difference in intensity of the beam on the two detectors:

$$\begin{aligned} S_{\text{EOS}}(\tau) &= \int_0^\infty |\mathcal{E}_x(\omega)|^2 - |\mathcal{E}_y(\omega)|^2 d\omega. \\ &= \int_0^\infty -\frac{1}{2} \mathcal{E}^{\text{p}}(\omega) \mathcal{E}^{\text{p}*}(\omega) \text{Im}(\varphi) d\omega \\ &= \int_{-\infty}^{+\infty} \frac{\omega^2}{8\epsilon_0 c^2 \kappa} \chi_{\text{eff}}^{(2)} \hat{E}^{\text{p}}(\omega) \hat{E}^{\text{p}*}(\omega - \Omega) \hat{E}_k^{\text{THz}}(\Omega) \frac{e^{-i\Delta\kappa L} - 1}{i\Delta\kappa} d\omega \end{aligned} \quad (\text{B.20})$$

where the effective susceptibility tensor $\chi_{\text{eff}}^{(2)} = \chi_{231}^{(2)}$ in the case of ZnTe.

From this, we can extract two transfer functions. The transfer function of the nonlinear behavior, including the susceptibility of the crystal and the phase matching of the beams, is [185, 249]:

$$T_{\text{crystal}}(\Omega) = \chi_{\text{eff}}^{(2)} \frac{e^{-i\Delta\kappa L} - 1}{i\Delta\kappa} = \chi_{\text{eff}}^{(2)} \frac{e^{-i\frac{\Omega}{c}(n_g(\omega) - n(\Omega))L} - 1}{i\frac{\Omega}{c}(n_g(\omega) - n(\Omega))}, \quad (\text{B.21})$$

As we derived in Eq. (2.20), the phase matching depends on the THz refractive index and the group index of the probe. The second is the spectrum of the envelope of the

probe and represents the loss of temporal resolution due to the duration of the probe pulse [249]:

$$T_{\text{env}}(\Omega) = \int_{-\infty}^{+\infty} \hat{E}^{\text{p}}(\omega) \hat{E}^{\text{p}*}(\omega - \Omega) d\omega. \quad (\text{B.22})$$

T_{crystal} and T_{env} are plotted for ZnTe in Fig. B.1.

B.4 Polarization angles: T_{pol}

The value of $\chi_{\text{eff}}^{(2)}$ depends on the angle between the crystal axes and the polarization of the THz and probe beams. ZnTe is usually used with a (1 1 0) cut, so that both beams propagate along the [1 1 0] axis. The plane of the sample contains only the [0 0 1] or Z axis. With α and β the angles between the Z axis and the THz and probe polarization respectively, we get the transfer function [252]:

$$T_{\text{pol}}(\Omega) = \cos \alpha \sin 2\beta + 2 \sin \alpha \cos 2\beta. \quad (\text{B.23})$$

The signal is maximum for $\alpha = \pm \frac{\pi}{2}$ and $\beta - \alpha = 0$ or $\pm \frac{\pi}{2}$. It is thus best to have the probe beam polarized orthogonal or parallelly to the THz beam.

B.5 Propagation to the EOS crystal: T_{prop}

If we want to reconstruct the generated THz field and not the field incident on the crystal, the optical path between the generation point and the crystal should be taken into account. In general, it consists of the propagation through air or vacuum, as well as a collecting optic and a focusing optic, such as a pair of off-axis parabolas (OAPs).

In collinear geometry, a Gaussian pump with a radius r_p generates a Gaussian THz beam with a radius of $r_0 = r_p / \sqrt{2}$. For frequencies satisfying the condition $kr_0 \gg 1$, the paraxial approximation holds and the typical diffraction length of the THz beam is the Rayleigh length $z_R = kr_0^2 / 2$, while for $kr_0 \ll 1$ the beam is in Bethe's regime and the smaller diffraction length is $z_B = k^2 r_0^3 / 2$ [253]. Faure et al. [185] showed that a good approximation in both cases for the transfer function of a collecting optic of half diameter D_{col} and focal length f_{col} is:

$$T_{\text{col}}(\Omega) = \sqrt{1 - \exp\left(-\frac{\tan^2 \theta_{\text{col}} z_{\text{diff}}^2}{r_0^2}\right)} \quad (\text{B.24})$$

where $\theta_{\text{col}} = \arctan(D_{\text{col}} / 2f_{\text{col}})$ is the half collection angle, and $z_{\text{diff}} = z_R$ or z_B .

The radius of the collected THz beam for each frequency is either determined by the initial diffraction or limited by the diameter of the collecting optic: $r_1(\Omega) = \min[D_{\text{col}} / 2, r_0 \sqrt{1 + f_{\text{col}}^2 / z_{\text{diff}}^2}]$. Assuming that the beam is collimated between the collecting and focusing optics, the radius on the focusing optic is then $r_2(\Omega) = \min[D_{\text{foc}} / 2, r_1]$. If $D_{\text{foc}} < D_{\text{col}}$, some energy is lost: $T_{\text{clip}} = \text{erf}(r_2 / r_1)$.

In the focus, the spot size of each frequency component is $r_{\text{foc}}(\Omega) = 2cf_{\text{foc}} / (\Omega r_2)$. The larger it is, the weaker is the sampled field amplitude. The transfer function for the focusing is thus $T_{\text{foc}} = r_2 / r_{\text{foc}}$ [185].

The total transfer function for the propagation of the THz radiation is thus:

$$T_{\text{prop}}(\Omega) = T_{\text{col}} T_{\text{clip}} T_{\text{foc}}. \quad (\text{B.25})$$

It is accurate in the case of two perfectly aligned OAPs. For propagation in humid air, the absorption of water over the propagation distance should also be taken into account, as it creates an oscillatory tail following the pulse [254].

B.6 Probe size: T_{overlap}

As in the previous section, this transfer function can be left out if the aim is to reconstruct the THz waveform as encountered by the probe, for example in the case of the FeBO₃ sample replacing the EOS crystal in Section 2.3.2. Since the different THz frequency components have different spot sizes in the focus, the overlap with the probe is frequency-dependent.

If the two beams are centered on one another on the crystal, the EOS signal can be expressed as a function of the radial distance to the center [185]:

$$S_{\text{EOS}}(\Omega) \propto |\hat{E}^p(r)|^2 E^{\text{THz}}(r, \Omega). \quad (\text{B.26})$$

Assuming that both beams are Gaussian and integrating over r gives the transfer function [185]:

$$T_{\text{overlap}}(\Omega) = \frac{r_{\text{foc}}^2}{\sqrt{2r_{\text{foc}}^2 + r_{\text{probe}}^2}}. \quad (\text{B.27})$$

B.7 Balanced photodetectors

The amplitude of the probe transmitted through the EOS crystal is acquired using a balanced photodetector. Such a detector works by separating the two components of the probe polarization and measuring each separately. The EOS signal is then given by the normalized voltage difference of the two channels, so as to be insensitive to the total energy in the probe: $S = (V_A - V_B) / (V_A + V_B)$. The beam is aligned to hit both detectors and the angle of the polarizer is manually balanced such that $V_A = V_B$ in the absence of THz generation.

The electric signal from the detector is transmitted to a lock-in amplifier, whose goal is to amplify a precise frequency within the signal. In the case of the measurements of Chapter 4, its internal oscillator generates a reference oscillation at $\omega_r = 1.5$ kHz, which

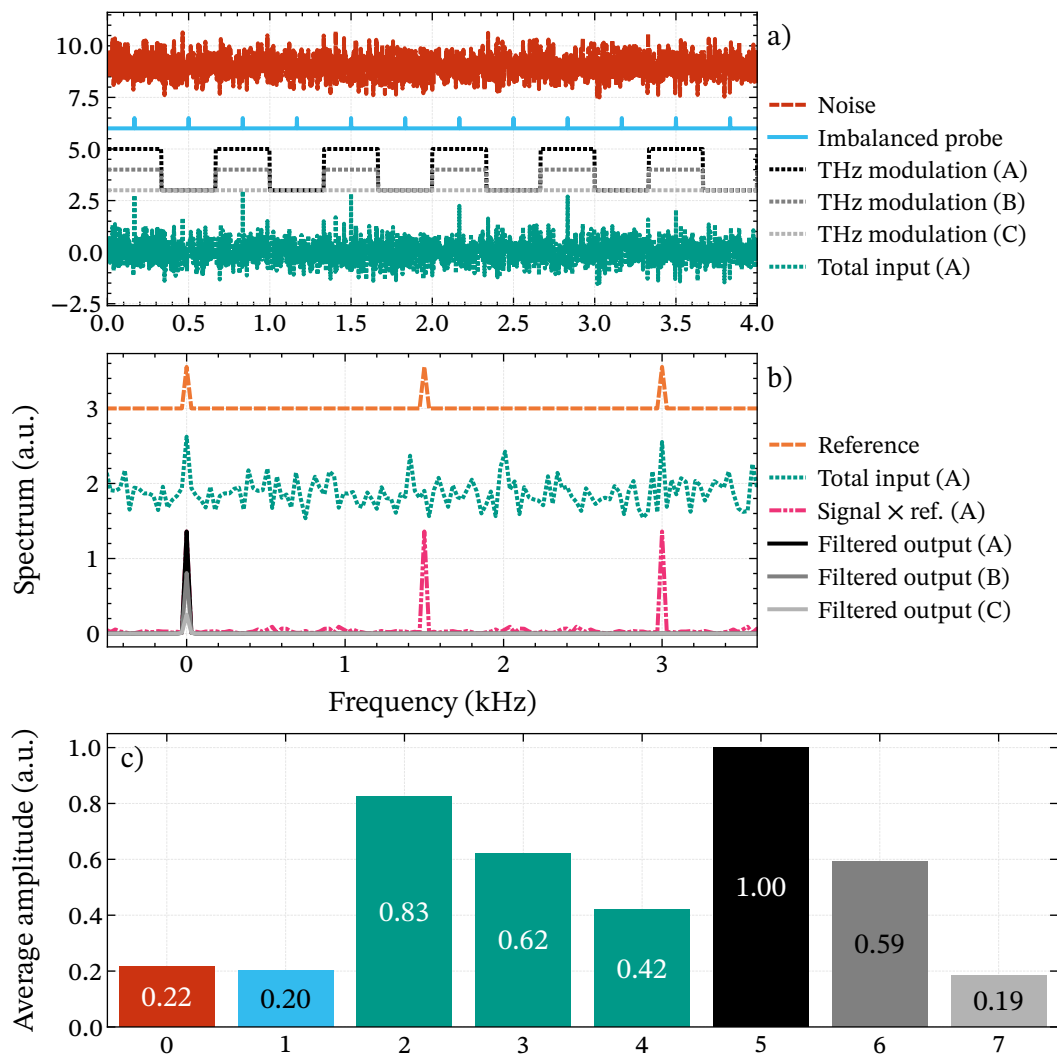


Figure B.2: Simulation of a signal cleaned by the lock-in amplifier. a) The original signal is composed of noise, a component at 3 kHz from the unbalanced probe, and a component at 1.5 kHz with a relative amplitude of 1 (case A), 0.5 (case B) or 0 (case C). b) The lock-in amplifier mixes the signal with a reference signal at 1.5 kHz and uses a narrow low-pass filter to keep only the DC component. c) The lock-in amplifier returns the average amplitude of the filtered signal, which has a better signal-to-noise ratio than the original signal.

we synchronize with the rest of the laser system. The input signal S is then multiplied by this reference R :

$$\begin{aligned} SR &= (R_0 e^{i(\omega_r t + \theta_r)} + \text{c.c.}) \cdot (S_0 e^{i(\omega_s t + \theta_s)} + \text{c.c.}) \\ &= S_0 R_0 e^{i(\omega_r + \omega_s)t + i(\theta_r + \theta_s)} + S_0 R_0 e^{i(\omega_r - \omega_s)t + i(\theta_r - \theta_s)} + \text{c.c.} \end{aligned} \quad (\text{B.28})$$

and the Fourier spectrum of the mixed signal shows two peaks at the frequencies $\omega_r + \omega_s$ and $\omega_r - \omega_s$. The signal is then averaged for $\tau = 300$ ms, which corresponds to using a low-pass filter of bandwidth $1 / (2\pi\tau) = 0.53$ Hz, to keep only the $\omega_s = \omega_r$ component. In the time domain, this makes use of the fact that the average of $\cos^2(\omega t + \theta)$ is 1: if $\omega_s = \omega_r$ and $\theta_s = \theta_r$, the product of both oscillations averages to a non-zero value, while, for any other frequency, the oscillations average to zero given sufficient time. The lock-in amplifier then outputs the amplitude of the filtered signal.

This process is simulated in Fig. B.2. The input signal is created by superposing a high level of random noise, a parasitic signal with a repetition rate of 3 kHz representing the improper balancing of the probe, and a second probe signal with a 1.5 kHz modulation representing the THz beam. Three different modulations strengths are used, indicated as A, B and C on the plot, with relative amplitudes 1, 0.5 and 0, respectively.

In the time domain (Fig. B.2a), the peaks due to the THz pulses are distinguishable in the total signal, but the level of noise is high. In the frequency domain (Fig. B.2b), the 1.5 kHz component is buried in the noise. Fig. B.2c shows the average amplitude of the different components after integrating for $\tau = 300$ ms. The amplitude of the total input signal for the case C (no THz radiation) consists only of the noise and unbalanced probe. It is half as high as the amplitude of the full input signal. If we were to record the signal without lock-in amplifier, the signal-to-noise ratio would thus be 1.98.

After mixing the input signal and the reference, the spectrum has a significantly lower noise level and shows a well-defined peak at 1.5 kHz. The filtering operation then discards everything except for the zero-frequency component. We see that the amplitude of the noise (filtered output C) is reduced, while the amplitude of the THz signal (filtered output A) increases. The signal-to-noise ratio is now 5.26 and the output signal reproduces better the original THz amplitude. The random noise is almost completely filtered, but the output is still biased by the unbalanced probe, as its spectrum overlaps with the THz signal.

Spintronic THz emitters sources

The transfer-matrix method [255, 256] is used to calculate the one-dimensional propagation of a beam through thin multilayered structures where multiple reflections at the interfaces need to be taken into account. It uses two-component vectors to represent forward- and backward-propagating fields, and two-by-two matrices representing each a layer. In the frequency domain, the field at the beginning of each layer m is related to the field in the previous layer by the matrix $C_m(\omega)$:

$$\begin{aligned} \begin{bmatrix} E_{m-1}^+ \\ E_{m-1}^- \end{bmatrix} &= \begin{bmatrix} e^{i\delta_{m-1}} & 0 \\ 0 & e^{-i\delta_{m-1}} \end{bmatrix} \begin{bmatrix} 1/t_m & r_m/t_m \\ r_m/t_m & 1/t_m \end{bmatrix} \begin{bmatrix} E_m^+ \\ E_m^- \end{bmatrix} \\ &= \frac{1}{t_m} \underbrace{\begin{bmatrix} e^{i\delta_{m-1}} & r_m e^{i\delta_{m-1}} \\ r_m e^{-i\delta_{m-1}} & e^{-i\delta_{m-1}} \end{bmatrix}}_{C_m} \begin{bmatrix} E_m^+ \\ E_m^- \end{bmatrix}. \end{aligned} \quad (\text{C.1})$$

This matrix is formed from the product of the propagation matrix, representing the propagation through the layer $m - 1$, and the interface matrix, where r_m and t_m are the complex Fresnel coefficients at the $m - 1 | m$ interface [214]:

$$r_m = \frac{Z_m - Z_{m-1}}{Z_m + Z_{m-1}}, \quad t_m = \frac{2Z_m}{Z_m + Z_{m-1}}. \quad (\text{C.2})$$

As the layers are metallic, $\mu_r \neq 1$ and we use the impedance $Z = \sqrt{\mu/\epsilon} = n / (c\epsilon)$ where $n = \sqrt{\epsilon_r \mu_r}$ is the frequency-dependent complex refractive index. The factor $\delta_m = k_m L_m = n_m \omega L_m / c$ represents the added phase and the absorption during the propagation through the layer m of thickness L_m . $E_m^+ = t_m E_{m-1}^+ e^{-i\delta_{m-1}}$ is then the positively propagating field taken directly after entering the layer m . By setting $L_0 = 0$, E_0 represents the field incoming on the sample.

Using this recurrence relation, one can relate the field at the input and output of a

M -layer structure by the product of the matrices:

$$\begin{aligned} \begin{bmatrix} E_0^+ \\ E_0^- \end{bmatrix} &= \mathbf{C}_1 \mathbf{C}_2 \dots \mathbf{C}_{M+1} \begin{bmatrix} E_{M+1}^+ \\ E_{M+1}^- \end{bmatrix} \\ &= \begin{bmatrix} C_{11} & C_{12} \\ C_{21} & C_{22} \end{bmatrix} \begin{bmatrix} E_{M+1}^+ \\ E_{M+1}^- \end{bmatrix}. \end{aligned} \quad (\text{C.3})$$

In the case of a beam incoming on one side of the sample ($E_{\text{in}} = E_0^+$), there is no incoming field on the other side ($E_{M+1}^- = 0$), and one can easily calculate the incoming, transmitted (E_{M+1}^+) and reflected (E_0^-) fields, provided one of them is known:

$$E_0^+ = C_{11} E_{M+1}^+, \quad (\text{C.4})$$

$$E_0^- = C_{21} E_{M+1}^+. \quad (\text{C.5})$$

However, in the case of spintronic THz emitters, the THz field is generated inside the structure, so the transfer function needs to be adapted.

C.1 Single punctual source

We use a source vector $\vec{\mathcal{S}}_m$ representing the THz field generated by inverse spin Hall effect (ISHE) in a layer m , assuming in a first time that the THz field is emitted directly at the input interface. The total field in layer m is then constituted of $\vec{\mathcal{S}}_m$ and the reflections $\Delta \vec{\mathcal{S}}_m$ created at the interfaces and propagating back and forth, as represented in Fig. C.1:

$$\begin{bmatrix} E_m^+ \\ E_m^- \end{bmatrix} = \begin{bmatrix} S_m^+ \\ S_m^- \end{bmatrix} + \begin{bmatrix} \Delta S_m^+ \\ \Delta S_m^- \end{bmatrix}. \quad (\text{C.6})$$

When considering the layers $m + 1$ to the end of the sample, the forward emission of the source is visible while S_m^- only contributes in the form of reflections. The recurrence relation then reads:

$$\begin{bmatrix} S_m^+ + \Delta S_m^+ \\ \Delta S_m^- \end{bmatrix} = \underbrace{\mathbf{C}_{m+1} \mathbf{C}_{m+2} \dots \mathbf{C}_{M+1}}_{F_m} \begin{bmatrix} E_{M+1}^+ \\ E_{M+1}^- \end{bmatrix}. \quad (\text{C.7})$$

Reciprocally, when considering the layers before the source, only the backward emission contributes directly:

$$\begin{bmatrix} E_0^+ \\ E_0^- \end{bmatrix} = \underbrace{\mathbf{C}_1 \dots \mathbf{C}_{m-1} \mathbf{C}_m}_{B_m} \begin{bmatrix} \Delta S_m^+ \\ S_m^- + \Delta S_m^- \end{bmatrix}. \quad (\text{C.8})$$

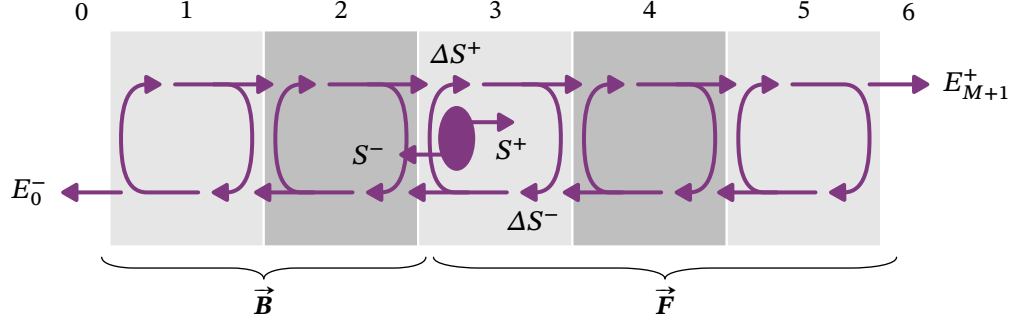


Figure C.1: Multiple internal reflections of the electric field generated by the source S inside a multilayer structure.

We call F_m and B_m the forward and backward products of the transfer matrices for the source S_m . Since there is no field incoming on the structure, $E_0^+ = E_{M+1}^- = 0$. We can expand Eq. (C.7) and Eq. (C.8) as:

$$\begin{bmatrix} 0 \\ E_0^- \end{bmatrix} = \begin{bmatrix} B_{11} & B_{12} \\ B_{21} & B_{22} \end{bmatrix} \begin{bmatrix} \Delta S_m^+ \\ S_m^- + \Delta S_m^- \end{bmatrix} \quad (\text{C.9a})$$

$$\begin{bmatrix} S_m^+ + \Delta S_m^+ \\ \Delta S_m^- \end{bmatrix} = \begin{bmatrix} F_{11} & F_{12} \\ F_{21} & F_{22} \end{bmatrix} \begin{bmatrix} E_{M+1}^+ \\ 0 \end{bmatrix}. \quad (\text{C.9b})$$

In the case of the spintronic emitters, the THz field is generated by accelerated electrons moving in the plane of the layers, thus we set $S_m^+ = S_m^- = S_m$. The system has five unknowns: E_0^- , E_{M+1}^+ , S_m , ΔS_m^+ and ΔS_m^- . Solving the system provides two frequency-dependent transfer functions, mapping the amplitude of the initial source field to the emitted THz amplitude on each side of the sample:

$$S_m = \frac{B_{11}F_{11} + B_{12}F_{21}}{B_{11} - B_{12}} E_{M+1}^+, \quad (\text{C.10a})$$

$$S_m = \frac{B_{11}F_{11} + B_{12}F_{21}}{B_{11}B_{22}F_{11} + B_{11}B_{22}F_{21} - B_{12}B_{21}F_{11} - B_{12}B_{21}F_{21}} E_0^-. \quad (\text{C.10b})$$

C.2 Single punctual source at the output interface

As shown in Fig. C.1, the transfer functions in Eq. (C.10) assume the THz field to be emitted at the input interface of the layer m . To replicate spintronic emitters, we also need the transfer functions for a source on the output interface of a layer.

The recurrence relation of the transfer-matrix model in Eq. (C.1) defines every field at the input interface, irrespective of the point where it is generated. Hence we can define, for the source S_m located at any position $0 < z < L_m$ in the layer, the corresponding

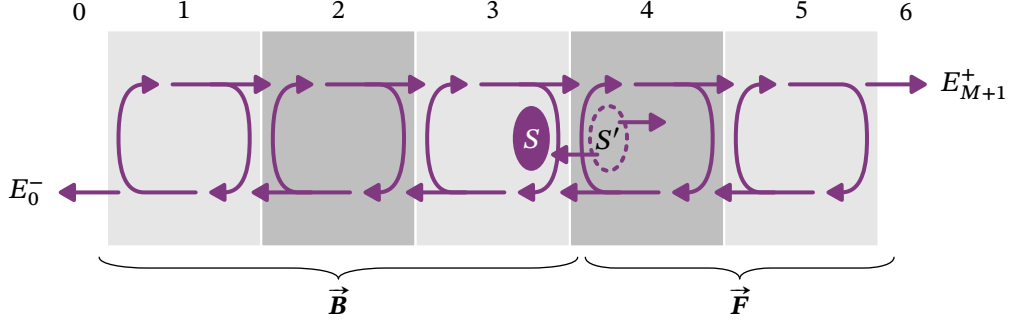


Figure C.2: Multiple internal reflections of the electric field generated by the source S inside a multilayer structure, calculated as coming from the virtual source S' .

virtual source S'_m at the input interface ($z = 0$). To maintain the correct amplitude of the field at the position of the real source, we substitute in Eq. (C.9) S_m by S'_m , defined as:

$$\begin{bmatrix} S'_m{}^+ \\ S'_m{}^- \end{bmatrix} = \begin{bmatrix} e^{ik_m z} & 0 \\ 0 & e^{-ik_m z} \end{bmatrix} \begin{bmatrix} S_m^+ \\ S_m^- \end{bmatrix}. \quad (\text{C.11})$$

Another option, illustrated in Fig. C.2, is to replace a source at the output interface of the layer m by a virtual source at the input interface of the layer $m + 1$, using the interface matrix defined in Eq. (C.1):

$$\begin{bmatrix} S_m^+ \\ S_m^- \end{bmatrix} = \begin{bmatrix} 1/t_{m+1} & r_{m+1}/t_{m+1} \\ r_{m+1}/t_{m+1} & 1/t_{m+1} \end{bmatrix} \begin{bmatrix} S'_{m+1}{}^+ \\ S'_{m+1}{}^- \end{bmatrix}. \quad (\text{C.12})$$

This second version is numerically more robust than Eq. (C.11) in the case of thick layers through which some frequencies are completely absorbed, as the Fresnel coefficient t_{m+1} of the $m | m + 1$ interface only approaches zero when $n_{m+1} \gg n_m$. In addition, the isotropy of the source is preserved: if $S_m^+ = S_m^- = S_m$, then Eq. (C.12) gives:

$$S'_{m+1}{}^+ = S'_{m+1}{}^- = S'_{m+1} = \frac{t_{m+1}}{r_{m+1} + 1} S_m. \quad (\text{C.13})$$

Using Eq. (C.10) to calculate the virtual source S'_{m+1} and Eq. (C.13) to convert it to the real source S_m , the transfer functions for a source at the output interface are:

$$S_m = \frac{r_{m+1} + 1}{t_{m+1}} \frac{B_{11}F_{11} + B_{12}F_{21}}{B_{11} - B_{12}} E_{M+1}^+ \quad (\text{C.14a})$$

$$S_m = \frac{r_{m+1} + 1}{t_{m+1}} \frac{B_{11}F_{11} + B_{12}F_{21}}{B_{11}B_{22}F_{11} + B_{11}B_{22}F_{21} - B_{12}B_{21}F_{11} - B_{12}B_{21}F_{21}} E_0^-. \quad (\text{C.14b})$$

where the coefficients of the matrices \mathbf{B} and \mathbf{F} are defined with respect to the virtual source in layer $m + 1$.

C.3 Several punctual sources

We are generally interested in calculating the amplitude of the sources from an experimental value of E_{M+1}^+ , for example the Fourier transform of an electro-optic sampling (EOS) measurement. As the layers are thin compared to the wavelength of THz radiation, the emission from all the sources propagate in the sample at the same time and their output will be superposed in the measurement:

$$E_{\text{tot}} = \sum_m E_{M+1}^+(S_m). \quad (\text{C.15})$$

As the individual $E_{M+1}^+(S_m)$ are linear functions of the source S_m , we can solve this equation if we can express the amplitudes of every source as a function of a single one.

We make the following assumptions:

- The spin current j_s inside a ferromagnetic layer is proportional to the absorbed IR power A_m in this layer [21] and is the same in the forward and backward directions.
- The charge current in a nonmagnetic layer is proportional to the spin current in the adjacent ferromagnetic layer and its spin Hall angle: $j_c = \vartheta_H j_s$.
- The amplitude of the source is proportional to the charge current and the conductivity of the layer: $S_m \propto j_c / \sigma_m$.

This allows us to express each source as $S_m \propto A_m \vartheta_{H,m} \sigma_m$. The absorbed power A_m can be calculated as the difference of the Poynting vector at the entrance of each layer using the usual transfer matrix method [202], while $\vartheta_{H,m}$ and σ_m are known properties of the material. We arbitrarily choose one of the sources as reference S_0 . The other sources are thus:

$$S_m = S_0 \frac{A_m \vartheta_m \sigma_m}{A_0 \vartheta_0 \sigma_0}. \quad (\text{C.16})$$

Inserting either Eq. (C.10a) or Eq. (C.14a) in Eq. (C.15) depending on whether each source is at the input or output interface of its layer, we can express Eq. (C.15) as a function of S_0 :

$$\begin{aligned} E_{\text{tot}} &= \sum_m \frac{B_{11} - B_{12}}{B_{11}F_{11} + B_{12}F_{21}} S'_m \\ &= \sum_{\text{in}} \frac{A_m \vartheta_m \sigma_m}{A_0 \vartheta_0 \sigma_0} \frac{B_{11} - B_{12}}{B_{11}F_{11} + B_{12}F_{21}} S_0 + \sum_{\text{out}} \frac{A_m \vartheta_m \sigma_m}{A_0 \vartheta_0 \sigma_0} \frac{t_{m+1}}{r_{m+1} + 1} \frac{B_{11} - B_{12}}{B_{11}F_{11} + B_{12}F_{21}} S_0 \end{aligned} \quad (\text{C.17})$$

where the dependency on m or $m + 1$ of the coefficients of \mathbf{F} and \mathbf{B} is implied. This equation can be analytically solved without specialized computational resources for a small number of sources. The solution can be then applied to any sample with the same number of sources, and at the same positions. We performed the analytical calculations for 1 to 4 sources in Python with the SymPy module, and later numerically evaluated the value of the matrix coefficients for specific samples.

C.4 Extended sources

The THz wavelength is significantly larger than the few-nanometer thickness of the layers of the spintronic emitters used in [Chapter 4](#). In addition, the absorption for the materials measured in [Appendix A](#) is negligible at this scale. The THz field within a layer is thus almost constant and it makes little difference where in the layer the field is generated. We could then so far assume that the sources were punctual and located at the interfaces.

However, in certain samples we are interested in observing the behavior of the spin currents, by comparing the amplitude of the THz emission while varying the thickness of the non-magnetic (NM) layer where the THz source is located. The thickness of the layers is similar to the spin diffusion length, which means that the spin current is only partially converted into charge current, and thus into THz field. Each point in the NM layer m contributes to the emitted THz radiation proportionally to the local amplitude of the spin current, which decays exponentially [[155](#)] with a decay length of λ_m . To quantify the THz emission, we integrate it over the source layer of thickness L_m , where the spin current enters the layer at $z = 0$:

$$S_m^{\text{part}} = \frac{\int_0^{L_m} S_m \exp\left(-\frac{L_m}{\lambda_m}\right) dz}{\int_0^\infty \exp\left(-\frac{L_m}{\lambda_m}\right) dz} = S_m \left(1 - \exp\left(-\frac{L_m}{\lambda_m}\right)\right). \quad (\text{C.18})$$

The transfer-matrix formalism only supports punctual sources. In a first time, we represented the delocalized THz emission by dividing the source layer into several identical sub-layers, each emitting at its interface parts of the total THz radiation according to [Eq. \(C.18\)](#). Calculating numerically the sample output E_{tot} , we found only a negligible difference on the THz waveform compared to using a single source layer. We thus continue assuming that all the energy of the reduced source is generated at the interface of the layer. We thus update [Eq. \(C.16\)](#):

$$S_m = S_0 \frac{A_m \vartheta_m \sigma_m \left(1 - \exp\left(-\frac{L_m}{\lambda_m}\right)\right)}{A_0 \vartheta_0 \sigma_0 \left(1 - \exp\left(-\frac{L_0}{\lambda_0}\right)\right)}. \quad (\text{C.19})$$

We neglect in this model that a significant part of the spin current reaching the end of the layer is reflected at the interface [[257](#)]. Although a part of the spin current then flips its spin, the spin polarization of the whole current is conserved as long as the spin flip ratio is less than $1 / 2$. This means that the reflected spin current contributes to a charge current with the opposite sign, and the overall THz generation in the layer is reduced. We however neglect this contribution, as there is no available data on the spin reflection coefficients of the layers.

List of Publications

Journal articles

E. Kueny et al., “Spin-structured multilayer THz emitters by oblique incidence deposition”, *Journal of Applied Physics* **133**, 33903 (2023), DOI: 10/gr7m5v.

A.-L. Calendron et al., “Bulk, cascaded pulse compression scheme and its application to spin emitter characterization”, *Applied Optics* **60**, 912–917 (2021), DOI: 10/gr7m39.

W. Tian et al., “ μ J-level multi-cycle terahertz generation in a periodically poled Rb:KTP crystal”, *Optics Letters* **46**, 741–744 (2021), DOI: 10/gjmtz9.

E. Kueny et al., “Wavefront analysis of a white-light supercontinuum”, *Optics Express* **26**, 31299–31306 (2018), DOI: 10/gfjz25.

Conferences

E. Kueny et al., “Spin-structured multilayer THz emitters”, in *Joint Magnetic European Symposia* (July 24, 2022).

A.-L. Calendron et al., “Destructive interferences of THz emission by spin emitters”, in *Joint Magnetic European Symposia* (Dec. 7, 2020).

E. Kueny et al., “Characterization of kapton, FeBO₃ and sapphire in the THz region”, in *45th International Conference on Infrared, Millimeter, and Terahertz Waves* (Nov. 8–13, 2020), DOI: 10/gmx8kf.

A.-L. Calendron et al., “Strong-field THz source for magneto-optic experiment”, in *International Photonics and OptoElectronics Meeting* (Nov. 11–14, 2019), TW2F.2, DOI: 10/ggnb3c.

E. Kueny, A.-L. Calendron, and F. X. Kärtner, “Electro-optic sampling of terahertz pulses in multilayer crystals”, in *Advanced Solid State Lasers* (2019), JTU3A.16, DOI: 10/ggfj9g.

A.-L. Calendron et al., “Excitation and control of spin waves in FeBO₃ by a strong-field THz pulse”, in *XXI International Conference on Ultrafast Phenomena*, Vol. 205, *EPJ Web of Conferences* (July 15–20, 2018), p. 7008, DOI: 10/ggnb29.

E. Kueny et al., “Wavefront analysis of white-light supercontinuum”, in *Conference on Lasers and Electro-Optics* (2018), FW4E.4, DOI: 10/gr7m2g.

S. Valente et al., “Timing stabilization of solid-state, Yb-based laser system”, in *Conference on Lasers and Electro-Optics* (2018), JTh2A.140, DOI: 10/ggnb3b.

Bibliography

- [1] M. Julliere, “Tunneling between ferromagnetic films”, *Physics Letters A* **54**, 225–226 (1975), DOI: 10/crznw9.
- [2] G. Binasch et al., “Enhanced magnetoresistance in layered magnetic structures with antiferromagnetic interlayer exchange”, *Physical Review B* **39**, 4828–4830 (1989), DOI: 10/fgvgfc.
- [3] M. N. Baibich et al., “Giant magnetoresistance of (001)Fe/(001)Cr magnetic superlattices”, *Physical Review Letters* **61**, 2472–2475 (1988), DOI: 10/bwp×zk.
- [4] E. Beaurepaire et al., “Ultrafast spin dynamics in ferromagnetic nickel”, *Physical Review Letters* **76**, 4250–4253 (1996), DOI: 10/b2z8dz.
- [5] S. A. Wolf et al., “Spintronics: a spin-based electronics vision for the future”, *Science* **294**, 1488–1495 (2001), DOI: 10/bjg×9x.
- [6] S. Maekawa et al., “Spin and spin current—from fundamentals to recent progress”, *Journal of Applied Physics* **133**, 20902 (2023), DOI: 10/gtwn5f.
- [7] C. D. Stanciu et al., “All-optical magnetic recording with circularly polarized light”, *Physical Review Letters* **99**, 47601 (2007), DOI: 10/cj8628.
- [8] M. Fähnle, “Review of ultrafast demagnetization after femtosecond laser pulses: a complex interaction of light with quantum matter”, *American Journal of Modern Physics* **7**, 68 (2018), DOI: 10/gfjz7p.
- [9] S. R. Tauchert et al., “Polarized phonons carry angular momentum in ultrafast demagnetization”, *Nature* **602**, 73–77 (2022), DOI: 10/gpb9ss.
- [10] A. Eschenlohr et al., “Ultrafast spin transport as key to femtosecond demagnetization”, *Nature Materials* **12**, 332–336 (2013), DOI: 10/f22dhd.
- [11] M. Battiato, K. Carva, and P. M. Oppeneer, “Theory of laser-induced ultrafast superdiffusive spin transport in layered heterostructures”, *Physical Review B* **86**, 24404 (2012), DOI: 10/f24fw6.
- [12] A. V. Chumak et al., “Magnon spintronics”, *Nature Physics* **11**, 453–461 (2015), DOI: 10/gfvz4n.
- [13] A. Mahmoud et al., “Introduction to spin wave computing”, *Journal of Applied Physics* **128**, 161101 (2020), DOI: 10/gnqwfg.
- [14] O. Gomonay et al., “Antiferromagnetic spin textures and dynamics”, *Nature Physics* **14**, 213–216 (2018), DOI: 10/gmcmfb.

-
- [15] M. B. Jungfleisch, W. Zhang, and A. Hoffmann, “Perspectives of antiferromagnetic spintronics”, *Physics Letters A* **382**, 865–871 (2018), DOI: 10/gc6pz9.
- [16] T. Kampfrath et al., “Coherent terahertz control of antiferromagnetic spin waves”, *Nature Photonics* **5**, 31–34 (2011), DOI: 10/b4q7b6.
- [17] T. Kampfrath et al., “Ultrafast and terahertz spintronics: guest editorial”, *Applied Physics Letters* **123**, 50401 (2023), DOI: 10/gtwn5b.
- [18] C. Evain et al., “Stable coherent terahertz synchrotron radiation from controlled relativistic electron bunches”, *Nature Physics* **15**, 635–639 (2019), DOI: 10/gk4dhx.
- [19] T. S. Seifert et al., “Terahertz spectroscopy for all-optical spintronic characterization of the spin-hall-effect metals Pt, W and $\text{Cu}_{80}\text{Ir}_{20}$ ”, *Journal of Physics D: Applied Physics* **51**, 364003 (2018), DOI: 10/ggkp47.
- [20] T. S. Seifert et al., “Femtosecond formation dynamics of the spin seebeck effect revealed by terahertz spectroscopy”, *Nature Communications* **9**, 2899 (2018), DOI: 10/gdzvbq.
- [21] T. Seifert et al., “Efficient metallic spintronic emitters of ultrabroadband terahertz radiation”, *Nature Photonics* **10**, 483–488 (2016), DOI: 10/f3rr77.
- [22] T. Seifert et al., “Ultrabroadband single-cycle terahertz pulses with peak fields of 300 kV cm^{-1} from a metallic spintronic emitter”, *Applied Physics Letters* **110**, 252402 (2017), DOI: 10/gnpgc8.
- [23] X. Ropagnol et al., “Intense THz pulses with large ponderomotive potential generated from large aperture photoconductive antennas”, *Optics Express* **24**, 11299 (2016), DOI: 10/gtwn5h.
- [24] H. Hirori et al., “Single-cycle terahertz pulses with amplitudes exceeding 1 MV/cm generated by optical rectification in LiNbO_3 ”, *Applied Physics Letters* **98**, 91106 (2011), DOI: 10/fqjdhc.
- [25] T. H. Kim et al., “Coherently controlled spin precession in canted antiferromagnetic YFeO_3 using terahertz magnetic field”, *Applied Physics Express* **7**, 93007 (2014), DOI: 10/gft8nf.
- [26] S. Wienholdt, D. Hinzke, and U. Nowak, “THz switching of antiferromagnets and ferromagnets”, *Physical Review Letters* **108**, 247207 (2012), DOI: 10/grgkd8.
- [27] S. Baierl et al., “Terahertz-driven nonlinear spin response of antiferromagnetic nickel oxide”, *Physical Review Letters* **117**, 197201 (2016), DOI: 10/gcr634.
- [28] A. Pashkin et al., “Electric and magnetic terahertz nonlinearities resolved on the sub-cycle scale”, *New Journal of Physics* **15**, 65003 (2013), DOI: 10/gtj49x.
- [29] R. C. LeCraw, R. Wolfe, and J. W. Nielsen, “Ferromagnetic resonance in FeBO_3 , a green room-temperature ferromagnet”, *Applied Physics Letters* **14**, 352–354 (1969), DOI: 10/bfbct5.
- [30] A. D. Koulouklidis et al., “Observation of extremely efficient terahertz generation from mid-infrared two-color laser filaments”, *Nature Communications* **11**, 292 (2020), DOI: 10/ghwbzw.
- [31] W. R. Huang et al., “Highly efficient terahertz pulse generation by optical rectification in stoichiometric and cryo-cooled congruent lithium niobate”, *Journal of Modern Optics* **62**, 1486–1493 (2015), DOI: 10/gr7m23.
-

- [32] J. Kerr, "A new relation between electricity and light: dielectrified media birefringent", *The London, Edinburgh and Dublin philosophical magazine and journal of science* **50**, 337–348 (1875), DOI: 10/gr7m3f.
- [33] R. W. Boyd, *Nonlinear optics*, 3rd (Academic Press, Amsterdam ; Boston, 2008),
- [34] Y. V. G. S. Murti and C. Vijayan, *Physics of nonlinear optics* (Springer International Publishing, Cham, 2021), DOI: 10/mzqn.
- [35] G. New, *Introduction to nonlinear optics* (Cambridge University Press, Cambridge, 2014).
- [36] P. N. Butcher and D. Cotter, *The elements of nonlinear optics*, Cambridge Studies in Modern Optics 9 (Cambridge University Press, Cambridge ; New York, 1990),
- [37] F. A. Vallejo and L. M. Hayden, "Simplified model for optical rectification of broadband terahertz pulses in lossy waveguides including a new generalized expression for the coherence length", *Optics Express* **21**, 24398 (2013), DOI: 10/gr7m3d.
- [38] J. Hebling et al., "Velocity matching by pulse front tilting for large area THz-pulse generation", *Optics Express* **10**, 1161 (2002), DOI: 10/gkb564.
- [39] J. A. Fülöp et al., "Design of high-energy terahertz sources based on optical rectification", *Optics Express* **18**, 12311 (2010), DOI: 10/ccn4p3.
- [40] J. Hebling, "Derivation of the pulse front tilt caused by angular dispersion", *Optical and Quantum Electronics* **28**, 1759–1763 (1996), DOI: 10/dj3xtp.
- [41] Zs. Bor and B. Rácz, "Group velocity dispersion in prisms and its application to pulse compression and travelling-wave excitation", *Optics Communications* **54**, 165–170 (1985), DOI: 10/c58xrw.
- [42] Z. Bor, "Femtosecond pulse front tilt caused by angular dispersion", *Optical Engineering* **32**, 2501 (1993), DOI: 10/fk5hvs.
- [43] C.-C. Shih and A. Yariv, "A theoretical model of the linear electro-optic effect", *Journal of Physics C: Solid State Physics* **15**, 825–846 (1982), DOI: 10/bzbszd.
- [44] E. Wooten et al., "A review of lithium niobate modulators for fiber-optic communications systems", *IEEE Journal of Selected Topics in Quantum Electronics* **6**, 69–82 (2000), DOI: 10/cx44q2.
- [45] Y. Kim et al., "Investigation of THz birefringence measurement and calculation in Al_2O_3 and LiNbO_3 ", *Applied Optics* **50**, 2906 (2011), DOI: 10/dk6m6k.
- [46] D. E. Zelmon, D. L. Small, and D. Jundt, "Infrared corrected Sellmeier coefficients for congruently grown lithium niobate and 5 mol. % magnesium oxide-doped lithium niobate", *Journal of the Optical Society of America B* **14**, 3319 (1997), DOI: 10/fdbw8h.
- [47] Q. Meng et al., "Damage threshold of lithium niobate crystal under single and multiple femtosecond laser pulses: theoretical and experimental study", *Applied Physics A* **122**, 582 (2016), DOI: 10/gr7mz4.
- [48] F. Bach et al., "Laser induced damage studies of LiNbO_3 using 1030-nm, ultrashort pulses at 10-1000 kHz", *Optical Materials Express* **7**, 240 (2017), DOI: 10/gtwn46.
- [49] M. M. Hossain, "First-principles study on the structural, elastic, electronic and optical properties of LiNbO_3 ", *Heliyon* **5**, e01436 (2019), DOI: 10/gq6zm2.

- [50] Y.-S. Lee et al., “Temperature dependence of narrow-band terahertz generation from periodically poled lithium niobate”, *Applied Physics Letters* **77**, 1244–1246 (2000), DOI: 10/b7nz4k.
- [51] J.-i. Shikata et al., “Enhancement of terahertz-wave output from LiNbO₃ optical parametric oscillators by cryogenic cooling”, *Optics Letters* **24**, 202 (1999), DOI: 10/ctqkxg.
- [52] D. R. Bosomworth, “The far infrared optical properties of LiNbO₃”, *Applied Physics Letters* **9**, 330–331 (1966), DOI: 10/cvzh6x.
- [53] X. Wu et al., “Temperature dependent refractive index and absorption coefficient of congruent lithium niobate crystals in the terahertz range”, *Optics Express* **23**, 29729 (2015), DOI: 10/gj3b85.
- [54] S.-W. Huang et al., “High conversion efficiency, high energy terahertz pulses by optical rectification in cryogenically cooled lithium niobate”, *Optics Letters* **38**, 796 (2013), DOI: 10/gnfnvf.
- [55] C. Herzog, G. Poberaj, and P. Günter, “Electro-optic behavior of lithium niobate at cryogenic temperatures”, *Optics Communications* **281**, 793–796 (2008), DOI: 10/bg3kvt.
- [56] J. van Tilborg, “Coherent terahertz radiation from laser-wakefield-accelerated electron beams”, PhD thesis (Technische Universiteit Eindhoven, 2006), DOI: 10/gf32rx.
- [57] J. Lau et al., “Millimeter-wave antireflection coating for cryogenic silicon lenses”, *Applied Optics* **45**, 3746 (2006), DOI: 10/cs44hb.
- [58] F. D. J. Brunner and T. Feurer, “Antireflection coatings optimized for single-cycle THz pulses”, *Applied Optics* **52**, 3829 (2013), DOI: 10/gsbn7k.
- [59] Y.-F. Zhong et al., “Measurement of stress optical coefficient for silicone adhesive based on terahertz time domain spectroscopy”, *Photonics* **9**, 929 (2022), DOI: 10/gsbprn.
- [60] K. Ravi et al., “Limitations to THz generation by optical rectification using tilted pulse fronts”, *Optics Express* **22**, 20239 (2014), DOI: 10/gknbnw.
- [61] M. Cronin-Golomb, “Cascaded nonlinear difference-frequency generation of enhanced terahertz wave production”, *Optics Letters* **29**, 2046 (2004), DOI: 10/b225xq.
- [62] H. Haus, “Power-flow relations in lossless nonlinear media”, *IEEE Transactions on Microwave Theory and Techniques* **6**, 317–324 (1958), DOI: 10/d2m9tx.
- [63] H. B. Callen, “A note on the Manley-Rowe energy relations for parametric amplifiers”, *Journal of the Franklin Institute* **269**, 93–96 (1960), DOI: 10/bctfjf.
- [64] J. Ma et al., “Origin and suppression of back conversion in a phase-matched nonlinear frequency down-conversion process”, *Chinese Optics Letters* **15**, 21901–21904 (2017), DOI: 10/gr9wx3.
- [65] K. Ravi et al., “Theory of terahertz generation by optical rectification using tilted-pulse-fronts”, *Optics Express* **23**, 5253 (2015), DOI: 10/gnfnvx.
- [66] L. Tokodi, J. Hebling, and L. Pálfalvi, “Optimization of the tilted-pulse-front terahertz excitation setup containing telescope”, *Journal of Infrared, Millimeter, and Terahertz Waves* **38**, 22–32 (2017), DOI: 10/f9njft.
- [67] W. R. Huang et al., “Toward a terahertz-driven electron gun”, *Scientific Reports* **5**, 14899 (2015), DOI: 10/gnfns9.

- [68] X. Wu et al., “Generation of 100-GHz radiation in lithium niobate driven by 4.7-ps, 22-mJ, 1030-nm Yb:YAG laser pulses”, in Conference on Lasers and Electro-Optics, Conference on Lasers and Electro-Optics (June 5, 2016), FTh3M.6, DOI: 10/gtwn5m.
- [69] M. Hemmer et al., “Efficient extraction from a multi-pass Yb:YAG amplifier via multi-pulse amplification”, in Conference on Lasers and Electro-Optics Europe (June 2019), pp. 1–1, DOI: 10/gr7m5t.
- [70] M. Naftaly and R. Dudley, “Terahertz reflectivities of metal-coated mirrors”, Applied Optics **50**, 3201 (2011), DOI: 10/fpzntk.
- [71] X. Wu et al., *Half-percent terahertz generation efficiency from cryogenically cooled lithium niobate pumped by Ti:sapphire laser pulses*, (2016) DOI: 10/mzqp, preprint.
- [72] X. Wu et al., “Terahertz generation in lithium niobate driven by Ti:sapphire laser pulses and its limitations”, Optics Letters **39**, 5403 (2014), DOI: 10/gfvqgx.
- [73] A. E. Siegman, “How to (maybe) measure laser beam quality”, in Diode Pumped Solid State Lasers: Applications and Issues (1998), MQ1, DOI: 10/gmh35.
- [74] Y. Mou et al., “Determination of the complex refractivity of Au, Cu and Al in terahertz and far-infrared regions from reflection spectra measurements”, Infrared Physics and Technology **80**, 58–64 (2017), DOI: 10/gr7m57.
- [75] M. Zahn, *Electromagnetic field theory: a problem solving approach* (MIT OpenCourseWare, June 1, 2003).
- [76] K. Ho et al., “Propagation in lossy rectangular waveguides”, in *Electromagnetic Waves Propagation in Complex Matter*, edited by A. Kishk (InTech, June 24, 2011), DOI: 10/mzqq.
- [77] R. Waldron, “Theory of reflections in a tapered waveguide”, Radio and Electronic Engineer **32**, 245 (1966), DOI: 10/cxhw2k.
- [78] *CST Studio Suite*, version 2020, Dassault Systèmes, 2020.
- [79] I. Bernal, C. W. Struck, and J. G. White, “New transition metal borates with the calcite structure”, Acta Crystallographica **16**, 849–850 (1963), DOI: 10/fd2q75.
- [80] M. P. Petrov et al., “Nuclear magnetic resonance and magnetic properties of FeBO₃-type crystals”, in Magnetism and Magnetic Materials, Vol. 5, AIP Conference Proceedings (1972), pp. 379–391, DOI: 10/gssp87.
- [81] I. Dzyaloshinsky, “A thermodynamic theory of “weak” ferromagnetism of antiferromagnetics”, Journal of Physics and Chemistry of Solids **4**, 241–255 (1958), DOI: 10/b8g96k.
- [82] N. M. Salanskii, E. A. Glozman, and V. N. Selenzev, “NMR and domain structure in thin single crystals of FeBO₃ and Fe_{1-x}Ga_xBO₃”, physica status solidi (a) **36**, 779–782 (1976), DOI: 10/c7fgd4.
- [83] J. Schober, “Precession modes and resonance absorption in the canted antiferromagnet FeBO₃”, IEEE Transactions on Magnetics **12**, 401–404 (1976), DOI: 10/bz7zgz.
- [84] E. A. Mashkovich et al., “Terahertz optomagnetism: nonlinear THz excitation of GHz spin waves in antiferromagnetic FeBO₃”, Physical Review Letters **123**, 157202 (2019), DOI: 10/ggnt38.

- [85] A. K. Zvezdin et al., “Ultrafast spin dynamics in the iron borate easy-plane weak ferromagnet”, *Journal of Experimental and Theoretical Physics* **131**, 130–138 (2020), DOI: 10/g52kq5.
- [86] A. M. Kalashnikova et al., “Impulsive excitation of coherent magnons and phonons by subpicosecond laser pulses in the weak ferromagnet FeBO_3 ”, *Physical Review B* **78**, 104301 (2008), DOI: 10/d6x4q8.
- [87] P. Němec et al., “Antiferromagnetic opto-spintronics”, *Nature Physics* **14**, 229–241 (2018), DOI: 10/gc6pv4.
- [88] P. S. Pershan, “Magneto-optical effects”, *Journal of Applied Physics* **38**, 1482–1490 (1967), DOI: 10/fkw7k3.
- [89] G. A. Smolenskiĭ, R. V. Pisarev, and I. G. Siniĭ, “Birefringence of light in magnetically ordered crystals”, *Soviet Physics Uspekhi* **18**, 410–429 (1975), DOI: 10/dg76nx.
- [90] I. Sh. Akhmadullin et al., “Magnetic birefringence of light in hematite”, *Physics of the Solid State* **44**, 333–337 (2002), DOI: 10/dkq56g.
- [91] A. J. Kurtzig et al., “Magneto-optical properties of a green room-temperature ferromagnet: FeBO_3 ”, *Applied Physics Letters* **14**, 350–352 (1969), DOI: 10/bnzqc7.
- [92] A. M. Kalashnikova et al., “Impulsive generation of coherent magnons by linearly polarized light in the easy-plane antiferromagnet FeBO_3 ”, *Physical Review Letters* **99**, 167205 (2007), DOI: 10/ddhmxs.
- [93] V. V. Tarakanov et al., “Excitation of magnetic polaritons in plates of FeBO_3 ”, *Physica B: Condensed Matter* **284–288**, 1452–1453 (2000), DOI: 10/fgc5s5.
- [94] W. Jantz and W. Wettleing, “Spin wave dispersion of FeBO_3 at small wavevectors”, *Applied Physics* **15**, 399–407 (1978), DOI: 10/c8qnbq.
- [95] R. B. Goldfarb, “The permeability of vacuum and the revised international system of units”, *IEEE Magnetics Letters* **8**, 1–3 (2017), DOI: 10/gct978.
- [96] J. M. D. Coey, *Magnetism and magnetic materials* (Cambridge University Press, Cambridge, 2010), DOI: 10/gdxxkp.
- [97] C. Soliv erez, *Electrostatics and magnetostatics of polarized ellipsoidal bodies: the depolarization tensor method* (July 15, 2016).
- [98] R. Prozorov and V. G. Kogan, “Effective demagnetizing factors of diamagnetic samples of various shapes”, *Physical Review Applied* **10**, 14030 (2018), DOI: 10/gd2vd8.
- [99] K. M. Krishnan, *Fundamentals and applications of magnetic materials*, First edition (Oxford University Press, Oxford, United Kingdom, 2016),
- [100] B. Friedrich et al., “One hundred years of Alfred Land e’s g-factor”, *Natural Sciences* **1**, e20210068 (2021), DOI: 10/gr7m37.
- [101] A. Blom, “Exact solution of the Zeeman effect in single-electron systems”, *Physica Scripta* **T120**, 90–98 (2005), DOI: 10/bxj92g.
- [102] A. Kramida and Y. Ralchenko, *NIST atomic spectra database, NIST standard reference database 78*, version 5.11 (National Institute of Standards and Technology, 1999), DOI: 10/dmk4.

- [103] L. H. Thomas, “The motion of the spinning electron”, *Nature* **117**, 514–514 (1926), DOI: 10/fp38vv.
- [104] G. Spavieri and M. Mansuripur, “Origin of the spin–orbit interaction”, *Physica Scripta* **90**, 85501 (2015), DOI: 10/gf6322.
- [105] J. M. D. Coey and S. S. Parkin, eds., *Handbook of magnetism and magnetic materials*, Springer Nature Reference (Springer, Cham, 2021), DOI: 10/mzqw.
- [106] J. D. Morgan and W. Kutzelnigg, “Hund’s rules, the alternating rule, and symmetry holes”, *Journal of Physical Chemistry* **97**, 2425–2434 (1993), DOI: 10/df5dwf.
- [107] G. Brooker, “LS coupling; hund’s rules”, in *Essays in Physics: Thirty-two thoughtful essays on topics in undergraduate-level physics*, edited by G. Brooker (Oxford University Press, July 16, 2021), pp. 191–202, DOI: 10/gr7m27.
- [108] B. R. Judd, “Group theory in atomic and molecular physics”, in *Symmetries in Science*, edited by B. Gruber and R. S. Millman (Springer US, Boston, MA, 1980), pp. 151–160, DOI: 10/mzqr.
- [109] K. W. H. Stevens, “Matrix elements and operator equivalents connected with the magnetic properties of rare earth ions”, *Proceedings of the Physical Society. Section A* **65**, 209–215 (1952), DOI: 10/bzc2z4.
- [110] B. Bleaney and K. W. H. Stevens, “Paramagnetic resonance”, *Reports on Progress in Physics* **16**, 108–159 (1953), DOI: 10/c6mzzm.
- [111] Z. Song and Q. Liu, “Basic crystal field theory—a simple and useful tool to understand the structure–property relationship in luminescent materials”, *Optical Materials: X* **16**, 100189 (2022), DOI: 10/gtwn5j.
- [112] B. Andlauer, J. Schneider, and W. Wuttling, “Optical and magneto-optical properties of YIG and FeBO₃”, *Applied Physics* **10**, 189–201 (1976), DOI: 10/dcpzfs.
- [113] S. G. Ovchinnikov and V. N. Zabluda, “The energy band structure and optical spectra of FeBO₃ calculated with allowance for strong electron correlations”, *Journal of Experimental and Theoretical Physics* **98**, 135–143 (2004), DOI: 10/cgd8j2.
- [114] M. Hutchings, “Point-charge calculations of energy levels of magnetic ions in crystalline electric fields”, in *Solid State Physics*, Vol. 16 (Elsevier, 1964), pp. 227–273, DOI: 10/dm46ht.
- [115] D. Pincini et al., “Role of the orbital moment in a series of isostructural weak ferromagnets”, *Physical Review B* **98**, 104424 (2018), DOI: 10/gjd942.
- [116] M.-C. Desjonquères et al., “Orbital contribution to the magnetic properties of iron as a function of dimensionality”, *Physical Review B* **76**, 24412 (2007), DOI: 10/bw47dd.
- [117] Z. Luo and Y. Huang, *Physics of solid-state laser materials*, Vol. 289, Springer Series in Materials Science (Springer Singapore, Singapore, 2020), DOI: 10/mzqz.
- [118] D. E. Dugdale, “The theoretical basis of spin hamiltonian theory”, *Journal of Physics: Condensed Matter* **5**, 7837–7846 (1993), DOI: 10/c9cps4.
- [119] K. Yosida, “On the antiferromagnetism of single crystals”, *Progress of Theoretical Physics* **6**, 691–701 (1951), DOI: 10/gtwn5n.
- [120] J. H. Van Vleck, “On the anisotropy of cubic ferromagnetic crystals”, *Physical Review* **52**, 1178–1198 (1937), DOI: 10/bh7cb8.

- [121] G. V. D. Laan, “Microscopic origin of magnetocrystalline anisotropy in transition metal thin films”, *Journal of Physics: Condensed Matter* **10**, 3239–3253 (1998), DOI: 10/fsh24s.
- [122] M. Mostafanejad, “Basics of the spin hamiltonian formalism”, *International Journal of Quantum Chemistry* **114**, 1495–1512 (2014), DOI: 10/gmwrwd.
- [123] G. Borghi, M. Fabrizio, and E. Tosatti, *Self-consistent Gutzwiller study of bcc Fe: interplay of ferromagnetic order and kinetic energy*, (July 22, 2013) DOI: 10/mzqt, preprint.
- [124] Y. O. Kvashnin et al., “Microscopic origin of Heisenberg and non-Heisenberg exchange interactions in ferromagnetic bcc Fe”, *Physical Review Letters* **116**, 217202 (2016), DOI: 10/f3r33c.
- [125] Y. Wang et al., “First-principles thermodynamic theory of Seebeck coefficients”, *Physical Review B* **98**, 224101 (2018), DOI: 10/gkq37m.
- [126] L. Landau, “Diamagnetismus der Metalle”, *Zeitschrift für Physik* **64**, 629–637 (1930), DOI: 10/dkft3h.
- [127] S. Blundell, *Magnetism in condensed matter*, Vol. 71, Oxford Master Series in Physics (Oxford University Press, Oct. 4, 2001), DOI: 10/mzq2.
- [128] G. Castellano, “Thermodynamic potentials for simple magnetic systems”, *Journal of Magnetism and Magnetic Materials* **260**, 146–150 (2003), DOI: 10/cgdx49.
- [129] N. Ganguli and K. S. Krishnan, “Magnetic and other properties of the free electrons in graphite”, *Proceedings of the Royal Society of London. Series A. Mathematical and Physical Sciences* **177**, 168–182 (1941), DOI: 10/b87832.
- [130] P. Langevin, “Sur la théorie du magnétisme”, *Journal de Physique Théorique et Appliquée* **4**, 678–693 (1905), DOI: 10/cgpkmq.
- [131] P. Curie, “Propriétés magnétiques des corps à diverses températures”, *Annales de chimie et de physique* **5**, 289–405 (1985).
- [132] J. H. Van Vleck, “Quantum mechanics: the key to understanding magnetism”, *Science* **201**, 113–120 (1978), DOI: 10/bxznsww.
- [133] J. Stöhr and H. C. Siegmann, *Magnetism: from fundamentals to nanoscale dynamics*, Springer Series in Solid-State Sciences 152 (Springer, Berlin ; New York, 2006),
- [134] O. Gunnarsson, “Band model for magnetism of transition metals in the spin-density-functional formalism”, *Journal of Physics F: Metal Physics* **6**, 587–606 (1976), DOI: 10/fd57xs.
- [135] A. Oleś and G. Stollhoff, “Influence of electron correlation on the Stoner parameter and on magnetovolume effect in ferromagnetic transition metals”, *Journal of Magnetism and Magnetic Materials* **54–57**, 1045–1046 (1986), DOI: 10/b4qcjc.
- [136] J. H. Wood, “Wave functions for iron d band”, *Physical Review* **117**, 714–718 (1960), DOI: 10/ccgjpb.
- [137] V. E. Dmitrienko et al., “An X-ray study of the Dzyaloshinskii-Moriya interaction in the weak ferromagnet FeBO₃”, *Journal of Physics: Conference Series* **519**, 12003 (2014), DOI: 10/gsst7g.

- [138] W. Jantz, J. R. Sandercock, and W. Wettleing, “Investigation of FeBO₃ by brillouin scattering from thermal magnons”, in *AIP Conference Proceedings*, Vol. 29 (1976), pp. 268–269, DOI: 10/ffq5tm.
- [139] T. Moriya, “New mechanism of anisotropic superexchange interaction”, *Physical Review Letters* **4**, 228–230 (1960), DOI: 10/bkn7wf.
- [140] M. T. Johnson et al., “Magnetic anisotropy in metallic multilayers”, *Reports on Progress in Physics* **59**, 1409–1458 (1996), DOI: 10/fc73vf.
- [141] L. Néel, “Anisotropie magnétique superficielle et surstructures d’orientation”, *Journal de Physique et le Radium* **15**, 225–239 (1954), DOI: 10/brjgff.
- [142] V. E. Dmitrienko et al., “Measuring the Dzyaloshinskii–Moriya interaction in a weak ferromagnet”, *Nature Physics* **10**, 202–206 (2014), DOI: 10/f5tzv7.
- [143] R. Diehl et al., “Growth and properties of iron borate, FeBO₃”, in *Current Topics in Materials Science*, Vol. 11, red. by E. Kaldis (North-Holland Pub. Co., Netherlands, 1984), pp. 241–387.
- [144] F. B. Hagedorn and E. M. Gyorgy, “Complex susceptibility and resonance frequencies of canted antiferromagnets”, *Physical Review* **174**, 540–545 (1968), DOI: 10/cwr fm4.
- [145] A. Gurevich and G. Melkov, *Magnetization oscillations and waves*, 1st ed. (CRC Press, London, 1996), DOI: 10/mzq3.
- [146] A. Borovik-Romanov and N. Kreines, “Brillouin-mandelstam scattering from thermal and excited magnons”, *Physics Reports* **81**, 351–408 (1982), DOI: 10/cf42h9.
- [147] L. V. Velikov et al., “High-frequency antiferromagnetic resonance in iron borate (FeBO₃)”, *Soviet Journal of Experimental and Theoretical Physics Letters* **15**, 511 (1972).
- [148] L. Bocklage, “The ferromagnetic resonance condition of FeBO₃”, private communication, Hamburg, Oct. 1, 2018.
- [149] G. Herrmann, “Resonance and high frequency susceptibility in canted antiferromagnetic substances”, *Journal of Physics and Chemistry of Solids* **24**, 597–606 (1963), DOI: 10/fg7jwp.
- [150] E. Beaupaire et al., “Coherent terahertz emission from ferromagnetic films excited by femtosecond laser pulses”, *Applied Physics Letters* **84**, 3465–3467 (2004), DOI: 10/cx5m3q.
- [151] D. J. Hilton et al., “Terahertz emission via ultrashort-pulse excitation of magnetic metal films”, *Optics Letters* **29**, 1805 (2004), DOI: 10/cj3bvm.
- [152] B. Koopmans et al., “Explaining the paradoxical diversity of ultrafast laser-induced demagnetization”, *Nature Materials* **9**, 259–265 (2010), DOI: 10/fpx44j.
- [153] G. Malinowski et al., “Control of speed and efficiency of ultrafast demagnetization by direct transfer of spin angular momentum”, *Nature Physics* **4**, 855–858 (2008), DOI: 10/dpfrjf.
- [154] M. Battiato, K. Carva, and P. M. Oppeneer, “Superdiffusive spin transport as a mechanism of ultrafast demagnetization”, *Physical Review Letters* **105**, 27203 (2010), DOI: 10/b8vmsf.
- [155] T. Kampfrath et al., “Terahertz spin current pulses controlled by magnetic heterostructures”, *Nature Nanotechnology* **8**, 256–260 (2013), DOI: 10/f23wsh.

- [156] H. Wang, P.-W. Ma, and C. H. Woo, “Exchange interaction function for spin-lattice coupling in bcc iron”, *Physical Review B* **82**, 144304 (2010), DOI: 10/fkhs9c.
- [157] E. Carpena et al., “Ultrafast demagnetization of metals: collapsed exchange versus collective excitations”, *Physical Review B* **91**, 174414 (2015), DOI: 10/ggbg zr.
- [158] V. P. Zhukov, E. V. Chulkov, and P. M. Echenique, “Lifetimes of excited electrons In Fe and Ni: first-principles GW and the T-matrix theory”, *Physical Review Letters* **93**, 96401 (2004), DOI: 10/bvsk4h.
- [159] E. Carpena et al., “Dynamics of electron-magnon interaction and ultrafast demagnetization in thin iron films”, *Physical Review B* **78**, 174422 (2008), DOI: 10/dw64xw.
- [160] S. Mankovsky et al., “Angular momentum transfer via relativistic spin-lattice coupling from first principles”, *Physical Review Letters* **129**, 67202 (2022), DOI: 10/gr7m59.
- [161] V. P. Zhukov, E. V. Chulkov, and P. M. Echenique, “Lifetimes and inelastic mean free path of low-energy excited electrons in Fe, Ni, Pt, and Au: *ab initio* GW + T calculations”, *Physical Review B* **73**, 125105 (2006), DOI: 10/b4gp7b.
- [162] K. Bühlmann et al., “Detection of femtosecond spin voltage pulses in a thin iron film”, *Structural Dynamics* **7**, 65101 (2020), DOI: 10/gr7m36.
- [163] R. Rouzegar et al., “Laser-induced terahertz spin transport in magnetic nanostructures arises from the same force as ultrafast demagnetization”, *Physical Review B* **106**, 144427 (2022), DOI: 10/nkcx.
- [164] A. Kirilyuk, A. V. Kimel, and T. Rasing, “Ultrafast optical manipulation of magnetic order”, *Reviews of Modern Physics* **82**, 2731–2784 (2010), DOI: 10/b2w6zc.
- [165] R. Chimata et al., “Microscopic model for ultrafast remagnetization dynamics”, *Physical Review Letters* **109**, 157201 (2012), DOI: 10/f2z45p.
- [166] E. Kueny et al., “Spin-structured multilayer THz emitters by oblique incidence deposition”, *Journal of Applied Physics* **133**, 33903 (2023), DOI: 10/gr7m5v.
- [167] A. Fernandez-Pañella et al., “Reduction of electron-phonon coupling in warm dense iron”, *Physical Review B* **101**, 184309 (2020), DOI: 10/ghcdcg.
- [168] A. P. Caffrey et al., “Thin film non-noble transition metal thermophysical properties”, *Microscale Thermophysical Engineering* **9**, 365–377 (2005), DOI: 10/d4qjh4.
- [169] J. W. Arblaster, “Thermodynamic properties of tungsten”, *Journal of Phase Equilibria and Diffusion* **39**, 891–907 (2018), DOI: 10/gr7m4p.
- [170] N. Medvedev and I. Milov, “Electron-phonon coupling in metals at high electronic temperatures”, *Physical Review B* **102**, 64302 (2020), DOI: 10/ghcdb9.
- [171] C. Guillemard et al., “Charge-spin current conversion in high quality epitaxial Fe/Pt systems: isotropic spin hall angle along different in-plane crystalline directions”, *Applied Physics Letters* **113**, 262404 (2018), DOI: 10/gr7m33.
- [172] C.-F. Pai et al., “Spin transfer torque devices utilizing the giant spin hall effect of tungsten”, *Applied Physics Letters* **101**, 122404 (2012), DOI: 10/ggc4cg.
- [173] H. Zhao et al., “Coherence control of Hall charge and spin currents”, *Physical Review Letters* **96**, 246601 (2006), DOI: 10/b8w9jf.

- [174] E. Saitoh et al., “Conversion of spin current into charge current at room temperature: inverse spin-Hall effect”, *Applied Physics Letters* **88**, 182509 (2006), DOI: 10/d7x366.
- [175] S. O. Valenzuela and M. Tinkham, “Direct electronic measurement of the spin hall effect”, *Nature* **442**, 176–179 (2006), DOI: 10/btqxp7.
- [176] B. F. Miao et al., “Inverse spin Hall effect in a ferromagnetic metal”, *Physical Review Letters* **111**, 66602 (2013), DOI: 10/gkgcvd.
- [177] Y.-H. Huang et al., “Spin hall angle and spin diffusion length of permalloy”, *AIP Advances* **10**, 15041 (2020), DOI: 10/gm93fm.
- [178] A. Hoffmann, “Spin Hall effects in metals”, *IEEE Transactions on Magnetics* **49**, 5172–5193 (2013), DOI: 10/f5bt68.
- [179] S. Maekawa, S. O. Valenzuela, and E. Saitoh, eds., *Spin current*, Second edition, Oxford Science Publications 22 (Oxford University Press, Oxford, United Kingdom, 2017),
- [180] T. Seifert et al., “Terahertz spin currents and inverse spin hall effect in thin-film heterostructures containing complex magnetic compounds”, *Spin* **7**, 1740010 (2017), DOI: 10/gfjz7c.
- [181] J.-C. Rojas-Sánchez et al., “Spin pumping and inverse spin Hall effect in platinum: the essential role of spin-memory loss at metallic interfaces”, *Physical Review Letters* **112**, 106602 (2014), DOI: 10/ggc33q.
- [182] M. Wawrzyniak and J. Barnaś, “Influence of interface spin-flip processes on spin accumulation and spin currents in magnetic multilayers”, *Materials Science-Poland* **Vol. 22, No. 4**, 8 (2004).
- [183] O. Gueckstock et al., “Terahertz spin-to-charge conversion by interfacial skew scattering in metallic bilayers”, *Advanced Materials* **33**, 2006281 (2021), DOI: 10/gr7m3x.
- [184] T. S. Seifert et al., “Spintronic sources of ultrashort terahertz electromagnetic pulses”, *Applied Physics Letters* **120**, 180401 (2022), DOI: 10/grvcz7.
- [185] J. Faure et al., “Modelling laser-based table-top THz sources: optical rectification, propagation and electro-optic sampling”, *Optical and Quantum Electronics* **36**, 681–697 (2004), DOI: 10/d5x5pb.
- [186] S. Chikazumi, C. D. Graham, and S. Chikazumi, *Physics of ferromagnetism*, 2nd ed, The International Series of Monographs on Physics 94 (Clarendon Press ; Oxford University Press, Oxford : New York, 1997),
- [187] Q. Zhang et al., “Terahertz emission from an exchange-coupled synthetic antiferromagnet”, *Physical Review Applied* **13**, 54016 (2020), DOI: 10/gr7m38.
- [188] M. Fix et al., “Spin valves as magnetically switchable spintronic THz emitters”, *Applied Physics Letters* **117**, 132407 (2020), DOI: 10/ghj33r.
- [189] T. G. Knorr and R. W. Hoffman, “Dependence of geometric magnetic anisotropy in thin iron films”, *Physical Review* **113**, 1039–1046 (1959), DOI: 10/d2d7j7.
- [190] D. O. Smith, “Anisotropy in permalloy films”, *Journal of Applied Physics* **30**, S264–S265 (1959), DOI: 10/bk7pt7.
- [191] K. Schlage et al., “Spin-structured multilayers: a new class of materials for precision spintronics”, *Advanced Functional Materials* **26**, 7423–7430 (2016), DOI: 10/f3rdtn.

- [192] D. Lundin and J. T. Gudmundsson, eds., *High power impulse magnetron sputtering: fundamentals, technologies, challenges and applications*, 1st ed. (Elsevier, Cambridge, 2019).
- [193] D. O. Smith, M. S. Cohen, and G. P. Weiss, “Oblique-incidence anisotropy in evaporated permalloy films”, *Journal of Applied Physics* **31**, 1755–1762 (1960), DOI: 10/ch8mhj.
- [194] A. Dirks and H. Leamy, “Columnar microstructure in vapor-deposited thin films”, *Thin Solid Films* **47**, 219–233 (1977), DOI: 10/fv5v8p.
- [195] R. Tait, T. Smy, and M. Brett, “Modelling and characterization of columnar growth in evaporated films”, *Thin Solid Films* **226**, 196–201 (1993), DOI: 10/dxjgvt.
- [196] J. M. Nieuwenhuizen and H. B. Haanstra, “Microfractography of thin films”, *Philips Technical Review* **27**, 87–91 (1966).
- [197] A. Barranco et al., “Perspectives on oblique angle deposition of thin films: from fundamentals to devices”, *Progress in Materials Science* **76**, 59–153 (2016), DOI: 10/gm3gkh.
- [198] S. Willing, “Oblique-incidence deposition of ferromagnetic thin films and their application in magnetoresistive sensors”, PhD thesis (Dissertation, University of Hamburg, 2020, 2020).
- [199] J. L. Bubendorff et al., “Origin of the magnetic anisotropy in ferromagnetic layers deposited at oblique incidence”, *Europhysics Letters (EPL)* **75**, 119–125 (2006), DOI: 10/dh7357.
- [200] Y. Hoshi and E. Suzuki, “Changes in angular distribution of incident sputtered particles in sputter deposition of iron films”, *Journal of the Magnetism Society of Japan* **18**, S1_323–326 (1994), DOI: 10/btr79s.
- [201] M. Ortner and L. G. Coliada Bandeira, “Magpylib: a free python package for magnetic field computation”, *SoftwareX* **11**, 100466 (2020), DOI: 10/gr7mx5.
- [202] S. J. Byrnes, *Multilayer optical calculations*, version 5, (Dec. 30, 2020) DOI: 10/gr7m52, preprint.
- [203] A.-L. Calendron et al., “Bulk, cascaded pulse compression scheme and its application to spin emitter characterization”, *Applied Optics* **60**, 912–917 (2021), DOI: 10/gr7m39.
- [204] R. Del Coso and J. Solis, “Relation between nonlinear refractive index and third-order susceptibility in absorbing media”, *Journal of the Optical Society of America B* **21**, 640 (2004), DOI: 10/dfnj4v.
- [205] P. Lassonde et al., “High energy femtosecond pulse compression”, *Laser Physics Letters* **13**, 75401 (2016), DOI: 10/f8s3rz.
- [206] S. Kumar et al., “Optical damage limit of efficient spintronic THz emitters”, *iScience* **24**, 103152 (2021), DOI: 10/gm5t3f.
- [207] S. Mukhopadhyay et al., “Investigation of ultrafast demagnetization and gilbert damping and their correlation in different ferromagnetic thin films grown under identical conditions”, *Nanotechnology* **34**, 235702 (2023), DOI: 10/gtwn5g.
- [208] S. Zhang et al., “Bursts of efficient terahertz radiation with saturation effect from metal-based ferromagnetic heterostructures”, *Journal of Physics D: Applied Physics* **51**, 34001 (2018), DOI: 10/gr7m58.

- [209] X. Zhang et al., “Understanding thermal annealing of artificial spin ice”, *APL Materials* **7**, 111112 (2019), DOI: 10/gtwn5p.
- [210] J. A. Murphy, “Distortion of a simple gaussian beam on reflection from off-axis ellipsoidal mirrors”, *International Journal of Infrared and Millimeter Waves* **8**, 1165–1187 (1987), DOI: 10/bxmgq.
- [211] Y. Ogasawara et al., “Laser-induced terahertz emission from layered synthetic magnets”, *Applied Physics Express* **13**, 63001 (2020), DOI: 10/gr7m5s.
- [212] D. Yang et al., “Powerful and tunable THz emitters based on the Fe/Pt magnetic heterostructure”, *Advanced Optical Materials* **4**, 1944–1949 (2016), DOI: 10/gnpgdg.
- [213] D. Y. Petrovykh et al., “Spin-dependent band structure, fermi surface, and carrier lifetime of permalloy”, *Applied Physics Letters* **73**, 3459–3461 (1998), DOI: 10/fdcp9f.
- [214] K. E. Oughstun and C. L. Palombini, “Fresnel reflection and transmission coefficients for temporally dispersive attenuative media”, *Radio Science* **53**, 1382–1397 (2018), DOI: 10/gr7m54.
- [215] A. Fognini et al., “Ultrafast reduction of the total magnetization in iron”, *Applied Physics Letters* **104**, 32402 (2014), DOI: 10/gtwn48.
- [216] G. Li et al., “THz emission from Co/Pt bilayers with varied roughness, crystal structure, and interface intermixing”, *Physical Review Materials* **3**, 84415 (2019), DOI: 10/gr7m3z.
- [217] J.-G. Wang et al., “Form birefringence in thin films with oblique columnar structures”, *Chinese Physics Letters* **22**, 2066–2068 (2005), DOI: 10/fc5dv3.
- [218] F. Ahr, “High energy multi-cycle terahertz generation”, PhD thesis (Universität Hamburg, 2017), DOI: 10/mx3s.
- [219] P. U. Jepsen and B. M. Fischer, “Dynamic range in terahertz time-domain transmission and reflection spectroscopy”, *Optics Letters* **30**, 29 (2005), DOI: 10/cpc23s.
- [220] R. Peretti et al., “THz-TDS time-trace analysis for the extraction of material and metamaterial parameters”, *IEEE Transactions on Terahertz Science and Technology* **9**, 136–149 (2019), DOI: 10/gf5dwk.
- [221] J. Liu et al., “Characterization of dielectric function for metallic thin films based on ellipsometric parameters and reflectivity”, *Physica Scripta* **94**, 85802 (2019), DOI: 10/gf75cw.
- [222] V. V. Gozhenko and A. O. Pinchuk, “On the choice of the phase constant of the fresnel transmission coefficient of a slab”, *Journal of Optics* **14**, 35705 (2012), DOI: 10/ggffrp.
- [223] G. A. Komandin et al., “Dielectric loss of thin-film SiO₂ samples on Al in THz–IR range”, *Physics of the Solid State* **62**, 267–272 (2020), DOI: 10/gh4279.
- [224] N. Chudpooti et al., “Wideband dielectric properties of silicon and glass substrates for terahertz integrated circuits and microsystems”, *Materials Research Express* **8**, 056201 (2021), DOI: 10/gtwn47.
- [225] A. Markelz, *Temperature dependent THz index for fused silica*, 4 (2015).
- [226] M. Naftaly and R. E. Miles, “Terahertz time-domain spectroscopy of silicate glasses and the relationship to material properties”, *Journal of Applied Physics* **102**, 43517 (2007), DOI: 10/bfv7x4.

- [227] V. D. Antsygin et al., “Terahertz optical properties of potassium titanyl phosphate crystals”, *Optics Express* **22**, 25436–25443 (2014), DOI: 10/gn6wr7.
- [228] P. Mounaix et al., “Characterization of non-linear Potassium crystals in the Terahertz frequency domain”, *Optics Communications* **242**, 631–639 (2004), DOI: 10/bgcjj9.
- [229] P. D. Cunningham et al., “Broadband terahertz characterization of the refractive index and absorption of some important polymeric and organic electro-optic materials”, *Journal of Applied Physics* **109**, 43505-43505-5 (2011), DOI: 10/cq59t5.
- [230] D. R. Smith and E. V. Loewenstein, “Optical constants of far infrared materials 3: plastics”, *Applied Optics* **14**, 1335 (1975), DOI: 10/fg5pdg.
- [231] E. E. Russell and E. E. Bell, “Optical constants of sapphire in the far infrared”, *Journal of The Optical Society of America* **57**, 543 (1967), DOI: 10/cf42qb.
- [232] E. V. Loewenstein, “Optical properties of sapphire in the far infrared”, *Journal of The Optical Society of America* **51**, 108 (1961), DOI: 10/ct32r2.
- [233] A. S. Barker, “Infrared lattice vibrations and dielectric dispersion in corundum”, *Physical Review* **132**, 1474–1481 (1963), DOI: 10/dh4chv.
- [234] G. Ren et al., “Terahertz dielectric properties of single-crystal MgO”, *Infrared and Laser Engineering* **46**, 825001 (2017), DOI: 10/gr7m55.
- [235] E. Sondheimer, “The mean free path of electrons in metals”, *Advances in Physics* **1**, 1–42 (1952), DOI: 10/d3nrfq.
- [236] H. J. K. Kim et al., “Electrical properties of ultrathin platinum films by plasma-enhanced atomic layer deposition”, *ACS Applied Materials & Interfaces* **11**, 9594–9599 (2019), DOI: 10/gtwn5c.
- [237] M. Kockert et al., “Absolute Seebeck coefficient of thin platinum films”, *Journal of Applied Physics* **126**, 105106 (2019), DOI: 10/gh4tb8.
- [238] S. Keller et al., “Determination of the spin Hall angle in single-crystalline Pt films from spin pumping experiments”, *New Journal of Physics* **20**, 053002 (2018), DOI: 10/gtvc62.
- [239] M. Rubinstein et al., “Electrical transport properties of thin epitaxially grown iron films”, *Physical Review B* **37**, 8689–8700 (1988), DOI: 10/d6ttt3.
- [240] K. L. Krewer et al., “Thickness-dependent electron momentum relaxation times in iron films”, *Applied Physics Letters* **116**, 102406 (2020), DOI: 10/gr7m4h.
- [241] Y. K. Kim and M. Oliveria, “Magnetic properties of sputtered Fe thin films: processing and thickness dependence”, *Journal of Applied Physics* **74**, 1233–1241 (1993), DOI: 10/bn3j5p.
- [242] P. Petroff et al., “Microstructure, growth, resistivity, and stresses in thin tungsten films deposited by rf sputtering”, *Journal of Applied Physics* **44**, 2545–2554 (1973), DOI: 10/b8tbkv.
- [243] S. M. Rosnagel, I. C. Noyan, and C. Cabral Jr., “Phase transformation of thin sputter-deposited tungsten films at room temperature”, *Journal of Vacuum Science & Technology B: Microelectronics and Nanometer Structures Processing, Measurement, and Phenomena* **20**, 2047–2051 (2002), DOI: 10/cmgd7s.

- [244] Y. Zhong et al., “Optical and electrical properties of indium tin oxide thin films with tilted and spiral microstructures prepared by oblique angle deposition”, *Journal of Materials Research* **23**, 2500–2505 (2008), DOI: 10/cm4ghx.
- [245] T. S. Kuan et al., “Fabrication and performance limits of sub-0.1 μm Cu interconnects”, *MRS Online Proceedings Library* **612**, 711 (2000), DOI: 10/bv3x3j.
- [246] K. K. Tikuišis et al., “Optical and magneto-optical properties of permalloy thin films in 0.7–6.4 eV photon energy range”, *Materials & Design* **114**, 31–39 (2017), DOI: 10/gq3vwn.
- [247] P. Zheng and D. Gall, “The anisotropic size effect of the electrical resistivity of metal thin films: Tungsten”, *Journal of Applied Physics* **122**, 135301 (2017), DOI: 10/gtwn5q.
- [248] S. Casalbuoni et al., “Numerical studies on the electro-optic detection of femtosecond electron bunches”, *Physical Review Special Topics - Accelerators and Beams* **11**, 72802 (2008), DOI: 10/bt4d2k.
- [249] G. Gallot and D. Grischkowsky, “Electro-optic detection of terahertz radiation”, *Journal of the Optical Society of America B* **16**, 1204 (1999), DOI: 10/bd453w.
- [250] A. Leitenstorfer et al., “Detectors and sources for ultrabroadband electro-optic sampling: experiment and theory”, *Applied Physics Letters* **74**, 1516–1518 (1999), DOI: 10/frxm3q.
- [251] M. Izdebski, W. Kucharczyk, and R. E. Raab, “On relationships between electro-optic coefficients for impermeability and nonlinear electric susceptibilities”, *Journal of Optics A: Pure and Applied Optics* **6**, 421–424 (2004), DOI: 10/c3mh8w.
- [252] P. C. M. Planken et al., “Measurement and calculation of the orientation dependence of terahertz pulse detection in ZnTe”, *Journal of the Optical Society of America B* **18**, 313 (2001), DOI: 10/fqv8qr.
- [253] H. A. Bethe, “Theory of diffraction by small holes”, *Physical Review* **66**, 163–182 (1944), DOI: 10/bjss3k.
- [254] H. J. Bakker et al., “Distortion of terahertz pulses in electro-optic sampling”, *Journal of the Optical Society of America B* **15**, 1795 (1998), DOI: 10/bgcc74.
- [255] O. S. Heavens, *Optical properties of thin solid films* (Dover Publications, New York, 1965),
- [256] F. Abelès, “La théorie générale des couches minces”, *Journal de Physique et le Radium* **11**, 307–309 (1950), DOI: 10/ch2cjw.
- [257] W.-T. Lu et al., “Interface reflectivity of a superdiffusive spin current in ultrafast demagnetization and terahertz emission”, *Physical Review B* **101**, 14435 (2020), DOI: 10/gtwn5d.